Electrospun nanostructured composite fibres for hydrogen storage applications

A THESIS

submitted by

Zeynep Kurban

for the award of the degree

of

Engineering Doctorate

Department of Physics and Astronomy
University College London
England

March 2011

Declaration

I, Zeynep Kurban, confirm that the work presented in this thesis is my own. Where information has been derived from other sources, I confirm that this has been indicated in the thesis. The work in this thesis is based on research carried out at the following institutions in the UK: Rutherford Appleton Laboratory, Department of Physics and Astronomy at University College London, and Department of Chemistry at University of Oxford. No part of this thesis has been submitted elsewhere for any other degree or qualification.

Abstract

The urgent realisation of the low carbon economy requires the development of cheap, safe and lightweight hydrogen storage, both for commercialisation of hydrogen fuel cell vehicles, and for the use of hydrogen as a reservoir of energy from intermittent renewable energy sources. The primary motivation of this PhD project was to investigate (co)electrospinning, a cheap and scalable fibre production technique, for nanostructuring potential solid state hydrogen storage materials. Solid state storage of hydrogen is being extensively investigated worldwide. However, many of the candidate materials are still not able to meet the practical requirements for mobile applications. The principal drawbacks are that these materials either have low capacity for hydrogen storage (physisorption systems), even at cryogenic temperatures, or high release temperatures with slow release rates (chemisorption systems). Because kinetic and thermodynamic properties can be improved by nanoscale processing, nanoengineering of selected materials has emerged as one of the most effective ways of overcoming their associated performance barriers. In this thesis I present two successful approaches to nanostructuring using electrospinning: firstly, by encapsulating chemical hydrides in polymeric nanofibres, as demonstrated by the development of co-axial ammonia borane-encapsulated polystyrene (AB-PS) fibres, and secondly, by post-processing of single-phase electrospun PAN fibres, resulting in the synthesis of potassium-intercalated graphitic nanofibres (K-GNFs). The results show that the micro and nano-structure imparted through electrospinning, can have the effect of reducing dehydrogenation temperatures in AB-PS fibres (from 110 to ~85 °C) and improving the (de)hydrogenation rates by an order of magnitude in both composite fibres (from ~50 to <5 mins in K-GNFs and from ~150 minutes to as low as 15 minutes in AB-PS fibres). The details of co-axial electrospinning as a novel approach to nanoengineering chemical hydrogen storage materials and as a way of possibly overcoming issues regarding reversibility, stability and clean hydrogen release from many of these materials is discussed. The solution selection method I have developed for use in the synthesis of co-axial composite fibres can be applied as an efficient solution selection formula for multi-phase electrospinning in general.

Dedicated

To my grandfather, Ahmet Kurban, who has taught me to be giving in a world where people are endlessly taking. Despite the faint memories I have of him from my childhood, he will always be the person I aspire to be like. I also dedicate this to all those selfless people who have devoted their lives to the freedom of others.

Midway upon the journey of our life
I found myself within a forest dark,
For the straightforward pathway had been lost.

Ah me! how hard a thing it is to say
What was this forest savage, rough, and stern,
Which in the very thought renews the fear.

So bitter is it, death is little more;
But of the good to treat, which there I found,
Speak will I of the other things I saw there.

Excerpted from
The Divine Comedy
[Dante Alighieri, 1307]

Acknowledgements

There are many people I am grateful to for making this thesis possible. First and foremost, I would like to thank my supervisor at Rutherford Appleton Laboratory, Prof. Steve Bennington, for his guidance, inspiration and constant encouragement throughout my research work. His unfailing optimism and enthusiasm for science made the most difficult problems and night long experiments all very exciting endeavors. He is a great adviser, who has always been there to answer my questions, and a great coach who has helped and encouraged me to learn many new skills. The discussions we have had in and out of meetings have been a major source of knowledge for me, I feel privileged to have worked with him.

I am no less indebted to my supervisor at UCL, Prof. Neal Skipper, who has guided and supported me immensely in the first year of my research degree while I was based at UCL. Thereafter, he has always been available for meetings and discussions whenever I needed his advice. His presence in meetings and experiments has made them ever more engaging. I thank him for all that he has taught me and for adding so much humour to our discussions.

I am thankful to my colleague and friend Dr. Arthur Lovell, for his constant help and support. Mere words are not sufficient to express my gratitude to him. This research project will not have been as smoothly conducted if he wasn't present. He has always been there for discussions at most difficult times. His enthusiasm to teach and to share his immense knowledge has made it easier for me to learn many of the things for my research. I would like to specifically thank him for his patience and for putting up with my never ending questions.

I also wish to express my sincere thanks to Prof. Felix Fernandez-Alonso, who has always been there to discuss my research and to answer

my questions. He is another inspiring scientist whose enthusiasm is matched to none. I want to thank him and Dr. Timmy Ramirez Cuesta for their assistance throughout neutron experiments.

I am also grateful to Derek Jenkins, for sharing his knowledge on electrospinning with me and teaching me how to do electrospinning. His help and guidance in the laboratory and contributions at meetings have all been very helpful for my research.

I want to thank my friends and colleagues at Rutherford Appleton Laboratory; Rob Bewley, for making RAL an even more enjoyable place to work at and for trying to help me to learn how to balance a life with science, I thank Rowan Hargreaves, Tatiana Guidi, Davide Raspino, Victoria Garcia-Sakai, Ross Stewart, Marco Alessandroni, Aziz Daoud-Aladine, and those at UCL; Emily Milner, Jacqueline Edge, Chris Rahnejat and Nick Shuttleworth. I thank them for their support and for making my stay at RAL and UCL so pleasant and fulfilling.

I want to express my gratitude to my parents Yeter Kurban and Cuma Kurban, for always being supportive and loving. I thank them for having worked so hard to give me and my sisters a better future. I thank my sisters Berfin Kurban and Berivan Kurban for cheering me up when I needed it; I couldn't imagine a world without them.

Finally, I give my heartfelt thanks to my dearest friends: Senay Yesil, for always being there for me at the most difficult times to listen to me and cheer me up; Nene de Tommasi, for her encouragement and for almost always starting her first sentence with the question "do you want to laugh?"; Francesca Norris, for being there for me since the first day of our time at university; Ercument Karakoc for telling me to "just get on with it"; and Federico Baradello for never getting tired of listening to me despite thinking that I'm like a broken record.

Zeynep Kurban

Contents

Abstract ii

Acknowledgements vi

Introduction 1

Chapter 1 Hydrogen Storage 5

- 1.1 Introduction 5
- 1.2 Hydrogen power plants 8
- 1.3 System performance targets & safety 10
- 1.4 Hydrogen storage systems 12
  - 1.4.1 Hydrogen storage as compressed gas 12
  - 1.4.2 Hydrogen storage in liquid form 14
  - 1.4.3 Cryo-compressed systems 14
  - 1.4.4 Chemical hydrogen storage (chemisorption) 15
  - 1.4.5 Hydrogen storage based on physisorption 23
  - 1.4.6 Hydrogen binding energies: the big challenge 32
- 1.5 Nano-engineering hydrogen stores 33
  - 1.5.1 Diffusion and nucleation 34
  - 1.5.2 Thermodynamics of reaction 35

Chapter 2 The Electrospinning Process 42

- 2.1 Introduction 42
- 2.2 History of electrospinning 44
- 2.3 Electrospinning applications 47

2.4 Electrospinning theory: jet instability 49

2.5 Electrospinning materials 56

2.5.1 Polymers and their properties 56

2.6 Electrospinning parameters 60

2.6.1 Solution parameters 61

2.6.2 Process parameters 70

2.6.3 Environmental (ambient) parameters 74

Chapter 3 Co-electrospinning: Technology and Control 76

3.1 Introduction 76

3.2 Co-electrospinning Process and Control 78

3.2.1 General set up and the process 78

3.2.2 Instability theory of a co-axial jet 81

3.2.3 Solution and process parameters 87

3.3 Solution Chemistry 96

3.3.1 The need for a solution selection model 96

3.3.2 Hildebrand and Hansen solubility parameters: Theory....98

3.3.3 Solution selection model 101

Chapter 4 Characterisation and Neutron Scattering Techniques . 109

4.1 Fiber Imaging Methods 109

4.1.1 Scanning electron microscopy (SEM) 109

4.1.2 Transmission electron microscopy (TEM) 112

4.2 Intelligent Gravimetric Analysis 114

4.3 Differential Scanning Calorimetry 116

4.3.1 DSC measurements and data analysis 118

4.4 ATR-FTIR 119

4.5 X-ray Powder Diffraction 120

4.6 Neutron Scattering 122

4.6.1 Introduction....122

4.6.2 Theory....123

4.6.3 Inelastic neutron scattering....129

4.6.4 Neutron diffraction....133

Chapter 5 Co-electrospun AB-PS Fibres....136

5.1 Introduction....136

5.2 Core and sheath materials....138

5.2.1 Ammonia borane....138

5.2.2 Polystyrene....154

5.3 Experimental Details....157

5.3.1 Materials: solutes and solvents....157

5.3.2 Solution preparation....157

5.3.3 Electrospinning Set-up....165

5.4 Results and Discussion6....165

5.4.1 Co-electrospinning of AB-PS fibres....167

5.4.2 Morphological characterisation of fibres: SEM/TEM....170

5.4.3 Fibre diameters and core structure....180

5.4.4 Fibre Porosity....187

5.4.5 Structural characterisation: X-ray diffraction....194

5.4.6 Thermolysis properties of AB-PS fibres: DSC, TGA....200

5.4.7 ATR-Fourier transform infrared spectroscopy....216

5.5 Summary and Conclusions....217

5.6 Prospects and Future Work....221

Chapter 6 KC_{24} nanofibres and Hydrogen....223

6.1 Introduction....223

6.2 Graphite and hydrogen....226

6.3 Graphite intercalation compounds....229

6.3.1 Graphite intercalates and hydrogen storage....................229

6.3.2 Structure of potassium-intercalated graphite 232

6.3.3 Hydrogen Storage in KC_{24} 235

6.3.4 Inelastic neutron scattering KC_{24} 236

6.3.5 Intercalation methods..241

6.3.6 Carbon fibres and their synthesis 243

6.4 Experimental details 249

6.4.1 Solution preparation...249

6.4.2 Electrospinning of PAN fibres 250

6.4.3 Thermal treatment of as-spun PAN fibres.......................252

6.4.4 Characterising fibre morphology and crystal structure ..253

6.4.5 Synthesis of KC_{24} nanofibres 253

6.5 Results and Discussion...256

6.5.1 Minimising fibre diameters 256

6.5.2 Carbonised fibres: SEM & TEM analysis 262

6.5.3 XRD Analysis of GNFs...267

6.5.4 Neutron scattering measurements on H_2-KC_{24} 271

6.5.5 Neutron diffraction 280

6.5.6 Enthalpy of adsorption 286

6.6 Summary and Conclusions..289

6.7 Future Work 290

Appendix A Polymer and solvent data sheet (solvent matrix) 292

Appendix B Permeability of selected polymers to selected gasses ... 294

List of Figures

Figure 1.1: Status of hydrogen storage materials [3]. 7
Figure 1.2: Schematic illustration of a hydrogen/oxygen fuel cell and its reactions based on the proton exchange membrane (PEM) fuel cell. 9
Figure 1.3:Design for high-pressure hydrogen tank [12] 13
Figure 1.4 : Lennard-Jones potential energy curve for hydrogen binding to a metal [17]. 18
Figure 1.5: (a) Hydrogen adsorption, dissociation and absorption;. 19
Figure 1.6: Saturation H_2 uptake plotted against Langmuir surface area for various MOFs at 77K (modified from ref [33]), ...31
Figure 1.7: Energy scale showing the targeted binding energy range (10-50 $kJmol^{-1}$) required for room temperature hydrogen storage 33
Figure 1.8: An illustration showing how the density of nucleation in a bulk particle (top path) and a nano-particle (bottom path) can vary and influence the interface energy between α- and β-phases; [18]. 35
Figure 1.9: a) The plateau pressure corresponding to phase transition from α- to β-phase is measured at different temperatures, (b) van't Hoff plot:. 38
Figure 2.1: Schematic diagram of set up of electrospinning apparatus [74]. 43
Figure 2.2: Some of the different fibre morphologies that can be produced for different applications [92]..48
Figure 2.3: The division of research on electrospun polymer nanofibres, as adapted from [73]. 49
Figure 2.4: Schematic diagram of electrospinning nozzle with positive and negatively charged electrode 50
Figure 2.5: The electrospinning envelope showing the conical jet path [67]. 51

Figure 2.6: (a) Axisymmetric and (b) non-axisymmetric instabilities in a fluid jet in an external electric field (E_{∞}), Δ denotes the pertubations of the surface charge density (σ) [97], (c) idealised nodes; the arrows in (b) and (c) indicate the forces that bends the jet, adapted from [73, 97]. 55

Figure 2.7: The change in the beaded structure of fibres electrospun from solutions with increasing viscosity. 62

Figure 2.8: Laminar shear of fluid between two plates (with one stationary and one moving).. 63

Figure 2.9: Collapsed (buckled) electrospun fibres; an effect attributed to high vapour pressure of the solvent used. 69

Figure 2.10: Fibre diameter vs. voltage plot of PMMA fibres electrospun at different concentrations of PMMA. 71

Figure 2.11: Schematic electrospinning set up showing tip-to-collector (flight) distance of electrospinning jet. 72

Figure 3.1: Co-axial nozzle set up used in co-electrospinning...........................80

Figure 3.2: A schematic illustration of the deformed compound jet, [133]. 82

Figure 3.3: Sketch of the unstable modes. [131]...84

Figure 3.4: Co-electrospun PAN (shell): PMMA (core) fibres. 89

Figure 3.5 Schematic diagram of compound Taylor cone formation under the influence of an electric field: [139]. 90

Figure 3.6: Co-electrospun 12 wt.% PAN in DMF (sheath) and 15 wt.% PMMA in DMF (core) at varying flow rates;. 93

Figure 3.7: The Hansen solubility plot showing the Hansen sphere as determined by the coordinates of the solute (polymer) (δ_{d1}, δ_{p1}, δ_{h1}) and its radius of interaction (R_0).. 102

Figure 3.8: A hypothetical δ_v-δ_h Hansen plot,...104

Figure 4.1: Schematic diagram of scanning electron microscope (SEM). 111

Figure 4.2: Schematic diagram of a transmission electron microscope. 113

Figure 4.3: Schematic diagram of IGA [149]. 115

Figure 4.4: Schematic illustration of the cell assembly of a differential scanning calorimeter. 117

Figure 4.5: Evanescent wave penetrating in the specimen placed in close contact with ATR crystal. 119

Figure 4.6: Schematic illustration of a powder X-ray diffractomer measuring 2θ. 121

Figure 4.7: Scattering triangles depicted for (a) inelastic scattering and (b) elastic scattering events. 125
Figure 4.8: Geometry for a typical scattering experiment [156]. 126
Figure 4.9: Schematic layout of a time-of-flight neutron spectrometer [48]....130
Figure 4.10: Schematic illustration of the IRIS neutron spectrometer [48]. ..132
Figure 4.11: Exploded schematic diagram of TOSCA layout [158]. 133
Figure 4.12: Schematic layout of a time-of-flight neutron diffractometer[48]. 135
Figure 5.1: (a) Crystal structure of AB at 15 K (orthorhombic). [171]. 141
Figure 5.2: DSC curves of thermal decomposition of BH_3NH_3: (—) heating rate 0.05 K/min, (---) heating rate 1 K/min [190]. 145
Figure 5.3: DSC curves of thermal decomposition of BH_3NH_3 at isothermal temperatures between 343 and 363 K. 147
Figure 5.4: Time resolved $^{11}B[^{1}H]$ MAS-NMR spectra (7.1 T) taken by Stowe *et al.* during thermal dehydrogenation of NH_3BH_3 at 88 °C taken at 2 min intervals from [191]. 148
Figure 5.5: The thermal dehydrogenation mechanism of AB (NH_3BH_3) proposed by Stowe *et al.* The induction, nucleation and growth steps leading to hydrogen release are as shown in the reactions [191]. 149
Figure 5.6. Optical micrograph images of a single crystal of NH_3BH_3 heated to 90 °C, [193]. 150
Figure 5.7. Schematic of (a) an unmodified carbon cryogel and (b) a CC-AB nanocomposite as constructed by Feaver *et al.* [185]. 152
Figure 5.8: Comparison of chemical structures of atactic, isotactic and syndiotactic polystyrene. 156
Figure 5.9: Two dimensional (δ_v vs. δ_h) diagram showing extent of solubility of polystyrene (PS) [●] in various solvents. 159
Figure 5.10: Core and shell solvent mixtures showing the difference between the immiscible (IS), semi-miscible (sMS) and miscible (MS) solution......162
Figure 5.11: Electrospinning apparatus setup. 163
Figure 5.12: Co-axial nozzle setup used in experiments:. 166
Figure 5.13: Electrospun fibre mesh (fibre mat) 169
Figure 5.14: (a) SEM and (b) TEM micrograph of fibres produced from semi-miscible solution set-1, sMS-1, ...173
Figure 5.15: Fibres co-electrospun with solution set sMS-2 showing reduction in beading with increasing core (AB) solution quantity. 175

Figure 5.16: (a)-(d) SEM micrographs of fibres produced from immiscible solution set-1, IS-1,. 177
Figure 5.17: Fibres produced from immiscible solution set-2 (IS-2) with *20 wt.% AB in water* as core solution, showing smooth (non-porous) and cylindrical (non-collapsed) fibres. 178
Figure 5.18: (a) SEM and (b) TEM micrograph of fibres co-electrospun from IS-1, *20 wt.% PS in 3:1:1 volume ratio Tol-DCE-PF (shell)* & *20 wt.% AB in water + 3 wt.% PEO (core)* (FR=500:200 µl/hr, voltage 19 kV, temperature 21°C, humidity 40%), showing collapsed bulk fibres with very little porosity; (c) SEM micrograph of fibres obtained with the core solution (*20 wt.% AB in water + 3 wt.% PEO*) electrospun on its own, AB has formed crystallites attached to the fine PEO fibres. 179
Figure 5.19: Fibres co-electrospun from solution set sMS-2 with 10 wt% AB in DMSO as the core solution,. 181
Figure 5.20: TEM images of fibres electrospun from (a) sMS-2 solutions set (b) IS-1 solutions set..182
Figure 5.21: Mean diameters of fibres electrospun from semi-miscible (sMS-2) and immiscible (IS-1) solutions sets:. 182
Figure 5.22: Graphs showing the variation of AB solution conductivity over time for different AB concentration in (a) DMSO and (b) in water. 186
Figure 5.23: a) A series of cross-section of some non-axisymmetric modes for a coaxial fibre. 191
Figure 5.24: XRD patterns of fibres produced from semi-miscible solutions (sMS-2), ordered by nominal AB content 195
Figure 5.25: XRD patterns of fibres produced from semi-miscible solutions (sMS-2),. 197
Figure 5.26: XRD patterns of fibres produced from immiscible solutions (IS-1), ordered by nominal AB content. 198
Figure 5.27: X-ray diffraction patterns of AB powder, electrospun PS fibres, electrospun AB-PS fibres spun using miscible and immiscible core-shell solution combinations.. 199
Figure 5.28: DSC measurements of neat AB at heating rates of 5 and 1°/m ..201
Figure 5.29: DSC measurements of pure Polystyrene (PS) fibres (post electrospinning) and PS pellets (prior to electrospinning) 202

Figure 5.30: DSC measurements of sMS-2 fibres electrospin with 10 wt.% AB in core,. 203

Figure 5.31: DSC measurements of IS-1 fibres electrospun with 10 wt.% AB in core, heating rate of 1°/min (plotted as green triangles in Figure 5.32)... 203

Figure 5.32: AB decomposition temperature vs. AB proportion in the fibres.. 204

Figure 5.33: SEM images of fibres corresponding to the DSC data in Figure 5.32; a) sMS-2 fibres with 10% AB, b) sMS-2 fibres with 20% AB, c) IS-1 fibres with 10% AB, d) IS-1 fibres with 20% AB. 204

Figure 5.34: Hydrogen mass spectrometry measurements of hydrogen from thermolysed neat AB and sMFs fibres into 1.0 bar Ar carrier gas, and IS-1 fibres into He carrier gas stream. Heating rate = 1°C min^{-1}. 205

Figure 5.35: Hydrogen mass spectrometry measurements of hydrogen from thermolysed sMS fibres into 0.12 bar Ar carrier gas (blue line) compared to that taken at ambient pressure (1 bar, red line)...................................... 206

Figure 5.36: Thermogravimetric mass loss as a function of temperature for fibres obtained from immiscible (IS-1) and semi-miscible (sMS-2) solution sets, at a heating rate of 1 °/min... 208

Figure 5.37: Thermogravimetric mass loss on heating at 1°/min to 200 °C immiscible (IS-1) and semi-miscible (sMS-2) samples, as a function of sample nominal wt.% AB, with linear fits. 209

Figure 5.38: Mass spectra of neat AB rapidly heated to and incubated at 88 °C for 4 hours, partial pressure of fragments detected under Ar carrier gas. 212

Figure 5.39: Mass spectra of a sMS sample rapidly heated to and incubated at 88°C for 4 hours, partial pressure detected under Ar carrier gas. 212

Figure 5.40: Mass spectra of an IS sample rapidly heated to and incubated at 88 °C for 4 hours, ... 213

Figure 5.41: Thermogravimetric and mass spectrometry measurements of hydrogen from neat AB into 1 bar He carrier gas with the sample rapidly heated to and incubated at 85 °C.. 214

Figure 5.42: Thermogravimetric and mass spectrometry measurements of hydrogen from a set of sMS fibres. 215

Figure 5.43: SEM image of sMS fibres prior to being incubated at 85 °C. 215

Figure 5.44: Mass spectrometry data from sMS fibres 216

Figure 5.45: FTIR spectra of AB powder, electrospun PS fibres, electrospun AB-PS fibres 217

Figure 6.1: Structure and unit cell of graphite showing the stacking sequence of the basal planes along the c-axis following a staggered -ABA- pattern [221]..227

Figure 6.2: Graphite stacking and interlayer spacings for pure graphite, stage-1 and stage-2 potassium graphite intercalation compounds [48]............230

Figure 6.3: Proposed in-plane potassium structures for K-GIC showing K registry with the graphite host [8]. 234

Figure 6.4: Domain model for CsC_{24} in which $(\mathbf{7}\ \boldsymbol{x}\ \mathbf{7})$ islands are separated by domain walls, or discommensurations [8]..235

Figure 6.5: INS spectra of $RbC_{24}(H_2)_x$ for x = 1:0, 1.5, 2.0, 2.1 (Beaufils *et al.*) [46]..237

Figure 6.6: View along the *c* axis (white lines define the unit cell). The trigonal subunit cell and its centre are shown in red. White circles denote three adjacent H_2 sites [218]. 239

Figure 6.7: Splitting pattern for the rotational energy levels of a hydrogen molecule in a cylindrically symmetric $\cos^2\theta$ potential showing transition energies from the ground state in meV. 240

Figure 6.8: Schematic diagram of (a) one-zone transport method with accurate stoichiometric amount of metal at the same temperature, and (b) two-zone vapour transport method where T_g and T_i indicate the temperature of the graphite and intercalant respectively [48]. 242

Figure 6.9: (a) Knibbs' identified three different types of structures for PAN [254]..245

Figure 6.10: Structural model of carbon fibres from PAN precursor as suggested by Diefendorf and Tokarsky [255] showing microfibrils..........246

Figure 6.11: A schematic 3D representation of the structure of a PAN based carbon fibre showing irregular space filling and the distortion of the carbon layers [256]..246

Figure 6.12: Mechanistic pathways for the thermal degradation of polyacrylonitrile according to Keller *et al.* [262]......................................248

Figure 6.13: Electrospun PAN fibres (white coating) on grounded collection plate..251

Figure 6.14: Quartz sample tube with valve for vapour transport synthesis..254

Figure 6.15: Graphitic nanofibres during the intercalation process of potassium, (left) shows the fibres at a point near the beginning and (right) towards the end of the intercalation. 256

Figure 6.16: Viscosity of PAN solutions in DMSO, the inset shows the fibre diameter as a function of viscosity 257

Figure 6.17: Polymer and 500 °C pyrolysed (CNF) fibre diameters as a function of concentration of PAN in DMSO solution,..258

Figure 6.18: Conductivity of PAN solutions in DMSO: 259

Figure 6.19: SEM images of fibres electrospun from 4.2 wt.% PAN/DMSO solution; a) fibres without SASH b) fibres with SASH 260

Figure 6.20: SEM images of heat treated non-oxidised fibres 262

Figure 6.21: Fibre diameters and normalized mass (inset) of fibres from 6.8 wt.% PAN in DMSO solution as a function of HTT.. 264

Figure 6.22: TEM images of fibres at a) HTT = 1500, b) HTT= 2200, and c) HTT = 2800 °C...265

Figure 6.23: TEM images of fibres heat treated at 2800C; Non-Oxidised fibres (a) and (b) and Oxidised fibre (c) ((b) and (c) magnification 400K)..........266

Figure 6.24: X-ray diffraction data from oxidised and (inset) non-oxidised fibres at HTT from 500 to 3000°C using Cu Kα source. The background from the glass slide has been subtracted from each pattern.................................267

Figure 6.25: Proportional sub-peak fits to the (002) peak showing the growth of the graphitic phase from a phase consisting of few-layer (1- and 2-layer stacked) graphite with increase in HTT;..269

Figure 6.26: KC_{24} nanofibre sample being loaded into the IRIS sample can...273

Figure 6.27: The IRIS sample can attached to the cryostat centre stick.........273

Figure 6.28: INS spectra of $KC_{24}(H_2)x$ using 25 Hz -0.8 to 2.0 meV energy window of IRIS..275

Figure 6.29: Ratio of peak areas obtained using two-peak Gaussian or Lorentzian fits to bulk-KC_{24} data shown in Figure 6.28 (a). 277

Figure 6.30: (a) Peak centres and (b) peak full-width half maxima derived from two-peak Gaussian fits to bulk-KC_{24} data shown in Figure 6.28 (a)........278

Figure 6.31: INS spectra of $KC_{24}(H_2)x$ nanofibres on TOSCA from forward-scattering banks; (a) data collected on bulk KC_{24} (from previous study) [48], (b) data collected on KC24 nanofibres (from this study). 279

Figure 6.32: Time-resolved diffraction patterns of (a) bulk KC_{24} sample from previous study on POLARIS [48] and (b) KC_{24} nanofibres from this study on GEM, taken during D_2 loading up to the saturation point at 50 K. Both data sets show c-axis expansion with 1 D_2 loading per KC_{24} (offset for clarity). The time resolution is 10 minutes in (a) and 5 minutes in (b)....283

Figure 6.33: The evolution of the (003) diffraction peak of (a) bulk and (b) nanostructured KC_{24} with increasing concentration. Data in (a) obtained from previous diffraction study on IRIS [48]..284

Figure 6.34: The pressure desorption curve of KC_{24} nanofibres with H_2 coverage of $1H_2/KC_{24}$, black line correspond to the original data and red line is that fitting obtained using Eq.(6.4)..288

Introduction

Society awaits a major technological breakthrough before we can reduce our dependence on fossil fuels that are rapidly depleting and causing serious damage to the planet. Hydrogen has emerged as one of the leading contenders in the search for a clean energy alternative for both automotive and stationary applications. The current challenge lies in finding a cheap and durable material that can store sufficient densities of hydrogen safely and practically within the vehicular constraints of weight, volume and efficiency. There is not yet such a system that satisfies such stringent storage requirements to make fuel cell vehicles competitive with their fossil fuel counterparts. Solid state storage of hydrogen is considered as the long term solution, while compressed gas or liquid hydrogen storage systems, currently tested on prototype fuel cell vehicles introduced into the market, are considered only as intermediary solutions. However the solid state stores, which can be categorised into chemisorption and physisorption based stores have intrinsic problems associated with their mode of storage. Physisorptive stores such as high surface area carbons and metal-organic frameworks display maximum uptake typically below 100 K, with enthalpies of adsorption less than 10 kJ mol^{-1}. Metal and complex hydrides have enthalpies of adsorption greater than 50 kJ mol^{-1}, and hydrogen desorption times are lengthy even at temperatures higher than 400 K, making them impractical for an operational store.

Nanotechnology is now being employed as a way of improving the hydrogenation properties of many of these materials. Though the influence of nanostructure on the (de)hydriding properties can vary depending on the material, the improvements seen as a result of nanostructuring are generally associated with increase in surface area, lowered diffusion distances and/or lowering in the energies required to drive a phase change. These effects can respectively lead to increased uptake, faster uptake and release rates of hydrogen in many materials and reduced decomposition temperatures in the case of chemical hydrides. Thus, a nanostructuring technique which enables successful tuning of the thermodynamic and kinetic sorption properties of these materials is necessary.

There are currently not many nanostructuring techniques available and the most commonly used methods have particular disadvantages. For example, the ball-milling method, typically used for chemical hydrides, is rather expensive to scale up and other options such as nano-scaffolding (e.g. with etched silica) have disadvantages such as added weight to the storage system. Furthermore none of these options address the issue of non-reversibility of hydrogen storage, or the instability of the materials in air, problems which are common to most chemical hydrides.

The requirement for a scalable and cheap nanostructuring technique, which can be used to address many of the issues surrounding most hydrogen stores, was what inspired this research to investigate electrospinning as way of nanostructuring hydrogen storage materials. Electrospinning is a well-developed versatile technique, widely used for the manufacture of polymeric fibres with micro-to-nano diameters. In this study it is used in its two variant forms to investigate 1) its function as a way of nanostructuring chemical hydrides by encapsulating them in permselective polymeric nanofibres, and 2) as a way of making alkali metal intercalated graphitic nanofibres (GNFs) from electrospun carbonisable polymer fibres. In the first study co-electrospinning is used to encapsulate ammonia borane (AB) in a polymeric (PS) sheath. AB is considered as one of the most promising hydrogen stores due to its high hydrogen density (19.5 wt.%), 2/3 of which is attainable at temperatures up to 150 °C. However, its slow dehydrogenation kinetics and its inability to reversibly store hydrogen make it unsuitable as a practical hydrogen store. Co-electrospinning offers the potential to overcome these issues through nanostructuring to enhance hydrogenation rates at reduced temperatures, and through encapsulation of its reaction products in a hydrogen permeable polymeric sheath for regeneration upon pressurisation with hydrogen. In the second study single-phase electrospinning is used to electrospin PAN nanofibres which are later graphitised and intercalated with potassium to yield K-GIC (KC_{24}) nanofibres. GICs, which are considered as ideal testbeds for exploring hydrogen storage in metal doped carbon nanomaterials, can be more controllably nanostructured using electrospinning to tune their hydrogen sorption properties.

This investigation, the first of its kind to employ (co)electrospinning as a way of nanostructuring chemical hydrides and carbon based materials, has proven to be a highly successful step in the direction of nanoengineering materials for deployment in hydrogen storage applications. The process which has been developed and the results that have emerged will not only constitute the basis of further research in this field but has been important for developing the knowhow on co-electrospinning in general.

This thesis is separated into a progression of literature studies that outline the current status of research in all fields related to the work discussed here, an elaborate description of the (co)electrospinning process and the results of the two separate studies. In Chapter 1, I present the background to hydrogen storage, outlining the requirements for and the issues surrounding hydrogen storage materials, and describe how nanotechnology can provide solutions. In Chapter 2, I introduce and describe single phase electrospinning, with a detailed description of how to control the process and solution parameters, as described in literature and tested throughout this study. In Chapter 3, I describe how the same parameters are controlled in the case of co-axial spinning where two co-flowing solutions are used instead of one, with significant input from the tests conducted in this study. In Chapter 4, I describe the main characterisation techniques used in this investigation. In Chapter 5, I outline the detailed study on co-electrospun ammonia borane encapsulated polystyrene (AB-PS) fibres and their hydrogenation properties. In Chapter 6, I discuss the details of the second (parallel) study on the synthesis of intercalated graphitic nanofibres (GNFs), and their hydrogen storage properties as investigated by neutron scattering techniques. Both experimental chapters (Chapter 5 and 6) are composed of a literature survey of the materials investigated, the experimental details of the studies and the results and discussion sections.

Chapter 1

Hydrogen Storage

1.1 Introduction

Hydrogen has attracted much attention as a next-generation energy carrier for both mobile and stationary applications [1]. It has a number of advantages compared to other chemical energy carriers. Firstly, hydrogen is a clean carrier of energy, the only by product in its energy conversion process is water. Secondly, hydrogen is plentiful in nature; it can be obtained from a diverse array of potential feedstocks, including water, fossil fuels and organic matter. If hydrogen is obtained through the electrolysis of water, with renewable energy sources used to power the electrolysers, we could essentially have a sustainable and clean production system. Lastly, hydrogen has a large chemical energy density on weigh basis (120 MJ/kg); nearly three times the energy content of gasoline (44 MJ/kg). However, on volume basis the energy content of hydrogen is much lower than that of gasoline (8 MJ/L for liquid hydrogen compared to 32 MJ/L for gasoline) [2]. In fact this is where the challenge arises; the low density of hydrogen makes it difficult to store sufficient amounts of it in a compact space on board a vehicle. For mobile applications it is required that the storage system occupies a small volume, has a low mass and a driving range of at least 480 km (300 miles) in a single fill. This corresponds to approximately 5 to 13 kg of hydrogen on board the vehicle, based on projected future fuel cell efficiencies. However, besides the amount of hydrogen stored, practical operability of the storage system at ambient conditions (e.g. pressure and temperature) and its safety are crucial for the success of the storage system developed for fuel cell applications. Therefore, in order to identify the type of storage system that would be practical and commercially viable, the US Department of Energy (DOE) has devised a set of targets for the researchers around the world to follow. Their outlined vision and system storage targets for fuel cell vehicles are presented in §1.3.

Hydrogen storage research has come a long way in the last two decades, with many potential systems developed and currently being optimised for both stationary and mobile applications. Yet, a major breakthrough is still awaited before fuel cell operated vehicles can replace their fossil fuel counterparts. Currently several options are available for storing hydrogen; these separate into three separate modes: i) cryogenic hydrogen storage (at 21 K), ii) compressed hydrogen storage (up to 800 bar) and iii) solid state hydrogen storage. The first two options, which have been used in prototype fuel cell vehicles as demonstration technologies, are considered only as interim solutions due to their high cost and problems regarding safety. The third option, solid state storage, which involves many different systems that store hydrogen chemically or physically or as a combination, e.g. metal hydrides, complex hydrides and high surface area sorbents, allows for the possibility of storing hydrogen at greater densities than the liquid state and without the risk of hydrogen leak in the event of an accident. Solid state storage, being the most extensively studied storage mode at research level, is thus considered as the only long term solution to satisfy market requirements.

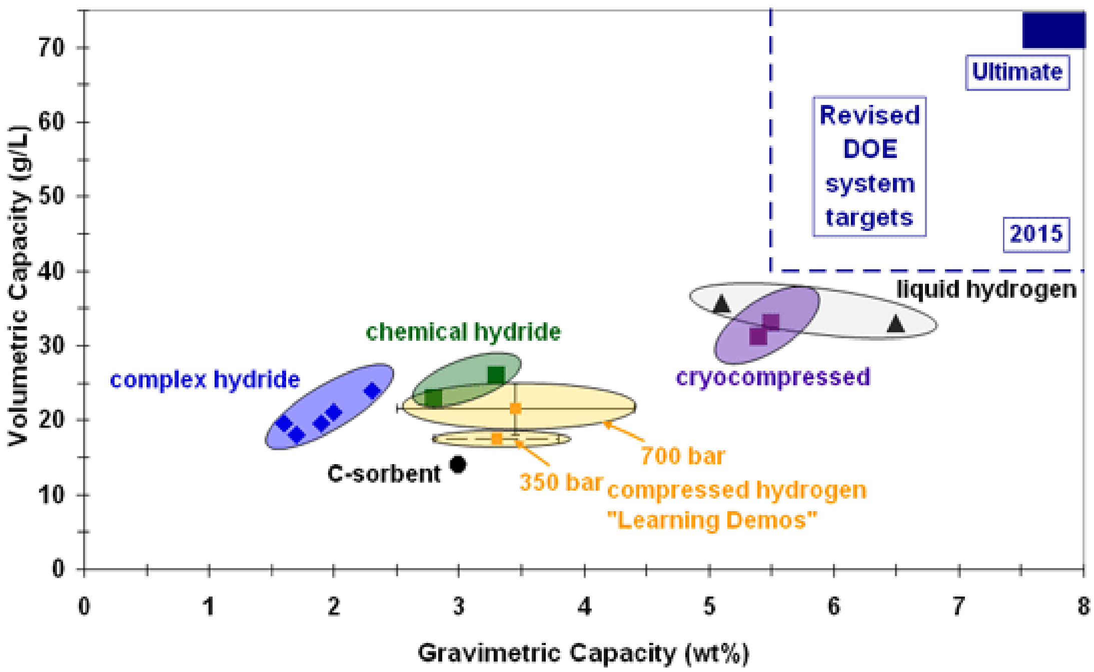

Figure 1.1: Status of hydrogen storage materials [3].

In this first chapter I will give a brief overview of the status of hydrogen storage systems by looking at existing technologies and those materials under strict scrutiny by the scientific community. Figure 1.1 shows the status of hydrogen storage materials in terms of their volumetric and gravimetric storage capacities compared to the targets set for 2015 and those ultimately required [3]. I will discuss the main issues associated with these storage systems and the way in which they are being tackled using nanotechnology. To elucidate the root cause of the problems associated with each material, I will categorise and discuss the materials in terms of their storage modes; liquid, gaseous, chemical and physisorbtive storage. Greater emphasis is placed on the latter two modes of storage since the materials that are of interest to this investigation; ammonia borane and intercalated carbon fibres, respectively, fall under these two categories of storage. Since knowing the technical requirements forms a key part of the assessment of these materials as potential hydrogen stores, I will start off this chapter with a section on hydrogen power plants (e.g. fuel cells) and another outlining the US Department of Energy storage targets and the safety considerations with regards to the use of hydrogen for transportation.

1.2 Hydrogen power plants

Hydrogen is an energy carrier and can be utilised in two different ways for power generation. Its chemical energy can be either converted to mechanical energy by burning it in an internal combustion engine (ICE) or to electrical energy by reacting it with oxygen in a fuel cell. The hydrogen ICE engine is simply a modified version of the conventional gasoline-powered ICE. The basic principle is the same, the burning of gas and air in the combustion chamber creates gasses of high temperature and pressure that expand, doing useful work, to move the piston inside a cylinder. However, as opposed to production of CO_2, CO and NO_2 as in the case of gasoline-powered ICE, the combustion of hydrogen with oxygen results only in production of water, though combustion of hydrogen with air can also produce small quantities of nitrogen oxides (NO_x).

Hydrogen fuel cells are considered as a better alternative to internal combustion engines and research within the hydrogen economy framework is mostly directed on developing fuel cell technology. This is because fuel cells are cleaner and can function with a greater efficiency: 50–60 % compared to ~25 % in the case of ICEs, in which the efficiency is limited by the Carnot cycle [4]. Of the fuel cell options available, the proton exchange membrane (PEM) fuel cell has emerged as the leading contender due to its high chemical-to-electrical energy conversion efficiency and high power density [5]. More importantly it has a more practical operational temperature range (60-120°C), as opposed to the high temperatures (500-1000°C) needed for molten carbonate and solid oxide fuel cells [5].

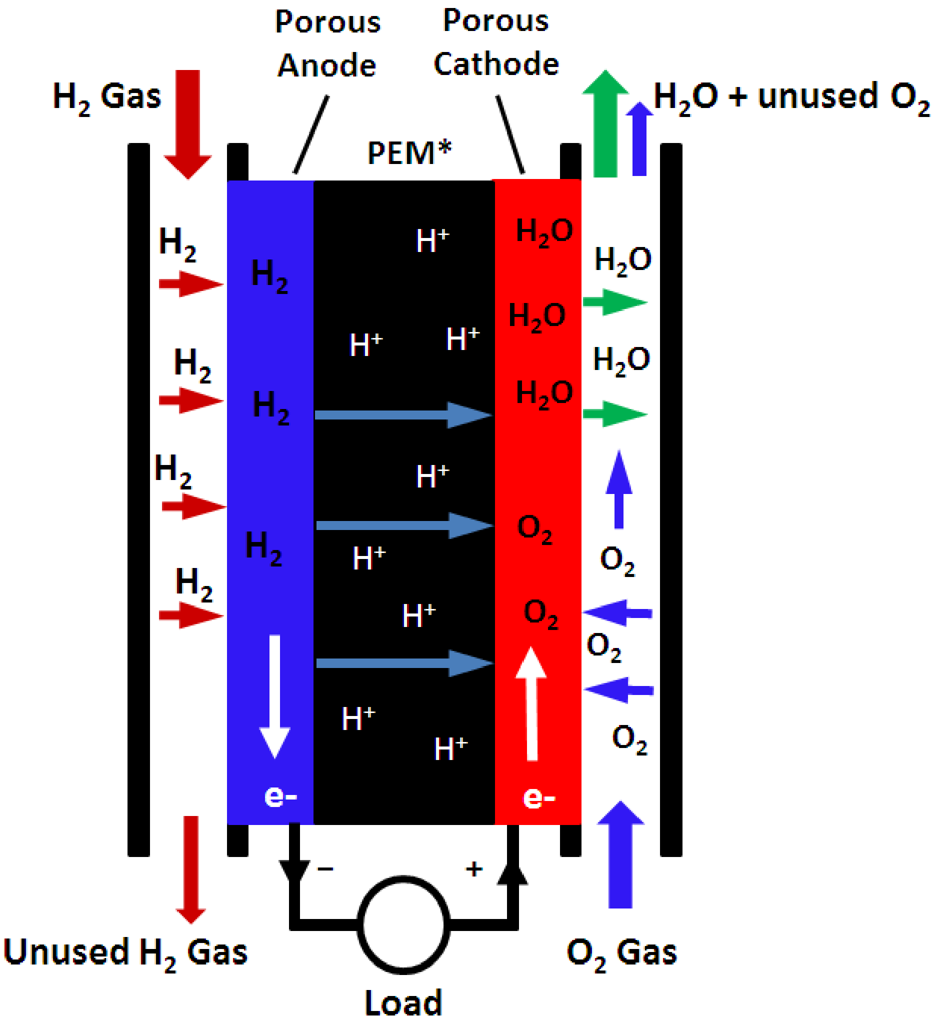

Figure 1.2: Schematic illustration of a hydrogen/oxygen fuel cell and its reactions based on the proton exchange membrane (PEM) fuel cell. *Protons crossing the PEM electrolyte.

A schematic diagram of a PEM fuel cell is shown in Figure 1.2. Like all battery systems that convert chemical energy to electrical energy, fuel cells also contain an electrolyte that separates the anode and cathode catalysts at each end. The hydrogen diffuses through the anode end where it dissociates into protons and electrons. The protons diffuse through the electrolyte (polymer membrane) to reach the cathode, while the electrons travel through the external circuit creating an electrical current. The oxygen diffusing through the cathode catalyst gets reduced upon arrival of the protons and electrons at the cathode to form water. In a PEM fuel cell the electrolyte is formed of a thin ion conducting polymeric membrane. To reduce any losses in proton flow the thickness of the polymeric membrane is minimised to diameters around 50 nm. While splitting hydrogen is relatively easy with a platinum catalyst at the anode, the splitting of the oxygen is more difficult, leading to significant electrical losses. So far platinum is found to be the best catalyst for the cathode. While the PEM fuel cell efficiencies are approximately 2 to 3 times greater than conventional gasoline based ICEs and up to 2 times greater than diesel-electric hybrids [5] the cost of the fuel cell is still significantly higher than these systems. Thus, every component of the PEM fuel cell requires specific attention to reduce costs and energy losses during operation for these power plants to become commercially viable [6].

1.3 System performance targets & safety

There are many requirements to achieve technical success and commercial viability of hydrogen storage technologies for transportation applications. The US Department of Energy (DoE) has devised a set of targets to quantify and specify these requirements on the basis of making a hydrogen power plant (e.g. fuel cell or internal combustion engine) operated vehicle competitive with those running on fossil fuels. The 300 miles (500 km) driving range target is supplemented by requirements on volume, weight, cost, refuelling time, durability, cycle life, and transient performance of the storage system, as shown in Table 1. These targets, which have been revised in 2009, provide a useful benchmark for comparing different storage methods. Table 1 provides a comparison of the original targets for 2010 and 2015 and the new 2010, 2015, and "Ultimate" targets. The ultimate targets are set with the aim of facilitating the introduction of hydrogen-fuelled propulsion systems across most vehicle classes. The targets were updated to account for differences in vehicle architecture between gasoline internal combustion engines and fuel cell vehicles; the current targets are based upon fuel economy of current fuel cell vehicles. It is important to note that these targets are for a complete system, including tank, material, valves, regulators, piping, mounting brackets, insulation, added cooling capacity, and/or other balance-of-plant components [7, 8]. Therefore, the gravimetric and volumetric storage capacity of the actual storage material will need to be significantly higher than the ultimately required values of 7.5 wt. % and 70 g/L. It is also required that all these targets are still met at the end of the required service life (approximately 1500 cycles or 5000 operation hours, equivalent of 150,000 miles) of the storage system. One important parameter not listed in table below is the operation temperature of the storage system, this is determined on the basis of what is practical (i.e. depending on ambient conditions) and the operation temperature range of the fuel cell; -40 to 85 °C is the range required on this basis [7].

Table 1. Performance targets as revised of 2009 [7].

Target	**2010** old	**2010** new	**2015** old	**2015** new	**Ultimate**
System Gravimetric Density [% wt.] (kWh/kg)	6 (2.0)	4.5 (1.5)	9 (3.0)	5.5 (1.8)	7.5 (2.5)
System Volumetric Density [g/L] (kWhr/L)	45 (1.5)	28 (0.9)	81 (2.7)	40 (1.3)	70 (2.3)
System fill time for 5-kg fill [min] (kg H_2/min)	3 (1.67)	4.2 (1.2)	2.5 (2.0)	3.3 (1.5)	2.5 (2.0)
System cost (\$/kg H_2) (\$/$kWhr_{net}$)	133 (4)	133* (4)*	67 (2)	67* (2)*	Tbd

*Cost targets are being considered as other H_2 fuel cell targets are assessed.

Safety considerations come before any of the above system requirements. It is vital that the storage system for transport applications must be crash-safe and not release hydrogen gas rapidly if damaged. Besides the system storage targets the safety implications have to be addressed at the research level; no material posing a serious risk will be considered as an option even if it can meet all the above performance targets. Although there are many important management and safety issues associated with the widespread use of hydrogen, if stored and used safely, it poses no greater danger than conventional fuels, methane and propane. Any release of hydrogen into atmosphere, on the other hand, incurs a large risk of explosion or rapid combustion. This risk is even higher if the storage container is maintained at a high pressure. The temperature for the spontaneous ignition of hydrogen in air is 585 °C compared to 540 °C and 487 °C for methane and propane respectively [9]. Furthermore, the minimum ignition concentration of hydrogen in air, 4 %, is four times higher than that of petrol vapour. Thus, hydrogen carries no greater risk than both these conventional fossil fuels. Furthermore, hydrogen's large buoyancy and diffusion properties mean that the released gas will rapidly rise and disperse rather than accumulate on the ground like petrol and propane, which present a hazard for major explosions. Nevertheless, the ignition of large amounts of hydrogen in the air can be very dangerous since the flame is almost invisible and the flame front moves very fast (~ 50 m/s) releasing more energy per unit weight than other fuel gasses. Thus, a hydrogen explosion can do substantial damage. For this reason, the security of the storage systems that are developed is of great importance.

1.4 Hydrogen storage systems

1.4.1 Hydrogen storage as compressed gas

At ambient conditions (1 bar and 25 °C) 1kg of hydrogen gas occupies a volume of approximately 11m^3 [1]. Thus, to contain it in smaller volumes it must be compressed to several hundred atmospheres and stored in specially designed pressure vessels. High pressure cylinders containing compressed hydrogen at 350 bar (5,000 psi) or 700 bar (10,000 psi) are currently the most commonly used systems in prototype fuel cell vehicles [10]. These cylinders are typically made of a high molecular weight polymer or aluminium liner wrapped with carbon/epoxy composites to ensure high strength while maintaining light weight. While the polymer or Al liner serves as a hydrogen gas permeation barrier the composite wrap is used to strengthen the cylinder for high hydrogen pressures (5,000 - 10,000 psi). An example of this type of cylinder, as developed by Quantum Technologies, is illustrated Figure 1.3. For example, in newer cylinders the H_2 weight capacity exceeds the old DOE target of 6 wt.% (for 2010) at maximum pressures of 350 bar, but the tank volume tends to be a factor of two or more higher than that acceptable for on-board applications. Increasing the hydrogen pressures from 350 to 700 bar enables approximately 30% reduction in the tank volume, but at the higher safety risk and increased compression energy requirements [11]. Compressed hydrogen tanks [5000 psi (~35 MPa) and 10,000 psi (~70 MPa)] have already been certified worldwide. Although high pressure composite cylinders are the most commonly used storage systems for fuel cell operation, their safe installation and operation and the cyclic stability remain as important drawbacks.

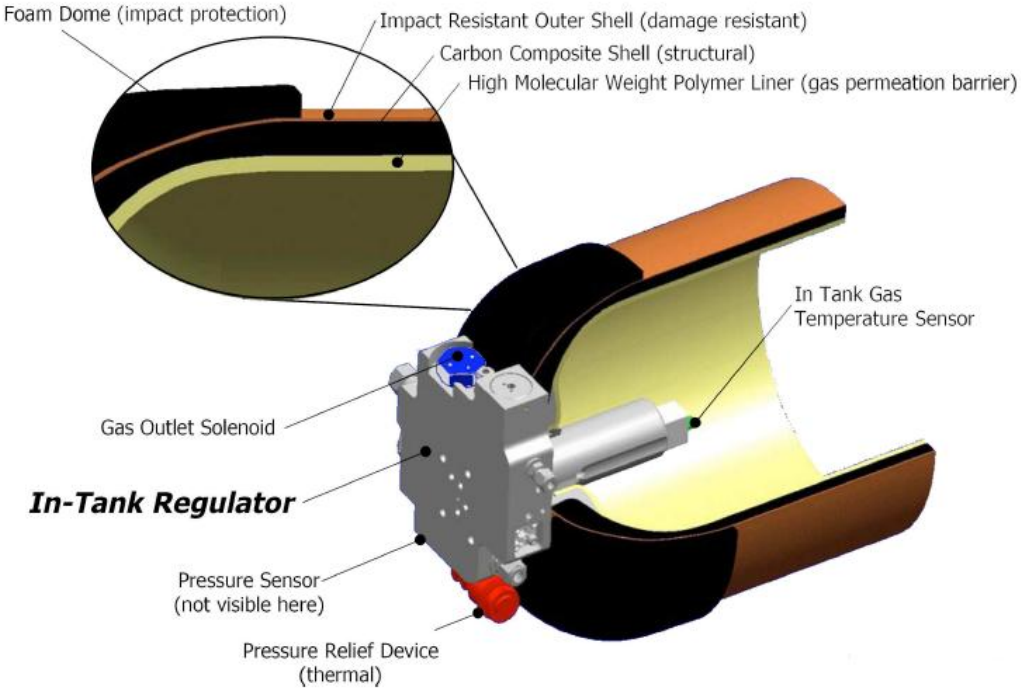

Figure 1.3:Design for high-pressure hydrogen tank by Quantum Technologies [12]

1.4.2 Hydrogen storage in liquid form

Another common way of storing hydrogen is in its liquid state in cryogenic tanks by cooling it to 21.2 K at ambient pressure [1]. The volumetric capacity of liquid hydrogen is 0.070 kg/L (compared to 0.039 kg/L at 700 bar) [2]. Thus, in principle, cryogenic tanks can store more hydrogen than compressed gas tanks. For example, the General Motors HydroGen3 Opel Zafira minivan is reported to have a driving range of 400 km (249 miles) with 4.6 kg liquid hydrogen. This compares to 270 km (168 mile) for 3.1 kg of H_2 at 700 bar in the same vehicle [2]. However, a key issue with liquid hydrogen storage is hydrogen boil-off, the rate of which depends on a number of factors such as the amount of hydrogen stored, effectiveness of the thermal insulation, ambient conditions and driving frequency. More hydrogen is lost if the system has been dormant (i.e. not in motion) and the pressure of the tank reaches the H_2 boil-off pressure. Though boil-off has been significantly reduced over the years through improved insulation systems (materials) to rates around 0.4% or 0.2% per day for tanks with a storage volume of $50m^3$ or $100m^3$ respectively [1], it remains an issue with safety implications in closed areas, such as car parks. Furthermore a trade-off between the amount of thermal insulation used and the system-level gravimetric and volumetric capacity has to be considered among all of these different factors. However, the cost of liquefying hydrogen remains an important drawback. Even with minimal or no boil-off, liquefying hydrogen costs one third of its energy content. Thus, liquid hydrogen storage is not an economically viable option unless low energy and cost effective liquefaction approaches are developed.

1.4.3 Cryo-compressed systems

The low volumetric and gravimetric storage capacities of above systems (compressed gas and cryogenic cylinders) are being tackled through the use of both storage modes simultaneously in cryo-compressed tanks. This approach uses the fact that at a fixed pressure and volume, the volumetric capacity of the tank increases as the tank temperature decreases. Cryo-compressed hydrogen storage tanks are cryogenic vessels with high gas pressure (up to 350 bar) capability for on-board hydrogen storage applications. These systems, which are the main choice for BMW, can contain between 6.2 kg and 10.7 kg of hydrogen if the tank is refuelled with subcritical liquid hydrogen at temperatures between 180 K and 300 K [13]. In this system, the hydrogen is not maintained in a liquid state but, depending on the temperature, as a two-phase mixture of liquid and gaseous hydrogen.

The gravimetric capacity is reported to be 5.4 wt.%, while the volumetric system capacity on average is around 32 g/L, a value higher than other storage options [13]. This system has several advantages over liquid hydrogen systems: no H_2 loss through boil off, the option to fill gaseous H_2 at ambient temperatures, and a simpler method for monitoring hydrogen in the tank [13]. Additionally, the cryo-compressed system has approximately twice the volumetric efficiency of 350 bar systems (with 20% lower cost) and a 40% higher volumetric efficiency than 700 bar systems (with 50% lower cost). However, these advantages come at the cost of increased off-board energy consumption due to liquefaction energy requirements.

1.4.4 Chemical hydrogen storage (chemisorption)

1.4.4.1 Introduction

Most materials currently being investigated for hydrogen storage applications store hydrogen chemically; hydrogen is either chemically bound to the materials via chemisorption (i.e. through absorption and dissociation of H_2) or chemically bound to the material through direct reactions between different hydrogen containing compounds. Chemical hydrides separate out in to different groups depending on the composition of the compound (e.g. whether binary or ternary) or nature of the chemical bonds (e.g. whether ionic, covalent or metallic or a combination of these). The two most common hydride families are *Metal Hydrides* and *Complex Hydrides;* the distinctions between these hydrides are described below. It should be noted that the demarcation between the different types is not very sharp [14] due to the co-existence of different types of bonds in some of the materials.

These hydride materials have attracted much attention due to their high gravimetric and volumetric storage capacities, some of which already exceed the US DOE targets, as detailed in the sections below. However, the main problem with these materials are the high desorption temperatures (ranging from 150-700 °C), resulting from the high binding energies of hydrogen, which is typically well above 50 kJ mol^{-1}, and slow hydriding/de-hydriding kinetics due to the nature of the absorption and desorption process (described in §1.4.4.2). Improving the fuelling rates and conditions are absolutely critical for the viability of these materials as on board hydrogen storage systems. Adding nano-texture to these hydrides leads to dramatic changes in their physical and chemical properties, resulting in reduced decomposition temperatures and hyriding/de-hydriding kinetics. Reducing the size of these materials (i.e. nanostructuring) is currently the starting point in most hydrogen storage investigations. For this reason nanostructuring has been the central point of this study. A discussion on how nanostructuring can improve hydrogenation properties of hydrides is provided in §1.5. Before that the properties of metal and complex hydrides are discussed.

1.4.4.2 Metal hydrides and their hydriding mechanism

A *Metal Hydride* is single phase compound composed of hydrogen atoms dispersed in a metal atom matrix. Binary hydrides with ionic bonds (e.g. MgH_2, NaH, CaH_2) are formed by alkali and alkaline earth metals, those with covalent bonds are formed by non-metal elements like S, Si, C or B, and those with metallic bonds (e.g. $LaNi_5H_6$, $PdH_{0.6}$, $FeTiH_2$) are composed of transition metal or a rare earth metal hydrides. The gravimetric and volumetric storage capacities, as well as the decomposition temperatures (T_{dec}) and reversibility of selected binary compounds are compared with that of gaseous and liquid hydrogen in Table 2 [6]. Of these materials, Magnesium hydride (MgH_2) has attracted most attention due to its low atomic weight, high hydrogen storage capacity (7.6 wt.%), and low cost [15]. However, like many other hydrides it suffers from slow kinetics and a high decomposition temperature (~330 °C). A more detailed overview about the status of Magnesium based hydrides and other metal hydrides can be found in references [6, 15, 16].

Table 2. Storage capacity, dehydrogenation temperature (T_{dec}) and the kinetic reversibility assessment of simple binary hydrides compared to that of liquid and gaseous H_2 [6].

Compound	**Gravimetric capacity wt.% H_2**	**Volumetric density N_H (H/ml x10^{-22})**	**T_{dec} (°C)**	**Kinetic reversibility**
H_2, liquid	100	4.2	–	–
H_2, gas	100	0.49	–	–
LiH	12.6	5.3	720	Poor
NaH	4.2	2.3	425	Good
MgH_2	7.6	6.7	330	Very poor
CaH_2	4.8	5.1	600	Good
AlH_3	10.0	8.84	150	Irreversible
TiH_2	4.0	9.1	380	–*

*No information available.

The absorption of hydrogen to form a metal hydride consists of several steps. This interaction between the hydrogen and the metal at different points of the adsorption process can be described by a simplified one-dimensional potential energy curve (1-D Lennard-Jones potential) as shown in Figure 1.4. Molecular hydrogen is first physisorbed on the surface of the metal (E_{Phys}~10 $kJmol^{-1}$ H_2). When the pressure and temperature becomes sufficiently high, the adsorbed hydrogen then dissociates at the surface and becomes chemisorbed (E_{Chem} ~50 $kJmol^{-1}$ H_2), as depicted in Figure 1.5; this happens when the conditions are right for the hydrogen to overcome a dissociation energy barrier for activation, which depends on the surface elements involved. As shown in Table 2 the reversibility of the process is an issue for some of the materials, which makes their use impractical for continuous use in any application.

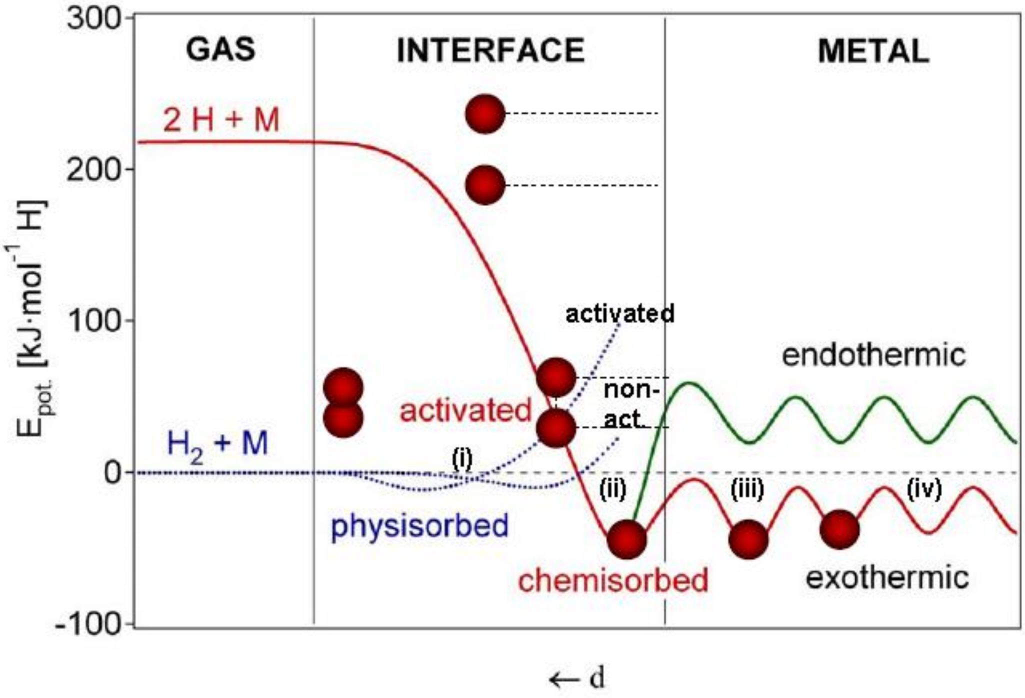

Figure 1.4 : Lennard-Jones potential energy curve for hydrogen binding to a metal at stages of (i) physisorption for both activated and non-activated processes; (ii) dissociation and surface chemisorption; (iii) surface penetration and chemisorption on subsurface sites; and (iv) diffusion [17].

The hydrogen atoms chemisorbed on the surface then move in to subsurface sites and rapidly diffuse through the material, forming a solid H-metal solution known as the α-phase (when $H/M<0.1$) (Figure 1.5 (a))[6]. With increasing hydrogen concentration ($H/M>0.1$) and lattice expansion the interaction between H atoms becomes important and the hydride phase (β-phase) nucleates and grows (Figure 1.5 (b)) [6, 18]. The hydrogen to metal ratio in a fully formed hydride is typically $H/M=1$ [6]. This phase transition causes change in crystalline structure and volume expansion (of ~10-20 % in some materials) [18]. The energy barrier associated with this volume expansion and interface energy between the phases reduces hydriding kinetics, which can be improved through nanostructuring, as described in §1.5 below. Furthermore, this absorption process is highly exothermic; requiring about 14.6 MJ of heat energy per kilogram of H_2 to be removed by a coolant in a metal hydride storage system [19].

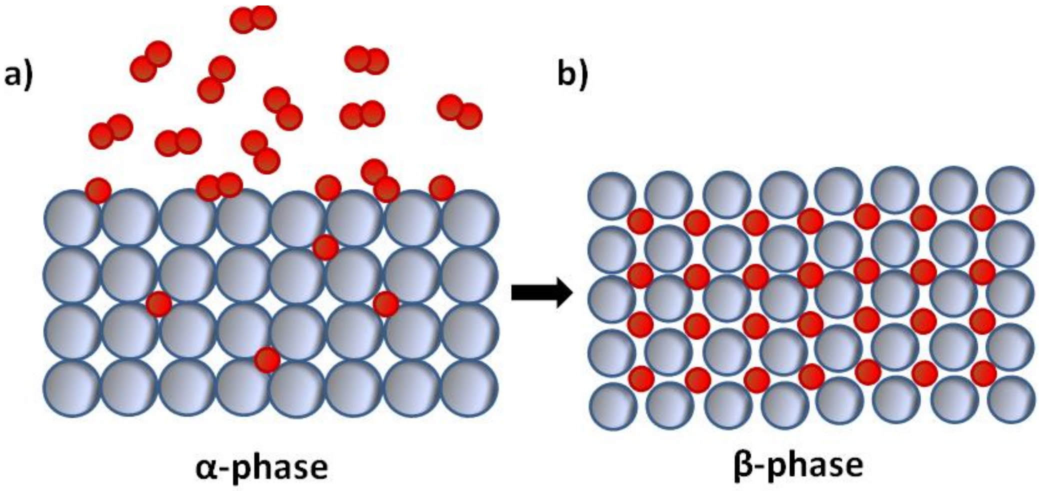

Figure 1.5: (a) Hydrogen adsorption, dissociation and absorption; a few hydrogen atoms have dissociated and diffused into the low density α-phase and (b) high hydrogen density β-phase formed through lattice deformation and expansion.

1.4.4.3 Complex hydrides

Complex hydrides, are formed of highly stable metal hydrogen complexes with $[AlH_4]^-$, $[BH_4]^-$, $[NH]^{2-}$ and $[NH_2]^-$ complex ions that form covalent or ionic bonds with a cation (e.g. Li, Na, K, Mg, or Ca) in which hydrogen usually resides at the corners of a tetrahedron with the metal (e.g. B or Al) at the centre. Complex hydrides, thus, divide into three main groups; (i) the *alanates* formed from the Aliminium based complex anion $[AlH_4]^-$ (e.g. $NaAlH_4$, $Mg(AlH_4)_2$), (ii) the *borohydrides* formed from the boron based complex anion $[BH_4]^-$ (e.g. $Li(BH_4)$, $Mg(BH_4)_2$) and (iii) *imides* and *amides* formed from the nitrogen based complex anions $[NH]^{2-}$ and $[NH_2]^-$ respectively; hydrogen is hydridic ($H\delta^-$) in the former two and protonic ($H\delta^+$) in the latter two systems [6].

Table 3 shows the storage capacities and hydrogen desorption temperatures of some selected complex hydrides. As shown in the table the ratio of hydrogen to metal atoms (H/M) in many cases is two; many of the materials exceed the DoE gravimetric storage capacity, with $LiBH_4$ having the largest gravimetric density at 18.4 wt.%. These materials are considered as more promising options for hydrogen storage than metal hydrides due to their higher storage capacities, lower desorption temperatures and greater stability. Yet, the kinetics and the thermodynamics of the reactions are still big issues. Furthermore, some of the materials decompose above their melting points; most non-reversibly decompose into several phases upon hydrogenation. As an example, borohydrides decompose according to the equation [1]:

$$M^{+x}[BH_4^-]_x \rightarrow MH_x + \frac{x}{2}B_2H_6 \rightarrow MH_x + xB + \frac{3x}{2}H_2 \tag{1.1}$$

Table 3. Gravimetric storage capacities and dehydrogenation temperatures of some complex hydrides, reproduced from ref [6, 15, 16].

Complex compound or reaction	Storage capacity (wt.%)	T_{des} (°C)	Dissociation Enthalpy (kJmol^{-1} H_2)
$LiBH_4$	13.5	380	-177.0
$NaBH_4$	10.8	400	-216.7
KBH_4	7.4	500	—
$Mg(BH_4)_2$	13.7	260-280	-39 to-57
$Ca(BH_4)_2$	9.6	350	32
$Al(BH_4)_3$	16.8	20	—
$LiAlH_4$ (1st,2nd reactions)	7.9	160,180	-10,25
$NaAlH_4$ (1st,2nd reactions)	5.6	210, >250	37,47
$KAlH_4$ (1st,2nd reactions)	5.7	300,340	55,70
$Mg(AlH_4)_2$	9.3	140-200	41
$Ca(AlH_4)_2$ (1st,2nd reactions)	5.9	127,250	-7,28
$Li_3N + H_2 \rightarrow Li_2NH + LiH + H_2$	5.4	>320	148
$Li_2NH + LiN + H_2 \leftrightarrow LiNH_2 + LiH + H_2$	6.5	280	45
$Mg(NH_2)_2 + 2MgH_2 \rightarrow Mg_3N_2 + 2H_2$	7.4	200	~3.5

Complex hydrides are formed through various chemical processes, involving reactions between compounds (elements) containing the constituent elements. Even though the dehydriding mechanism, which typically involves a series of reactions, is different to that in metal hydrides (described above), nanostructuring these materials also results in enhanced kinetics and lowered desorption temperatures [16]. For example, in the case of $NaAlH_4$, which releases hydrogen in several steps (3.7 wt% H_2 in the 1st and 1.9 wt% H_2 in 2nd step) [15], ball milling of the complex for 15 minutes in one study, is reported to have lowered the decomposition temperatures from 210 °C to 160 °C and from 260 °C to 220 °C, respectively, for the first and second steps [16]. The reaction kinetics were also found to be faster in both reaction steps [16]. Studies also show reduction in the enthalpy of desorption in nano-size materials. In the case of $NaAlH_4$, Balde *et al.* reports that the desorption activation energy to be reduced from 116 kJ mol^{-1} for 1−10 µm particles to 58 kJ mol^{-1} for 2–10nm; a value reported to be lower than Ti catalysed $NaAlH_4$ (Ti is generally used for catalysing the decomposition process of $NaAlH_4$) [20]. Nano-$NaAlH_4$ is also reported to lower re-hydrogenation pressure, with hydrogen absorption at pressures starting from only 20 bar, as compared to 45 bar in Ti catalysed $NaAlH_4$ [20]. The greatest challenge with many of these materials, however, remains to be the non-reversibility of the decomposition process of hydrogen. Some of them, like some metal hydrides, are also reactive in air. Thus, any nanostructuring process developed to enhance dehydrogenation properties will also need to address these issues before they can be considered as viable solutions for hydrogen storage.

1.4.4.4 Other chemical hydrides

Other chemical hydrides, which do not specifically fall in to any of the above categories, are being investigated as potential hydrogen storage materials. These include multiple component complex hydride systems formed of binary mixtures of hydrides such as borohydrides or aluminohydrides, which show improved thermodynamics and thus reduced decomposition temperatures. For example the Li–Mg–N–H system with varying ratios of $Mg(NH_2)_2$:LiH (or $LiNH_2$:MgH_2) displays a relatively low desorption temperature at 150 °C while the hydrogen storage capacity is maintained at ~ 5 wt% (as for the storage capacity of the individual compounds) [6]. Other materials of interest are Amino boranes (N-B-H compounds) which have ammonia addition. Of these ammonia borane (NH_3BH_3) has attracted the most attention due low molecular weight and high hydrogen content of 19.6 wt.%; it is in fact considered as one of the most promising chemical hydrogen storage candidates, though non-reversibility of the decomposition process remains a big challenge. Since ammonia borane is the chemical hydrogen storage material studied in this investigation an extended literature review of this material is provided in §5.2.1, where I discuss the study on nanostructuring ammonia borane through co-electrospinning by encapsulating it in a polystyrene sheath.

1.4.5 Hydrogen storage based on physisorption

Physical adsorption (physisorption) is a process where gas molecules (adsorbate) bind weakly onto the adsorbing material (substrate) through van der Waals forces. While charge fluctuations are present the electronic structure of the atoms or molecules are barely perturbed upon adsorption, i.e. chemical bonds are not formed. The interaction energy between the substrate (S) and the hydrogen molecule (H_2) is given by:

$$E_{S-H_2} = \frac{\alpha_S \alpha_{H_2}}{R^6} \tag{1.2}$$

where α is the polarizibility and R is the interaction distance [21]. Since $\alpha_{H_2}$is fixed, the only way to increase the interaction energy is to use substrates that contain highly polarisable species, such as those with outer π-electrons. The potential energy of the adsorbed molecule resulting from the attractive and repulsive forces tends to show a minimum at around one molecular radius, with the minimum interaction energy being in the order of 0.01–0.1 eV (1–10 kJ mol^{-1}). At temperatures above the boiling point of the absorbent physisorption usually results in just a single molecular layer of adsorbate being formed [21]. The remaining gas interacts with this solid or liquid monolayer and, therefore, the binding energy of a second layer is similar to the latent heat of sublimation or vaporisation. For this reason, besides the strength of the interaction, the equilibrium adsorption amount $n(T,p)$ of gas is proportional to the surface area available (i.e. the quantity of hydrogen that can be accommodated in a monolayer) [21].

The enthalpy of adsorption, or the energy needed to keep the atoms/molecules bound to the system at a given temperature can be calculated thermodynamically. Since the adsorbed layer and the bulk gas are in equilibrium, the Gibbs free energies are equal: $G_{gas} = G_{ads}$. Substituting G = H-TS yields:

$$H_{ads} - H_{gas} = T(S_{ads} - S_{gas}) \tag{1.3}$$

As adsorption results in a reduction in the molecular degrees of freedom, the entropy of the gas is taken to be much greater than that of the adsorbate ($S_{gas}>>S_{ads}$). For most adsorbents this change in entropy is estimated to be approximately -8R [22]. From this the required enthalpy change upon adsorption (enthalpy of adsorption) for room temperature is estimated to be:

$$\Delta H = H_{ads} - H_{gas} \approx -8RT \simeq -20\ kJ\ mol^{-1} \tag{1.4}$$

However, since the interaction strength is much weaker, significant adsorption is only obtained at temperatures less than 100 K; 77 K (liquid N_2 temperature) is typically used in studies of adsorption, though lower temperatures result in greater adsorption.

For the purposes of hydrogen storage, physisorption based systems have a number of advantages over other systems that involve a chemisorption or chemical reactions (those systems discussed in §1.4.4). Since there is no bulk solid diffusion and dissociation, as in the case of chemisorption storage systems, H_2 physisorption is very fast and reversible, allowing both refilling time and cycle-life targets to be met. Furthermore, since the adsorbed hydrogen does not react chemically, no fuel cell poisoning impurities are released during adsorption or desorption process. Also, since the binding energies are low, heat management issues during hydrogen charging and discharging is not an issue. It is these characteristics that make physical adsorption an attractive storage method. However, due to intrinsically low binding energies, the adsorbed hydrogen density is too low at room temperature and pressure.

Physisorption-based hydrogen storage systems can be separated out as carbon based materials; e.g. carbon nanotubes (CNTs) [23, 24], activated carbons (ACs) [25, 26], carbon and graphitic nanofibres (CNFs) [27-30], carbon aerogels [31], and high surface area materials; e.g. metal organic frameworks (MOFs) [32, 33] and zeolites [34, 35]. None of these materials satisfy the storage capacity targets and in fact have very low storage densities at room temperature. Even for modest densities a cooling system will be needed to lower the material temperature to that of liquid nitrogen (77K). While manufacturers will be reluctant to take up a system that requires such low temperatures, these systems will have economical advantage over liquid hydrogen storage. Studies have shown that the density of the adsorbed hydrogen at 77K approaches that of liquid hydrogen [36], with the refrigeration costs at this temperature being approximately 25% of the liquefaction temperature (20 K), with far less boil-off [37]. Nevertheless, increasing the operating temperature and uptake capacities of these materials requires going beyond purely physisorbtive storage. In this respect, hydrogen storage studies on these materials are presently focused on increasing surface areas, e.g. through nanostructuring, and their binding energies (i.e. enthalpy of adsorption) by doping them with metallic species, as discussed in §1.5 below.

1.4.5.1 Carbon adsorbents

Carbon adsorbents have gained much attention as physisorption hydrogen storage systems due to their ease of manufacture, light weight, and low cost. Many forms of carbon have been investigated (e.g. CNTs, CNFs, Fullerenes, AC and graphite) with large dispersions obtained for hydrogen capacity values, even for the same kind of carbon material between different experiments. Much hype was created around carbon stores in the late 90s when Dillon *et al.* [23] reported storage densities around 5 and 10 wt.% for nanotubes and Chambers *et al.* [38] reported 67 wt.% for graphite nanofibres. Although, none of these results were later reproducible, these publications have stimulated a lot of R&D activity in the field of hydrogen storage in carbon nanomaterials. Both experimental and theoretical research has been undertaken to determine the hydrogen storage potential of many of these systems [21, 39], though theoretical research has been limited due to the difficulty of modelling the dispersion interactions using first principle *ab initio* calculations. In the more initial studies, as in the case of above mentioned work, experimental errors such as little amount of sample and/or the use of both non-purified samples and gas has led to a high dispersion and low reproducibility of storage values in some carbon systems [40]. Today, these issues are less prevalent and a greater understanding exists on the real potential of these carbon stores.

Recent studies [21, 40, 41] have shown that in carbon materials where the specific surface area (SSA) is the main factor determining the quantity of hydrogen adsorbed (besides other factors such as polarisibility of the H_2 molecule), the pore volume and size distribution, as well as pore shape, have a large effect on the total hydrogen storage potential of the material. Beneyto *et al.* [40] have found that at 298 K, the hydrogen adsorption capacity is dependent on both the micropore volume and the micropore size distribution. At 77 K, they find that hydrogen adsorption is dependent on the surface area and the total micropore volume of the activated carbon. Through a set of systematic experimental investigations into a large number of carbide derived carbons (CDC) Gogotsi *et al.* [41] report finding that at 77 K, pores of 0.6 –0.7 nm in diameter provide the largest H_2 uptake per unit SSA at ambient and elevated pressures. It is found that pores larger than ~1.5 nm contribute little to hydrogen storage. The authors even report that the effect of pore size is stronger than the effect of surface chemistry on the hydrogen uptake.

The factors above are determined by the dynamic volume of the H_2 molecule and the interaction potential the hydrogen molecules experience. It is now accepted that high SSA carbons with micropores (i.e. pores with diameters < 2nm), specifically those that have slit-pore structures [42, 43], provide stronger binding sites to hydrogen. This is due to the overlap in the interaction potential from the walls of the pores. In a similar way, curved surfaces, as in the case of CNTs, leads to an overlap of the potential fields of carbon atoms and therefore to an increase in the adsorption energy; *ab initio* studies show that binding energies of hydrogen on curved graphenes can be three times that of planer graphenes [44]. The hydrogen storage potentials of the main carbon materials: *activated carbons, carbon nanotubes, graphite and graphitic nanofibres* are briefly discussed below.

Activated carbons (AC) with micropores (< 2nm) have attracted much attention as high SSA materials for hydrogen storage applications [21, 40]. The pore size and distribution can be tuned through variation of process and conditions, to allow for more optimised storage. The hydrogen uptake is typically proportional to the SSA, though pore size and volume make a difference as discussed above; the adsorption follows a Langmuir isotherm model (monolayer adsorption). Although at room temperature and pressure the storage capacity of these materials are very low (typically <1 wt%), at increased pressures and low temperatures this value is significantly increased. In some chemically activated carbons storage capacities as high as 5.6 wt.% can be obtained with the temperature at 77 K and pressure increased to 4 MPa [40]. However at ambient temperature (298K) this value is only 1.2 wt.% at 20 MPa. Carbide derived carbons (CDC), which are produced by selective thermo-chemical etching of metal atoms from carbides (e.g. ZrC, TiC, SiC, and B4C) [21, 41] are a promising class of materials for hydrogen storage. These carbon systems with SSA of up to 3000 m^2g^{-1} can store up to 3 wt.% at liquid nitrogen temperature and atmospheric pressure and up to 4.5 wt.% at 20 MPa [41].

Carbon nanotubes, typically with diameters of ~1nm, have attracted a lot of attention as potential hydrogen storage materials since their discovery in 1993. Both single- and multi-walled nanotubes have been extensively investigated since Dillon *et al.* [23] reported high storage capacities, though the excitement around the hydrogen storage potential of this material has since diminished with results being irreproducible and far less promising then the initial ones. A large range of H_2 storage capacity results, between 0.25 and 56 wt.%, have been reported for different experimental conditions. Studies show the storage capacity to be dependent on many factors, including their structure, structural defects, pre-treatment conditions, purification, geometry (surface area, tube diameter, and length), arrangement of tubes in bundles and/or 'ropes', as well as the storage pressure and temperature [21]. There is not yet an agreement on what the actual adsorption sites in CNTs are (i.e. whether H_2 is stored inside the tubes, outside the tubes, between tubes in 'bundles' and 'ropes' or between the shells in multi-walled nanotubes). However, with more recent studies it has become more evident that these materials are unlikely to meet the DoE targets unless more reactive sites (i.e. metallic species) are incorporated into the structures as in the case of other carbon materials, thus, current research on CNTs is being shaped is in this respect [40].

Graphite is another form of carbon that has been investigated for hydrogen storage application. However, due to its low interlayer distance and low SSA its hydrogen storage capability is very low. It has an adsorption enthalpy that is too low (4 kJ mol^{-1}), just like other carbon structures, requiring cryogenic temperatures for hydrogen storage. Ball milling to increase the SSA or intercalation with alkali metals to increase the interlayer spacing are approaches tested for potentially increasing the hydrogen storage capacity of graphite. In one study it is reported that after 80 hours of ball milling in a 1 MPa hydrogen atmosphere, up to 7.4 wt.% H_2 was stored, 80% of which could be desorbed at temperatures >600 K [21]. Intercalation of graphite with metal species is being used to tune the interlayer spacing of planes to distances considered optimal for hydrogen adsorption (6-7 A°) and to create binding sites for H_2 [21]. However, nanostructuring of these doped graphite systems appears to be necessary for increasing surface areas and hence the hydrogen adsorption capacities and kinetics. Besides ball milling, which is expensive and impractical, use of *Graphitic Nanofibres* (GNFs) is one option being investigated.

Graphitic nanofibres (GNFs), also known as *carbon nanofibres* (CNFs) depending on their crystallinity, are typically grown catalytically at high temperatures (>600 °C) from a mixture of carbon-containing gases over small metal particles [38, 45]. These nano-structures which consist of graphene sheets stacked at various angles with respect to the fibre axis, forming either ribbon like or in a tubular arrangement depending on the preparation process, have a structural conformation that enables enhanced hydrogen sorption. The arrangement of the graphite crystals along the fibre axis typically generates a nanofibre structure comprised of slit-pores, with edge sites exposed for adsorbates [38]. The exposed slit pores, with interplanar distance of 3.37 Å, enable the hydrogen with a kinetic diameter of 2.89 Å to easily seep through and be retained [38, 45]. The graphitic nanofibres which have small diameters (usually ranging from 5 and 100 nm) and high surface areas (BET normally ranging from 100 to 300 m^2g^{-1} but with values as high as 700 m^2g^{-1}) [21], have a structure that should reduce diffusion paths for hydrogen. The reduced diffusion path is expected to facilitate faster adsorption kinetics. Although improvements are observed in the hydrogenation properties of these nanostructures, compared to that of bulk graphite, the binding energies are still too low. GNFs can be intercalated with metallic species to tune the binding energy of hydrogen for greater hydrogen adsorption. Though intercalation of graphite has been investigated for hydrogen storage applications [8, 46-48], as far as we know the intercalation of GNFs has not been tested before. This is what we have attempted to do in the second part of this PhD study, as discussed in Chapter 6.

While nanostructuring is being employed for increasing the SSA in these carbon structures, doping with metallic species is crucial for sufficient H_2 storage densities to be obtained, because even the maximum theoretical storage capacity of a single graphene sheet (with a surface area of 1315 m^2g^{-1}) is calculated to be only around 3 wt.% at very low temperatures [21]. In this respect, *Fullerenes (e.g. C_{60} buckyballs),* which have shown no hydrogen storage capability have gained some interest in the last few years. Recent studies based upon first principle calculations within density functional theory have shown that decoration of carbon fullerenes C_n ($20 \leq n \leq 82$) with metal atoms (e.g. Ti, Sc, Ca, Be) can greatly increase their hydrogen storage potential [49-51]. These calculations show that the binding strength of the H_2 on either positively or negatively charged fullerenes increases due to enhanced polarizability of the H_2 molecule, with values ranging from 0.18-0.32 eV/H_2 [49]. This correspond to a storage densitiy of around 8 wt.% H_2 at ambient conditions. Some metals (e.g. Be) also show a Kubas like di-hydrogen binding [51]. However, it has been difficult to verify these studies experimentally due to the tendency of the metal atoms to coalesce, as opposed to being dispersed uniformly on the surface. Recent efforts are devoted to finding metal systems that do not coalesce, e.g. boron is being used to help disperse the metals on the fullerenes [51]. Experimental studies have not shown any promising results yet, due to the difficulty of maintaining the metal atoms dispersed; one recent study on (C-60-Fe-C-60-Fe)(n) complex has shown H_2 adsorption capacity of 0.5 wt.% at 77K and 2 bar [52].

1.4.5.2 Other high surface area materials for hydrogen storage

Metal-organic Frameworks (MOFs) are another set of high surface area materials that have attracted a lot of attention as potential hydrogen stores. These crystalline compounds consist of a framework in which metal ions or clusters are connected to each other by organic molecules called linkers in a three dimensional structure and have an exceptionally large surface area of up to 5500 m^2g^{-1} [32, 33]. The total H_2 adsorption on the surface of MOFs is determined by the surface area available (as shown in Figure 1.6) and the induced dipole moment interactions between the hydrogen metal ions on the surface. The most promising gravimetric storage value reported for MOFs is 10 wt.% for NOTT-112 at 77 bar and 77 K (or 2.3 wt.% at 1 bar) [53]. The storage values are still too low (<1 wt.%) at ambient temperature. The H_2 binding energy (typically between 5-10 kJ/mol) is still not sufficiently strong for room temperature storage. Thus, the challenge is to design and synthesise MOFs with frameworks that have high concentration of exposed metal sites that bind hydrogen [32]. Both theoretical and experimental research is very active in this respect.

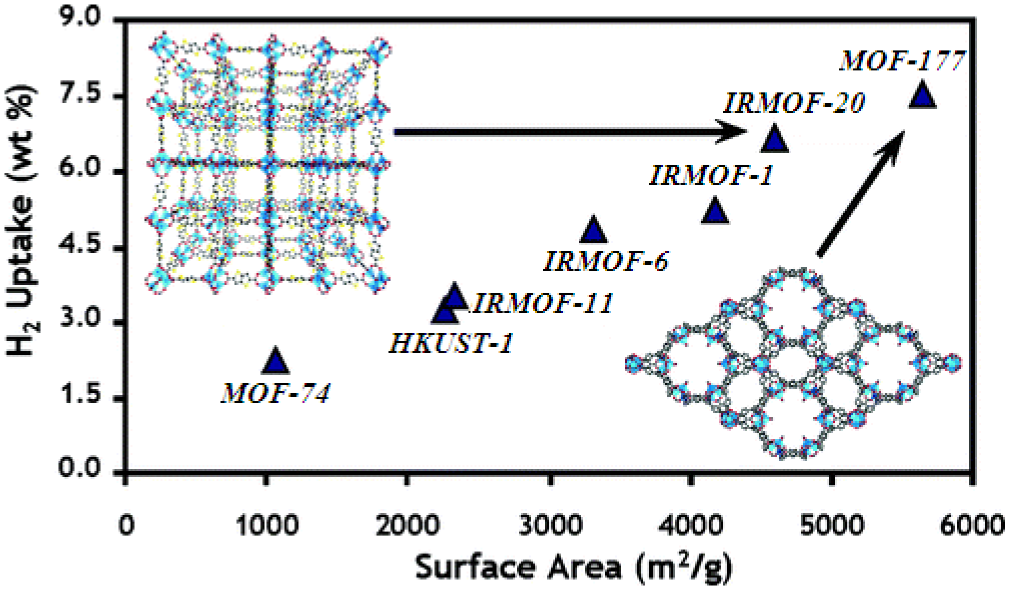

Figure 1.6: Saturation H_2 uptake plotted against Langmuir surface area for various MOFs at 77K (modified from ref [33]), saturation pressure varies between 10 to 80 bar for different MOFs. *IRMOF-X* are based on $Zn_4O(CO_2)_6$, *MOF-74* is based on $[Zn_3[(O)_3(CO_2)_3]]_\infty$ 3_1, *HKUST-1*, based on $Cu_2(CO_2)_4$ structures.

Zeolites, microporous crystalline aluminosilicates, are another set of high surface area materials investigated for hydrogen storage applications, though less so than above mentioned materials. They have an open 3D structure, which enables selective exchange of different cations. As in the case of MOFs the hydrogen storage capacity depends on the surface area of the material, which can be as high as 1000 m^2g^{-1}, the volume of the micropores and the polarisibility of the hydrogen molecule by the cations present. At ambient conditions hydrogen uptake is once again very low in these systems; ZSM-5, a typical high silica zeolite with a surface area of 430 m^2g^{-1}, has a hydrogen storage limit of 0.7 wt.% at 77 K and 1 bar, which is far lower than a typical activated carbon with a surface area of 2030 m^2g^{-1}

that adsorbs up to 2.1 wt.% of hydrogen [54]. Nevertheless, computational studies are being carried out with different cations (e.g. Ca, Na, Mg), to investigate H_2 binding sites and energies, so that zeolites with the optimal geometry and most polarising ions can be synthesised.

1.4.6 Hydrogen binding energies: the big challenge

As I have tried to portray in the sections above hydrogen storage is still a big challenge and the issues that have to be resolved are not one but many. While some materials meet the DoE storage capacity targets, none of these systems have hydrogen binding energies falling within the range desirable for practical applications. Figure 1.7 shows the range of binding energies targeted by DoE and how it compares to the binding energies in physisorption and chemisorption based materials. The binding energies are quite different for the two approaches: too low (typically around 5 $kJmol^{-1}$) for physisorption based systems and too high for chemisorption based systems (50-100 $kJmol^{-1}$ for metal hydrides and >100 $kJmol^{-1}$ for other chemical hydrides). The main challenge is therefore to shift the binding energies of these storage materials to within the desired range. As discussed above in chemisorption based systems this challenge is being tackled through chemical destabilization of the materials i.e. addition or mixing of different chemical species to form intermediate reaction steps that result in reduction in the heat of formation, or through nanostructuring as discussed in the next section. In physisorption based systems this challenge is being tackled through the addition of metallic species to these materials. For example in carbon based systems binding energies are either increased through '*Kubas binding*', where the metal additive (generally transition metals) interacts with the chemical bond in the hydrogen molecule and leads to a relatively strong adsorption of molecular hydrogen, as in the case of graphite intercalation compounds, or through '*spillover*' where the additives act as a catalytic active centre for the dissociation and bonding of hydrogen to the carbon networks [21].

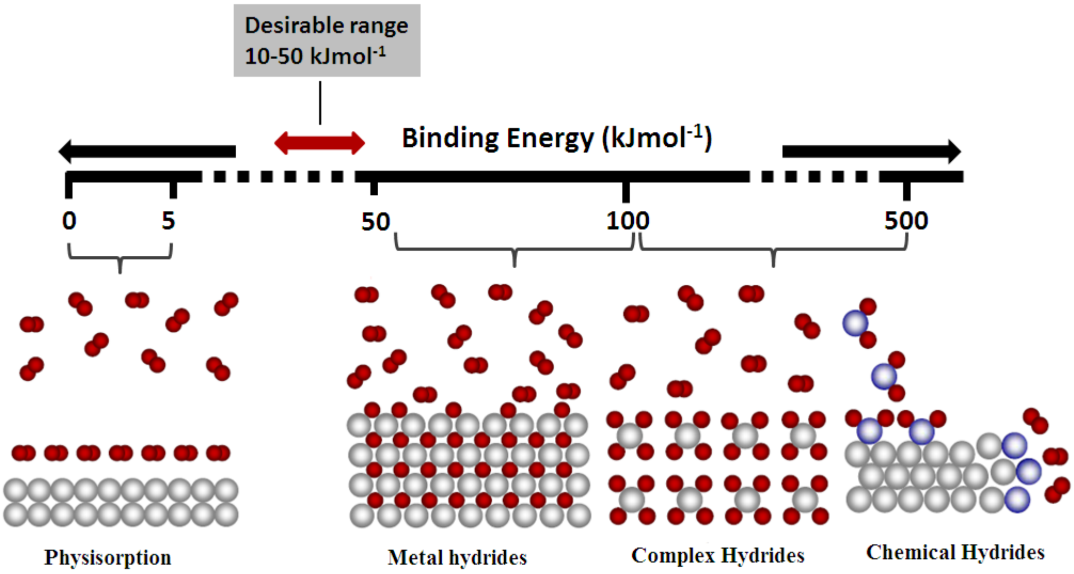

Figure 1.7: Energy scale showing the targeted binding energy range (10-50 $kJmol^{-1}$) required for room temperature hydrogen storage compared to the bond strengths found in physisorption and chemisorption based materials.

1.5 Nano-engineering hydrogen stores

Nano-structured materials are defined as materials having an average grain size not exceeding 100 nm, with the range 5-50 nm being most typical. Many studies have now confirmed the positive effect of nanostructuring hydrogen storage materials to improve the hydrogenation/de-hydrogenation kinetics, to reduce the enthalpy of formation/desorption and to increase the surface area [18, 55-61]. For this reason nano-structuring of selected physisorption and chemisorption based materials has been at the core of our investigation. The mechanisms that allow for enhanced properties in these nano-structured materials varies depending on the material, i.e. whether it is a metal or chemical (complex) hydride or whether it is a high surface area physisorption based material. One important factor promoting enhanced kinetics in nano-structured materials is the reduced diffusion paths of hydrogen due to reduced grain/particle size of the host materail. This effect is nicely explained in the case of metal hydrides, in which the hydrogenation/de-hydrogenation mechanism and the effects of nano-structuring are relatively well understood. For complex hydrides, where the decomposition process involves several reaction steps, the exact effect of nanostructuring on the decomposition process can vary for the specific hydride and in most cases it is not very well understood. In the case of physisorption based materials we have already discussed above (§1.4.5) that nanostructuring leads to increased surface area with greater density of edge sites and increased binding energy due to overlap of potential from the closely packed or curved walls. In this section I will look at the effects of nanostructuring in enhancing kinetics and reducing the enthalpy of reactions in metal hydrides. Since the physics discussed can be extrapolated to other materials, the knowhow gained in terms of the effects of nano-sizing of hydrides can be used to understand the effects of nanostructuring in other materials.

1.5.1 Diffusion and nucleation

In §1.4.4.2 it was discussed that for metal hydrides if the temperature and the pressure are high enough, the ß-phase (the pure hydride phase) will nucleate from the saturated α-phase (the H-metal solution phase) and grow. The limiting reaction rate is the diffusion of the hydrogen through the ß-layer once the ß-phase nucleates (Figure 1.8 (a)), this slows down hydride formation kinetics considerably [18]. However reducing the particle size can enable the hydrogen diffusion path to the ß-phase to be reduced and hydride formation kinetics to be enhanced. Figure 1.8 illustrates how a sufficiently small particle can prevent the formation of a closed hydride layer that slows down hydrogen from accessing the core metal phase during hydrogenation or from leaving the hydride phase during de-hydrogenation [18].

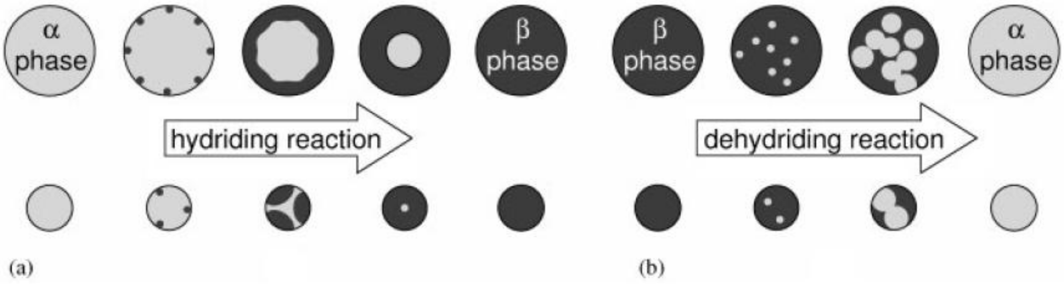

Figure 1.8: An illustration showing how the density of nucleation in a bulk particle (top path) and a nano-particle (bottom path) can vary and influence the interface energy between α- and β-phases; a) in the bulk particle multiple nucleation sites merge and form a closed loop to prevent fast diffusion of hydrogen, in the nano-particle the diffusion of hydrogen through the α-pahase remains possible even with a greater fraction of β-phase, b) during desorption the hydrogen in a bulk particle has to diffuse through a thicker layer of the β-phase, but in the nano-particle the diffusion is much quicker [18].

Since, nucleation of the β-phase particle results in interfaces being formed between the fully formed β-phase and the surrounding α-phase, the diffusing hydrogen atoms need to overcome an interface energy barrier, which slows down the reaction rate. Besides nanostructuring, the existence of a high density of cracks, lattice defects, dislocations and interfaces can also help speed up the kinetics by favouring the heterogeneous nucleation of the β-phase [18]. While, ball-milling can help induction of such defects into the system, other techniques may not. Thus, nanostructuring is ultimately the route for improving hydriding/de-hydriding kinetics.

1.5.2 Thermodynamics of reaction

Understanding the mechanisms that control the thermodynamic stability of the hydrogen storage material is important for tailoring the enthalpy of adsorption/desorption (ΔH) to be within the desired range (10-60 kJmol^{-1}), the value required for system operation at near ambient conditions. ΔH, also known as the enthalpy of reaction, represents the heat released or absorbed by the material at a given pressure during the reaction (e.g. hydriding or de-hydriding reaction). While other approaches such as the use of catalysts [62, 63] or destabilization through alloy formation (i.e. hydride mixtures) [61, 62, 64] are used to catalyse and change reaction pathways and to reduce the enthalpy of reactions, nanostructuring allows for the enthalpy to be tuned (lowered) in a more controlled manner in a diverse range of materials without compromising for the storage density. The brief discussion provided here on the thermodynamics of the reaction in metal hydrides is based on the derivations given in ref. [18]; for a more comprehensive discussion the reader is advised to look at this reference.

At a fixed temperature and pressure the force driving the reaction is the Gibbs free energy (ΔG) defined as:

$$\Delta G = \Delta H - T\Delta S \tag{1.5}$$

where ΔH and ΔS respectively denotes the enthalpy and entropy change in the reaction at a given temperature T. The reaction is thermodynamically favoured (i.e. takes place spontaneously) when ΔG is negative, even with the existence of a rate limiting energy barrier or slow diffusion process that makes the reaction kinetically unfavourable. The energy barrier in a reaction (also known as the activation barrier, E_{bar}), can be related to the temperature using the following Arrhenius rate equation:

$$K_r(T) \propto \exp\left(\frac{-E_{bar}}{k_B T}\right) \tag{1.6}$$

where $K_r(T)$ is the temperature dependent reaction rate.

In the case of metal hydrides, entropy change in the system mainly results from hydrogen being reduced from the gaseous phase to the chemisorbed phase (-130 kJmol^{-1} K^{-1}), as well as some change due to surface reconstruction and lattice expansion. At low temperatures, where ΔH is larger in magnitude than TΔS, the Gibbs free energy (ΔG) becomes negative and the hydriding reaction is favoured. However, at higher temperatures when TΔS becomes larger in magnitude, then ΔG becomes positive and the dehydriding reaction is favoured. This explains why high temperatures (typically in excess of 200 °C) are required to release the hydrogen in the material.

Ignoring any surface effects contribution to entropy change, the change in the Gibbs free energy for an ideal gas, in this case hydrogen, at a given temperature can be calculated from:

$$\Delta G = \Delta G_0 + \int_{P_0}^{P} \frac{RTdP}{P} \tag{1.7}$$

where ΔG_0 is the molar free energy at the reference state of the system ($\Delta G_0 = \Delta H_0 - T\Delta S_0$), R is the molar gas constant (8.31 m^2 kg s^{-2} K^{-1} mol^{-1}) and P is pressure (P_0 is typically 1 atm) [18]. Equation (1.7) can be applied to any non-ideal substance (gas, liquid or solid) by replacing the pressure, P, with activity, a, which takes account of the non-idealities in the system, the Gibbs free energy is redefined as:

$$\Delta G = \Delta G_0 + RTln\left(\frac{a_{mH_2}}{a_m P_{H_2}}\right) \tag{1.8}$$

The values for the standard enthalpy (ΔH_0) and (ΔS_0) can be obtained empirically from a van’t Hoff plot, as shown Figure 1.9. For a given compound the plateau pressure at given temperature corresponds to a phase transition in a material (in metal hydrides this corresponds to transition from the α-phase to the β-phase); Figure 1.9 (a) illustrates this for several temperatures. The van't Hoff plot is a logarithmic plot of the equilibrium pressure against inverse of the temperature (Figure 1.9 (b)), as defined by:

$$\ln p_{H_2}^{eq} = \frac{\Delta H_0}{RT} - \frac{\Delta S_0}{R} \tag{1.10}$$

Thus, at equilibrium where ΔG=0, the terms (ΔH_0) and (ΔS_0) can be, respectively, obtained from the slope and the intercept of the van't Hoff plot. When the pressure is equal to the reference state pressure, the decomposition temperature, T_{dec}, can be obtained from

$$T_{dec} = \frac{\Delta H_o}{\Delta S_0}.$$

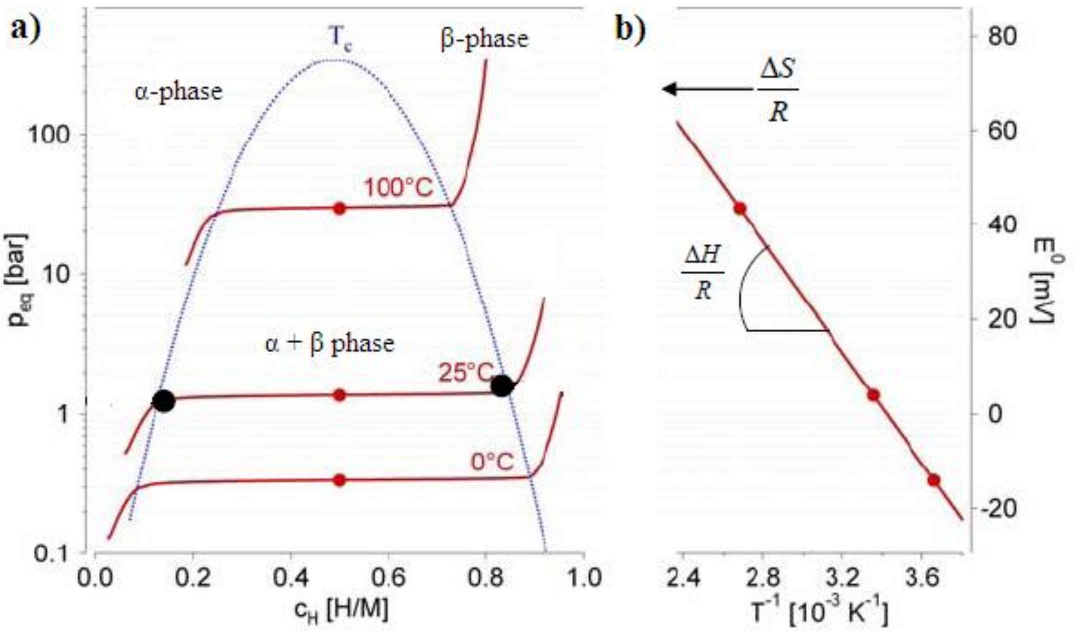

Figure 1.9: a) The plateau pressure corresponding to phase transition from α- to β-phase is measured at different temperatures, (b) van't Hoff plot: logarithm of the equilibrium pressures vs. inverse temperature, used to deduce the enthalpy (ΔH) and entropy (ΔS) of formation.

In reducing the size of the particles, the surface area and thus the surface energy contribution to Eq.(1.8) becomes important. In the case of nanomaterials this surface energy term is significantly large, and if it is larger for the hydride phase than it is for the metal then some of the heat of formation energy will be stored as the surface energy. Depending on whether this volume modified surface energy contribution is negative or positive upon nanostructuring, the enthalpy of absorption/desorption will be either lowered (if –ve) or increased (if +ve). In accounting for the surface energy term in the thermodynamic calculations, the molar free energy of reaction (Eq.(1.8)) becomes:

$$\Delta G = \Delta G_0 + RTln\left(\frac{a_{mH_2}}{a_m P_{H_2}}\right) + \frac{3V_M \Delta_{M\to MH_2}(\gamma, r)}{r} \tag{1.11}$$

where r is the radius of the particle (which is approximated to be spherical) and $\Delta_{M\to MH_2}$ is the surface term as given by:

$$\Delta_{M\to MH_2}(\gamma, r) = \left[\gamma_{MH_2}(r)\left(\frac{V_{MH_2}}{V_M}\right)^{\frac{2}{3}} - \gamma_M(r)\right] + \Delta E_{ads} \tag{1.12}$$

and V_i (where i= M or MH_2) denotes the molar volume of each phase; the molar volume of the system tends to increase by ~10-20% upon transition from the metal phase to the hydride phase [18, 19]. This surface reconstruction upon volume expansion changes the free energy as the bond energies and physical properties of the material change [18]. Since nanostructuring means an increase in the surface to volume ratio, which increases the adsorption sites due to the increased number of unsatisfied bonds, hydrogenation (i.e. binding of H_2) at the surface of both metal and hydride will reduce the surface energy by minimising the number of unsatisfied bonds. Since the surface energy reduction may be different for metal and hydride phases, an additional energy term ΔE_{ads}, which accounts for the difference in the magnitudes of surface energy reductions due to the adsorption of H_2 molecules, is included in Eq. (1.12). Taking these changes into account, a new van't Hoff relation is formed;

$$\ln P_{H_2}^{eq} = \frac{\Delta H'}{RT} - \frac{\Delta S_0}{R} \quad where\ \Delta H' = \Delta H_0 + \frac{3V_M \Delta_{M \to MH_2}}{r} \qquad (1.13)$$

which shows that there is a reduction in heat released (i.e. lowering of ΔH') in going from bulk to nano-structured materials, if $\Delta_{M \to MH_2}$ is positive (ΔH_0 is a negative quantity) or the surface energy of the hydride phase is larger than that of the metal phase. In this case, significant reduction in the enthalpy of adsorption/desorption is possible if particle sizes can be reduced. However, calculations suggest that particles with diameters no more than a few tens of nanometres are required for an observable difference [18].

The detailed mechanism resulting in improved hydrogenation/de-hydrogenation properties of materials may vary between different classes of materials, and in fact it is different for ammonia borane (AB) and graphite intercalation compounds (GICs) (the materials analysed for this PhD project). Nevertheless the above explanation, provided for metal-hydrides, can be used to understand any changes that may be seen as a result of nanostructuring these systems. The theory above can in particular shine light on any nanostructural changes seen in GICs, which involve diffusion of H_2 through a graphite lattice containing metallic species.

Nanostructuring materials or synthesising materials with nano-dimensions is generally a nontrivial process, especially with only a few nanostructuring techniques available. Ball milling and scaffolding of hydrides were described to be the most common methods employed. However, these techniques have important disadvantages associated with them; ball milling is an energy intensive process that can have problems such as sample contamination from the steel balls used for milling, and nanoscaffolding of metal hydrides can result in a significant reduction in the system storage capacity, especially if a heavy nanoscaffold (e.g. silicates) are used (as discussed in §5.2.1.4). Electrospinning, on the other hand, is a technique that can be used for nanostructuring hydrogen storage materials in a more controlled manner and has the advantages of being a cheap and scalable process.

Chapter 2

The Electrospinning Process

2.1 Introduction

Electrospinning is a highly versatile method that, through processing of polymeric solutions or melts, produces fibres with diameters ranging from a few microns to tens of nanometres [65-68]. This process, which has been used to produce continuous fibres for various different application, ranging from biomedical applications (such as tissue scaffolds, controlled drug release systems) [69-71] to filter systems, catalysis, protective clothing, optical applications (waveguides) and microelectronics [72, 73], is a technique that can potentially be used for nano-structuring hydrogen storage materials in a cheap and scalable way.

In a typical electrospinning set-up as shown in Figure 2.1, a solution or a melt is first fed through a spinneret with an inner diameter in the order of 100µm. When a sufficiently high electric field is applied to the spinneret, which simultaneously serves as an electrode, the repulsive force caused by the concentration of similar charges in the solution can overcome the opposing surface tension of the droplet at the tip of the spinneret, a Taylor cone is formed, from which a polymeric jet initiates. Although the jet is stable near to the tip of the spinneret, it soon enters a bending instability stage with the formation of a whipping cone under the influence of the columbic forces. This electrospinning jet stretches and coils, with an increasing diameter, until the solvent has evaporated, yielding fine fibres with diameters as low as few tens of nanometres. The fibres are collected as a nonwoven mesh of continuous fibres on an earthed collector, usually a metal plate or drum. The distance between nozzle and collector is set large enough to enable most of the solvent to evaporate and form dry fibres on the collection plate. The polymer chain entanglements within the solution prevents the electrospinning jet from breaking up and depending on the stability of the electrospinning process fibres with lengths of up to many hundreds of metres can be obtained.

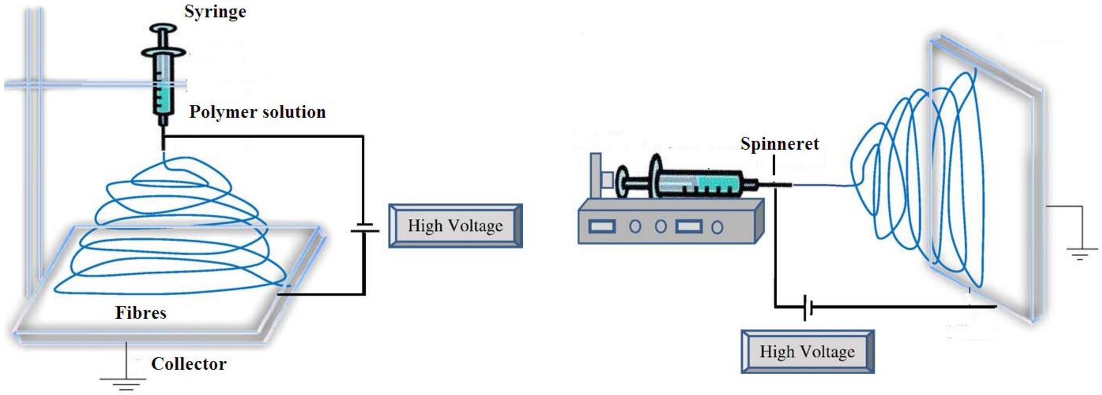

Figure 2.1: Schematic diagram of set up of electrospinning apparatus (a) typical vertical set up and (b) horizontal set up of electrospinning apparatus [74].

The versatility of the electrospinning process to produce fibres from a large range of polymeric materials or material combinations, including non-polymeric ones, either through mixing, co-axial or multiphase electrospinning of solutions, or through addition of dopants, provides the scope for this method to be used to fabricate fibres for many different applications. Post processing of the elecrospun fibres, e.g. heat or solvent treatments for creation of pores in fibres, further increases the field of applications, with more novel functions being realized through the use of different materials. We have been specifically interested in using this method to nanostructure materials for hydrogen storage applications, through co-axial (i.e. multiphase) spinning (Chapter 3) as outlined in Chapter 5 for ammonia borane-polystyrene fibres and through carbonisation of polymeric nanofibres as outlined in Chapter 6 for potassium intercalated carbon fibres.

While at first glance electrospinning appears to be a simple and easily controllable technique, it is in fact a very intricate process governed by a complex interaction of forces (electrical, rheological, molecular) and instabilities (Rayleigh and whipping instabilities). The success of this process and the control of the resulting fibre morphology and diameters is governed by a delicate balance between the process (e.g. voltage, nozzle tip-to-collector distance and solution feed rate), system parameters (e.g. polymer molecular weight, viscosity, conductivity, surface tension and solvent dielectric constant), ambient conditions (such as temperature, humidity and air velocity in the chamber) and finally motion of the target screen [73].

In order to pin down the factors that affect the formation of various nanofibre assemblies, it is important to understand the principles of electrospinning and the factors controlling the success of the process. In this chapter, the fundamentals of electrospinning process, such as the forces controlling jet evolution, the parameters controlling the success of electrospinning process and the influence of these parameters on the fibre morphology and diameters is explained.

2.2 History of electrospinning

The discovery of electrical effects on liquids was made in the late 1500s when William Gilbert [75] set out to investigate the phenomena of electricity and magnetism. Gilbert observed that a spherical droplet of water was drawn into a conical shape when a charged piece of Amber was placed near it, which caused small droplets of water to be emanated; a phenomenon now called electrospraying. This discovery came 2200 years after Thales of Miletus, the Greek philosopher discovered the phenomenon of electricity using the same special material, amber. Thales had noticed that light materials, such as feathers, were electrostatically lifted off the ground when an amber rod, which had been rubbed by a cloth, was placed near these materials.

It wasn't until 1898, that electrodynamics theory was used by Larmour [76] to explain the excitation of dielectric liquid under the influence of an electric charge. Four years later in 1902, Cooley [77] and Morton [78], patented the first devices to spray liquids through the application of an electrical charge. The electrospinning set up in Coley's patent included the use of rotating collector for the fibres produced from the jet directed by an auxiliary electrode [79].

In the 1930's electrospinning was further investigated by Antonin Formhals who attained the first patent [80] on electrospinning in 1934 for the fabrication of textile yarns from cellulose acetate using acetone and monomethyl ether of ethylene glycol as solvents [74]. Formhals came up with various innovative setups for fibre production and collection, including designs that do not require a spinneret or rotating fibre collection devices, as outlined in a series of patents he has authored [80-82]. Many of the recent electrospinning setups can in fact be traced back to these inventions and it is clear from these developments that the early researchers had already gained an in-depth knowledge of the electrospinning process [79].

However, it was not until 1964 that Sir Geoffrey Ingram Taylor, as continuation of the work started by John Zeleny in 1914 [83], looked at the behaviour of fluid droplets under the influence of an electric field and initiated mathematical studies on the jet forming process [84-86]. Taylor described that the onset of the jet in the electrospinning process was initiated by the formation of a conical shape, now known as the Taylor cone. He theoretically derived that a perfect cone formed under the influence of an electric field required a semi-vertical angle of 49.3° and demonstrated that the angle of the cone on a droplet approached this theoretical value just before jet initiation. Two years after, in 1966 Simons [87] patented the apparatus for the production of lightweight, ultra-thin, non-woven fabrics using electrospinning and in 1971, Baumgarten [88] reported electrospinning of acrylic fibres from a new set up that produced fibres with diameters in the range of 0.05–1.1 μm. Baumgarten showed how the diameters of the fibres changed with changing electric field.

Despite these early discoveries, electrospinning did not gain a lot of interest and was not utilized commercially until the 90s. It is only since the emergence of nanotechnology in the 1990s that electrospinning gained increasing attention as a way of manufacturing fibres at the nanoscale. Researchers have looked at the potential of electrospinning to produce complex and highly functionalized systems, which could be used in a variety of applications (as listed in §2.3) and applied on a commercial level. The possibilities presented by electrospinning in the fields of bio-medical research, electronics, catalysis, environmental and energy storage applications has led to an almost exponential increase in the number of scientific publications since the 90s [89, 90].

The research since the 1990s, initiated by certain research groups, notably Reneker and Rutledge [67, 91], has been focused on understanding the electrospinning process and system parameters that lead to reduced fibre diameters with different morphologies. Specifically in the last decade much theoretical work, i.e. mathematical calculations or modeling, has been carried out to gain an understanding of the electrohydrodynamic mechanism driving the electrospinning of electrically forced jets, such as the growth rate of various instabilities: the Rayleigh and whipping instabilities, as discussed in the next section.

Today, there are over 200 universities and research institutes worldwide that are looking at various aspects of electrospinning, mostly with the aim of producing nano-diameter fibres functionalised for specific applications. There are companies such as eSpin Technologies, NanoTechnics, KATO Tech, and The Electrospinning company that are using fibres obtained from electrospinning for more commercial applications, such as filtration, aerospace, structural composites, healthcare, energy storage, cosmetics, as well as research applications.

2.3 Electrospinning applications

Electrospinning is a very versatile process; by controlling the process parameters and conditions and the materials used, many essential properties of the electrospun scaffold can be adjusted, such as the fibre diameters, the morphology, the porosity and inner and outer chemistry of the fibres. The elecrospun fibres can be functionalised through the addition of various species depending on the application, i.e. nanotubes via heat treatment (Figure 2.2 (a)) [89], magnetic or conducting substances (Figure 2.2 (b)) for electronics applications or biological materials and/or drugs (Figure 2.2 (c)) [92] for biomedical applications. However, since the process requires the electrospun material to have viscous/viscoelastic properties, the electrospun solution almost always contains a polymeric component, if not fully made of a polymeric solution. Furthermore, post processing options such as heating or solvent processing allows for the morphology and the chemical composition of the fibres to be further controlled as necessary for the specific application; e.g. porosity can be introduced (Figure 2.2 (d)) through removal of a bi-component material via solvent treatment. As a result electrospun fibres with a diverse range of properties have gained interest for applications in a number of fields, including biomedical research, electronics, catalysis, environmental and energy storage applications and even applications for defence and security Figure 2.3 shows how electrospinning research has been divided within these targeted areas [73]. The fact that most of the research has been focused on developing an understanding of the process parameters and conditions (both experimentally and theoretically) (24 %) and the characterization of the fibres (36 %), outlines the complexity of the process and how every time it needs to be adjusted and controlled for each specific material and application. Electrospinning of fibres or even vesicles for biological applications, e.g. tissue engineering and wound dressing, affinity membrane and drug delivery, (at 20% of research) have attracted much interest in research.

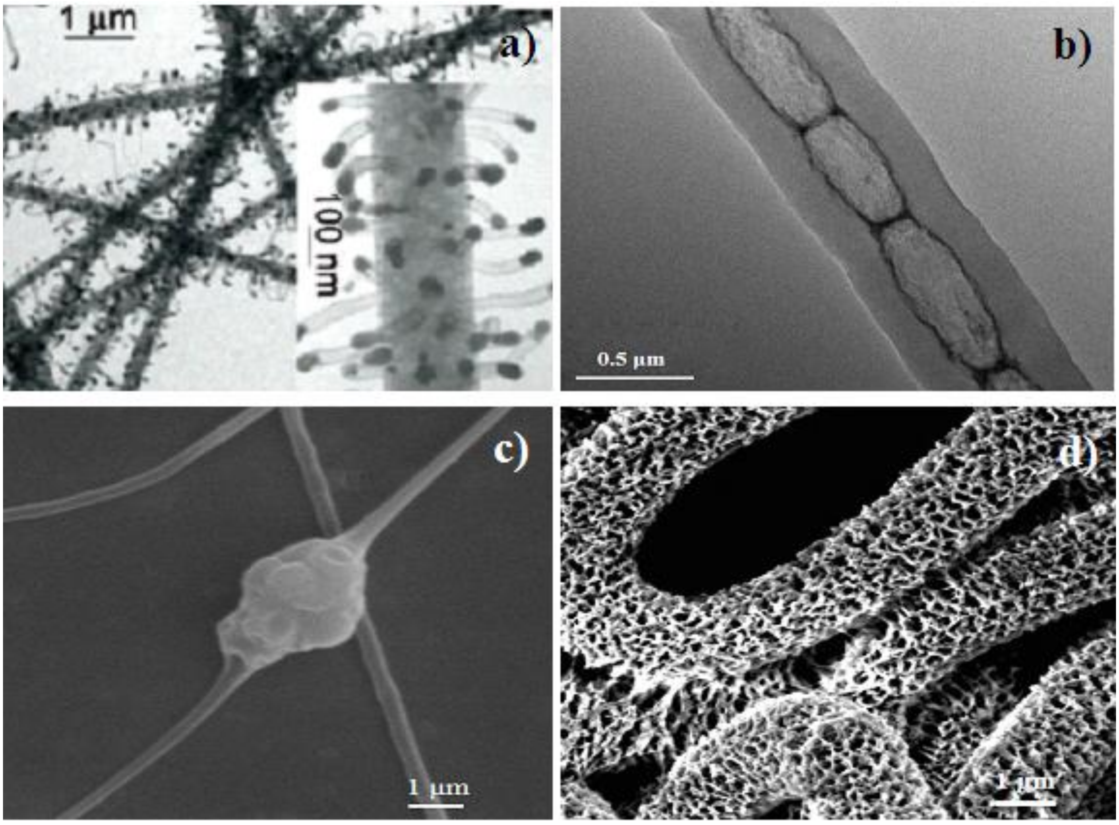

Figure 2.2: Some of the different fibre morphologies that can be produced for different applications a) TEM image of carbon fibres with grafted carbon nanotubes (CNTs), obtained from heat treatment of PAN fibres [89], b) Compartmented core–shell nanofibres with paramagnetic iron oxide particles at the interfaces, c) Poly(ethylene oxide) nanofibres that contain the bacteria *M. Letus*, d) Highly porous nanofibres produced from mixtures of polylactide and poly(ethylene oxide) after water treatment [92].

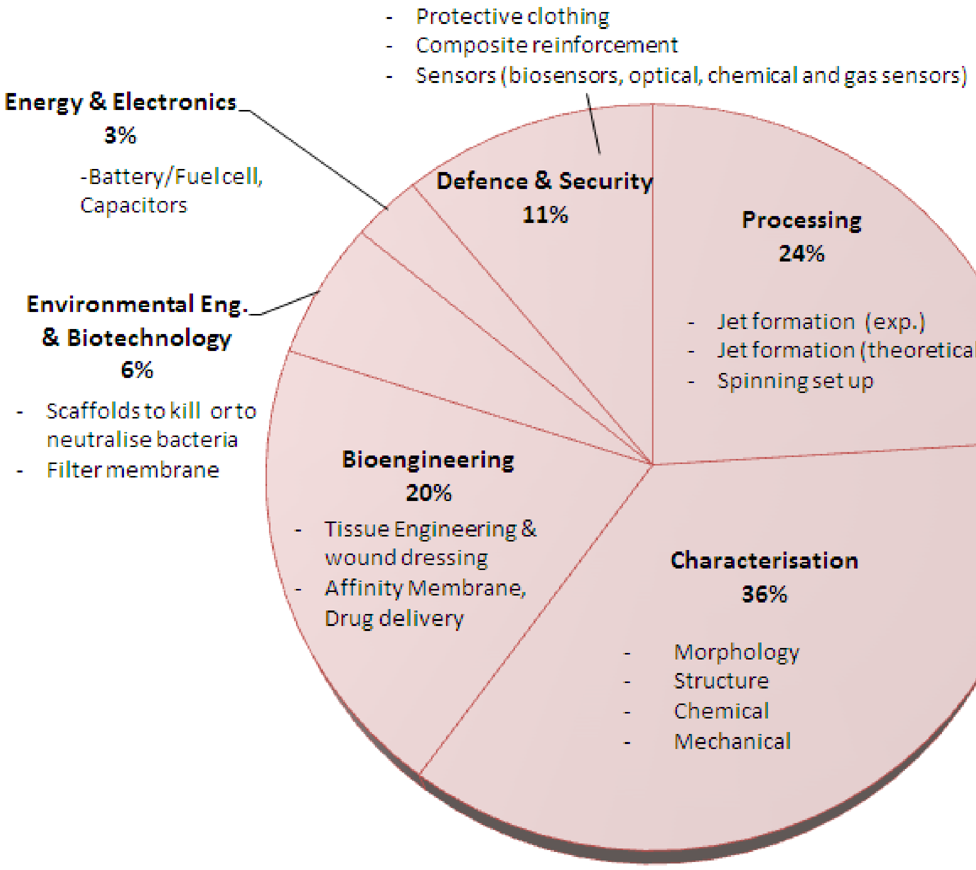

Figure 2.3: The division of research on electrospun polymer nanofibres, as adapted from [73].

2.4 Electrospinning theory: jet instability

Electrospinning works for liquids that are conducting, such that the theory presented here discusses the behaviour of viscous and ionic solutions under the influence of an applied electric field. When a voltage is applied between the nozzle and the collector, migration of electrons from the cathode to the anode causes charge build up on the surface of the solution, with the polarity of the charges dependent on the polarity of the nozzle. If the nozzle is charged negative, cations are attracted to the electrode, if it is positive, anions are attracted (Figure 2.4). The free surface of the liquid maintains an equipotential at all times, with the charges distributed in a way that maintains a zero electric field inside the liquid [93]. When a critical potential is established to enable the coulombic force, resulting from the repulsion of like charges on the liquid surface, to overcome the surface tension that keeps the droplet together, the liquid droplet acquires a conical shape referred to as the Taylor cone [94], having a half angle of 49.3° [93]. Although the size of the columbic force is correlated to the magnitude of the applied voltage, the density of ions and electrons in the overall neutral solution strongly influences the degree of charge build up.

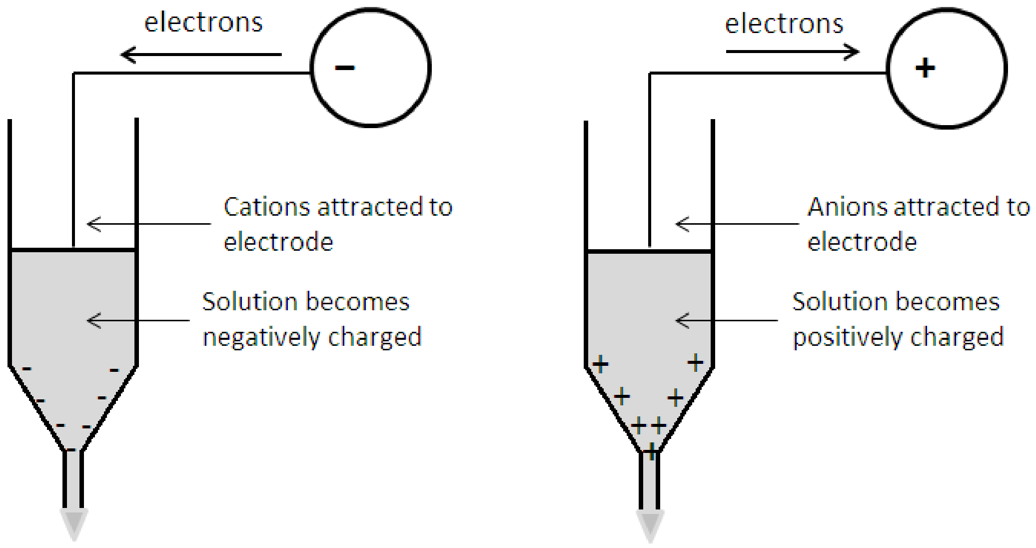

Figure 2.4: Schematic diagram of electrospinning nozzle with positive and negatively charged electrode: polarity of electrode determines polarity of charge build-up in solution

Once the Taylor cone is established, an electrically charged jet issues from the tip of the cone and accelerates down or across to the collection plate, depending on the direction of the set up (as shown in Figure 2.1). This jet, if formed of a polymeric solution, undergoes a multi-component jet stretching mode with an initial straight jet portion followed by a radially spiralling conical jet part (see Figure 2.5), which respectively arises as a result of axisymmetric and whipping (or bending) instabilities [18]. These instabilities, which arise as a result of coupling of the coulombic forces in the jet with the electric field, enable stretching of the jet to yield fine fibres.

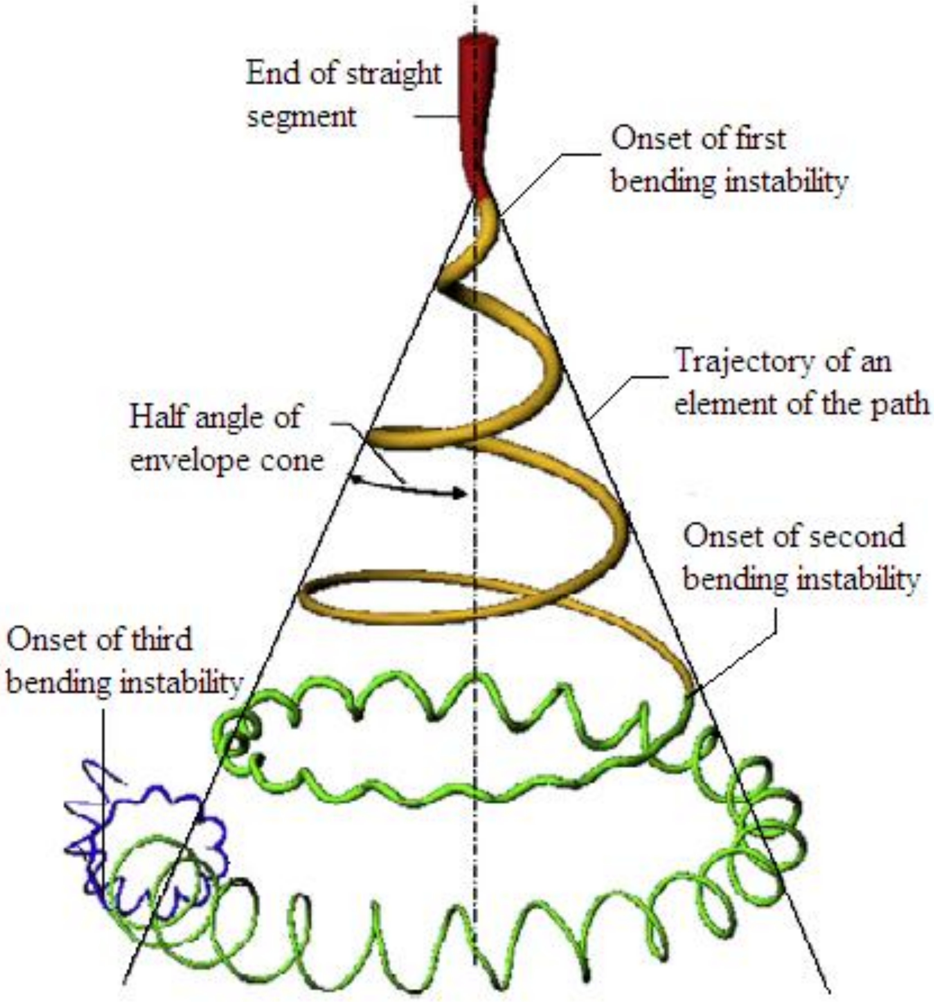

Figure 2.5: The electrospinning envelope showing the conical jet path and the way in which the bending instabilities cause thinning of the electrospun jet; three successive bending instabilities that cause spiralling and hence thinning of the jet are shown [67].

The mechanics of bending polymer jets under the influence of an electric field deserves special attention since the instability experienced by the jet plays a central role in the electrospinning process. Gaining an understanding of the electrohydrodynamics of the process is particularly important for developing predictive tools for control of the process and optimization of the electrospun fibre morphology. Since, gaining control of the fibre diameters and their morphology was critical to nanostructuring of the materials that are of interest to us, developing an understanding of the instability mechanism and the parameters that control the electrospinning process formed an important part of this investigation.

The mechanisms of the process relates to the pioneering studies of Taylor on the electrified liquid jets of low-molecular mass Newtonian liquids [95]. Taylor had shown the existence of the bending instability in electrified jets and derived equations for the bending perturbations in an inviscid liquid. Due to the complexity in modeling the electro-hydrodynamics of the process, theoretical studies have been limited in comparison to the experimental ones, though in the last one decade the number theoretical studies on the instability mechanisms in the electrified jets have shown significant growth [91, 94, 96-98]. Both simple one-dimensional (1-D) models, used for determining jet diameters, and more complex three-dimensional (3-D) models, used for modelling the growth, size and instability modes of the jet, exist. While discussing the details of these models are beyond the subject of this investigation, outlining some of the equalities that are used in 1-D and 3-D modelling of the jet can help us understand the main control parameters that affect the jet behaviour and hence the fibre morphology. While in this section I will merely define the 1-D equations used to calculate the jet radius of a single phase electrical jet, in §3.2.2, for the purpose of understanding the formation of specific morphologies in co-axial fibres, I will discuss the instability theory used for 3-D modelling of co-axial jets.

The most commonly used equation for determining the jet radius r as a function of axial distance z from the nozzle is the differential equation developed by Spivak *et al.* [99], which takes the form:

$$\frac{d}{dZ}\left[R^{-4} + (N_W R)^{-1} - N_E^{-1} R^2 - N_R^{-1}\left(\frac{dR^{-2}}{dZ}\right)^m\right] = 1 \qquad (2.1)$$

where R is the dimensionless jet radius, Z is the dimensionless axial coordinate, N_W, N_E and N_R are the Weber number, Euler number, and the effective Reynolds Numbers respectively. The dimensionless Weber number N_W describes the ratio of inertial forces to surface tension in the jet:

$$N_W = \frac{\rho Q^2}{2\pi^2 \sigma_s R_0^3} \tag{2.2}$$

The dimensionless Euler number N_E describes the ratio of inertial forces to electrostatic field pressure:

$$N_E = \frac{4\varepsilon_0 \rho Q^4}{\pi^2 J^2 R_0^6} \tag{2.3}$$

The effective Reynolds number N_R for the fluid, characterised by the power law, describes the ratio of inertial forces to viscous forces:

$$N_R = \frac{Q^2\rho}{2\pi^2 \mu R_0^4}\left[\frac{6\pi E J R_0^2}{Q^2 \rho}\right]^m \tag{2.4}$$

where ρ = fluid density, σ_s = coefficient of surface tension, E = electric field, ε_0= permittivity of vacuum, Q = volumetric flow rate, J = electric current.

Spivak *et al.* have reported a power law asymptote for R with an exponent -1/4 for the jet radius; $R \sim Z^{1/4}$ [99]. Ji-Huan *et al.* have gone further to suggest a different relationship between jet radius and distance from the orifice [100] for different parts of the jet, with $R \sim z^{-1/2}$ for the initial steady stage, $R \sim z^{-1/4}$ for the instability stage, and $R \sim z^0$ for the terminal stage by allometrical method. While these equations enable estimates of the jet radius to be made, using the parameters defined in Eq.(2.2(2.4, these 1-D models are considered as oversimplification of the real process and additional correlations are in fact needed to solve the stable jet profiles through 3-D models. One of the first extensive studies on 3-D modelling of the electrospinning jet was done by Reneker *et al.* 2000 [91], and Shin *et al.* 2001 [97]. Both groups have developed a theoretical approach based on empirical observations of the jet profiles and report obtaining theoretical results that are in good agreement with the experimental data.

Evaluation of the dispersion relations attained from these 3-D models suggests the existence of three different types of instabilities: two axisymmetric modes and one non-axisymmetric mode, which determine the size and geometry of the deposited fibres or beads. The first axisymmetric mode is associated with the classical Rayleigh instability, which is dominated by the surface tension [91, 97]. The Rayleigh instability results in the formation of vesicles or beads, as opposed to fibres, in a process called electrospraying. This happens if the viscosity of the solution is below the optimum value (i.e. the density of chain entanglements in the solution is less than the value needed to maintain sufficient resistance to the electrostatic field) and the charge density is not high enough to overcome the opposing surface tension force that causes the jet to break up into small droplets [101]. In the case of a sufficiently viscous solution, the jet formed enters the electrospinning regime and undergoes a multi-component jet stretching mode, with an initial straight jet portion followed by a radially spiralling conical jet part, as shown in Figure 2.5. The trajectory and size of this jet and hence the size and morphology of the as spun fibres is determined by the latter two instabilities mentioned above; the axisymmetric and non-axisymmetric ‘whipping’ (bending) modes, which cause the spirals to transform into smaller spirals until the jet solidifies.

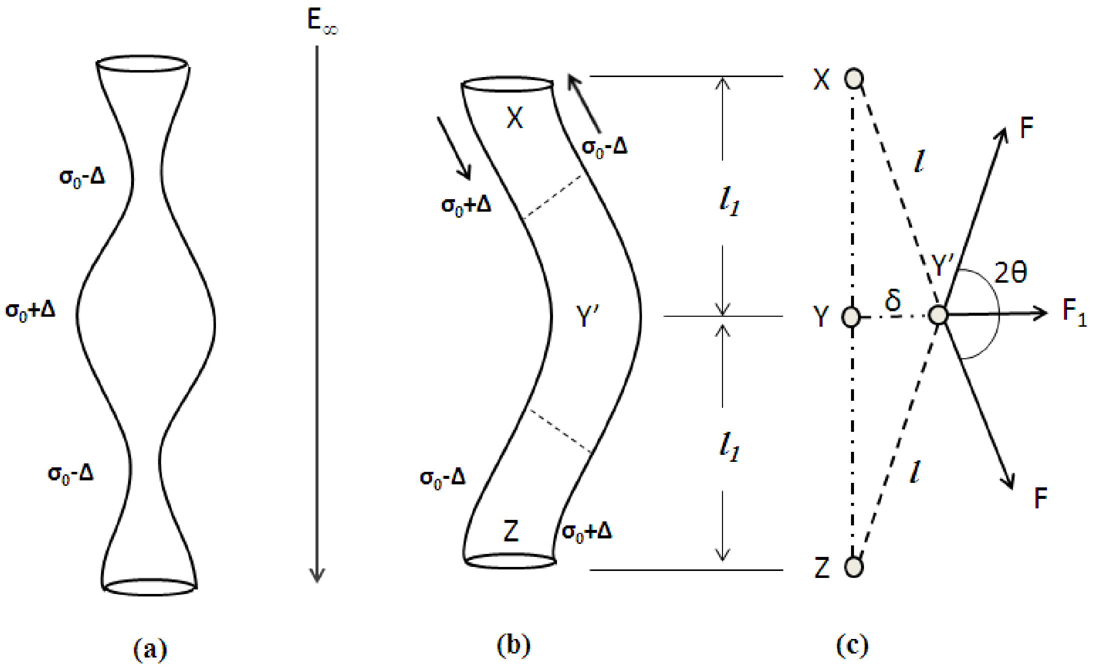

Figure 2.6: (a) Axisymmetric and (b) non-axisymmetric instabilities in a fluid jet in an external electric field (E_∞), Δ denotes the pertubations of the surface charge density (σ) [97], (c) idealised nodes; the arrows in (b) and (c) indicate the forces that bends the jet, adapted from [73, 97].

These instabilities arise as a result of coupling of the columbic forces in the jet with the electric field that cause the stretching of the jet, and are therefore primarily sensitive to fluid conductivity (or charge density) [97]. A schematic representation of the axisymmetric and non-axisymmetric instabilities is shown in Figure 2.6 (a) and (b) respectively; the local variations in the charge density ($\sigma \pm \Delta$) are shown. The straight, tapered segment of the jet which is accelerated towards the collector (parallel to the axis of the jet), experiences charge-driven axisymmetric instability as the statistical variance of the jet's radius causes a modulation of the surface charge density (Figure 2.6 (a)). This leads to a non-uniform charge distribution along the jet and gives rise to formation of dipoles oriented perpendicular to the jet. These dipoles set up a localized torque that bends the jet, which gives rise to the non-axisymmetric perturbation that couples to the radius modulation of the axisymmetric mode under the influence of the electric field, and amplifies it.

The magnitude of the coulombic force bending the jet can be estimated as follows. With reference to Figure 2.6 (c), when node Y moves to node Y' under the influence a perturbing force, the coulomb forces from X and Z pushes it further away [73, 91]. Taking the coulomb force, F= $(e/l)^2$, along the lines XY' and ZY', the horizontal force component from both coulomb forces can be resolved as

$$F_1 = 2Fcos\theta = 2\left(\frac{e^2\delta}{l^3}\right) \tag{2.5}$$

However, surface tension and viscoelastic forces counteract these deflections that cause the bending to result in an energetically unfavorable increase in surface area. The bending stops when the viscosity of the jet reaches a critical point as a result of solvent evaporation, at which point the colulombic force is no longer sufficient to overcome the viscoelastic force being exerted. While the whipping instability controls the extent of bending and stretching of the jet, the specific process and system parameters that control the whole of the electrospinning process, including these instabilities, and hence the size and morphology of the as spun fibres, are discussed in the sections to follow.

2.5 Electrospinning materials

2.5.1 Polymers and their properties

Polymers consist of long chain of molecules (or repeating units called monomers) that are typically connected via covalent bonds. An example of a polymer is polyethylene, which consists of repeating units of $[-CH_2CH_2-]_n$. The long polymer chains have the tendency to entangle in solutions, with the extent of entanglement dependant on the chain lengths. For this reason polymers and some ceramics are the only materials that enable sustained electrospinning, which is essentially the elongation of polymer chains in a fluid jet. The polymer material to be used is generally the first consideration for the choice of the solution system to be electrospun and is chosen on the basis of desired fibre properties and suitability for the specific application. The parameters taken into consideration in choice of polymer include melting and glass transition temperatures, solubility or compatibility with other polymers-solvent systems when forming blends, chemical and biological compatibility (i.e. availability of specific functional groups) and/or suitability for post processing (e.g. whether it can be carbonised to make composite fibres). There are a wide variety of polymers that can be used for electrospinning and narrowing down the options available depends very much on the specific application.

Natural polymers are generally preferred over synthetic polymers for biomedical applications, due to their better biocompatibility and immunogenicity. Most natural polymers can be degraded by enzymes and hence electrospun fibres from these polymers are commonly used for biomedical applications such as tissue engineering, biosensors, wound dressing, drug delivery and enzyme immobilization. Most polymers that have been electrospun are proteins and polysaccharides, examples include collagen (a prominent biopolymer used extensively for tissue engineering applications), chitosan, gelatine, cellulose acetate, silk protein, chitin, casein etc. [73]. Silk protein obtained from silk worms and spiders provide the best mechanical properties, besides advantages such as biocompatibility, biodegradability, good oxygen and water permeability and minimal inflammatory reaction [73, 102].

Synthetic polymers, which are generally more readily available and less costly, are used for a wider range of applications due to their versatility to be tailored to have a wider range of properties, such as high viscoelasticity, strength for improved mechanical properties, and desired degradation rates. Examples of synthetic polymers include Polystyrene, Polyacrylonitrile, Polycarbonate, Poly(benzimodozal), Pol(vinylidene chloride), Poly(vinylidene fluoride), as well as bio-degradable polymers such as poly(ε-caprolactone), poly(L-lactic acid), polygylcolide, etc. [73]. When mechanical properties and control of degradation rates is also important for biological applications, synthetic bio-degradable polymers are instead used.

In the production of carbon fibres for applications such as filters [103], supercapacitors [104], batteries [105], and bottom-up assembly in nanoelectronics [104] and photonics [106], carbonaceous polymers, such as polyacrlonitrile (PAN), rayon or petroleum pitch are typically used. A detailed description of the synthesis process of carbonised and graphitised nanofibres, from PAN precursor, is given in §6.3.6.1. Further details on the various polymers and polymer-solvent systems used in electrospinning, and their applications, can be found in references [73, 102].

For this investigation the choice of polymers were firstly determined on the basis of suitability for the application, secondly on the basis of the fibre morphology/structure envisioned and thirdly on the basis of availability of polymers that met the requirements for the former two conditions. While the polymer melting point (T_m), glass transition point (T_g) and molecular weight (M_w) were the main parameters considered, the exact reasons for the choice of polymers used in this investigation for making 1) chemical hydride encapsulated co-axial fibres, and 2) graphitic fibres, are detailed out in Chapter 5 and 6 respectively. For the former study, the permselectivity of the polymer and its compatibility with the core chemical hydride solution, and for the latter, the carbonisibility of the polymer, were the defining factors in the selection of polymers used.

2.5.1.1 Polymer molecular weight

Polymer chains are made of repeated monomer units and the molecular weight defines the sum of the weight of the individual monomer units in a polymer chain. Though this value is not exact, due to a given molecular weight distribution, it represents the average molecular weight of the polymer chains. Polymer molecular weight is important for controlling solution viscosity as determined by the extent of the polymer entanglements and hence the control of fibre diameters.

Generally molecular weight of the polymer is important for controlling physical properties such as the temperatures for transitions from liquids to waxes to rubbers to solids and the mechanical properties of the electrospun fibres such as stiffness, strength, viscoelasticity and toughness. Use of higher molecular weight polymers will generally yield fibres with higher transition temperatures and better mechanical properties. In this investigation molecular weight of the polymer was mostly used to control the viscosity of the solutions while maintaining low polymer concentrations. Minimising polymer concentration was important for lowering of electrospun fibre diameters, but a balance had to be maintained between the concentration and the solution viscosity to enable sufficient entanglement of polymer chains for electrospinning to yield polymer nanofibres.

There are various ways of calculating the average molecular weight, by either using number average (M_N) or weight average (M_W) for a given distribution of molecular weights. The choice of method used to determine the molecular weight depends on the type of property being studied. If the property, for example, is sensitive to the number of molecules present and influenced by the size of any particle in the mixture (e.g. boiling and freezing point, or osmotic pressure) then the number average molecular weight (M_N) is used. M_N is the total weight of polymer divided by the number of polymer molecules and is defined by

$$\overline{M_N} = \frac{\sum_{i=1}^{\infty} N_i M_i}{\sum_{i=1}^{\infty} N_i} \tag{2.6}$$

where N_i is the number of polymers with molecular weight M_i .

On the other hand if the polymer property of interest depends not just on the number of polymer molecules but also on the size or weight of each polymer molecule (e.g. light scattering), then the weight averaged molecular weight (M_W) is used, as given by

$$\overline{M_W} = \frac{\sum_{i=1}^{\infty} N_i M_i^2}{\sum_{i=1}^{\infty} N_i M_i} \tag{2.7}$$

In this investigation since consideration of the physical and mechanical properties of the electrospun fibres came second to the diameters of the fibres, polymer molecular weight was selected on the basis of creating sufficiently viscous solutions with minimal polymer concentration. The type of the molecular weight used was therefore not considered as an important factor, other than for maintaining consistency in viscosity studies.

2.6 Electrospinning parameters

Success of the electrospinning process and control of the resultant fibre morphology is governed by many parameters, classified broadly as polymer-solvent solution (or system) parameters, process parameters and environmental parameters. Solution parameters include, polymer viscosity as determined by polymer molecular weight and concentration, solution conductivity, surface tension, dielectric constant of solvent, process parameters include applied electric field (or voltage), feed-rate, diameter of spinneret/needle and distance between the spinneret tip and collector. The environmental parameters typically include ambient temperature and humidity of the atmosphere. The processing conditions are largely dependent on the system parameters and hence the process parameters have to be empirically determined for each solution system.

Most of these parameters have a range in which they allow for stable electrospinning of polymeric solutions. However, due to the sensitivity of the fibre morphology to small changes in these parameters, optimisation of these parameters is usually necessary for controlling the process to yield the desired fibre morphologies and diameters. However, attempts to control one parameter, especially properties of the solutions, can lead to unwanted changes in another, e.g. adding a salt to increase the conductivity can result in a change in the solution viscosity, making mutual optimisation of these parameters difficult. Understanding the effects of each parameter on the process and the resultant fibre morphologies and diameters, followed by the optimisation of each parameter for each system, formed a large part of this investigation. In this section, the key parameters of electrospinning and their effect on electrospun fibre morphologies will be discussed with reference to literature and some of our own findings.

2.6.1 Solution parameters

2.6.1.1 Viscosity

One of the conditions for electrospinning to yield fibres is that the solution used must have sufficient viscosity, such that polymer entanglement during stretching of the electrically driven jet is sufficient to prevent the jet from breaking up. Viscosity of the polymer-solvent system (solution) is mostly determined by the molecular weight and concentration of the polymer, though the interaction between the polymer and the solvent can also have an effect. Generally the solution viscosity increases with increasing polymer concentration and molecular weight, both of which control the extent of polymer entanglement.

The solution viscosity should be above a minimum for fibre formation, if the viscosity is too low the process results in electrospraying to yield vesicles under the influence of an electric field. On the other hand if the viscosity is too high it can be difficult to pump the solution through the nozzle or the droplet at the tip of the nozzle may dry up too quickly as a result of insufficient amount of solvent. Likewise the molecular weight of the polymer should be above a minimum to enable sufficient entanglement, but below a maximum to allow for uniform dissolution of the polymer (i.e. to prevent congregation or curling of the highly entangled units) [107]. The lower and upper viscosity limits that enable continuous electrospinning varies between systems and will need to be determined empirically for each system.

The effect of increasing the viscosity has a direct effect on the fibre diameters and morphology. At low viscosity, above the critical point for fibre formation, the fibres formed are beaded (e.g. beads attached to a string with gaps) and as the viscosity is increased the shape of the beads change from being spherical to more spindle-like and finally uniform fibres are formed (as shown in Figure 2.7) [108, 109]. Fibre beading is attributed to the effect of surface tension, which acts to reduce the surface area of the jet, and when the surface tension dominates over the repulsive columbic force on the jet beaded fibres are formed. With increasing viscosity, the resistance to jet breaking increases (i.e. chain entanglement increases) while the effect of surface tension exerted by the solvent molecules decreases and, thus, the effect of beading is reduced or removed.

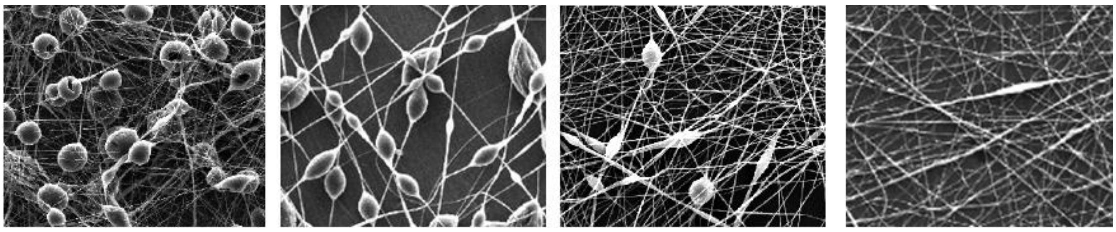

Figure 2.7: The change in the beaded structure of fibres electrospun from solutions with increasing viscosity from left to right.

Increasing viscosity also typically leads to an increase in the fibre diameters. The existence of a power law relationship between solution concentration and fibre diameters is reported [110]. Thus, to obtain non-beaded low diameter fibres, it is important to control solution viscosity by increasing molecular weight of the polymer (to increase entanglement) while decreasing its concentration.

2.6.1.1.1 Determination of solution viscosity

Viscosity is a measure of a solutions resistance to flow [73] and in the case of electrospinning where solution flow is initiated, the solution will experience a shearing stress. For Newtonian liquids the relationship between viscosity and the shearing force, in the case of straight, parallel and uniform flow, is generally explained in terms of the velocity gradient of a fluid moving between two layers spaced at a distance y, as shown in Figure 2.8.

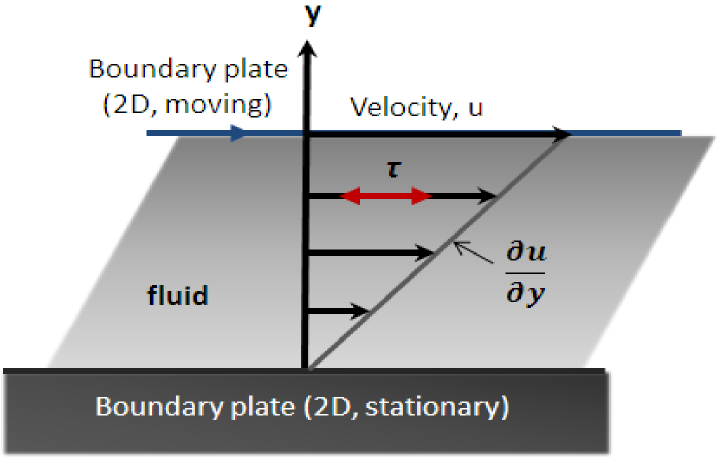

Figure 2.8: Laminar shear of fluid between two plates (with one stationary and one moving). The viscosity between the fluid and the moving boundary causes shearing of the fluid. This type of flow is known as Coutte flow.

For a given solution velocity gradient $\partial u/\partial y$, the size of the shearing force (τ) is controlled by a proportionality factor known as the viscosity (η) as defined by:

$$\tau = \eta\left(\frac{\partial u}{\partial y}\right) \tag{2.8}$$

Thus, there is a linear relationship between the applied stress and the rate of shear; the τ vs. $\partial u/\partial y$ plot passes through the origin. The viscosity can easily be determined using techniques that exhibit e.g. Coutte flow, as shown in Figure 2.8 [73]. However, the polymeric solutions used in this study are non-Newtonian fluids and exhibit a non-linear τ vs. $\partial u/\partial y$ relationship. Polymer solutions tend to exhibit shear thinning in which the apparent viscosity $\frac{\tau}{\partial u/\partial y}$ decreases with increasing shear rate, while some simultaneously experience time dependent variation in viscosity.

The viscosities of solutions in this investigation were determined using the technique of Coutte flow in a co-axial cylinder; with the fluid placed in the gap between the inner (rotating) spindle and the outer (stationary) cylinder. The viscosity of the solutions was determined by measuring viscosity as a function of spindle rotational frequency and fitting the data to obtain the high shear limit of viscosity. Further explanation of this technique can be found in ref [73].

It is also possible to get an estimate of viscosity by just using the concentration and the intrinsic properties of the polymer solution from the following equation:

$$\eta_{spec} = \exp\left([\eta]c\right) \tag{2.9}$$

where c is the polymer concentration and $[\eta]$ is the limiting (intrinsic) viscosity of the solution, which is dependent on the dimensions of the isolated polymer molecule and defined as :

$$[\eta] = KM_W^a \qquad (2.10)$$

where K and a are empirically determined constants that are characteristic of the polymer-solvent system at a given temperature, and M_w is the molecular weight of the polymer. The intrinsic viscosity of the polymer solution depends on the configuration adopted by the polymer chain in the solution; if the polymer chain is curled up the viscosity decreases but if the polymer chain is extended the intrinsic viscosity increases. This configuration is dependent on the molecular weight and the interaction of the polymer with the solvent, i.e. the extent to which the solvent molecules can break the curled chain configuration. Generally, the intrinsic viscosity is high in “good” solvents and low in “poor” solvents [73].

2.6.1.2 Surface tension

The initiation of the polymeric jet from the droplet requires the repulsive influence of the surface charges to overcome the surface tension acting in the opposite direction. Also, as described above, as the jet travels to the collector, the stretching force by the repelling charges needs to dominate over the surface tension of the jet to prevent beading of the fibres. It is therefore important to reduce the surface tension of the solutions to the minimum possible. Lower solution surface tension enables the use of lower solution conductivities or electric fields to conduce jet initiation and production of uniform fibres [109].

Surface tension is mostly determined by the solvent composition and the interaction of the solvent with the polymer and thus varies depending on the solvent used to dissolve a given polymer. Surface tension is determined by the strength of the cohesive force between the surface molecules in a liquid, which bind more closely together than they do to the molecules of the surrounding medium (e.g. air). This leads to the formation of a thin film around the fluid, making it harder to break it apart. Since surface tension has dimensions of force per unit length or energy per unit area, and a spherical configuration is favoured to keep the surface energy to minimum. Due to this tendency for solvent molecules to retain a minimum energy configuration, in the presence of a high concentration of free solvent molecules in a solution, there is a greater tendency for solvent molecules to congregate and act against the influence of the charges that push the liquid apart. Conversely, a higher concentration of polymer can reduce this effect by causing solvent molecules to be dispersed more readily over the polymer molecules and hence lowering their tendency to come together [73]. The surface tension of solutions, which is typically 30 mNm^{-1} [102], can be lowered through blending of solvents with low surface tension values or through the addition of surfactants.

2.6.1.3 Conductivity/surface charge density

For electrospinning to take place the solution needs to be sufficiently conducting to enable the surface charges to overcome the surface tension of the droplet and initiate jet flow. Thus, non-conducting solutions will not electrospin. Increasing the conductivity results in an increase in the repulsive columbic force stretching out the solution jet, and thus, enables the formation of finer fibres. In fact, increasing the solution conductivity can be the simplest root to reducing fibre diameters or fibre beading in low viscosity solutions.

The conductivity of the solution is largely determined by the type of solvent and polymer used, although addition of salts and/or surfactants may be needed to increase the charge density (i.e. the number of ions). While salts and surfactants readily dissolve in most solvents with significant polarity, dissolution of salts in non-polar solvents (such as toluene) may be difficult and hence the ionic conductivity required to initiate electrospinning may be difficult to achieve. This is a problem we have encountered in our research, as further discussed in §5.3.2. In such cases blending of solvents with higher conductivities or those that enable dissolution of salts can be used to increase the conductivity (as we have done to overcome this problem). It should be noted that the size of the ions in the solution may also have an effect on the fibre morphology. Zhong *et al.* has demonstrated the removal of fibre beading on addition of salt, with smallest fibre diameters obtained for solutions containing NaCl and largest diameters obtained for solutions containing KH_2PO_4; while solutions containing NaH_2PO_4 yielded fibres with intermediate diameters [111]. This observation is attributed to the greater elongational force, caused by the greater mobility of the smaller ions, under the influence of the external electrostatic field.

However, even with increased conductivity, there is a limit to the reduction in fibre diameter due to the increasing effect of viscoelastic forces on the stretched solution. As the solution jet is being stretched, the opposing viscoelastic force acts with an increasing magnitude against the coulombic force, halting solution stretching beyond a critical point. Also, in some cases addition of ions can increase the viscosity of the solution, and although conductivity may be increased, the increased viscosity may counteract the effect of increased charge density and hence result in an increase in the fibre diameters [112].

2.6.1.4 Dielectric constant

The dielectric constant, also known as static relative permittivity of a material, is a measure of how well the material concentrates electrostatic lines of flux under the influence of an electric field. It is essentially the ratio of amount of stored electrical energy relative to the permittivity of vacuum when a voltage is applied. With an increasing dielectric constant the ability of the material to withstand larger electric fluxes increases and hence the materials capacity to hold larger quantities of charge for longer periods of time also increases. This parameter therefore has a significant influence on electrospinning. Using a solvent with a higher dielectric constant results in enhancement of the bending instability of the electrospinning jet, which enables the reduction of the fibre diameters as facilitated by the increased jet path [113] and helps prevent or reduce bead formation in fibres [114].

Solvent mixtures containing solvents with high dielectric constants, such as DMF, water or acetonitrile, can be used to increase the dielectric constant of a solution. However, it is important to also consider other parameters of the solvents when forming mixtures, as parameters such as solvent conductivity or vapour pressure could have reverse effects on the fibre morphology or diameters. The dielectric constant of a solvent also has an effect on the solvating ability of the solvent, with higher values enabling easier dissolution of salts or ionic liquids [115]. This is an important point to consider for increasing conductivity of solutions through salt dissolution.

2.6.1.5 Vapour Pressure

Solvent vapour pressure (P_0) is another important parameter for success of co-electrospinning and morphology of the as spun fibres; a too high P_0 will cause the droplet at the tip of the nozzle to dry, preventing electrospinning, and a P_0 too low will cause the fibres to go down wet to form a film. Lower vapour pressure solvents can enable the electrospinning jet to remain fluid for longer and hence delay the solidification of the jet into fibres. A longer flight time will enable the jet path to increase with further stretching to yield fibres with lower diameters. A too high vapour pressure solvent may also result in the formation of collapsed or elongated fibre cross-sections, as shown in Figure 2.9. This happens as fast evaporation of the solvent from the surface layer of the solution jet leads to formation of a skin layer that buckles under the pressure difference created [116]. It is therefore important to use a sufficiently low vapour pressure solvent to retain a sufficiently liquid droplet at the nozzle tip to enable jet initiation, and for control of the fibre morphologies and diameters. Once again, solvent mixtures can be used to control the vapour pressure.

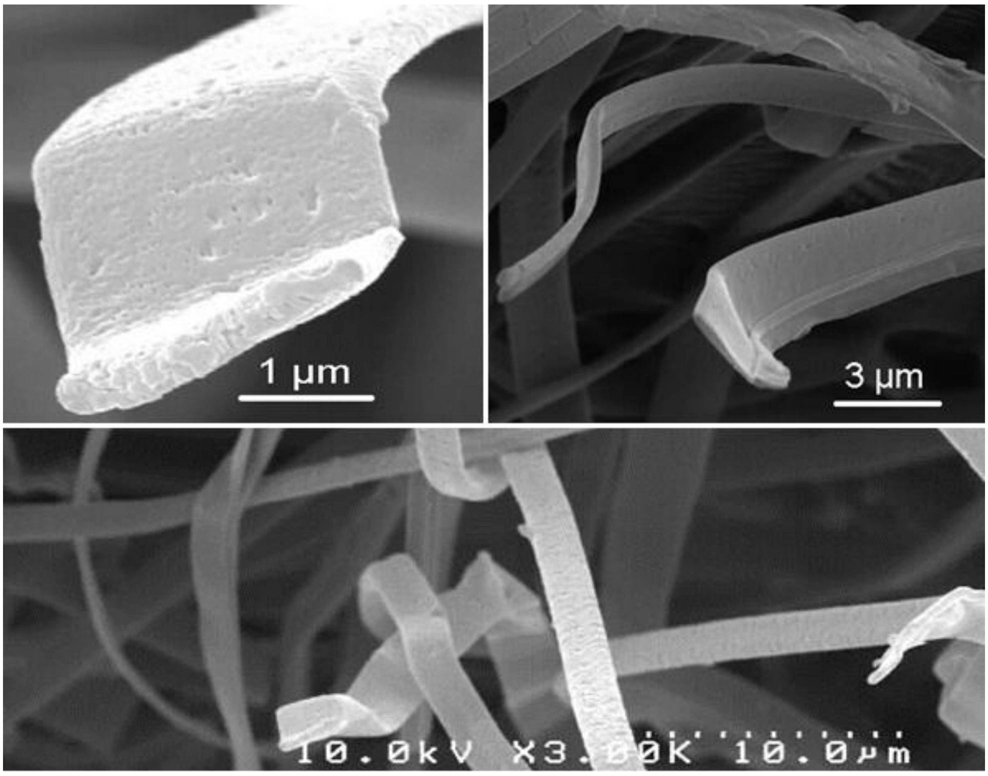

Figure 2.9: Collapsed (buckled) electrospun fibres; an effect attributed to high vapour pressure of the solvent used.

The vapour pressure, P_0, of a solvent can be calculated from its boiling point T_B and heat of vaporisation ΔH_{vap} using the Clausius-Clayperon equation [117]:

$$P_0 = exp\left[-\frac{\Delta H_{vap}}{R}\left(\frac{1}{T_B}-\frac{1}{T_0}\right)\right]P_{atm} \tag{2.11}$$

where R is the ideal gas constant (8.314 J $mol^{-1}K^{-1}$), T_0 is the temperature of measurement (in Kelvin or other absolute temperature units) and P_{atm} is the atmospheric pressure (in units of *atm*).

2.6.2 Process parameters

2.6.2.1 Voltage

Electrospinning only takes place when a minimum threshold voltage is applied to a charged solution and this threshold varies depending on the solution system used, though typically a positive voltage of more than 6 kV is needed [73]. The applied voltage will cause charges to collect on the surface of a droplet and together with the applied electric field it induces the formation of a Taylor cone, with an electrospinning solution jet emanating from the tip of the cone. Generally, the greater the voltage is the greater the stretching of the electrospinning jet due to the increase in columbic force exerted by the charges [73]. Increasing the voltage also has the effect of increasing the jet acceleration and hence decreasing the flight time of the electrospinning jet. Both these effects greatly influence the fibre morphology and diameters. It is suggested that while increasing the voltage can reduce fibre diameters, due to increased stretching, going beyond a critical voltage can cause more solution being ejected from the nozzle, which leads to formation of fibres with greater diameters [118]. This is illustrated by the results of a voltage vs. fibre diameter experiment conducted using different concentrations of poly(methyl methacrylate) (PMMA) in dimethylacetamide (DMA) solutions in this study. Figure 2.10 shows the different regimes that exist as voltage is increased; a saddle point exists in the data. The region before the saddle point (marked as 1) corresponds to the dripping region when the voltage is too low for the set flow rate (500 µl/hr in this case); in this region the fibre diameters increase gradually as voltage increases up to the saddle point. At the top of the saddle point a stable Taylor cone is obtained at the tip of the nozzle (i.e. the rate of draw of the voltage matches the flow rate). With the voltage further increased (point 2) the fibre diameters once again decrease in diameter as the Taylor cone recedes into the nozzle up to the point of the saddle minima. Beyond this point the fibre diameters start increasing again (region 3) as a result of the increased voltage causing more solution to be drawn out of the nozzle than that is available with the set flow rate. In this scenario the electrospinning process is intermittent as the jet breaks with the solution depleting in the nozzle and re-issues as more solution flows through after a short interval. Figure 2.10 also shows how these effects are much more pronounced for more viscous (i.e. higher PMMA concentration) solutions.

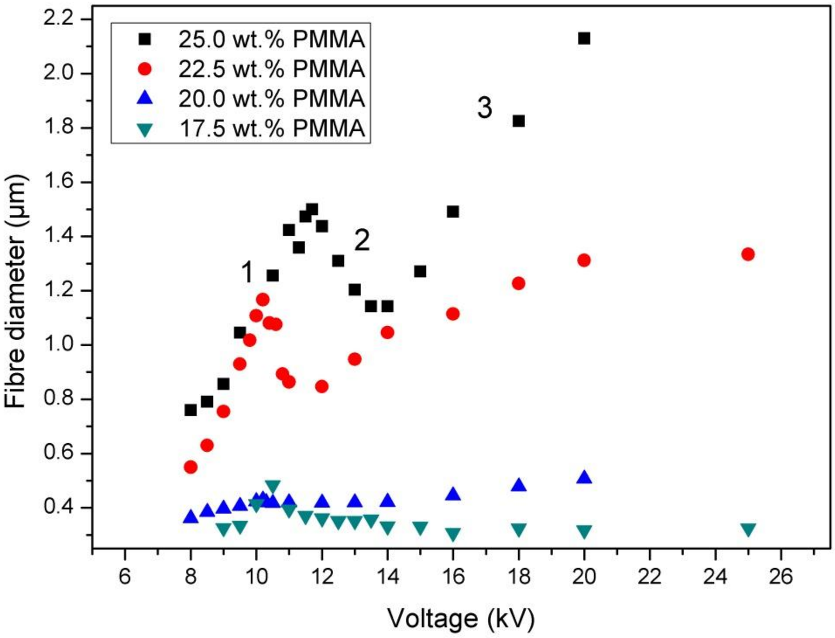

Figure 2.10: Fibre diameter vs. voltage plot of PMMA fibres electrospun at different concentrations of PMMA.

When a solution of low viscosity is used a high voltage may lead to the formation of multiple jets from the droplet, leading to fibres with lower diameters to be formed, but with a greater fibre diameter distribution. The voltage can also affect the crystallinity of the polymer fibres as the electrostatic field causes stretching of the entangled polymer chains (molecules) [73]. However, this effect is said to be true up to a given voltage, beyond which the jet acceleration is too high (i.e. flight-time too low) for polymer molecules to be aligned before they are deposited on the collection plate. Therefore, in order to investigate the effect of voltage on fibre morphology and diameters for a given system, it is important to test a range of voltages within the range that enables stable electrospinning. This range is heavily dependent on the solution properties and the feed rate, as well as the collector distance from the tip of the nozzle, which are discussed next.

2.6.2.2 Tip to collector distance

Varying the tip to collector distance will change the flight distance as well as the electric field strength for a given voltage (Figure 2.11). When this distance is reduced the flight path will be reduced and the field strength that accelerates the jet downward will be increased. As a result there may not be sufficient time for the solvent to evaporate and the fibres will go down wet, forming either an interconnected fibre mesh or a polymer film, depending on the wetness of fibres.

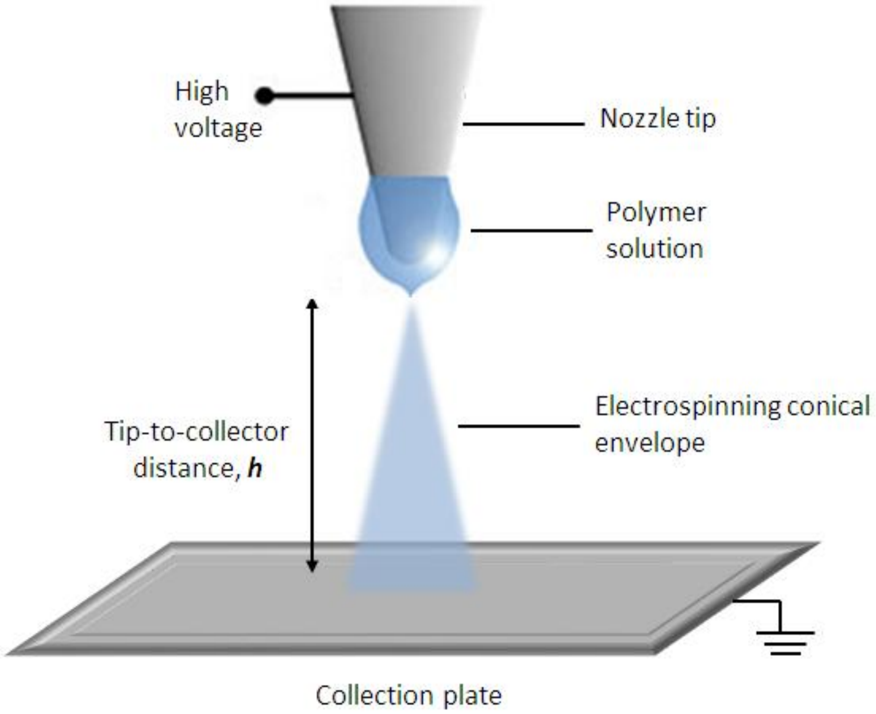

Figure 2.11: Schematic electrospinning set up showing tip-to-collector (flight) distance of electrospinning jet.

The effect of varying tip-to-collector distance depends on the solution system. In some cases increasing the distance has the effect of reducing fibre diameter, as facilitated by the increase in the flight path enabling greater stretching of the electrospinning jet [73]. But in other cases increasing the distance too far can also lead to increase in fibre diameters, due to reduced stretching of fibres under the lowered electric field strength [73].

Reducing the distance can also lead to beading of fibres, this is associated with the increased field strength, which, when it is too high, can cause instability in the jet and lead to the formation of beads, in the same way described above. It is therefore important, for a given system, to find the optimum tip-to-collector distance that is sufficiently high to enable evaporation of the solvent from the fibres, while enabling formation of a stable jet that stretches out the fibres as much as possible.

2.6.2.3 Feed-rate

The solution feed-rate (or flow-rate) determines the amount of solution that is available for electrospinning over a given time. The voltage needs to be varied for a given feed-rate to sustain a stable Taylor cone. If the solution extraction rate (as determined by the magnitude of the voltage) is not balanced by the feed rate, the solution at the tip of the nozzle will continuously drip during electrospinning. We have found that increasing the feed rate results in increased fibre diameters and bead sizes. This is not surprising since increasing the feed rate results in a greater volume of solution to be drawn away from the nozzle tip. However, it is reported that there is a limit to the increase in the fibre diameters due to feed-rate [73]. For a given voltage that balances the feed-rate, increasing the feed rate (or the volume of solution) further results in more charges in the droplet at the apex of the nozzle, which means a corresponding increase in the stretching of the solution [73]. Thus, once again the fibre diameter is controlled by balancing the effect of separate parameters.

2.6.3 Environmental (ambient) parameters

The effect of ambient conditions on the polymer solution and hence electrospinning process and/or the fibre morphologies is not as thoroughly investigated as the process and system parameters, but increasing amount of research is pointing to the importance of the environmental conditions for controlling fibre morphology and diameters. These parameters include temperature, humidity, atmospheric pressure etc. The first two are discussed below.

2.6.3.1 Temperature

The ambient temperature, which determines the solution temperature, influences the solvent evaporation rate and solution viscosity, with the former increasing and the latter decreasing with temperature. As a result higher temperatures are shown to yield finer fibres [73]. This is because with a lower viscosity the columbic forces have a greater fibre stretching potential, while the lower evaporation rate of the solvent enables the jet to be stretched over a longer time period.

2.6.3.2 Humidity (water content of atmosphere)

Humidity (atmospheric water concentration), above a certain level, is found to cause pores on the surface or interior of the fibres. The size of the pores are found to increase with increasing humidity, eventually coalescing to form large, non-uniform structures [119]. The formation of pores at high humidity is attributed to water condensation on the surface of the fibres or formation of water islands within the fibres. As in the case of most parameters discussed above, the effect of humidity on the fibre morphology changes depending on the solvent-polymer system. For example, pores caused by humidity may be more prevalent in some polymer fibres than others. Casper *et al.* [119] report the presence of pores in Polystyrene (PS) fibres when electrospun in an atmosphere with more than 30% relative humidity. In the case of Polysulphone (PSU) dissolved in Tetrahydrofuran (THF), the maximum humidity for smooth fibre formation is 50%. On the other hand, a very low humidity may aid rapid evaporation of a highly volatile solvent, as the partial pressure is decreased, causing the polymer jet to dry out too quickly, without sufficient stretching to form fine fibres. In this case the nozzle tip may also become clogged. Therefore, the humidity of the surrounding atmosphere has to be adjusted according to the chosen solvent-solution system to attain smooth (non-porous) fibres.

Chapter 3

Co-electrospinning: Technology and Control

3.1 Introduction

As discussed in Chapter 2, electrospinning has been widely recognised, both at the research and industrial level, as a cost effective and versatile way of producing nanofibres. More recently, as a result of increasing demand for specialised nanostructured composite materials, a more complex variant of this process, called co-electrospinning (or co-axial electrospinning) [71, 72, 120-126] has been developed. Co-electrospinning involves the use of two concentric nozzles to deliver two separate solutions to make functionalised bicomponent nanofibres with a core-shell configuration. This process works in a similar way to its single phase variant, such that an electric field is applied to a suspended droplet at the tip of the nozzle to yield co-axial fibres with diameters typically in the sub-micron range. The main difference is that two solutions, instead of one, are delivered independently through the concentric nozzles, with one solution being the precursor for the core and the other for the shell of the fibres. The core material is not required to be polymeric, which enables a wide variety of materials either in melt or solution form to be encapsulated and structured, with properties of the polymeric shell chosen to enhance fibre functionality. This technique is therefore highly useful for encapsulating and nanostructuring non-polymeric materials for a wide range of uses with the possible benefits of:

- enabling improved material properties as a result of nanostructuring,
- isolating the core material that may be unstable in air to minimise its chance of decomposition,
- enabling controlled release of the core component over time through the use of a shell material that decomposes in a given environment, e.g. controlled release of a substance/drug contained in a biodegradable polymer,
- enabling one material, usually the shell, to act as a scaffold for the other, such that fibres can be functionalised for a specific use, e.g. doping with metals for *optoelectronics* applications,
- reinforcing a material to improve its mechanical properties [72].

Co-electrospinning has already gained attention for a variety of applications including biomedical (tissue engineering, controlled drug release systems) [69-71], filter systems, catalysis, optical applications (waveguides) or as nanocables for microelectronics [72]. Its use for generating nanostructured materials for hydrogen storage applications has not been reported previously, yet the benefits described above and its potential as a cheap commercial process makes it a powerful tool for hydrogen storage research. With this idea in mind we have endeavoured to investigate co-electrospinning as a means to encapsulate metal or complex hydrides inside a sheathing nanofilament of hydrogen-permeable polymer for hydrogen storage applications.

Since this is the first investigation looking at encapsulating hydrides in nanofibres through co-electrospinning, a large part of this study was composed of understanding the parameters that will be important for successfully controlling the process. Though, co-electrospinning works in a similar way to its single phase variant, such that it involves the control of the same process and system parameters (e.g. viscosity, electrical conducivity, voltage, etc) as described in Chapter 2, the use of two solutions instead of one, introduces additional complexity to the process. Also, due to the limited amount of work published on co-electrospinning, there is not yet a concrete understanding of the exact mechanisms that enable confinement of the core in the shell solution and hence how the core and the shell parameters have to be balanced to ensure the success of the process. The use of a highly reactive (i.e. polar) non-polymeric core material, such as AB, enabled us to see some of the issues that may arise and the factors that may require specific attention when using co-axial spinning to encapsulate complex materials, such as chemical hydrides. Thus, through this study we have attempted to bring clarity to some of the inconsistencies reported in experimental studies. We have also looked at some of the theoretical work published on the instability mechanism of compound jets to explain some of the fibre morphologies we have obtained.

In the first part of this chapter I will discuss the co-electrospinning process in terms of the instability theory of the compound jet and in turn discuss conditions (i.e. balance between parameters) required for successful co-electrospinning of co-axial fibres, mostly based on what is outlined in literature (and verified in this study) and some of our supplementary findings based on the results of this study. In the second part I will describe a solution selection model I have developed as a way of efficiently selecting compatible solution combinations and as a way of effectively optimising the solution parameters described in the first part of the chapter.

3.2 Co-electrospinning Process and Control

3.2.1 General set up and the process

The general set up is similar to that used for electrospinning described in §2.1, the only modification made is through the use a co-axial spinneret system where a smaller (inner) capillary is inserted into a bigger (outer) capillary. The core capillary is connected to a reservoir (syringe) containing the core solution while the outer capillary is connected to a reservoir containing the shell solution and the feed rates of each solution is controlled separately using metering pumps or air pressure. It is important to have the co-axial nozzle system fully concentric, with the axis of both capillaries maintained parallel at all times; this requires careful designing and manufacture of the co-axial spinneret. The nozzle set up used in this investigation is shown in Figure 3.1; it has a vertical arrangement, but as in the case of single phase electrospinning a horizontal set up can also be used.

The process of co-axial electrospinning is conceptually similar to single phase electrospinning, such that when a sufficiently large potential difference is applied between the nozzle tip and collector, charge accumulation predominantly on the surface of the sheath liquid causes a co-axial jet to emanate from the compound Taylor cone formed. The jet goes through the bending instability regime (as described in the next section) and forms fibres with the core-shell configuration once most of the solvent has evaporated. The entrainment of the core solution by the shell solution is enabled by the shearing forces such as “viscous dragging” and “contact friction” exerted by the shell onto the core solution when the shell solution is rapidly stretched under the influence of the columbic forces (Maxwell stresses) [72, 127, 128].

The challenge is in ensuring that the core solution is uniformly confined in the shell solution through the creation of a co-axial jet that forms fibres with a core-shell configuration. While stability of the Taylor cone is a primary requisite [72], the compatibility of the core and shell solutions, as well as the balance between the solution and process parameters are highly important factors for ensuring success of the process.

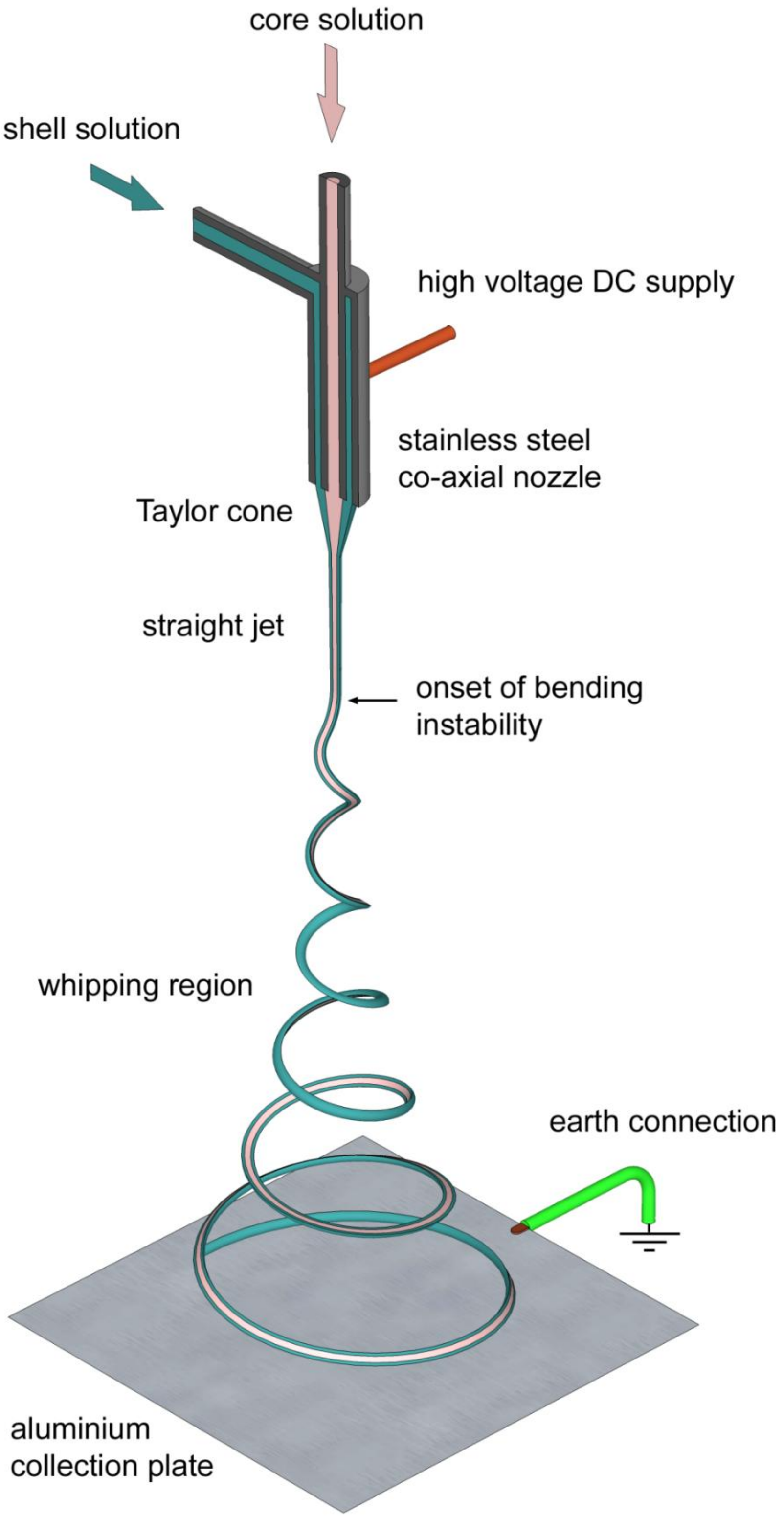

Figure 3.1: Co-axial nozzle set up used in co-electrospinning.

3.2.2 Instability theory of a co-axial jet

The behaviors of electrified co-axial jets are closely connected with the propagation and growth of disturbance waves on them. Amplified disturbance waves propagate downstream under the influence of surface tension and electrostatic force, making the jet break up ultimately [129]. Instability analysis of the co-flowing jets is therefore highly important for understanding the mechanisms that enable the compound bending jet to be sustained and formed. We were specifically interested in understanding how the instability modes in a compound jet can influence fibre morphology, especially in the case of unconventional core-shell solution combinations, such as the solution sets used in the production of ammonia borane-polystyrene fibres (i.e. a highly conducting non-viscous core solution surrounded by a low conductivity viscous shell). After an analysis of the theoretical work in literature on co-axial instabilities, I deduced the main instability mechanisms controlling the behavior of the co-electrospinning jet (as described in these studies) [96, 102, 129-131]. In this section I present a summary, from literature, on the theory of the instabilities in a co-axial jet and the way in which some of the solution and process parameters control these instabilities. This literature study was specifically important for providing an explanation for the atypical porosity of our fibres and for investigating the possibility of gaining control of fibre porosity through the control of these instability modes. This will be discussed further in §5.4.4, here I will just focus on the theory.

As in the case of single phase electrospinning the compound jet flowing under an electric field is subject to both axisymmetric and non-axisymmetric forces i.e. the Rayleigh, axisymmetric conducting and whipping conducting modes, which control the flow of the jet and whether it results in the production of hollow or compound micro/nanoparticles (co-axial electrospraying) or micro/nanofibres (co-axial electrospinning). There have been a substantial number of theoretical studies [102, 129-132] aimed at understanding the mechanisms responsible for the instability behaviour of co-axial jets under the influence of an electric field. In §2.4, the instability in the electrospinning process was identified as being controlled by three different instability modes; the Rayleigh, the axisymmetric and the non-axisymmetric (whipping or bending) modes. As in the case of single phase electrospinning, these modes control the continuity and the final morphology of the electrospun fibres. However compared with single liquid jets the behaviours of coflowing jets are much more complicated because of the existence of two liquids with two interfaces (the inner liquid-liquid interface and the outer gas-liquid interface) [129].

Theoretically, the behaviour of a coaxial jet is determined by the type of instability in the jet, such that when it is perturbed by an arbitrary infinitesimal disturbance, its inner and outer interfaces will be modulated accordingly, depending on the type of disturbance waves propagating downwards under the influence of the surface tension and electrostatic force (electric field) [129, 131]. The theoretical models generally attempt to solve for the electrohydrodynamics of the compound jet flowing from a capillary tube, as schematically illustrated in Figure 3.2.

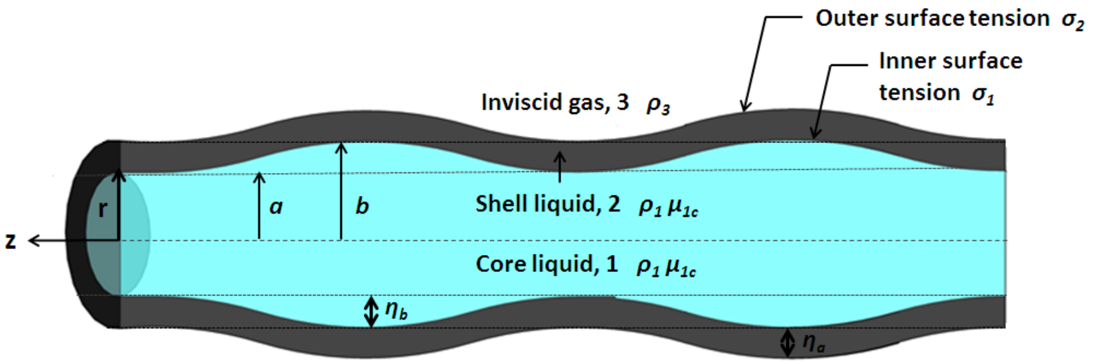

Figure 3.2: A schematic illustration of the deformed compound jet, ρ_1, ρ_2 and ρ_3 are mass densities of the core, shell and outer fluids respectively, η_1 and η_2 are the core and shell viscosities respectively, figure adapted from [133].

In general, the behaviour of capillary waves under the influence of gravity can be described by the dispersion relation:

$$\omega^2 = |k|\left(\frac{\rho - \rho'}{\rho + \rho'}g + \frac{\sigma}{\rho + \rho'}k^2\right) \tag{3.1}$$

where ω is the angular frequency (with units of radians per second), ρ and ρ‘ are the mass density of the two fluids (with units of kg m^{-3}, $\rho > \rho$‘) , σ is the surface tension (with units of N m^{-1} or J m^{-2}), g is the acceleration due to gravity (with units of ms^{-2}) and k = 2π/λ is the wavenumber (λ has units of metres). The first term in Eq. (3.1) is for the gravity wave and the second term is for the capillary wave. At short wavelengths (i.e. large k), the capillary term dominates:

$$\omega^2 = \frac{\sigma}{\rho_1 + \rho_2}|k^3| \tag{3.2}$$

The amplitude a of these waves depend on the total energy E_t

$$a = \sqrt{\frac{E_t}{k\sigma}} \approx \sqrt{\frac{k_B T}{k\sigma}} \tag{3.3}$$

where T is the temperature of the liquid. Thus, the surface tension controls both the frequency and the amplitude of the capillary waves between the two fluids. If the fluids are viscous then the waves will be damped with a time constant approximately given by:

$$\tau \approx 2k^2\frac{\rho_1+\rho_2}{\eta_1+\eta_2} \tag{3.4}$$

i.e. the viscosity of the fluid can have a stabilising effect on the capillary waves.

Applying an external electric field causes the surfaces of these fluids to become unstable as the curvature of the surface creates a destabilising force that acts against the dampening effects of viscosity or the restoring force of the surface tension. The instability characteristics of co-axial jets have been studied under axial or radial fields by many authors, who have predominantly looked at the axisymmetric instability modes due to the complexity of modelling the non-axisymmetric modes [102, 129, 130]. More recently Li *et al.* [131] have carried out a linear study on both the axisymmetric and non-axisymmetric instability modes of a viscous co-axial jet in a radial electric field, where the outer liquid is considered to be a leaky dielectric and the inner a perfect dielectric. Based on the findings of this study, I will discuss how the solution and process parameters affect these instability modes and hence the way in which the compound jet is formed.

3.2.2.1 Axisymmetric and non-axisymmetric instability modes

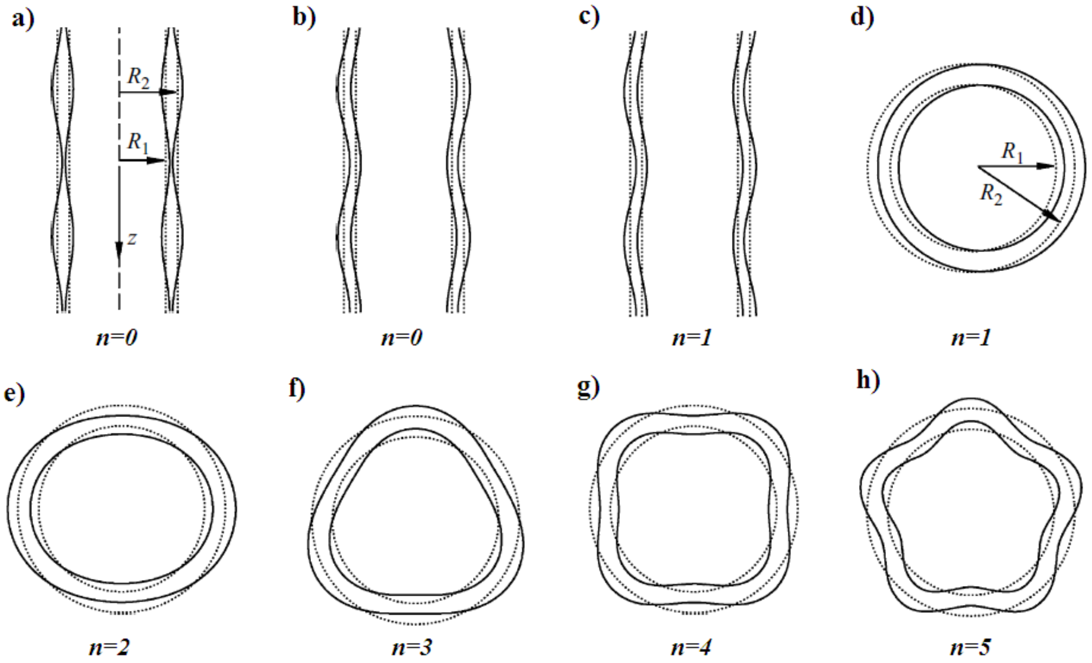

Figure 3.3: Sketch of the unstable modes. (a) The para-varicose mode, (b) the para-sinuous mode, (c) and (d) the helical mode (e) the non-axisymmetric mode n=2, (f) the nonaxisymmetric mode n=3, (g) the non-axisymmetric mode n=4 and (h) the non-axisymmetric mode n=5. Solid curves: the interfaces after perturbation; dotted curves: the interfaces before perturbation [131].

Using a normal mode it is possible to decompose the capillary waves on a cylindrical surface into modes characterised by an azimuthal wavenumber *n* and the axial wavenumber *k*:

$$f(r,\theta,z,t) = \hat{f}(r)e^{\omega t+i(kz+n\theta)} \tag{3.5}$$

where r, θ, z are the radial, azimuthal and axial coordinates respectively and $i=(-1)^{1/2}$

The axisymmetric instability (*n*=0) is described by the existence of two unstable modes; para-varicose and para-sinuous modes, as determined by the phase difference of the flowing core and the shell solutions along the r-z plane. In the case of the para-varicose mode the core-shell interfaces are perturbed out of phase, whereas for the para-sinuous mode the interfaces are deformed in phase, as shown in Figure 3.3 (a) and (b) respectively [102, 129-132].

For the non-axisymmetric instability (*n*>0) modes there is a single unstable mode for any given azimuthal wavenumber. The interface configurations of the first few non-axisymmetric instability modes with small azimuthal wavenumbers (*n* = 1, 2, 3, 4, 5) are shown in Figure 3.3 (c)-(h), respectively [131]. In the first non-axisymmetric mode (*n*=1), also called the helical mode, the interfaces and the central line of the jet are displaced in phase with the area of cross-section unchanged, as shown in Figure 3.3 (c) and (d). On the other hand for the larger non-axisymmetric modes (*n* = 2, 3, 4, 5 etc.) the central line of the jet is unperturbed, but the core-shell interfaces experience periodic variation in the r–θ plane, the period of which is determined by the value of *n*.

The solution viscosity, as characterised by the Reynolds number, is found to control the growth of these instability modes; especially the para-sinuous and non-axisymmetric *n*>1 modes. Thus, with increased solution viscosity the helical instability predominates over axisymmetric instability, such that the Rayleigh instability is suppressed, leading to bending of the jet in space without breakup, i.e. (co-axial) electrospinning. Increasing the electric field has the effect of increasing the instability of all the modes, especially the helical mode, as well as increasing the number of possible wavenumbers of all modes [131]. Thus, the destabilising effect of the field on the flowing jet can be controlled by varying the electric field accordingly.

The interfacial tension between the core-shell interfaces is reported to have a particularly important effect on the jet instability growth. This is intuitively obvious since the cohesion energy between the two liquids will increase as they become more miscible, such that the interfacial surface tension will tend to zero as their mutual interaction becomes as strong as their self-cohesion. Fang Li *et al.* [131], report that the influence of the para-sinous mode is destabilized by interface tension in long wavelength region, whereas the helical mode and the non-axisymmetric modes $n>1$ are stabilized by interface tension.

Most of the theoretical studies are carried out with some form of variation between the conditions set for each study (e.g. direction of the electric field, relative electrical properties of the solutions, viscosity etc.), such that it is difficult to make generalisations to describe the exact instability mechanisms in the jets and the factors influencing it. However, it is easier to generalise the mechanism that enable the switch from electrospraying to electrospinning. In general, it is found that a relatively small radial electric field, low liquid viscosity and high interface tension favour the predominance of the para-sinuous mode and hence electrospraying of the jet. Conversely, a relatively large radial electric field, high liquid viscosity and low interface tension enables the helical mode to dominate and cause electrospinning of the jet. The effects of these and other electrospinning parameters in co-electrospinning are discussed in more detail in the next section.

3.2.3 Solution and process parameters

3.2.3.1 Core-shell solution miscibility & compatibility

Depending on the likeness between the molecular forces in the solutions (as determined by the strength and type of bonds in each component) the solutions will have varying degree of miscibility. Also, if the solutions interact in such a way that the solvent in one causes precipitation of the solute (e.g. polymer) in the other, then the solutions are considered incompatible. The interaction between the core and the sheath solutions, as determined by their solubility parameters and as manifested in the miscibility and compatibility behaviour of the solution when they come in contact at the tip of the capillary, is one of the first factors to consider when selecting the solution combinations. It was mentioned in the previous sections that the primary requisite for successful co-electrospinning is the formation of a stable Taylor cone at the tip of the co-axial capillary system. If the polymer in either of the solutions is precipitated out of its solution then the droplet will not be sufficiently liquid to enable the formation of a Taylor cone and/or ejection of the co-axial jet. Also in order to obtained fibres with uniform core shell structures it is important that the core and shell solutions remain phase-separated throughout the spinning process. However if the two solutions mix before the bending instability sets in then a core-shell configuration will not be obtained.

There is not yet a consensus in literature on the importance of the miscibility of the core and shell solutions. Some authors demonstrate the feasibility of obtaining fibres with a core-shell configuration when using miscible solutions [121, 134]. It is postulated that the characteristic time of the bending instability is significantly smaller than the characteristic time of “diffusion spreading of a sharp boundary” between two miscible solutions and thus the solutions remain phase separated [121]. On the other hand others report that the immiscibility of the core and shell solvents was critical to the production of well-defined core-sheath nanofibres [127, 135]. In these studies it is reported that porous fibres are obtained when miscible solution combinations are used. However the extent of miscibility as defined by the solution solubility parameters, the inter-boundary diffusion of the solutions and the residence time of the core solution in the shell droplet is not discussed in any of these studies. In order to determine the importance of the degree of core and shell solution miscibility and to clarify some of the discrepancies in literature, the effect of solution miscibility on the success of the co-axial electrospinning process and the core-shell morphology of the fibres was investigated. This was done by the use of solutions with varying degrees of miscibility (i.e. miscible, semi-miscible and immiscible solutions), as discussed further in §5.3.2.

3.2.3.2 Solution viscosities

In co-electrospinning controlling the solution viscosities is highly important for ensuring that the core is uniformly entrained by the sheath material. The viscosity of the sheath solution should be high enough to ensure the viscous stress imparted by it on the core is sufficient to overcome the interfacial surface tension between the two solutions in the droplet and enable the formation of a compound Taylor cone, with a co-axial jet emanating from it [72, 136]. Since the sheath solution guides the core solution during the stretching of the jet, it is essential for sheath solution to be electrospinnable on its own, even though the core solution does not have to be. Nevertheless, the viscosity of the core solution should be neither too high or too low to ensure continuous entrainment of the core in the shell; if it’s too low then the core jet will break up [78, 136], if it’s too high (i.e. higher than the that of the shell) then the shearing force exerted by the shell will not be enough to stretch the core. Therefore it is important to use a sufficiently viscous core solution, but with a viscosity lower than that of the shell.

As in the case of single phase electrospinning the inner and outer fibre diameters can be controlled by respectively varying the core and shell solution viscosities; with the diameter of each component increasing with their respective viscosities [137, 138]. Likewise, low viscosity solutions results in beaded fibres, as we found for PAN-PMMA (shell-core) solutions, shown in

Figure 3.4 (a) and (b), which can be removed by increasing the viscosity of the solutions (Figure 3.4 (c) and (d)).

.

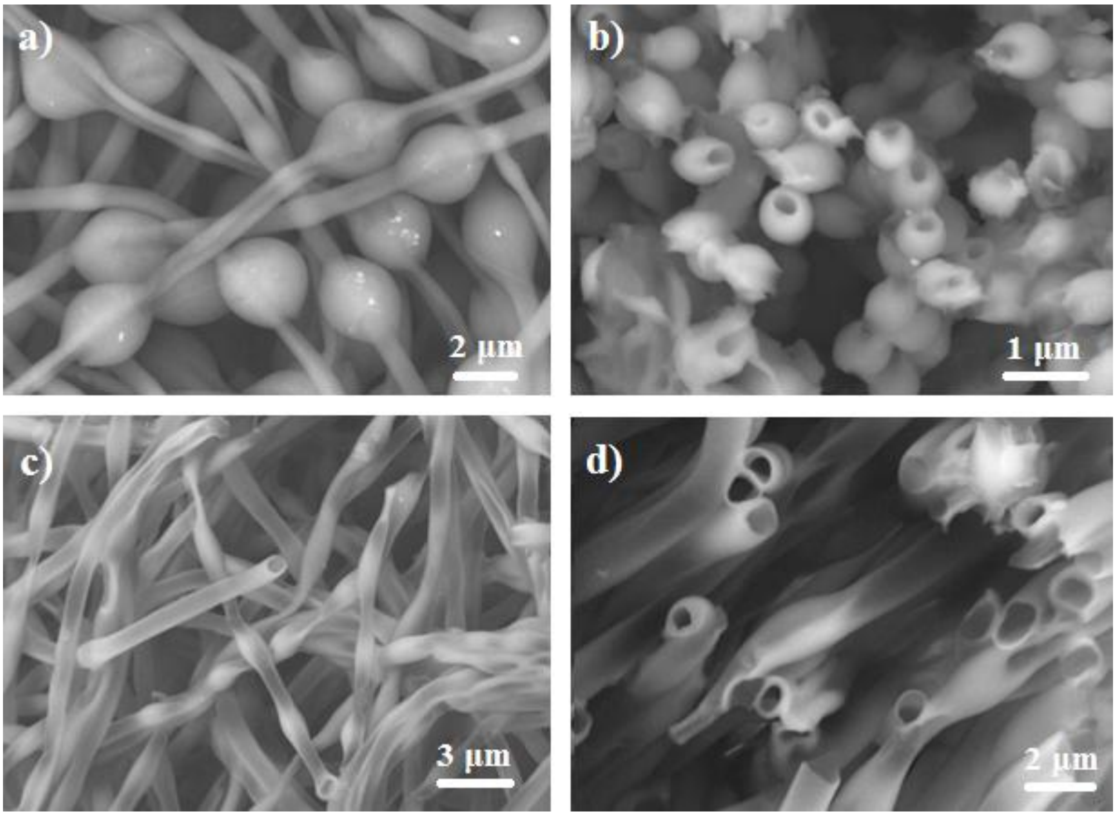

Figure 3.4: Co-electrospun PAN (shell): PMMA (core) fibres at core-shell flow rates of 500-500 µl/hr from solution of (a) 10 wt.% PAN in DMF and 12.5 wt.% PMMA in DMF, (b) fibres in (a) heated at 500 °C to remove PMMA core, (c) 10 wt.% PAN and 15 wt.% PMMA, (d) fibres in (c) heated at 500 °C to remove PMMA core.

3.2.3.3 Solution conductivities

The electrical conductivity of the solutions is another variable that is highly important for controlling the co-electrospinning process and the quality of the co-axial fibres obtained. As described in §2.6.1.3 for the single-phase electrospinning, an increase in solution conductivity means an increase in charge density and hence an increase in the columbic force (Maxwell stress) causing elongation of the whipping jet, which results in the reduction of fibre diameters.

There appears to be discrepancies in literature on the way the conductivity must be controlled in co-electrospinning. While some experimental studies report on the necessity of having higher shell solution conductivity for continuous entrainment of the core by the shell [72, 127] since the shell needs to act as the driver of the compound jet, theoretical studies on the electrodynamics of the process suggest that this is not necessary. Reznick *et al.* [139] show that when a sufficiently large electric field is applied to the compound Taylor cone "the free charges migrate very rapidly from both fluids and their interface to the free surface of the shell", suggesting that the electric field is acting only on the free surface (as shown in Figure 3.5). Thus the entrainment of the core would be controlled only by the viscous forces generated in the shell. This is found to be true even when the droplet is modelled as a leaky dielectric with very low conductivities used. It is reported that the behaviour of the liquid droplet rapidly approaches that of a perfect conductor under the applied electric field even when inner and outer solution conductivities are as low as $\sigma_{in}=\sigma_{out}=3.75 \times 10^{-9}$ S/m in their model, which is said to be in good agreement with their experimental observations [139].

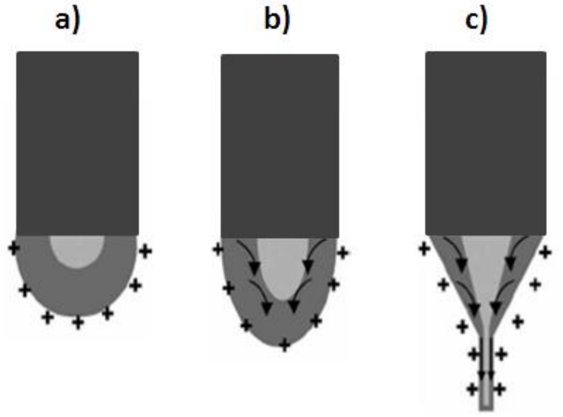

Figure 3.5 Schematic diagram of compound Taylor cone formation under the influence of an electric field: (a) charges migrate to surface of shell, (b) viscous drag exerted on the core by the deformed sheath droplet, (c) compound Taylor cone formed due to continuous viscous drag [139].

Carol *et al.* [102] report the same findings as above for when outer liquid is a conductor and the inner is a dielectric. They point out that the electrical relaxation time of the charges in a conducting medium is much smaller than that in a dielectric. Thus, if the outer liquid is a conductor and the inner is a dielectric, the charges will collect on the outer liquid-gas interface, and the outer liquid will be driver for the compound jet. However, if the inner liquid is a conductor and the outer a dielectric then the electrical relaxation time of the inner liquid (as compared to the time taken for the bending instability to set in) is significantly smaller than that of the outer one and the charges are concentrated on the inner liquid-liquid interface; the inner liquid is then the driving component of the jet [102].

Further support for the varying effect of having different core and shell conductivities on the co-electrospinning jet comes from Li *et al.* [129], who have, through a linear instability analysis of the co-axial jet under an axial field, analysed four different cases of core-shell solution conductivity; IDOC (inner: dielectric; outer: conductor), ICOD (inner: conductor; outer: dielectric), ICOC (inner and outer: conductor), and IDOD (inner and outer: dielectric). For each case the authors report finding a separate dispersion relation. This result is particularly important for gaining control of electrospinning bi-component liquids, especially in the case of complex materials where it may be difficult to control the relative conductivities in a way that enables the production of uniform, non-porous core-shell fibres. This will be discussed further in §5.4.4, where the porosity of the ammonia borane encapsulated polystyrene (AB-PS) fibres is attributed to the higher core solution conductivity of the co-axial jet.

3.2.3.4 Solvent vapour pressure

The vapour pressure of the core and shell solvents used is highly influential in controlling the core-shell morphology of the co-electrospun fibres. It is important to use solvents with sufficiently low and similar vapour pressures in the core and the shell solutions for two reasons. Firstly, because if the shell solvent evaporates too quickly at the droplet before a stable Taylor cone is formed then either a jet will not emanate from it or multiple jets may be formed, halting the formation of uniform co-axial fibres [140]. Secondly, if there is a difference in the evaporation rates of the core and shell solvents such that either one of the core or shell solvents evaporates too quickly then the fibres may buckle to form ribbon like structures instead of co-axial fibres. This happens as a result of either the shell solvent evaporating too fast, forming an external skin layer that buckles under atmospheric pressure [128], or when the core evaporates faster and creates a thin layer at the core-shell interface, which also causes fibre buckling under atmospheric pressure once all the solvent evaporates leaving a vacuum behind [140].

We have found fibre collapsing to be a common issue in our attempts to co-electrospin AB-PS fibres with the core and shell solvents chosen on the basis of compatibility. It is very difficult to satisfy all solution parameters in the right way to enable successful co-electrospinning, for example choosing an immiscible solution combination may mean choosing solvents with different vapour pressures, since both factors are controlled by differences in the internal molecular forces of the solvents. Thus, a systematised solution selection process is necessary to efficiently select the right combinations of core and shell solutions. In this respect I have developed a solution selection model, which will be discussed in §3.3.3. But before that I will outline the processing conditions that need to be controlled for co-electrospinning.

3.2.3.5 Solution flow rates

Considering that other parameters are kept fixed, increasing the flow rates results directly in the increase of fibre diameters, with the inner (core) and outer (shell) diameters, respectively, determined by the core and shell flow rates. This is illustrated in Figure 3.6 for co-electrospun PAN: PMA fibres (with concentrations of 12 wt.% PAN in DMF (shell) and 15 wt.% PMMA in DMF (core)), where the core:shell flow rate ratio was varied with total flow rate fixed at 1000 µm/hr. While the relative core-shell diameters (i.e. shell thickness) can easily be varied through control of flow rates, the balance between the flow rates should be such that the formation of a stable compound Taylor cone is not compromised. If, for a given shell flow rate, the core flow rate is too low, then an insufficient amount of core fluid will be delivered and the continuity of the core entrainment will be broken down and fibres with a discontinuous core-shell structure will be obtained. On the other hand if the core flow rate is too high, such that the core Taylor cone becomes too large, then the viscous shearing force exerted by the shell on the core may be insufficient to confine the core solution [134, 136]. Therefore, in order to ensure the continuous encapsulation of the core in the shell solution it is important to maintain the core flow rate lower than that of the shell.

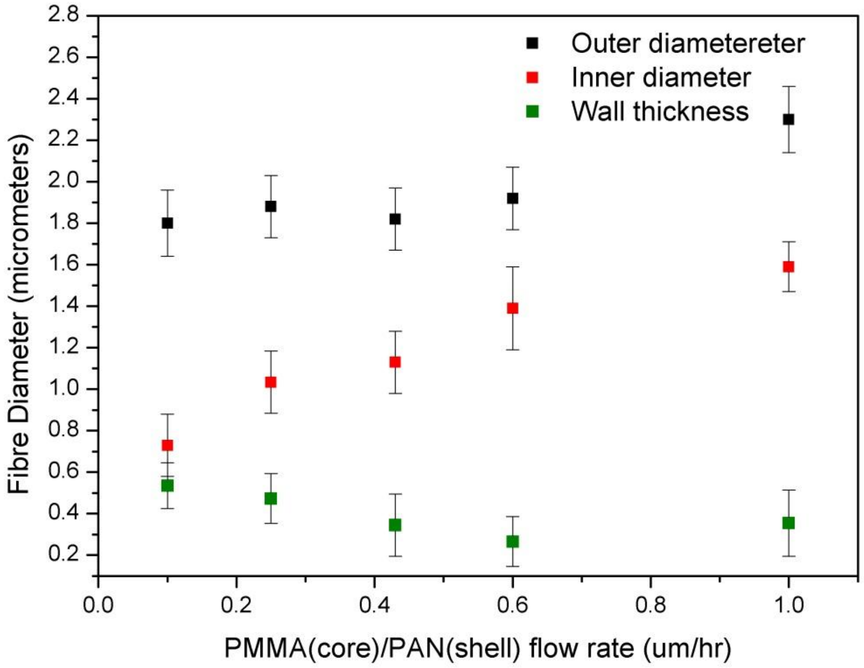

Figure 3.6: Co-electrospun 12 wt.% PAN in DMF (sheath) and 15 wt.% PMMA in DMF (core) at varying flow rates; shell flow rate increased from 500 to 900 µl/hr, with 100 µl/hr increments while core flow rate reduced from 500 to 100 µl/hr (total flow rate fixed at 1000 µl/hr).

3.2.3.6 Core nozzle protrusion

Several authors have reported, based on theoretical and experimental results, that the entrainment of the core solution in the shell and hence formation of core-shell jets is greatly facilitated by the protrusion (extension) of the core nozzle (capillary) from the shell nozzle [128, 141]. While the protrusion distance of the core nozzle is required to be about several tens of per cent of the radius of the outer nozzle, the optimal protrusion distance is said to be dependent on several factors: "the viscosity ratio of the liquids, the interfacial tension, and the feeding rates of the inner and the outer liquids." [128, 141]. Reznik *et al.* [139] suggest 0.5 r_{out} (where r_{out} is the outer radius of the outer nozzle) to be an optimal value for the protrusion distance of the core nozzle. With the same control parameters a higher protrusion distance (e.g. r_{out} 0.6) was found to cause multiple jets to be emitted from the droplet. However, this value may vary depending on the solution and process parameters. Thus, if theoretical models are unavailable, the optimal protrusion distance can be determined empirically for a given solution set at selected process parameters. The co-axial nozzle system used in this experiment was set up with the core nozzle protruded by 0.5 r_{out}.

3.2.3.7 Applied voltage

The effect of voltage in co-electrospinning is not as thoroughly investigated as the above parameters, and reports on the influence of voltage on the success of co-electrospinning and the fibre morphology is limited to the works of Li and Xia [127], and Moghe and Gupta [72]. In all other studies only one value of voltage, the value that enables a stabilised Taylor cone, is reported. Li and Xia report that both the inner and the outer diameters of the fibres decrease with increasing voltage. Moghe and Gupta report that for a given pair of solutions at a given combined flow rate there is a "small range of applied voltages in which a stable Taylor cone was formed". With voltages below this range the solutions drip and a jet issues only intermittently. This is in agreement with our observations in this study. We have also found that lower voltages, which allowed for the droplet to get bigger in a given time, increase the chance of solution mixing in the droplet. On the other hand, with voltages above the critical range, the Taylor cone was found to recede into the capillary and multiple jets were issued from the solution. It is therefore important, for a given pair of solution set at a given flow rate, to empirically determine the most suitable voltage (or voltage range) that enables the formation of a stable Taylor cone and production of uniform core-shell fibres.

3.2.3.8 Required co-electrospinning conditions: a summary

The degree of miscibility is a necessary but not a complete guide to whether co-axial spinning is possible; it also is required to control the relative scale of a number of other parameters. At the nozzle tip, a stable liquid Taylor cone is needed to enable a consistent and continuous core-shell structure to form. In a normal case for electrospinning compound (core-shell) solutions, the outer solution is chosen to have a higher conductivity than the core; in which case the driving force of the compound jet comes from the electrostatic charge build up on the outer surface of the shell. Stable spinning then depends on the outer shell solution drawing out the inner core solution through shearing and contact forces, ‘viscous dragging’ and ‘contact friction’, which keep the inner solution confined to the core while the fibres are being stretched. For this reason the shell solution should be electrospinnable on its own and based on the discussion above (formulated from what is in literature [72] and some of my own work) the following conditions must be satisfied:

- The shell solution must have a higher viscosity than the core solution such that the viscous force imparted by the shell on the core is enough to overcome the interfacial tension,
- The shell solution must have a higher flow rate than that of the core, so that the viscous drag applied by the sheath solution is sufficient to confine the core solution within the cone [136],
- The vapour pressure of both solutions must be sufficiently low and comparable so both the core and shell dry at similar rates to stop fibres collapsing,

- The conductivity of the shell solution should ideally be higher than that of the core to enable continuous entrainment of the core by the shell, though higher core conductivity will also allow for co-axial spinning,
- The two solutions must possess low interfacial tension to prevent large stresses at the core-shell interface reducing fibre stability and to produce a stable Taylor cone [134, 136].

3.3 Solution Chemistry

3.3.1 The need for a solution selection model

Controlling and optimising the solution parameters, as discussed in the section above, is critical for ensuring success of co-electrospinning. To attain the required balance between the solution parameters it is necessary to optimise the parameters of each solution individually. The core and shell solution combinations should be such that the two sets of solutions are compatible. Solution compatibility in this context is defined as the suitability of two dissimilar solution systems to be electrospun together. Two solutions are considered as incompatible if the solvent in one causes the precipitation of the solute in the other, such that when the two come in contact at the tip of the co-axial nozzle, the droplet becomes insufficiently liquid to enable the formation of a Taylor cone and/or initiation of the co-axial jet. As well as ensuring compatibility of the solutions, the extent of solution miscibility needs to be controlled also, so that the core and the shell remain phase separated in the electrospinning jet. This is important for the formation of fibres with core-shell configuration. Both the compatibility and miscibility of solutions depend on the relative affinities between the different components of the two solution systems. If for example, the solvents used in each solution have a greater affinity for each other, while the solvent in one solution is a non-solvent for the solute in the other, then the dissolving power of the mixed solvent system decreases as the two solvents blend together. In such a case, where the solvent and the solute are considered as incompatible, the mixing of the solvents promotes polymer aggregation and precipitation.

The interaction between the solvent-solvent, solvent-solute or solution-solution systems is controlled by the similarity/difference between the intermolecular forces in each component of the solutions. The strength of these molecular forces are represented by the solubility parameters, one widely used set being Hansen solubility parameters [142]. These parameters can be used to predict the affinities between the solution components and hence the extent to which a given set of solutions are compatible and/or miscible.

As discussed in §3.2.3, the effect of many of the parameters that control the physical spinning mechanisms such as solution viscosity ratio, interfacial tension, solution conductivity, solvent vapour pressure etc., are relatively well understood, but there is still a lack of understanding of the importance of the interaction (e.g. miscibility) between the core and shell solutions for the success of co-electrospinning. This is mostly because it is difficult to eliminate the influence of other parameters on the fibre morphology, such that the results observed on the nature of core-shell configuration cannot be solely attributed to miscibility of the solutions. Additionally, the use of co-electrospinning has been mostly limited to polymeric core and the shell materials, though non-polymeric innocuous (e.g. non-polar) core materials such as heavy mineral/olive oil and glycerol [125, 127] have also been used, the use of strongly interacting solutions composed of highly polar materials, such as AB, has not been previously reported. Our preliminary studies on co-electrospinning AB in a polymeric shell solution have highlighted the importance of core-shell solution interaction (e.g. miscibility) in controlling the success of co-electrospinning. We were unable to produce fibres from core-shell solution sets with solvents selected purely on the basis of their suitability for dissolving a solute. Solution miscibility is expected to be more pronounced in highly polar, complex materials that form low viscosity solutions, such as AB, which impose severe restrictions on the choice of sheath solutions that can be used for the fabrication of co-axial fibres.

Therefore, on the basis of identifying the importance of solution miscibility for the success of co-electrospinning and resultant fibre morphology, a range of different solution combinations with varying degree of miscibility were tested, these are categorised as: miscible, semi-miscible and immiscible.

In a large parameter phase space where the values of many variables have to be optimised simultaneously, while solution immiscibility is controlled and compatibility is ensured, trial and error selection method for a given solute can be highly time consuming and ineffective at ensuring success of co-electrospinning. I have, therefore, formulated a solution selection method using Hansen solubility parameters to assist in the choice of compatible solutions with the required solution properties and varying degrees of miscibility. In the second part of this chapter the details of this systematic model are outlined. This solution selection method, which can be used for efficiently selecting solvents and solutes with the required properties, is applicable to all multiphase electrospinning systems.

3.3.2 Hildebrand and Hansen solubility parameters: Theory

Solubility parameters have long been used in industries such as paints and coatings where understanding and controlling solvent/polymer interactions are vital for optimization of polymer dissolution in solvents. They can be used for various applications to predict the compatibility of polymers, chemical resistance and permeation rates [142]. The basic principle behind solubility parameters is based on the idea that like-dissolves-like, or like-seeks-like, such that liquids with similar solubility parameters are expected to be miscible or a polymer with a given solubility value is expected to dissolve in solvents with solubility parameters similar to its own.

The interaction between the different materials is strongly dependent on the strength of the molecular attractions, as given by the cohesive energy density between the materials, E_{coh}:

$$E_{coh} = \Delta H_{vap} - p\Delta V \approx \Delta H - RT \tag{3.6}$$

where ΔH (measured in J mol^{-1}) is the heat of vaporisation, R is the universal gas constant (8.314 J K^{-1}mol^{-1}), T is the absolute temperature (in Kelvin) and ΔV is the volume occupied (in units of m^3). Cohesive energy, defined as the energy needed to completely remove a unit volume of molecules from their neighbours to infinite separation (an ideal gas), is an indirect reflection of the degree of the intermolecular forces holding the liquid together, measured in units of J/cm^3. The solubility of a given solute in a solvent depends on the ability of the solvent molecule to overcome these intermolecular attractions between the solute molecules, so that a homogeneous solution can be formed.

In 1936 Joel H. Hildebrand (who laid out the foundations of solubility theory in his classic work on the solubility of nonelectrolytes in 1916) [142] proposed that the measure of solubility of a given substance is determined by the solubility parameter, δ, which is given by the square root of the cohesive energy density:

$$\delta = \sqrt{\frac{E_{coh}}{V_m}} = \sqrt{\frac{\Delta H - RT}{V_m}} \tag{3.7}$$

where V_m = molar volume. This solubility parameter provides a numerical estimate of the degree of interaction between materials and its definition is based on thermodynamic considerations. Thermodynamically for two substances to be mutually soluble the free energy of mixing, ΔG_M, is required to be zero or negative. By definition:

$$\Delta G^M = \Delta H^M - T\Delta S^M \tag{3.8}$$

where ΔH^M is the enthalpy of mixing and ΔS^M is the entropy of mixing. According to Hildebrand, the enthalpy of mixing can be calculated by:

$$\Delta H_M = \varphi_1 \varphi_2 V_m (\delta_1 - \delta_2)^2 \tag{3.9}$$

where V_M is the volume of the mixture, φ_1 and φ_2 volume fractions of components 1 and 2 (e.g. solvent and polymer), and δ_1 and δ_2 are solubility parameters of components 1 and 2.

The accuracy of the solubility parameter depends on the accuracy in determining strength of the interactions contributing to the cohesive energy. In the equations derived by Hildebrand Eq. (3.7) and (3.9) only the dispersive forces are taken into account when defining the cohesive energy, so the predictions made on the basis of their Hildebrand solubility parameters are generally useful only for non-polar or slightly polar systems without hydrogen bonding. In a more refined calculation, Charles Hansen (1966) divides the total Hildebrand parameter into three components [142]; the Hansen parameters, to account for molecular forces arising from dispersion (Van der Waals), polar, and hydrogen bonds between the molecules of a given material. In this more generalizable approximation E_{coh} is defined as:

$$E_{coh} = E_d + E_p + E_h \tag{3.10}$$

where E_d, E_p, and E_h are, respectively, the dispersion, polar and hydrogen bonding contributions to the cohesive energy. The corresponding equation for the solubility parameter becomes:

$$\delta^2 = \delta_d^2 + \delta_p^2 + \delta_h^2 \tag{3.11}$$

where the δ_d, δ_p, and δ_h are the partial Hansen solubility parameters representing the strength of the dispersion, polar and hydrogen bonding forces, respectively, for a given material. The equivalent of Eq. (3.9) then becomes:

$$\Delta H_M = \varphi_p \varphi_s V_m \left[(\delta_{d1} - \delta_{d2})^2 + \left(\delta_{p1} - \delta_{d2}\right)^2 + (\delta_{h1} - \delta_{h2})^2 \right] \tag{3.12}$$

Hansen solubility parameters are found to be particularly useful at predicting solubility and swelling of polymers by solvents [142]. These parameters were used within a solvent selection model to construct a systematic method for selecting compatible core and shell solutions, while at the same time optimising the core and shell solution parameters that are important for co-electrospinning. The details for this solution selection method are described in the next section.

3.3.3 Solution selection model

The Hansen solubility parameters (HSPs) that quantify the interaction strengths as the polar (δ_p), dispersive (δ_d), and hydrogen bonding (δ_h) components are empirically determined and tabulated in literature in units of $MPa^{1/2}$ [142]. These three parameters can be treated as co-ordinates for a point in a three dimensional space, known as the Hansen space, with a radius of interaction, R_0, for a given solute. R_0 is also calculated empirically as the fourth value of the HSPs [142]. If the Hansen co-ordinates of a potential solvent (or solvent blend) lie within the solubility sphere of a polymer, then the solvent would be expected to dissolve that polymer, i.e. it will be considered as a good solvent. In order to determine whether this is the case, the distance of the solvent from the centre of the polymer solubility sphere, R_a, needs to be calculated using the following equation [142]:

$$R_a^2 = 4(\delta_{d1} - \delta_{d2})^2 + \left(\delta_{p1} - \delta_{d2}\right)^2 + (\delta_{h1} - \delta_{h2})^2 \tag{3.13}$$

The HSPs of the solute (e.g. polymer) δ_{d1}, δ_{p1}, and δ_{h1}, marks the centre of the Hansen solubility sphere, with the solubility parameters of the solvents, δ_{d2}, δ_{p2}, and δ_{h2}, dispersed in the solubility region within the sphere (as shown in Figure 3.7). If this distance (R_a) is less than the radius of interaction (R_0) of the solute (polymer), then the solvent is expected to dissolve the polymer. The dispersion term is described as being twice as important as the polar- and hydrogen-bonding terms and hence more weight is put on it in Eq. (3.13) [142].

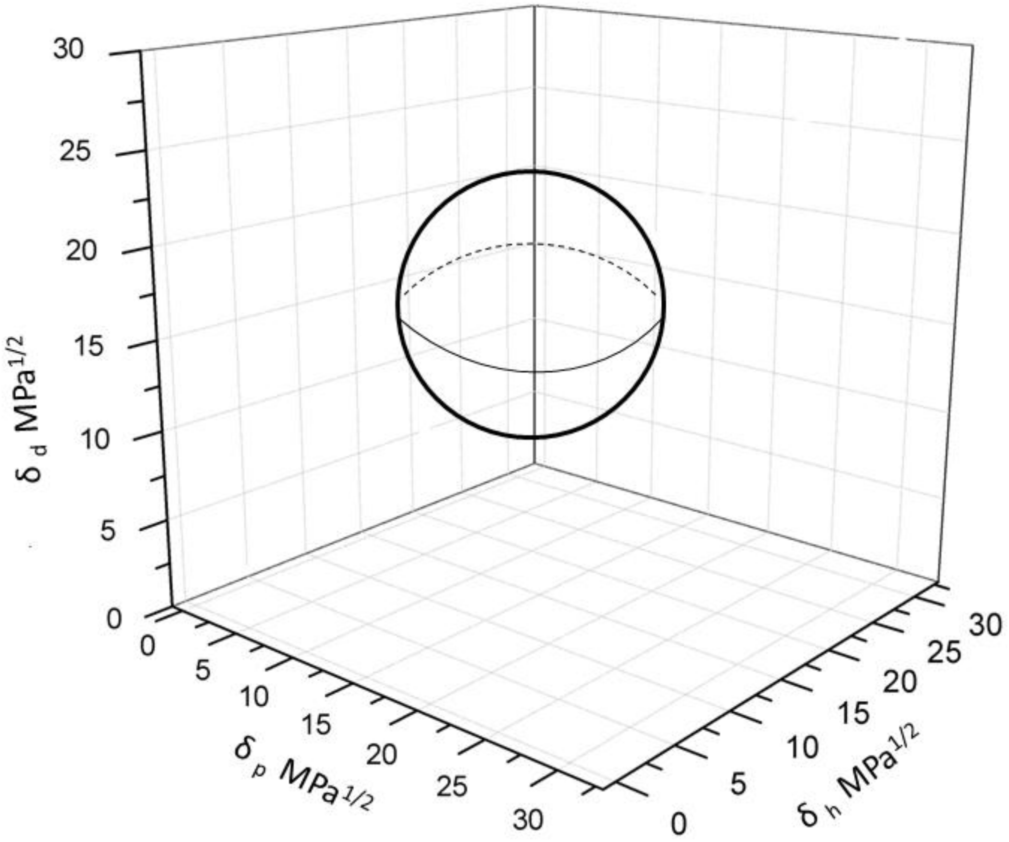

Figure 3.7: The Hansen solubility plot showing the Hansen sphere as determined by the coordinates of the solute (polymer) (δ_{d1}, δ_{p1}, δ_{h1}) and its radius of interaction (R_0). Liquids with solubility parameters within the volume are active solvents for that solute (polymer).

A convenient index for the relative goodness of a solvent for a polymer is the ratio R_a/R_0, which gives the relative energy difference (RED) of the system: RED= R_a/R_0; if RED<1, the molecules are alike and the system will dissolve, if RED≈1 then the system will partially dissolve, and if RED >1 the system will not dissolve, with progressively higher values of RED suggesting progressively more unfavourable interactions [143]. If one does not have an estimate for R_0, then solvents can be ranked by R_a, with the smaller R_a indicating the better solvents.

Since a three dimensional (3-D) graphical presentation is not always easy to produce, two-dimensional (2-D) methods for representation of solubility data have been proposed. These include various variations; δ_p-δ_h diagram proposed by Henry (1974), δ-δ_h diagram proposed by Hoernschemeyer (1974), or the δ_v-δ_h diagram [144]. The latter combines the polar dispersive (δ_p) and dispersive (δ_d) parameters to give a new parameter $\delta_v= (\delta_d^2+\delta_p^2)^{1/2}$, which is plotted against δ_h to produce a 2-D graphical representation of the solubility parameters. This 2-D representation was chosen as the method of choice, as it is considered to provide a sufficiently accurate approximation of the interaction parameters, since thermodynamic calculations initiated by Bagley *et al.*, suggest close similarity between the effects of δ_d and δ_p on the total cohesive energy [144]. This particular method has the advantage of being a more accurate predictive tool that enables greater efficiency compared to other methods that rely on empirical analysis such as a Teas-graph: a triangular graph with each side being a scale for the percentage contribution of δ_h, δ_p, δ_d from a given solvent. The percentage contribution of each Hansen parameter is calculated and plotted on the teas graph, with the solvents close together on the graph being considered as more likely to be miscible than the solvents marked farther apart [144].

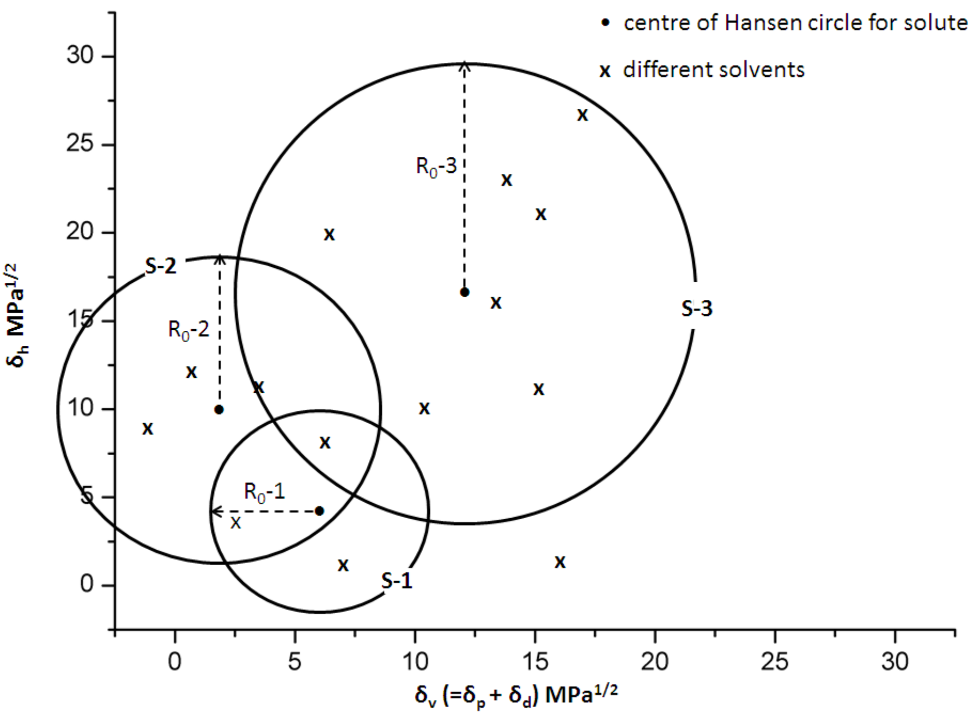

Figure 3.8: A hypothetical δ_v-δ_h Hansen plot, circles mark the Hansen area for solutes (polymer) S-1, S-2 and S-3 as defined by the Hansen coordinates (δ_v, δ_h) of each solute marking the centre of the circles (•) and the radius of interaction for each solute respectively: R_0-1, R_0-2, and R_0-3. The crosses (**x**) mark the coordinates of different solvents, those that fall inside a given polymer circle are predicted to be good solvents for that solute, those that fall outside are non-solvents, and the closer they are to the centre of the circle the better solvents they are.

Using this representation of the Hansen solubility space a 2-D, δ_v vs. δ_h, graphical diagram for polystyrene (PS), the sheath materials selected for encapsulating ammonia borane, was constructed. The solubility space of the polymer is delimited by a circle with a radius R_0 as for the hypothetical polymer-solvents systems shown in Figure 3.8. In the case of PS the coordinates of the centre of the circle correspond to the solubility parameters δ_v=18 and δ_h=5 $(Mpa)^{1/2}$ and the radius of interaction R_0=5 [144]. The solvents with δ_v and δ_h parameters that fall within the circle are considered as good solvents for PS, those that fall outside are predicted to be poor or non-solvents.

The exact Hansen parameters for AB are unknown, however, the polar nature of AB gives it an affinity for solvation in large pool of polar solvents, such as water, N,N-dimethylformamide (DMF) and dimethyl sulfoxide (DMSO). These AB solvents can be plotted on the Hansen plot containing PS solubility circle and used to predict the degree of miscibility of a PS-solvent solution with an AB-solvent solution. Using this plot I was able to predict which core-shell solvent combinations would be miscible, semi-miscible or immiscible, based upon the location of a given solvent on the δ_v vs. δ_h diagram, i.e. whether the solvent was inside, near the boundary or outside the solubility circle. Water, for example, has a very high δ_h parameter (42.3 MPa $^{1/2}$), which is a long distance away from the PS solubility circle; therefore, it is predicted to be a non-solvent for PS and immiscible with those solvents in the circle.

Once all the solvent and non-solvents for PS and AB were identified, these solvents were plotted on a *solution matrix* with all the important solution parameters listed, including HSPs, RED, conductivity, dielectric constant, boiling point, vapour pressure and dipole moment values of all the solvents (see Appendix A). This matrix was used to select solvents with the optimal parameters for co-electrospinning of the core and shell solutions. In order to create PS solutions with properties suitable for electrospinning, it was necessary to use solvent mixtures to optimise properties such as conductivity, dielectric constant, vapour pressure and viscosity. The parameters of the core and shell solution mixtures were controlled as described in below.

Throughout this solution selection process, the main objective was to control the balance between the core and shell solution parameters in accordance with the requirements listed in §3.2.3, while maintaining control over the degree of miscibility between the solutions. This formulation is clearly a method that can be used for all multi-phase electrospinning applications and provides a systemised approach to selecting solvents and solution combinations much more efficiently than most other solvent selection methods (such as the teas graph approach), which typically rely on time consuming empirical analysis.

3.3.3.1 Calculating the solution parameters of mixtures

Using the correct solvent ratio of each solvent in the mixtures was important for optimising parameters in the right direction as well as gaining control of the degree of miscibility between the core-shell solutions, which varies depending on the resultant Hansen solubility parameters of the mixtures. The way in which solution parameters were controlled is described below.

3.3.3.1.1 Hansen Solubility Parameters

The specific solvent ratio used in the mixtures was chosen to keep the overall HSPs of the solvent mixture within the Hansen circle. The HSPs of the mixtures are calculated using:

$$\delta_n^{mix} = \sum_i a_i \delta_n^i \tag{3.14}$$

where i is a component index and a_i is volume fraction of solvent, δ_n is in units of MPa$^{1/2}$.

3.3.3.1.2 Viscosity

Solution viscosity (η), which is required to be higher for the shell solution, is important for controlling shear resistance exerted on the core, such that the viscous force imparted by the shell on the core is enough to overcome the interfacial and draw it out along with it. While solution viscosity depends on a combination of factors such as the effectiveness of the solvent at dissolving the polymer, average molecular weight of the polymer (M_w) and polymer concentration, variation of only the latter was sufficient for controlling solution viscosity. The viscosity of the solution in co-electrospinning was controlled and measured in the same way as for single phase electrospinning (as discussed in §2.6.1.1.1).

3.3.3.1.3 Conductivity

Most of the liquids identified as good solvents for PS had very low conductivities, making them unsuitable for electrospinning in their pure form. Toluene, which is immiscible with water and a non-solvent for AB, was selected as the main shell solvent. However, we were not able to spin a PS-toluene solution despite trying a wide range of PS concentrations and voltages as high as 30kV. Solvent conductivity can often be increased through the addition of ionic or protonic salts. The ability of a solvent to dissociate a salt and hence the increase in its conductivity is dependent on its dielectric constant (i.e. its polarity); as discussed in §2.6.1.4 solvent conductivity is shown to increase with dielectric constant at different salt concentrations [145, 146]. Toluene has a very low dielectric constant and thus dissolution of salts was unsuccessful. Despite this, by using a binary or ternary solvent system we were able to selectively change the dielectric constant and hence increase shell-solution conductivity to enable fibre drawing without rendering the shell solution incompatible (or miscible) with the core. The dielectric constant of the mixtures (ε_{mix}) was calculated using:

$$\varepsilon_{mix} = \sum_{i} a_i \, \varepsilon_i \tag{3.15}$$

where a_i is the volume fraction of solvent i, ε has units of farads per metre (F m^{-1}).

3.3.3.1.4 Vapour pressure

Controlling the vapour pressure (P_0) of the solvents is essential for success of co-electrospinning and core-shell morphology of the as spun fibres; a too high P_0 will cause the droplet at the tip of the nozzle to dry, preventing electrospinning, and a P_0 too low will cause the fibres to go down wet to form a film. While it is important to use the right vapour pressure solvent in the shell solution to avoid these issues, it is important to use solvents (or solvent mixtures) with similar P_0 values in the core and the shell solutions to avoid fibre buckling (collapsing) [147]. The vapour pressure P_0 of a solvent can be calculated from its boiling point T_B and heat of vaporisation ΔH_{vap} using the Clausius-Clayperon equation (Eq. (2.11))[117]. The resultant vapour pressure of the solvent mixtures was calculated using Rault's law [117]:

$$P_{mix} = \sum_i P_i X_i \tag{3.16}$$

where i is the solvent component index and X_i is the mole fraction, P has units of Pascal (Pa).

Chapter 4

Characterisation and Neutron Scattering Techniques

4.1 Fiber Imaging Methods

4.1.1 Scanning electron microscopy (SEM)

Scanning electron microscopy (SEM), a technique capable of producing high resolution images of a sample surface, was used for inspecting topographic morphology of the electrospun fibres. The signals that produce the SEM micrographs result from interactions of the electron beam with atoms at or near the surface of the sample imaged and, therefore, surface of the sample is required to be conducting for greater sample resolution. A wide range of magnification is available, ranging from 10,000X up to 30,000X and the spatial resolution ranges from 10 to 100 nm. SEM images typically have a large depth of field due to the narrow electron beam used, which result in images with a three-dimensional appearance and show the variation in surface morphology.

A schematic diagram of a typical SEM is shown in Figure 4.1. The electrons thermionically emitted from a tungsten cathode are accelerated towards an anode with a set energy typically ranging from a few hundred to 100,000 eV. The electron beam is focused by one or two condenser lenses into a spot sized 1 to 5 nm. On its trajectory the beam passes through pairs of scanning coils, which deflect the beam horizontally and vertically, such that it scans in a raster fashion over a rectangular area of the sample surface. The electrons that come in contact with the sample surface lose energy by repeated scattering and absorption over an area extending from less than 100 nm to around 5 µm on the specimen surface. Energy exchange between the electron beam and the sample results in emission of secondary and backscattered electrons as well as emission of electromagnetic radiation from the sample. The secondary and backscattered electrons detected are then amplified by a photomultiplier tube to produce an image; secondary electrons are good for obtaining morphological information from sample surface, while backscattered electrons are useful for illustrating contrasts in composition in multiphase samples [148]. The combination of highe magnification, large depth of focus, greater resolution, and ease of sample preparation makes the SEM one of the most commonly used technique for fibre analysis.

Two separate scanning electron microscopes were used in this investigation depending on availability at the time of the investigation For analysis of AB-PS fibres we have used a field effect-scanning electron microscopy (FE-SEM, Hitachi S4000) using an accelerating voltage of 10 kV, which had 45 degree rotatable sample holder that was used to look at fibre tips. For the analysis of polymeric and carbonised PAN fibres we have used a FE-SEM (Carl Zeiss XB1540).

SEM samples were easily prepared for imaging, a section of the electrospun fibre mesh was placed on a SEM stub or fibres were directly collected on small washers that were placed on to the SEM sample holder for imaging, tyoically after plasma deposition of a few atomic layers of platinum. Fibres imaged on washers generally produced better quality images due to the dark background of the hollow cores. For examination of the co-axial structure, it was important to expose the ends for imaging the fibre cross-section in the SEM. However, due to tendency of the fibres to lie flat on a surface it was difficult to expose fibre tips. Therefore, the fibres were aligned and sealed between two layers of adhesive tape, which was submersed in liquid nitrogen and then cut with a scissors using the embrittled tape as support. This was the only method that successfully enabled SEM imaging of the fibre cross-section.

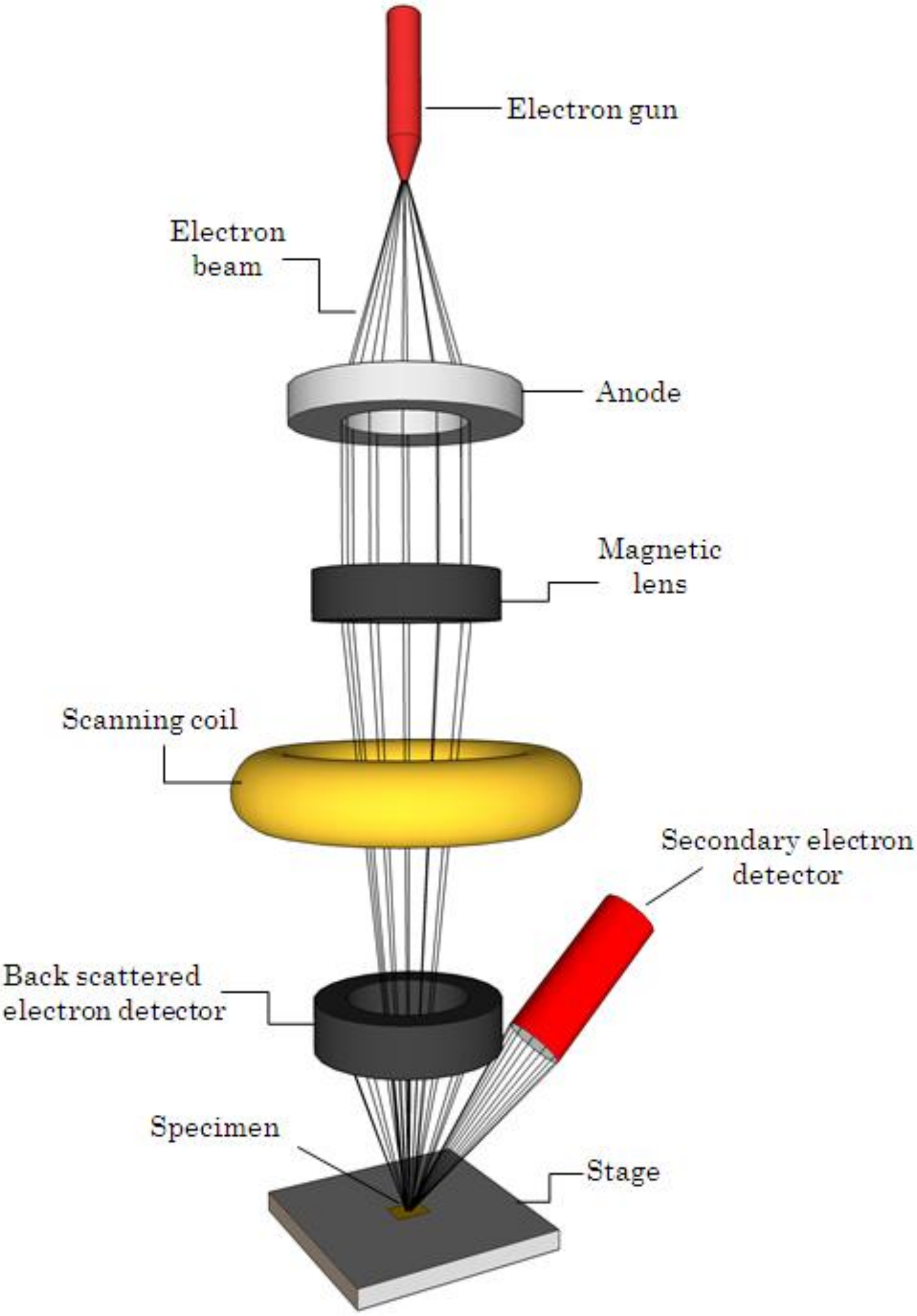

Figure 4.1: Schematic diagram of scanning electron microscope (SEM).

4.1.2 Transmission electron microscopy (TEM)

Transmission electron microscopy (TEM) is a microscopy technique that uses a highly energetic beam of electrons that is transmitted through an ultra-thin specimen to provide a more penetrative image of the sample analysed. TEM was specifically used to image the core-shell morphology of the fibres along the fibre axis, which was not possible with the SEM. A schematic diagram of a typical TEM is shown in Figure 4.2. The electrons emitted from a light source at the top of the microscope travel through vacuum in the column of the microscope, which get focussed into a very thin beam before being transmitted through the specimen being analysed. The electrons transmitted through the sample scatter at different angles depending on the density of atoms in the specimen and some get lost. The transmitted electron signal is then magnified by a series of electromagnetic lenses and can be analysed through electron diffraction or direct electron imaging with the transmitted electrons projected on to a fluorescent screen or a layer of photographic film at the bottom of the column (as shown in Figure 4.2). This gives rise to a "shadow image" of the specimen, with a varying degree of darkness according to their density, which can be studied directly by the operator or viewed with a camera. The diffraction pattern obtained with the TEM in the diffraction mode can be used to determine the crystallographic nature of the sample analysed [24].

TEMs have a very high resolution (10^{-10} m) due to the small de Broglie wavelength of electrons, capable of imaging fine detail, as small as a single column of atoms, which is tens of thousands of times smaller than the smallest resolvable object in a light microscope. Sample preparation is rather difficult, since the samples imaged have to be typically thinner than a few tens of nanometres for the electrons to be transmitted through. However, due to the high degree of porosity in most our fibre samples, fibres with diameters as large as a couple of microns could be imaged with the internal structure visible most of the time.

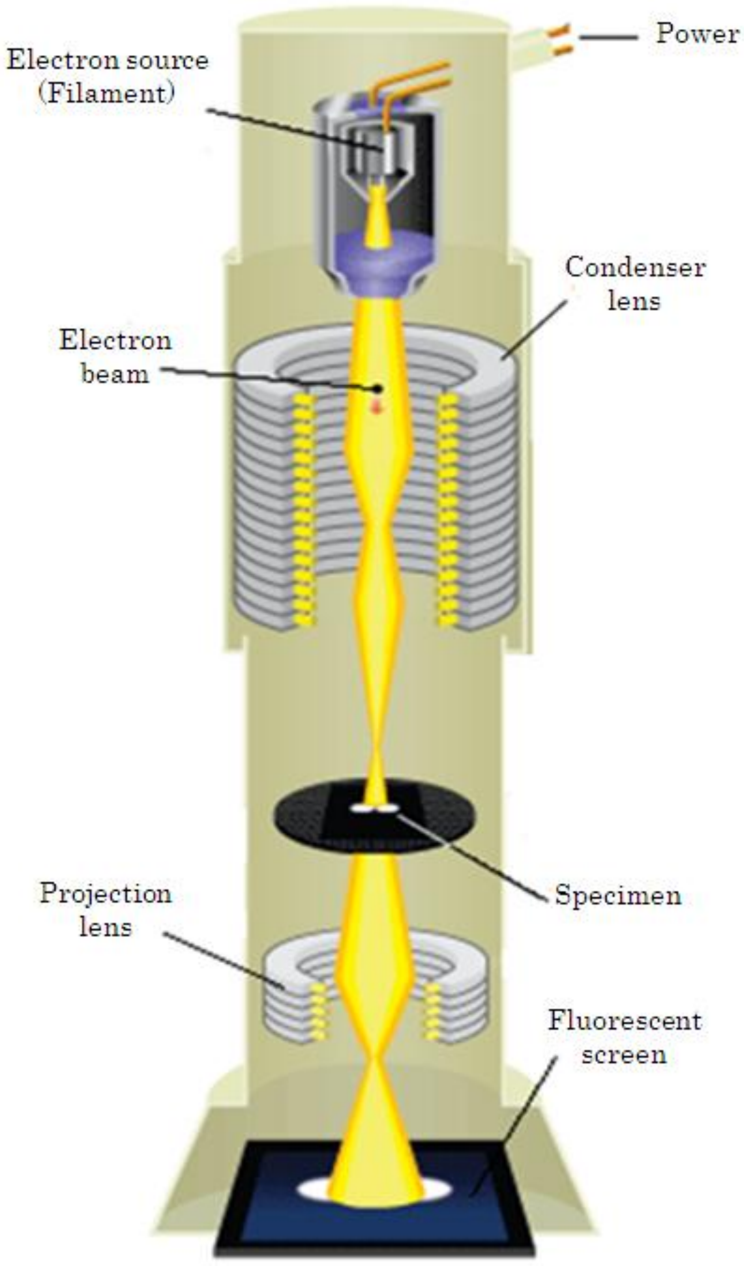

Figure 4.2: Schematic diagram of a transmission electron microscope.

For analysis of all fibres in this investigation we have used TEM, JEOL JEM-2010 (LaB_6 filament) at an accelerating voltage of 200 kV. Sample preparation involved solvating the fibres in a non-solvent in a tube that was placed in an ultrasonic bath to break the fibres into smaller fragments. Droplets of the suspension were then placed onto TEM copper grids that captured fibre fragments (fibrils) for analysis in the TEM. While this method worked very well for the carbon fibres, which were more brittle, a polymeric fibre mesh was less easy to separate into separate fibres, thus, tweezers were used to break small fragments off the mesh. The solvent used for solvation of PAN and carbon fibres was ethanol, and that used for AB-PS fibres was ether.

4.2 Intelligent Gravimetric Analysis

Intelligent Gravimetric analysis (IGA) system (Figure 4.3) uses the gravimetric technique to monitor the change in a sample's mass as a function of time with the sample under controlled pressure and/or temperature. The technique was used in conjunction with mass spectrometry to measure desorption products of ammonia borane, polystyrene or ammonia borane-polystrene (core-shell) fibres during the thermolysis processes of the samples.

The IGA system used in this investigation was a Hiden Isochema IGA-003 analyser, which integrates computer-control and measurement of weight change, pressure, temperature and gas flow. The samples to be analysed are placed in a stainless steel mesh sample bucket connected to a large capacity microbalance (5 g) with a resolution of 0.1 µg via a fine gold chain and a tungsten wire hang-down. This is sheathed, along with a platinum resistance thermocouple (accurate to ± 0.2 °C) and a gas inlet/outlet tube, by A UHV stainless steel reaction vessel (Figure 4.3). Software compensations for non-ideal gas behaviour and buoyancy effects due to the different temperatures and volumes of the sample and counterweight are all integrated into the system.

Temperature was controlled using a fast response furnace capable of ramp rates between 0.2 and 20 °C min^{-1} up to a maximum temperature of 500 °C. Using the mass spectrometer in conjunction with the IGA required it to be operated in flowing mode with an inert background gas. The set up was such that the flowing background gas (which was either helium or nitrogen in this study) mixed with the desorbed gas from the sample, which was then carried to the mass spectrometer chamber through a 10 bar capillary tube for analysis of the desorption products.

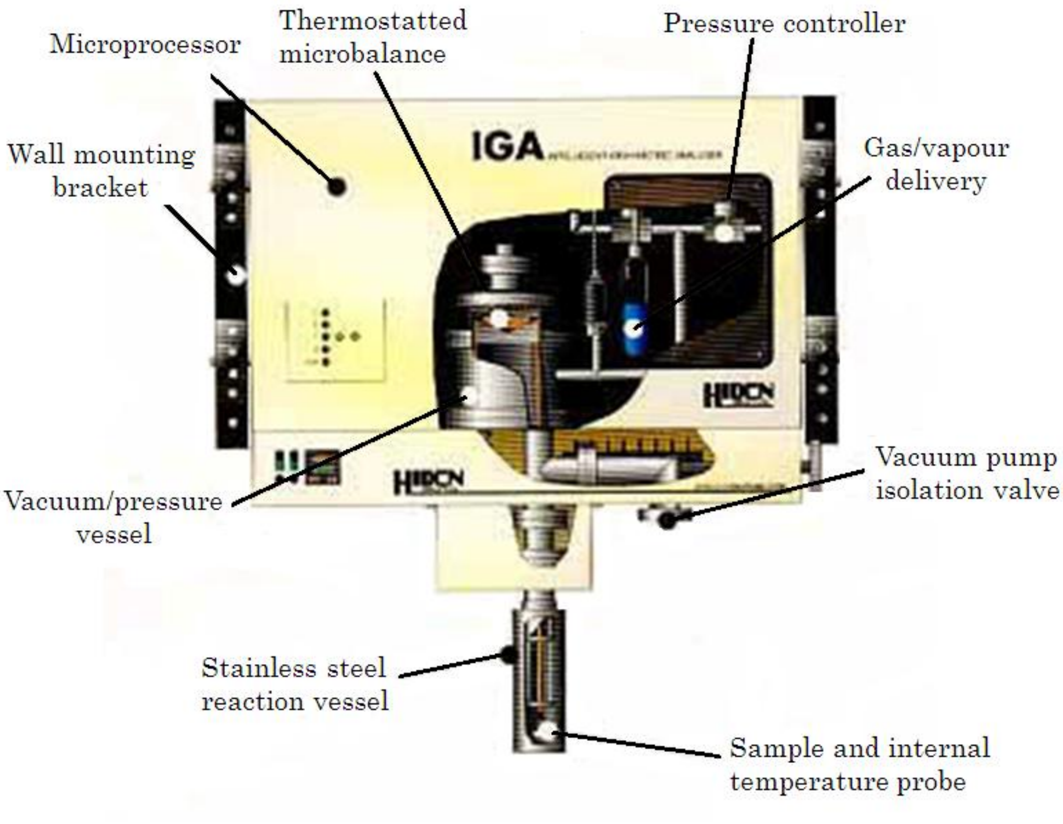

Figure 4.3: Schematic diagram of IGA [149].

Two separate IGA-mass spectrometer set ups were used. The IGA was of the same type in both cases, the mass spectrometer however was different. Majority of the studies were carried out with a Hiden Analytical Dynamic Sampling Mass Spectrometer system (DSMS type HPR-20) with a HAL 201, type 124100, with dual a Faraday/Electron Multiplier detector capable of detecting an atomic mass range of up to 200 AMU (with a limit of

0.1 to 1 ppm). Ionisation was via electron impact using a thoria coated iridium filament and the system can follow the partial pressures of up to six molecular ions simultaneously. The second mass spec was of the same model but with an atomic mass range of up to 50 AMU and this was used only when we had no access to the first IGA-mass spectrometer setup. For a typical experiment 50 mg of sample was loaded into a stainless steel mesh bucket, which was then placed on to the tungsten hang-down in air. The reactor was then raised and sealed with a copper gasket. The sample was then left under dynamic vacuum for 12 hours to remove all traces of contaminant gases. The chamber was refilled with 1 bar of He (or Ar) and the flow rate set to 100 ml min^{-1}. The furnace was then attached and the experiment commenced with the set heating rate. All variables were sampled every 12.5 seconds.

4.3 Differential Scanning Calorimetry

Differential scanning calorimetry is a thermoanalytical technique commonly used for investigating the nature of phase transitions in a material. Figure 4.4 provides a schematic illustration of the cell compartment of a differential scanning calorimeter. The setup, consisting of two identical cells (one for the sample investigated (S) and another for a reference sample (R)), is configured in a way to enable the heat capacity between two materials to be measured. With the cells heated at a set rate and maintained at the same temperature throughout the measurement, the difference in the amount of heat required for increasing the temperature of the sample and reference is measured as a function of temperature.

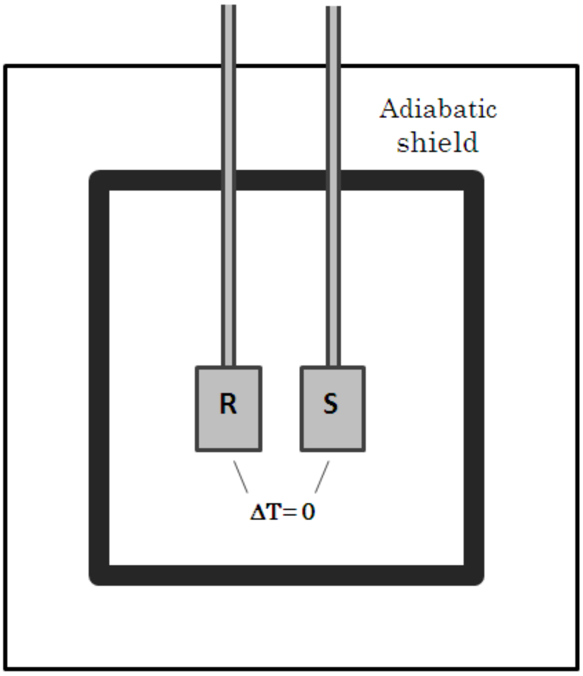

Figure 4.4: Schematic illustration of the cell assembly of a differential scanning calorimeter. The temperature difference between the sample and reference cells (S and R) is maintained at zero ($\Delta T = 0$) by a feedback mechanism as the temperature is increased or decreased at a constant scanning rate. The differential power needed to maintain zero temperature difference is continuously recorded as a function of T.

Usually, when the main sample undergoes a phase change, more or less heat will need to flow to it to maintain both samples at the same temperature. The amount of heat that flows to it depends on the nature of the transition i.e. whether it is exothermic or endothermic. This differential electrical power required to maintain the same temperature in both cells enables the heat absorption or release from the sample to be determined and after normalisation by scanning rate, yields the difference in heat capacity between the two cells. DSC is also typically used to observe more subtle phase changes, such as glass transitions in materials.

4.3.1 DSC measurements and data analysis

DSC results are typically plotted as a curve of heat flux (with units of μJ/s or μcal/s) as a function of temperature or time. Depending on the specific technology used exothermic or endothermic reactions in the sample are illustrated as a positive or negative peak in the plot respectively. The area under the exothermic peak can be used to calculate enthalpies of transitions $\Delta H = KA$, where ΔH is the enthalpy of transition, K is the calorimetric constant, and A is the area under the curve. The calorimetric constant will vary from instrument to instrument, and can be determined by analysing a well-characterized sample with known enthalpies of transition [150]. On the other hand, the endothermic peak is used to determine melting points of materials.

The DSC measurements for this study were taken using *Netzsch DSC 200, F3 Maia*, at a heating rate of 1° min^{-1} and nitrogen was used as the purge gas with a flow rate of 20 ml min^{-1}. The reference was an empty aluminium pan calibrated previously. The calorimetric constant was calibrated into this instrument, thus, the enthalpy of transitions could simply be obtained from the area under DSC plot. The sample analysed was placed in another bucket.

The DSC was specifically used to look at phase transitions in composite AB-PS fibres; the temperatures at which reactions took place (corresponding to hydrogen release) and the enthalpies of these reactions. Neat AB powder and pure PS fibres and pellets were also analysed for comparison. Since the mass loss in the sample is associated with the exothermic events in the data, the DSC data was compared to the TGA data for samples heated at the same rate. The amount of sample used for DSC (~ 5-10 mg), was typically 10% of the sample used for the IGA by weight.

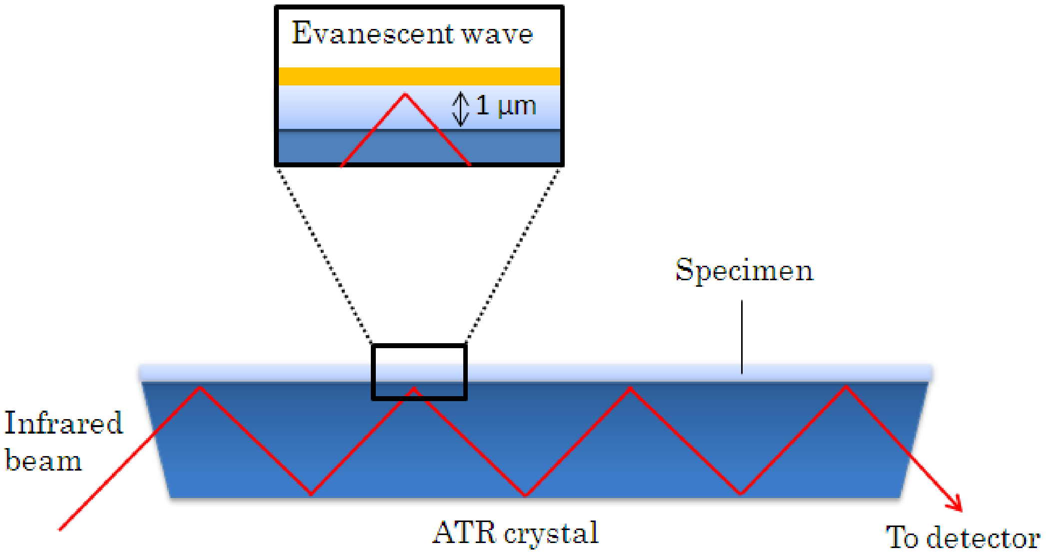

Figure 4.5: Evanescent wave penetrating in the specimen placed in close contact with ATR crystal.

4.4 ATR-FTIR

Fourier Transform Infrared Spectroscopy (FTIR) is one of the most powerful techniques used for identifying the types of bonds (functional groups) in both organic and inorganic compounds. In this study we have used attenuated total reflectance (ATR)-FTIR to identify the chemicals present in the composite AB-PS fibres, both prior to and after thermolysis of the samples. A schematic diagram of an ATR-FTIR is shown in Figure 4.5. The infrared (IR) beam from the spectorometer is passed through an IR transmitting crystal with a high refractive index, typically a silicon or glass prism, which allows the IR radiation to be reflected internally (usually several times) at the surface. On reflection, the IR beam penetrates the immediate environment above the prism, where the sample is placed in close contact with the prism, via the so called “evanescent” wave. The penetration depth of the beam, as determined by its wavelength and refractive index of the prism, is usually of the order of a micron or so [23].

On its final internal reflection the beam is directed out of the crystal into the detector.

The resulting data, obtained from Fourier transformation (FT) of the output wave, is a single beam spectrum of intensity versus wavenumber (in cm^{-1}). From this spectrum the particular vibrational modes of molecules (or functional groups) can be identified. While identification of the vibrational modes of a functional group can be done more easily for common materials using spectra available in spectral libraries, identification of less common materials in a spectrum may be more challenging. The spectra of AB and PS were obtained from ref [151] and [152, 153] respectively.

The ATR-FTIR spectrometer used in this study was a Bruker Optics Vertex 70 FTIR spectrometer with an ATR Diamond/ZnSe diamond prism crystal. The wavelength of the IR beam was λ=15798 cm^{-1} (633 nm) at a resolution of 1 and 4 cm^{-1} with an incidence angle of 45° and a penetration depth of 2 µm. AB-PS fibres were analysed before and after heating to fingerprint the chemical makeup of the as spun fibres and to deduce if any phase change took place after heating or if AB and PS reacted during thermolysis of the fibres. The AB-PS fibres analysed had average diameters ranging from 1-2.5 µm, thus the IR beam could penetrate into most of the fibre cross-section if not all, considering that the fibres were aligned flat along the fibre axis on the ATR crystal.

4.5 X-ray Powder Diffraction

X-ray powder diffraction (XRD) is a common technique used for fingerprinting materials with a crystalline or semi-crytalline structure. The technique is based on measuring the scattered intensity of an X-ray beam from a sample as a function of incident and scattered angle and wavelength (as schematically illustrated in Figure 4.6). The diffraction pattern generated as a function of 2θ provides information on the crystallite size, preferred crystal orientation, preferred orientation in polycrystalline materials as well as the relative abundance of a particular crystallographic phase in heterogeneous solid mixtures. While diffraction pattern is typically compared to data from a database of known materials for specific identification of a given phase, lattice refinement techniques, such as *Rietveld refinement*, can be used to obtain structural information on unknown materials. As this is one of the most common techniques used in the characterisation of materials, many books and sources are available on the physics of X-ray diffraction and interpretation of the diffraction data; for further information the reader is advised to refer to reference [154].

The XRD instrument used in this study was a Siemens D5000 diffractometer with Cu-Kα X-ray source. X-ray diffraction was used extensively in this study to characterise both AB-PS and graphitic nanofibres. A detailed fitting was not made in the case of AB-PS fibres since we were primarily interested in looking for any phase changes in AB and PS in the post electrospinning samples. The data was also used for checking the relative amounts of each species in the sample.

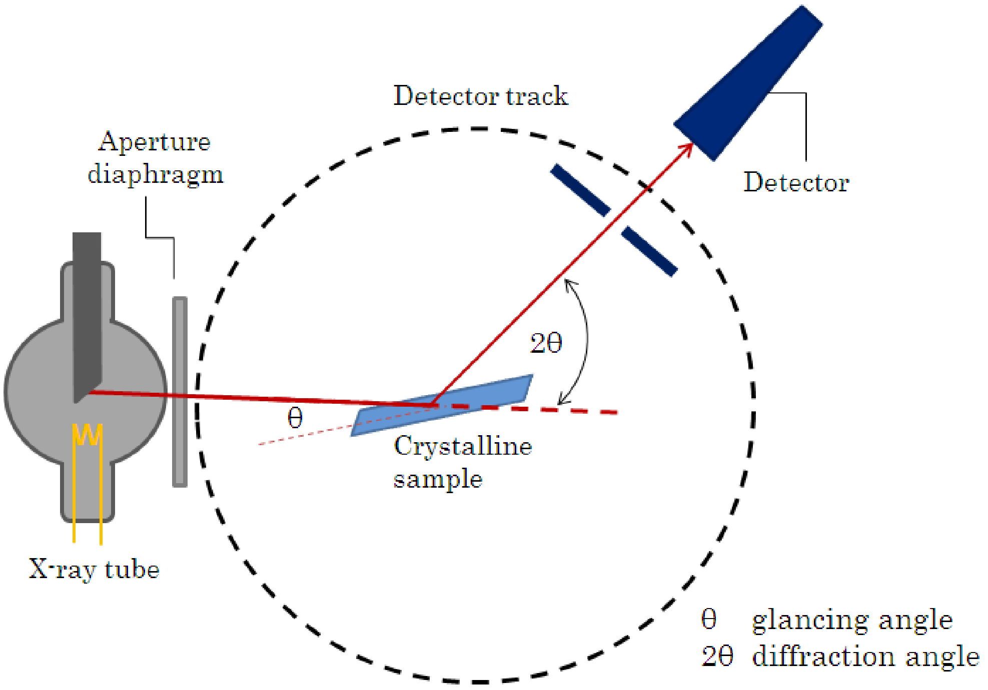

Figure 4.6: Schematic illustration of a powder X-ray diffractomer measuring 2θ.

4.6 Neutron Scattering

4.6.1 Introduction

Neutron scattering is a very important tool for investigating the structure and dynamics of condensed matter systems. This is mainly because neutrons can be moderated to have 'thermal' energies corresponding to a *de Broglie* wavelength in the order of interatomic distances in solids and kinetic energies that are comparable to those of dynamic processes in materials [155]. Thus, elastically scattered neutrons can be used to deduce the structure of crystalline materials and their amorphous component, if any. Since their kinetic energies (typically in the range 5-100 meV) are similar to excitations in condensed mater systems, the momentum change undergone by a neutron in an inelastic neutron scattering (INS) event can be used to measure the dynamics of atoms or molecules in materials; phenomena such as phonon states, diffusion and tunnelling can be measured.

Neutron scattering is in fact the most powerful tool for characterising the behaviour of hydrogen in materials and for studying the structural changes that take place in materials during hydrogen uptake. There are several reasons for why this technique is better than other scattering techniques such as electron or X-ray scattering for studying hydrogen. Firstly, hydrogen has the largest interaction cross-section with neutrons, higher than all other elements in the periodic table (the concept of neutron cross-sections is discussed in section §4.6.2.) Neutrons are scattered by nuclear forces and thus the scattering cross-section has no systematic dependence on the atomic number Z, unlike X-rays which have a scattering cross-section that varies with Z^2. This scattering strength is such that even in a carbon adsorbent containing only 1wt.% hydrogen, more than half of the neutron scattering comes from the hydrogen. Also, the 'scattering length' which defines the strength of the interaction (as discussed in the next section) can vary between isotopes of an atom, allowing for chemical labelling of a particular type of species, such that atoms of the same kind in different materials or compounds can be differentiated through substitution of the isotope of a given species. In the case of isotopes of hydrogen, deuterium is typically used to differentiate between the hydrogen already present in the system and that loaded during neutron studies (or vice versa). Secondly, compared to electrons or X-rays, neutrons interact weakly with matter. Since neutrons have mass and no charge, they can penetrate beyond the surface of the material to give information about both the bulk structure and the dynamics of the atoms (or molecules) in the material. Furthermore, even though certain materials undergo ionisation and remain radioactive for a short while after experiment, neutron scattering is typically non-destructive.

In this section I will briefly outline some of the fundamental concepts of neutron scattering to show how it is used for extracting information from materials. I will not provide a detailed mathematical explanation of these concepts; instead I refer the reader to ref. [156] for further reading on the subject. I will then a give a brief description of the neutron scattering techniques and instruments used in this study to look at the structure and dynamics of hydrogen in potassium intercalated graphitic nanofibres (KC_{24} nanofibres).

4.6.2 Theory

Upon scattering from materials neutrons can transfer energy and momentum to the scattering sample. Depending on whether the scattering is elastic or inelastic, and coherent or incoherent, information on the structure and dynamics of the species in the sample can be obtained. These concepts are discussed in some detail below. The main principle of neutron scattering is simply explained in terms of scattering of a quantum particle, which exhibits wave phenomena, from a fixed nucleus. In this regime the energy E_n of the neutron travelling in space is defined by:

$$E_n = \frac{\mathbf{p}^2}{2m_n}, \tag{4.1}$$

where m_n neutron mass and $\mathbf{p}$ is its momentum. Using the de Broglie relationship the momentum is defined as

$$\mathbf{p} = \hbar\mathbf{k}, \tag{4.2}$$

where k is the wavevector, the magnitude of which is given by

$$|\mathbf{k}| = \frac{2\pi}{\lambda} \tag{4.3}$$

In a scattering event the momentum transfer vector **Q** is typically used to determine the magnitude and direction of the interaction. As illustrated in Figure 4.7, the momentum transfer **Q,** which depends on both the scattering angle and the energy transfer, varies depending on whether the scattering is inelastic or elastic. In the case when scattering is inelastic, i.e. energy is gained or lost by the neutron (Figure 4.7 (a)), the overall energy and momentum transfer is respectively given by:

$$\hbar\omega = E_n - E_n' = \frac{\hbar^2}{2m_n}(k^2 - k'^2) \tag{4.4}$$

and

$$\hbar\mathbf{Q} = \hbar\mathbf{k} - \hbar\mathbf{k}' \tag{4.5}$$

where E_n and E_n' are the initial and final energies of the neutron repectively, **Q** is the momentum transfer vector, m_n is the neutron mass, **k** and **k'** the incident and final neutron wavevectors. Alternatively, in the case when the scattering is elastic, i.e. when no energy is exchanged between the sample and the neutron (Figure 4.7 (b)), the magnitude of **Q** is given by:

$$Q = \frac{4\pi \, sin\theta}{\lambda} \tag{4.6}$$

The direction of **Q** with respect to the sample orientation is important for samples with preferred orientation, since information on structure is gathered along **Q**. Thus it is important to have the sample placed in its position in the correct geometry. Since the fibres were randomly aligned in all directions, the sample geometry was not an issue in looking at KC_{24} nanofibres.

(a) Inelastic scattering (k' ≠ k)

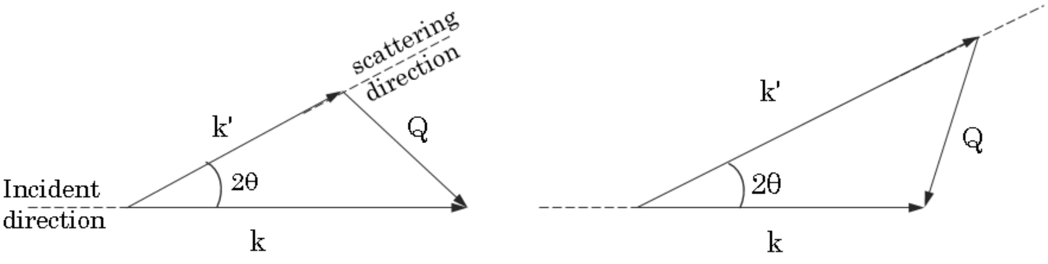

Neutron loses energy (k'<k) Neutron gains energy (k'>k)

(b) Elastic scattering (k' = k)

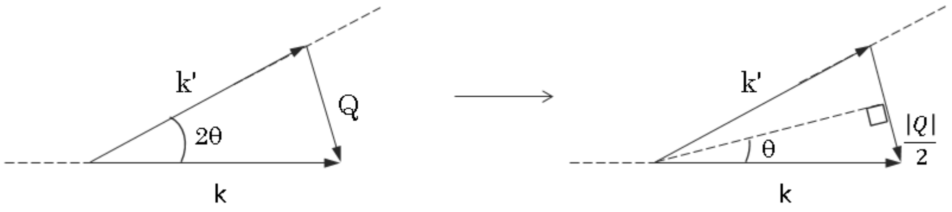

Figure 4.7: Scattering triangles depicted for (a) inelastic scattering and (b) elastic scattering events.

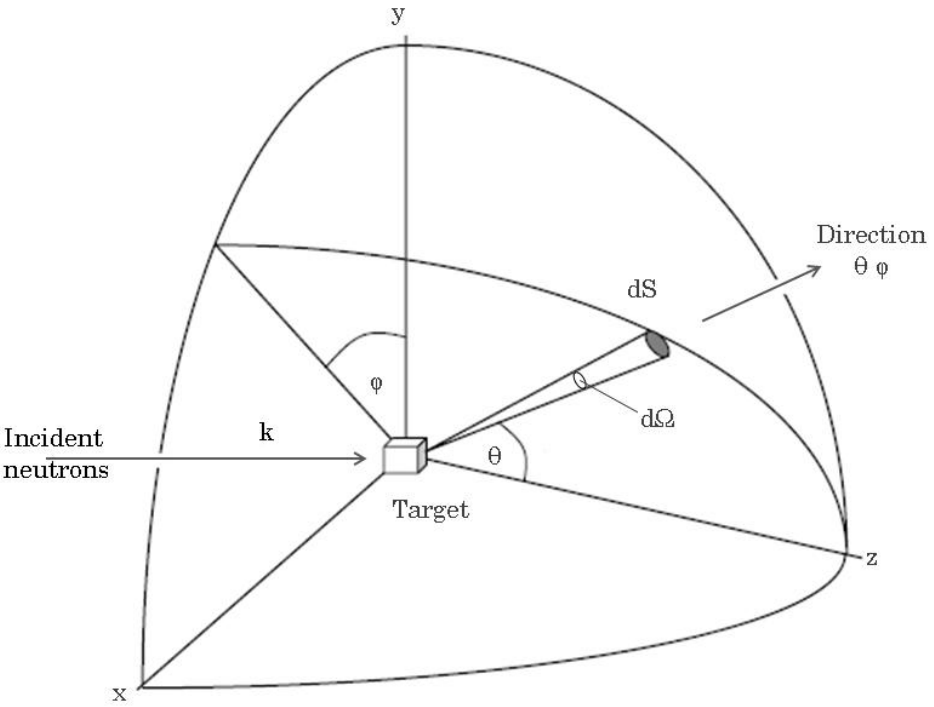

Figure 4.8: Geometry for a typical scattering experiment [156].

The quantity that is directly measured in a neutron scattering experiment is called the partial differential cross-section. It quantifies the fraction of neutrons with incident energy E scattered per second into a small solid angle $d\Omega$ in the direction θ, φ with final energy E' and $E'+dE'$. It is defined by

$$\frac{d^2\sigma}{d\Omega dE'} = \frac{N_{d\Omega dE'}}{\Phi d\Omega dE} \tag{4.7}$$

where $N_{d\Omega dE'}$ is the number of neutrons scattered per second into a solid angle $d\Omega$ in direction θ, φ with final energy E' and $E'+dE'$, and Φ is the incident neutron flux. Figure 4.8 shows the geometry of a typical scattering experiment, in which these parameters are diagrammatically defined. The total scattering cross-section, which accounts for total number of neutrons scattered in all directions per second, is given by

$$\sigma = \int dE \int d\Omega \frac{d^2\sigma}{d\Omega dE} = 4\pi b^2 \tag{4.8}$$

where b is the scattering length of the nucleus.

Scattering does not take place from a single nucleus but from system of a large number of scatterers. Even if the system is composed of a single type of species the scattering length b_i of an individual nuclei can differ depending on nuclear spin or isotopic variations between the atoms. This causes coherent or incoherent scattering from the system, the cross-sections for each is respectively given by

$$\sigma_{coh} = 4\pi\langle b\rangle^2 \tag{4.9}$$

$$\sigma_{inc} = 4\pi(\langle b^2\rangle - \langle b\rangle^2) \tag{4.10}$$

Coherent scattering essentially describes the interference of the waves resulting from the scattering of a single nuclei from all the atoms in the system. The intensity of coherently scattered waves, which gives structural information about the system, depends strongly on the scattering angle. *Incoherent scattering*, on the other hand involves the correlations between position of an atom at time zero and the position of the same atom at time t; there is no interference between waves scattered from different nuclei. Thus, it gives information about the position and dynamics of a single atom, whereas as the coherent scattering gives information about the relative position and motions of atoms. Generally, the incoherent intensity is the same for all scattering angles, and thus, it can be ignored when observing diffraction since it just adds intensity to the structureless background. There is no systematic variation of the coherent and incoherent scattering lengths between different elements and isotopes in the periodic table. In the case of hydrogen, the incoherent scattering length is quite large (25.18 fermis) but the coherent scattering length is quite small (–3.74 fermis). But for deuterium the coherent scattering length (6.67 fermis) is larger than the incoherent scattering length (3.99 fermis). This makes deuterium more desirable in diffraction studies.

The van Hove correlation function, $G(\mathbf{r},t)$, which describes how the correlation between two particles evolves with time, is interpreted as being equal to the probability of an atom being located at the origin at time zero and an atom being at position **r** at time *t*. The incoherent scattering function $S_{inc}(\mathbf{Q}, \omega)$ is the Fourier transform in time and space of the van Hove self-correlation function:

$$S_{inc}(\boldsymbol{Q}, \omega) = \frac{1}{2\pi} \iint exp[i(\boldsymbol{Q}.\boldsymbol{r} - \omega t)]\, G_s(\boldsymbol{r}, t) d\boldsymbol{r} dt \tag{4.11}$$

This quantity is measured in an inelastic neutron diffraction experiment through the measurement of the partial differential cross-section as defined by

$$\left(\frac{d^2\sigma}{d\Omega dE'}\right)_{inc} = \frac{\sigma_{inc}}{4\pi\hbar}\frac{k'}{k} S_{inc}(\boldsymbol{Q}, \omega) \tag{4.12}$$

In this representation **Q** and ω are special and temporal frequencies obtained by Fourier transform from the real space variables **r** and *t*. This is why measurements at small Q are sensitive to changes in large characteristics lengths and measurements of small energy loss hω correspond to slow processes.

In this study we have used both elastic scattering (diffraction) and inelastic scattering (INS) to investigate the structure of potassium intercalated graphitic fibres (KC_{24}) and its dynamics during hydrogen loading of the samples. Due to differences in the interaction energies upon scattering and hence differences in the vector momentum transfer, different instrumental set ups are required to extract the necessary information from the sample. All neutron scattering experiments were conducted at ISIS pulsed neutron source in Oxfordshire, UK. Below is a brief description of the type of neutron scattering experiments conducted on the KC_{24} fibres using both elastic and inelastic scattering techniques along with some details of the instruments used for the particular experiments.

4.6.3 Inelastic neutron scattering

Inelastic neutron scattering (INS) is used to measure the dynamics of a system through measurements of the energy transfer spectrum of the neutrons. As described above the quantity extracted from INS experiments is $S_{inc}(Q, \omega)$, as defined by Eq. (4.11). Upon scattering from a system the kinetic energy and momentum vector of the neutrons are changed and as long as the incident energy or final energy is known, the loss or gain in energy of the neutron at the sample can be calculated from the total time of flight. We were specifically interested in looking at the diffusion dynamics and the molecular rotations of hydrogen in KC_{24} fibres during hydrogenation. But this technique can also be used to look at thermal motions and other excitations in the material with energy transfers of up to several hundred meV, depending on the source and instrument set up.

Experiments that involve a small energy transfer are known as quasi-elastic neutron scattering (QENS). QENS looks at excitations very close to E=0 point, which result from those large fraction of neutrons that scatter elastically. Thermal processes lead to broadening of the peak at E=0, which can be qualitatively analysed to obtain the diffusion coefficients of molecules, which is a very useful tool for studying hydrogen diffusion in materials.

A schematic diagram of a typical time-of-flight neutron spectrometer is shown in Figure 4.9. Just as in the start of the diffractometer flight path, the neutrons from the source are moderated and passed through a chopper system to select a specific energy range before being transmitted on to the sample. The neutrons that are scattered from the sample at an angle φ are passed through a crystal analyser to select a single monochromatic energy through Bragg scattering (as described above). These single-energy neutrons are then detected by the detector at the end. The time taken for the monochromitised neutrons to arrive at the detector is compared with the time since the initial neutron pulse left the source. Since the neutron time-of-flight, t_2, over the secondary flightpath, L_2, is known, the time-of-flight over the primary flight-path, t_1, can be calculated to obtain the energy transfer to the sample. On an *S(Q, ω)* vs. *energy transfer* plot the neutron energy loss (that is energy transfer to system) appears on the positive energy transfer scale, and the energy gain (energies transferred from dynamic processes in the system to neutron) appears on the negative energy transfer scale. Inelastic neutron scattering measurements on the KC_{24} fibre samples were carried out using IRIS and TOSCA instruments at the ISIS facility. Details of these instruments are summarised below.

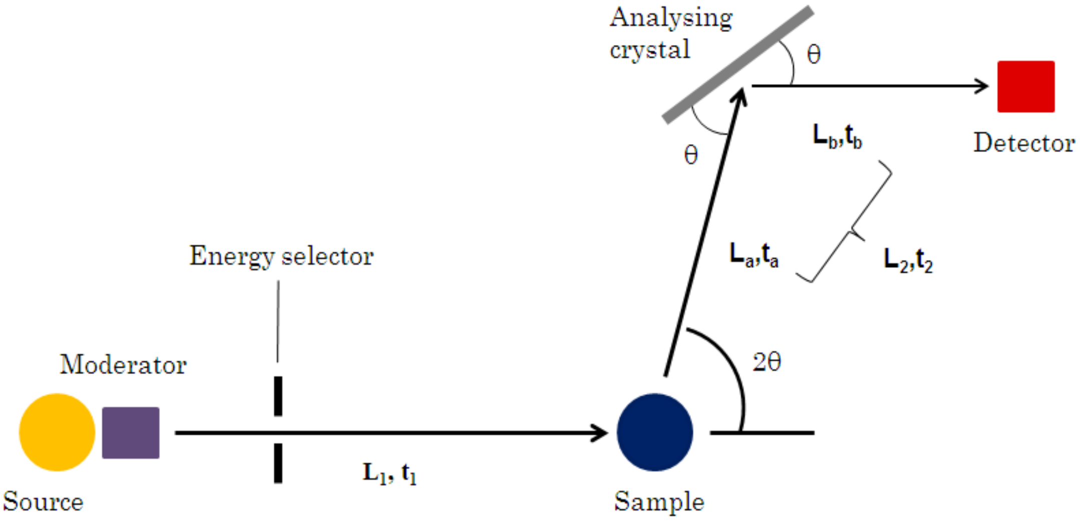

Figure 4.9: Schematic layout of a time-of-flight neutron spectrometer. Incident neutrons that are energy selected scatter inelastically from the sample. Only neutrons that Bragg scatter from the analyser are detected; i.e. the detector collects only neutrons at constant energy and their time of arrival is used to determine the energy loss ΔE in the sample. The primary flight-path$L_1 >> L_2$, the secondary flight-path [48].

4.6.3.1 IRIS

IRIS is a high resolution spectrometer with quasi-elastic and inelastic neutron scattering capabilities and diffraction at long d-spacing. It has a time-of-flight inverted-geometry [157]. Figure 4.10 shows a schematic illustration of IRIS instrument set up. The neutrons scattered off the sample are energy analysed using one of the two single crystal analysers available (pyrolytic graphite and muscovite mica) in close to backscattering geometry. Thus the data can be collected in two separate energy windows -0.8 – 2.0 meV (1st energy window using the PG 002 analyser and a chopper frequency of 25 Hz giving an energy resolution of 15 μeV) and 0 – 20 meV (2nd energy window). The neutrons are then counted by a set of 51 ZnS scintillator detectors associated with each analyser bank in the semicircle geometry. These analysers, which can be operated simultaneously, enable high resolution over wide energy and momentum transfer ranges. Also, the graphite analyser can be cooled to liquid He temperature to reduce background contributions from thermal diffuse scattering. The diffraction capability of the instrument, which ranges from 1-12 Å, allows for the collection of structural data simultaneously with the dynamical data. A 25 K beryllium filter is also available for extending the accessible energy transfer range when the graphite analyser is used. The sample environment allows for the use of a thermal sensors and standard orange cryostat [48].

The IRIS spectrometer was specifically selected to do low-energy inelastic neutron scattering (INS) and quasi-elastic neutron scattering (QENS) on the potassium intercalated graphitic nanofibres (K-GNFs) so that we could study both the dynamics and diffusion properties of hydrogen adsorbed in the nanostructured KC_{24} fibres and compare it to the results for KC_{24} synthesised from bulk papyex carbon from ref [48]. Good resolution close to the elastic line and sensitivity to hydrogen made IRIS a natural choice for this work.

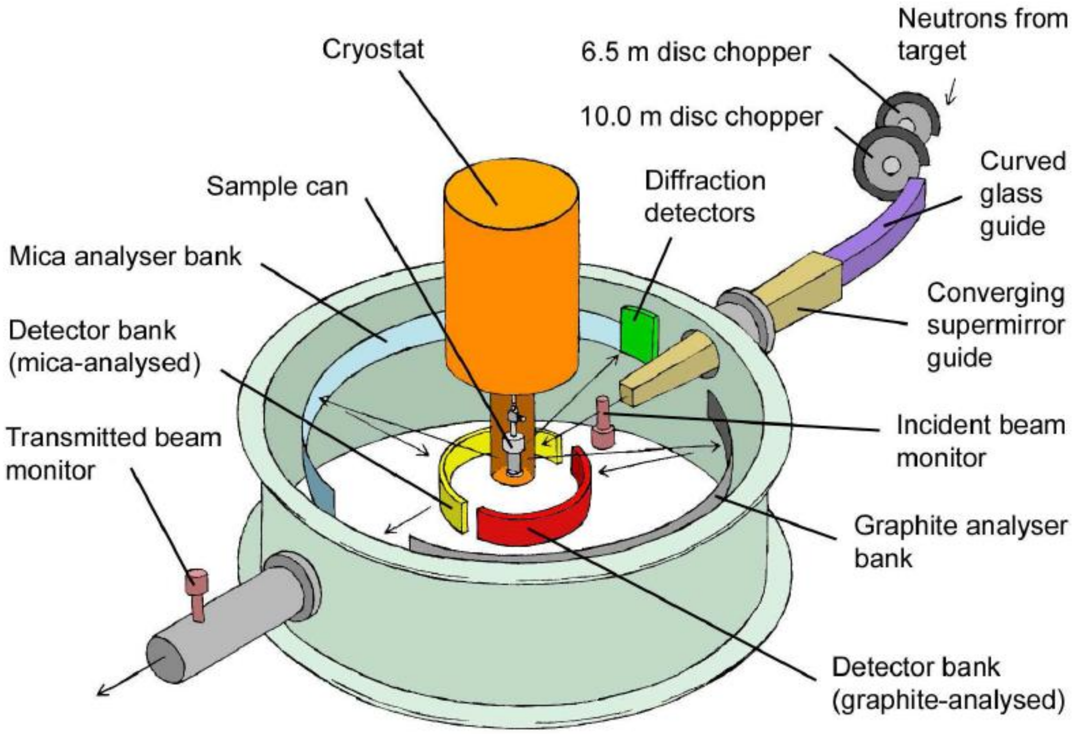

Figure 4.10: Schematic illustration of the IRIS neutron spectrometer [48].

4.6.3.2 TOSCA

TOSCA is an indirect geometry spectrometer designed for inelastic neutron scattering only [158]. It is optimised for the study of molecular vibrations in the solid state, with an energy transfer range 0-500 meV, but best resolution is below 250 meV [48]. This instrument (Figure 4.11) was used to look at the H_2 dynamics over a much larger energy range than was accessible with IRIS, but with lower energy resolution. TOSCA has a Nimonic chopper which reduces the fast neutron background and a tailcutting absorber on the leading edge that suppresses slow neutrons and prevents frame overlap. It has two banks of detectors arranged annularly, which detect neutrons scattered both forward and backwards from the sample. Neutrons scattered off the sample are incident on a graphite analyser at angles of 45 and 135°. The analyser selects certain wavelengths and transmits these neutrons through a cooled beryllium filter to ^{3}He detector tubes.

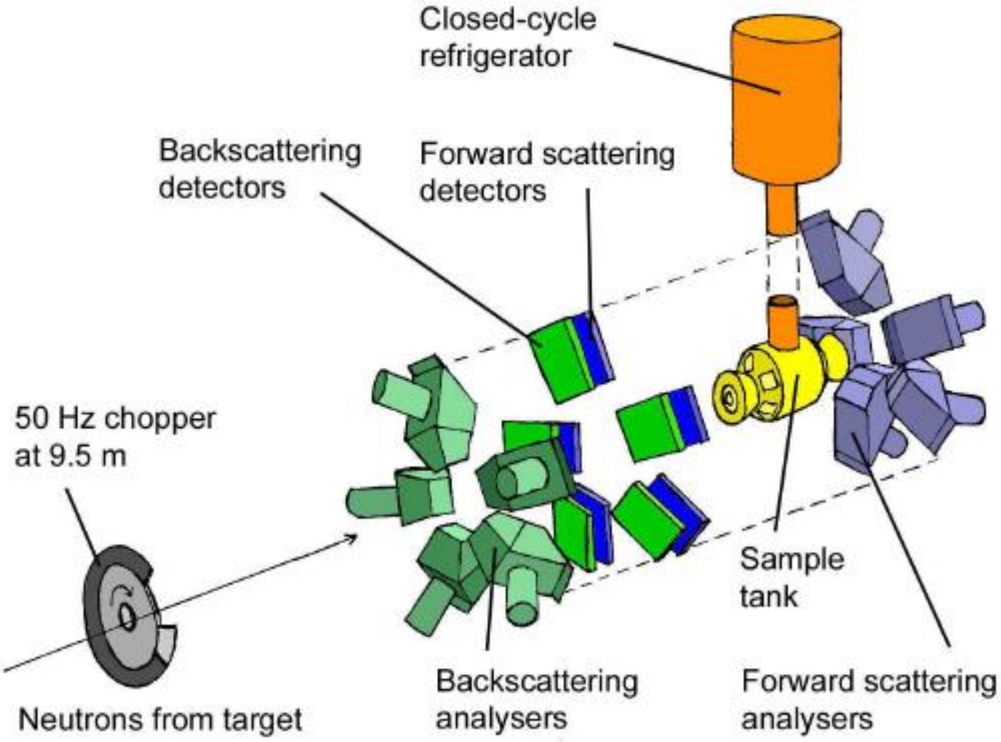

Figure 4.11: Exploded schematic diagram of TOSCA layout [158].

4.6.4 Neutron diffraction

Diffraction experiments are analysed only as a function of Q (i.e. momentum transfer and not energy transfer).Thus, the instrument is set up so the detectors integrate over all energy transfers. This means the diffraction picture is an ensemble average of the material for t = 0. The momentum transfer is used to obtain structural information about the crystalline sample analysed, i.e. to obtain the angle of scattering Eq. (4.6), which can be used with Bragg's law to determine the d-spacing.

A schematic diagram of a typical diffractometer set up is shown in Figure 4.12. The neutrons moderated from the source are collimated to select only neutrons with a specific angular range, which are then transmitted on to the sample after traversing a distance of some metres. The incident neutrons diffract at the sample through an angle 2θ and are picked up by the detector. The scattered neutrons arrive at a distribution of times after the initial pulse leaves the moderator and since the scattering is elastic, their final energies can be deduced from the time-of-flight taken, $t_1 + t_2$, over the entire flight-path $L_1 + L_2$. Since only the neutrons with wavelengths satisfying Bragg's law for a set of crystal planes arrive at the detector, a complete diffraction pattern can be assembled from the different energies (wavelengths) arriving at the detector. This is how the diffraction data discussed in §6.5.5 was collected.

We have used the General Materials Diffractometer (GEM) at the ISIS pulsed neutron source (Rutherford Appleton Laboratory) for the diffraction experiment. GEM is a powder diffractometer that can be used to perform high intensity and high resolution experiments for studying structure of disordered materials and crystalline powders. It has an incident flight path L_1=17 metres. The beam incident on the sample has dimensions 40mm x 20mm height to width, and can be changed using a set of adjustable apertures and a beam-scraper. GEM has zinc sulphide scintillator detectors covering a solid angle of ~3.5 steradians, which gives a scattering angle ranging from 1.1° to 169.3°.

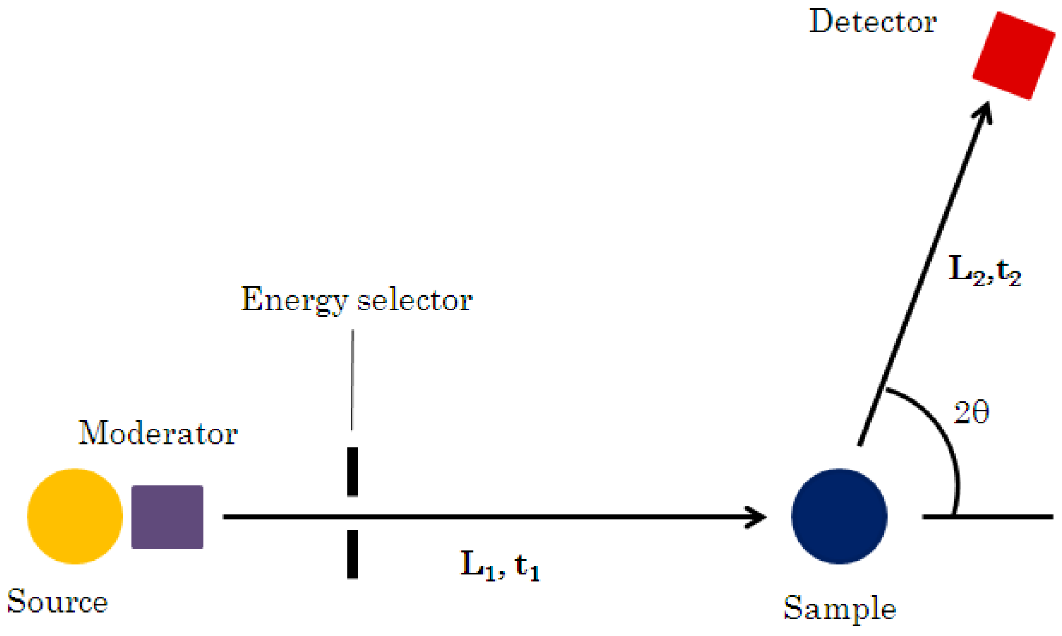

Figure 4.12: Schematic layout of a time-of-flight neutron diffractometer. The Incident neutrons are collimated and selected by energy before being scattered elastically from the sample at an angle 2θ. The scattered neutrons arrive at the detector with a distribution of times, as determined by their energy, which can be calculated from the total time-of-flight t_1+t_2 using the total flight path L_1+L_2. [48].

Chapter 5

Co-electrospun AB-PS Fibres

5.1 Introduction

One of the main aims of this study has been to investigate the possibility of using co-electrospinning as a way of encapsulating chemical hydrides in a polymer sheath, which besides enabling the hydride materials to be nanostructured in a cheap and scalable way it can, if controlled in the right way, provide the benefit of containing the spent materials inside the sheath for regeneration, as well as preventing oxidation of those hydrides reactive in air. Of the many chemical hydrides available (as discussed in §1.4.4) ammonia borane (AB, NH_3BH_3) was chosen as the initial core material, firstly because of its high hydrogen content and secondly because it has a number of properties that make it suitable for co-electrospinning, such as its ease of solubility in many organic and inorganic solvents (e.g. water) and its stability in air; making materials handling significantly less difficult. Polystyrene was selected as the sheathing polymer material primarily due to its permselectivity i.e. good hydrogen permeability (23.8 barrer) and because of its relatively high melting point (240 °C) [159], which had to be significantly higher than that of AB (114 °C) so that it could be heated up to 150 °C to remove AB without degrading the polymer sheath. PS was also considered as a suitable polymer to be electrospun with AB based on its solubility parameters.

The use of co-electrospinning for hydrogen storage applications, specifically for encapsulating and nanostructuring hydrides, to our knowledge, has not been reported previously. This study is therefore the first for investigating and identifying some of the problems that may be encountered when co-electrospinning hydrogen storage materials e.g. highly polar (strongly interacting) non-polymeric materials such as AB, which impose severe restrictions on the choice of sheath solutions (materials) that can be used. As described in §3.2, the effect of many of the parameters that control the physical spinning mechanisms of a compound jet are relatively well reported. However, there appears to be a lack of understanding regarding the importance of the interaction between the core and shell solutions (e.g. solution miscibility) for the success of co-electrospinning. I have found that controlling the solution chemistry and the interaction between the two solutions (i.e. compatibility) is highly important for ensuring success of co-electrospinning, especially when a highly polar, non-polymeric material such as AB is used. The selection of solution sets purely on the basis of solubility of the core and shell material in a given solvent (i.e. without a chemical compatibility appraisal) may result in the selection of incompatible core-shell solutions that fail to co-electrospin. Problems such as mixing of core and shell and precipitation of the polymer at the nozzle orifice, due to incompatibility of the solutions, can prevent the synthesis of core-shell fibres, as it was found for some of AB and PS solutions initially tested.

To overcome these challenges the solvent selection method described in §3.3.3 was developed and used for preparation of core and shell solutions for co-electrospinning of AB-PS fibres. To investigate the effect of core-shell solution miscibility on both the success of co-axial electrospinning and the morphology of fibres, we have looked at a range of solutions with varying degrees of miscibility. In doing this we were aiming to find out the importance of core-shell solution miscibility and settle the uncertainty surrounding this. The fibres produced had varying degrees of porosity, depending on the core-shell solution sets used, which appear to affect the dehydrogenation properties of AB differently. The highly porous fibres displayed nanostructured AB characteristics in their thermolysis measurements, while the non-porous fibres did not. To understand how to control the fibre porosity, and hence the nanostructure of the fibres, I have developed a theory to explain the kind of porosity observed in some of the fibres based on the jet instability theory of co-axial electrospinning described in §3.2.2.

This chapter is based on the synthesis of composite AB-PS fibres from different core-shell solution combinations and the detailed investigation conducted on their chemical, physical and hydrogenation properties. The first part gives a detailed account of the materials used, ammonia borane (AB) and polystyrene (PS) and provides a detailed explanation for why these particular materials were selected through a more in-depth discussion of their properties. The second part details the experimental process, describing the solution preparation process (including control and optimisation of their properties using the Hansen solubility model and solvent matrix discussed in §3.3.3), the electrospinning set up and process details. The third section is on the morphological and structural analysis of the fibres, with the results presented and discussed on the basis of solution properties and mechanisms that govern co-electrospinning (i.e. the jet instability). The fourth section presents the result on the thermolysis and the hydrogenation characteristics of the AB-PS fibres and provides an assessment on the performance of AB-PS fibres as a potential hydrogen store. Finally, the conclusions are presented with possibilities for future work highlighted.

5.2 Core and sheath materials

5.2.1 Ammonia borane

Ammonia borane (AB), is a donor-acceptor adduct formed as a result of a dative bond between a Lewis acid (BH_3) and a Lewis base (NH_3), in which the lone electron pair of NH_3 delocalises over an unoccupied p_z orbital of boron in BH_3. It is a white crystalline solid with chemical formula NH_3BH_3. The strong B–N bond results in hydrogen loss being favoured over the dissociation to ammonia and borane under most heating conditions. AB has attracted a lot of attention as a source of hydrogen fuel as it contains one of the highest total hydrogen densities (19.5 wt.%) of all potential hydrogen storage materials [2, 160], of which up to 2/3 is accessible at temperatures up to 150 °C. In addition, its high volumetric capacity (0.145 kg/L), which is twice that of liquid hydrogen (0.070kg/L), and its stability in air, a prerequisite for a hydrogen generation system, makes it one of the most prominent hydrogen stores available.

Ammonia borane along with its amine-borane adducts, after being synthesised and characterised by Shore and Parry in the 1950s [96], was initially studied as potential rocket fuel [161], an idea that was later abandoned until the late 1990s when Wolf *et al.* [162] realised its potential as a good hydrogen storage medium for fuel cell applications. What makes this molecule particularly interesting is its bonding structure; while it adopts a molecular structure like ethane (C_2H_4), which is a gas at room temperature, NH_3BH_3 constitutes a structure that makes it solid at ambient conditions. The short intermolecular contacts it exhibits due to the protic N–H and hydridic B–H bonds creates a network of $N{-}H\delta^{+}\cdots{}^{-}\delta H{-}B$ dihydrogen bonds with a separation of 2.02 Å, a value less than the sum of Van der Waals radii of hydrogen (2.4 A°) [93, 163, 164]. This somewhat unusual nature of bonding (between the proton and hydride) is conferred to be the reason for its stability (ca. 90.4 kJ/mol) [165] and its comparatively high melting point (112-114 °C) [166] compared to its isoelectronic counterpart ethane (-181.3 °C) [167].

Knowledge of the solid state structure of AB at different temperatures is particularly important for gaining an understanding of its thermal behaviour (i.e. decomposition temperatures and (de)hydrogenation kinetics) and possible mechanisms for regeneration of its decomposition products back to AB. In this respect many studies have been carried out using different analysis techniques, including spectroscopy (nuclear magnetic resonance (NMR), infrared and Raman spectroscopy), diffraction (X-ray crystallography) and scattering (inelastic or quasielastic neutron scattering).

For the purpose of this investigation, in this section I will primarily focus on the structure of AB and thermal decomposition properties in its solid state, as a way of understanding the dehydrogenation mechanism of neat (bulk) and nanostructured AB. For a more detailed consideration of the work that has been conducted on AB through the use of above-mentioned techniques the reader is directed to a recently published review by Staubitz *et al.* [166], which gives a succinct account of all the work that has been conducted on "ammonia borane and related compounds as dihydrogen sources" up until 2010.

5.2.1.1 Crystal structure of ammonia borane

The structure of ammonia borane has been investigated by several groups since its discovery in 1955 by Shore and Parry [168]. In 1956, Hughes determined a body-centre tetragonal cell at room temperature, and proposed the polar space group (I4mm), where the NH_3BH_3 molecules are located at the vertices and the centre of the unit cell. In a subsequent study by Lippert and Lipscomb [169] these results were confirmed, but neither of these studies could locate the hydrogen atoms. In a more detailed study on the crystal structure of AB, Hoon and Reynhardt, using powder X-ray [170] found that at low temperatures the structure is an orthorhombic (space group $Pmn2_1$), with the transition between the orthorhombic and tetragonal phase taking place at around 220 K [164].

Single crystal X-ray studies on the orthorhombic phase of ammonia-borane enabled H positions to be determined, enabling the di-hydrogen bond separation to be ascertained [93, 164]. The results from these studies, which also showed the nitrogen and boron atom positions to be reversed, were subsequently verified through neutron powder diffraction of fully deuterated ammonia borane (ND_3BD_3) [171, 172]. The neutron data also enabled the molecular orientations to be more precisely assigned. Hess *et al.* [171] looked at the structural changes in AB over a temperature range of 15-340 K and found that with increasing temperature the AB molecules rotate about the B-N bond, with N being the pivotal point, while the crystal lattice contracts along the *a*-axis and expands along the *b*-axis, resulting in the tetragonal phase (see Figure 5.1). The results also showed that both phases contained two molecules of NH_3BH_3 with B-N bonds aligned parallel to the *c*-axis in each phase. In the orthorhombic $Pmn2_1$ phase the B-N bonds were found to be inclined toward the *c*-axis (Figure 5.1 (a)), where as in the tetragonal *I4mm* structure they were aligned parallel to the 4-fold *c*-axis (Figure 5.1 (b)). These results, which are supported by *ab initio* molecular dynamic simulations, also show that hydrogen bonding is significantly reduced in the tetragonal phase, even though intramolecular geometry is unchanged, which could explain the loss of hydrogen with further increase in temperature.

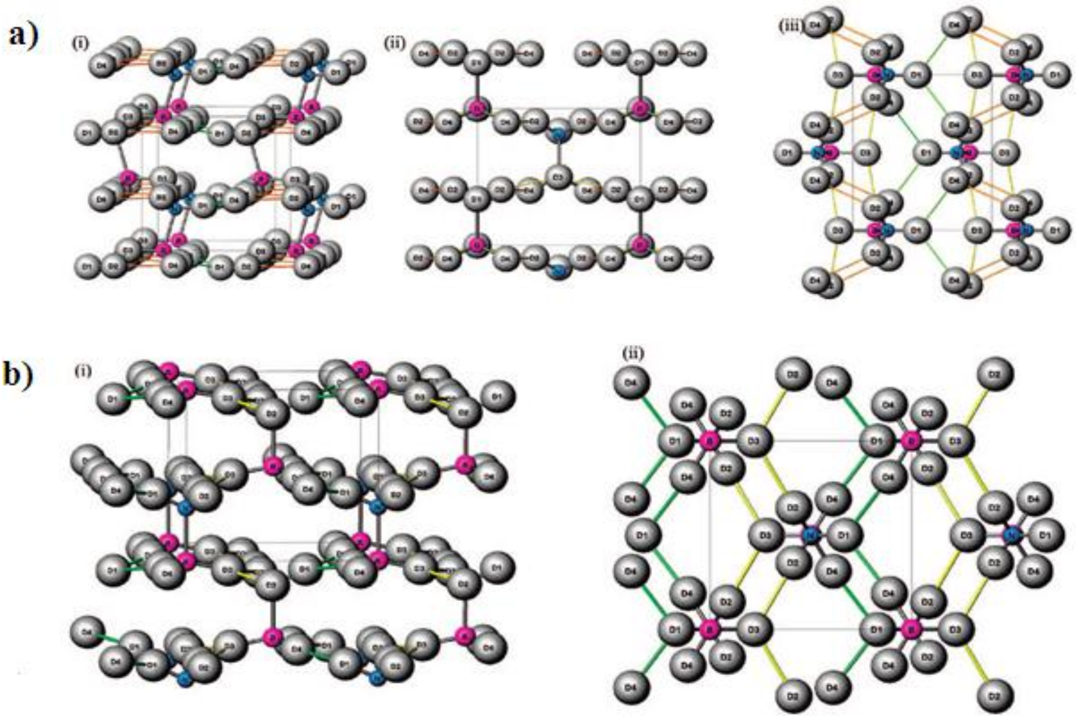

Figure 5.1: (a) Crystal structure at 15 K (orthorhombic). The dihydrogen bonding network is shown: D2 ··· D3, yellow; D2 ···D4, orange; D1 ··· D4, green. (i) b-c plane; (ii) a-c plane; (iii) a-b plane. (b) One of four possible orientations of AB in the tetragonal phase at 240 K including the dihydrogen bonding network D2 ···D3 (yellow) and D1 ···D4 (green), (i) a-c plane; (ii) a-a plane [171].

5.2.1.2 Thermal decomposition of ammonia borane

Ammonia borane releases H_2 upon heating; two of the three H_2 moles available (12 wt.%) can be obtained through heating up to 150 °C, which exceeds the stringent gravimetric hydrogen storage target of 7.5 wt% H_2 ultimately required [173]. Although the overall reaction is exothermic, external heating is required to overcome kinetic barriers, but once the compound is heated to a sufficiently high temperature the decomposition reaction proceeds on its own. The stepwise thermolysis process is summarised in equations (5.1) through (5.4):

$$nNH_3BH_3 \rightarrow (NH_2BH_2)_n + (n-1)H_2 \tag{5.1}$$

$$(NH_2BH_2)_n \rightarrow (NHBH)_n + H_2 \tag{5.2}$$

$$2(NHBH)_n \rightarrow (NHB-NBH)_n + H_2 + \text{borazine} + \text{other products} \tag{5.3}$$

$$(NHBH)_n \rightarrow BN + H_2 \tag{5.4}$$

The first reaction (Eq. (5.1)) occurs around a peak temperature of 110 °C (depending on heating rate) near the melting point (~114 °C) and results in the formation of polyaminoborane -(NH_2BH_2)n- [174]; the second reaction (Eq. (5.2)) occurs at around 150 °C, concurrent with the formation of polyimidoborane -(NHBH)- and the emission of borazine (c-$(NHBH)_3$) and diborane ($(BH_3)_2$ or B_2H_6), either of which can poison the fuel cell membrane [160, 174]. At a slightly higher temperature the cross-linking between NHB–NBH molecules is observed to release additional hydrogen (Eq. (5.3)). For the release of the third dihydrogen molecule (Eq. (5.4)), temperatures above 1200 °C are required. While over 12 wt.% of hydrogen is released in the first two decomposition steps [174], the slow speed of the polymerisation reaction results in a delay of many minutes before hydrogen is released.

A number of issues can be highlighted in this decomposition process. First of all, the hydrogen release temperatures are still above the fuel cell operation range (-40 to 85 °C) and the rate of release below 100 °C is still too low for practical applications. Additionally the small amount of volatiles released (borazine and diborane) pose major risk to the fuel cell and will have to be eliminated in the decomposition process if AB is to be used for fuel cell operation. While these issues are being tackled in various ways, the greatest challenge remains as the regenerability of AB. Since dehydrogenation of ammonia borane results in the formation of polymeric species, regeneration of products back to NH_3BH_3 (e.g. through rehydrogenation) is rather difficult. Despite the large amount of research into to dehydrogenation properties of AB, there has been very little research published on tackling regeneration of AB as of late 2010, some recent references are [175-177]; this highlights the difficulty of the challenge being tackled in regenerating AB. Lowering the thermolysis temperatures to below 80 °C, improving the reaction kinetics and devising an energy efficient chemical process to regenerate NH_3BH_3 from dehydrogenated BNH_x material, are all critical steps toward realisation of AB as a sustainable transportation fuel.

In attempts to overcome these challenges, a number of alternative dehydrogenation processes are being investigated besides solid state thermolysis of neat (pure) AB. These include solution phase thermal decomposition [178-180], catalysis of dehydrogenation process through the use of transition metals [160, 181], additives, ionic liquids [182], Lewis- and Brønsted Acid-Catalyzed dehyrogentaion [183], metal hydrides and amides [184] as well as scaffolding processes that facilitate the dehydrogenation mechanism [185, 186]. The details for these processes can be found in the references cited, with a summary of the results from these studies given in the review by Staubitz and co-workers [166].

Since in this investigation we were predominantly interested in the thermolysis properties of nanostructured AB in the solid state, I will only discuss studies on solid state thermolysis of neat AB and its thermolysis as facilitated by mesoporous silica and carbon cryogels [185, 186]. The encapsulation of AB in mesoporous silica and carbon cryogels has shown improved dehydrogenation properties attributed to the nanostructuring of AB in these materials. The effect of nanostructure on the decomposition process of AB, is clearly important for this particular investigation.

5.2.1.3 Solid-state thermolysis

Thermolysis of neat AB in the solid state yields the maximum gravimetric density of hydrogen, since no additional material weight has to be accounted for as in the case of other thermolysis methods involving the use of other materials as hosts or additives. Geanangel and co-workers (1978) [187] were the first to look at thermal decomposition of neat AB using a variety of techniques including pyrolysis, thermogravimetric analysis (TGA), differential thermal analysis (DTA), and thermomanometry [187, 188]. DTA data taken at heating rates of 2, 5 and 10 °C/min showed the effect of heating rate on the thermal decomposition process, with the reaction temperature moving up to higher values with increasing heating rates. The thermal decomposition reaction was found to be initially endothermic, corresponding to the melting point of solid AB, followed by an exothermic peak as the reaction proceeded in the melt form. At a heating rate of 2 °C/min the melting exotherm had a trough at 114 °C, some 5° lower than that found for 10 °C/min heating rate. The melting point is now typically stated as being in the range 112-114 °C , depending on heating rate [189]. The DTA curves, showing the features more distinctively at lower heating rates, were used to discern the four separate reactions, identified through chemical analysis (IR and mass spectroscopy) of the trapped gas at each decomposition point during pyrolysis of AB.

At the heating rates of 2 °C/min and 10 °C/min the first exothermic reaction peaked at 125 °C and 130 °C respectively; the reaction in the former case had a starting point 30 °C lower than the later. This peak was attributed to the rapid evolution of hydrogen from the molten NH_3BH_3 as shown by the reaction in Eq. (5.1) above. The second peak was associated with hydrogen loss from monomeric aminoborane [NH_2BH_2] (Eq. (5.2)), which begins near 100°C and continues in steps over a broad temperature range with a peak at 155 °C .

In this temperature range NH_2BH_2 rapidly polymerises to form poly(aminoboranes), which then undergo further decomposition releasing additional hydrogen along with borazine and other products (Eq. (5.3)). The loss of the last hydrogen, forming the residual boron-nitride (Eq. (5.4)), was found to require temperatures in excess of 500 C. At a heating rate of 5 °C/min a mass loss of 35% was measured by the TGA with the sample heated up to 200 °C. The authors also reported the foaming and swelling of the mixture during thermal decomposition (as a result of formation and release of volatiles) causing contact to be made with the thermobalance furnace walls, which can be a problem for making measurements of the thermal decomposition of ammonia-borane. These particular findings are important for us, as we have made similar observations, discussed further in the results section below.

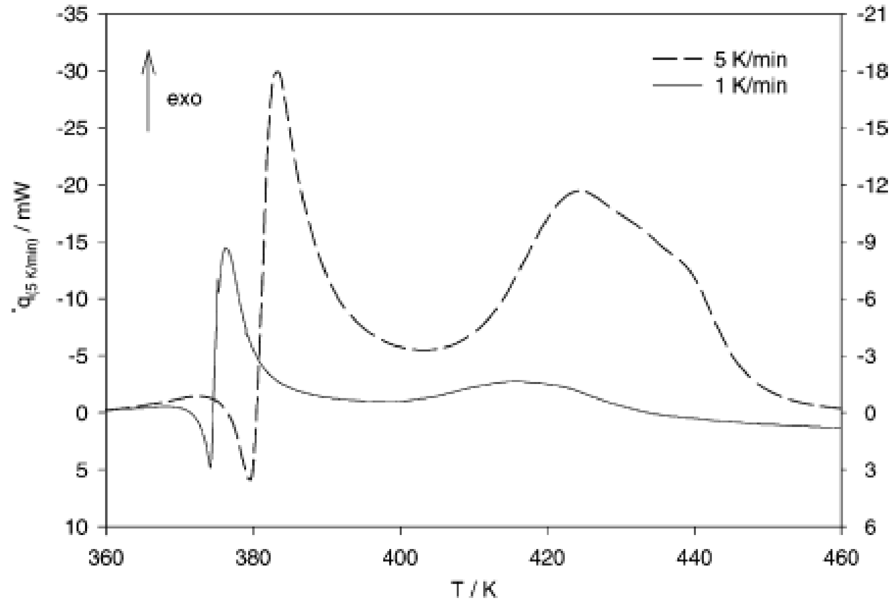

Figure 5.2: DSC curves of thermal decomposition of BH_3NH_3: (—) heating rate 0.05 K/min, (---) heating rate 1 K/min [190].

In more recent studies, Wolf and co-workers [174, 190] have investigated the decomposition process of AB by means of DSC, volumetric measurements, coupled TG/DSC and TG/FTIR, which enabled direct comparison between the methods and isolation of the products throughout the reaction. They have specifically looked at the influence of heating rate on the decomposition process and carried out isothermal studies at a range of temperatures. Their results confirm that the temperature of the first exothermic reaction is reduced with decreasing heating rate and the temperature range of the exotherm corresponding to the reaction is also narrowed down (as shown in

Figure 5.2). At a heating rate of 1 degree/min the exotherm precedes the melt endotherm, which interrupts the exothermic process causing a dip at a temperature few degrees higher than the start of the exotherm at 370 K (97 °C), the exotherm then continues increasing with a maximum at ~378 K (~105 °C), with the second reaction initiated before the first is complete, as represented by the broad peak centred around 415 K (142 °C) overlapped by another peak starting at 125 °C, corresponding to the second reaction releasing H_2, which starts before the second is complete. On the other hand with the heating rate increased to 5 degrees/min, each reaction step is shifted to higher temperatures by approximately 8 degrees and the second peak is much more pronounced (as shown in

Figure 5.2). They have also found that 'given enough time at lower temperatures, the decomposition process of AB is complete before the melt, as shown by the DSC data in Figure 5.3, where AB is heated is heated isothermally at values below 90 °C, showing peak temperatures and intensities lowered with relative reduction in temperature. The enthalpy change at the decomposition of AB (BH_3NH_3), as determined from the isothermal data, was –21.7 ±1.2 kJ/mol, which remained unchanged regardless of the isothermal temperature [190].

Dehydrogenation steps outlined by Geanangel *et al.* Eqs. (5.1)-(5.4) were confirmed with these results. The total amount of H_2 released below 200 °C, which did not change with heating rate, was 2 mol H_2/mol BH_3NH_3, accounting for 14.3 wt.% of AB. The heating rate, however, had a measurable effect on the thermal events and the quantity of volatile products formed. The total mass loss of AB increased from 14 to 33 wt.% when the heating rate was increased from 0.5 to 10 °C/min. The greater mass loss at higher heating rates, which clearly exceeds that caused by the release of hydrogen was attributed to higher quantities of borazine c-$(BHNH)_3$ and diborane B_2H_6 being released at higher heating rates. At low heating rates (1 < °C/min) only H_2 was observed in the gas phase and the major solid product was PAB $(BH_2NH_2)_x$. It is reported that for the complete release of the third mole of dihydrogen, temperatures above 1200 °C are required. The data also suggests the occurrence of simultaneous reactions, such as the simultaneous formation of BH_2NH_2 and borazine, the latter of which is said to form through dehydrogenation of the former above 125 °C to the highly reactive monomeric iminoborane BHNH [22] and the trimerization of BHNH [174]. However, the formation of monomeric aminoborane BH_2NH_2 at temperatures above 125 °C cannot be explained.

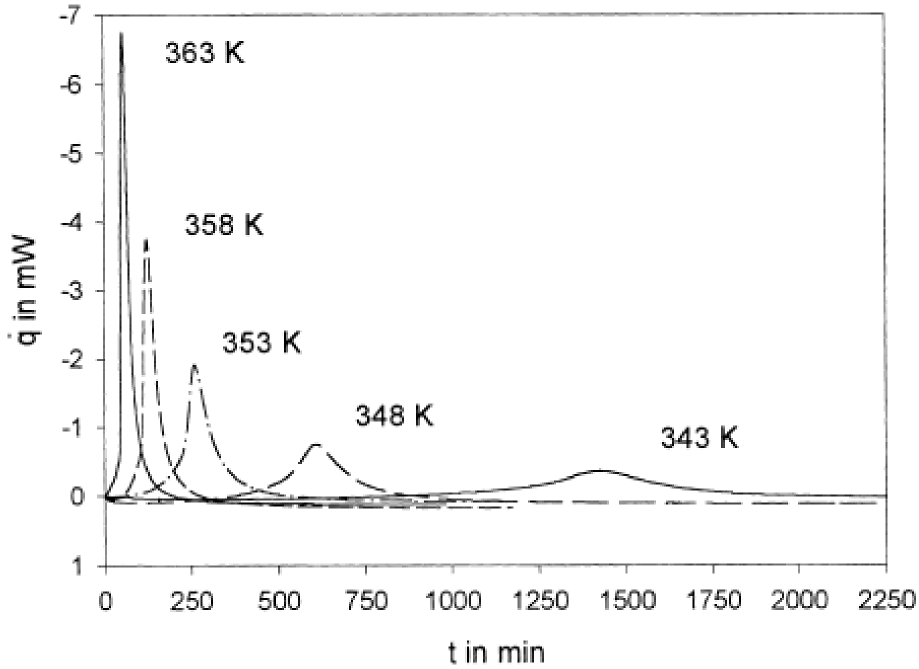

Figure 5.3: DSC curves of thermal decomposition of BH_3NH_3 at isothermal temperatures between 343 and 363 K.

The exact mechanism and the intermediates leading to the release of hydrogen are still not very clear. Gaining fundamental insight into the reaction mechanism can potentially enable control of the hydrogen release rates and the release of those volatiles (e.g. borazine and diborane) that are harmful for the fuel cell. In a recent study Stowe *et al.* [191] provides a much more detailed picture of the decomposition mechanism of AB, using solid state ^{11}B and $^{11}B[1H]$ MAS NMR spectroscopy to follow the reaction in situ under isothermal conditions at 88 °C, a temperature well below the reported melting point (112-114 °C). The authors proposed a mechanism for the thermal dehydrogenation of AB through three distinct steps: induction, nucleation, and growth steps leading to hydrogen release (Figure 5.4).

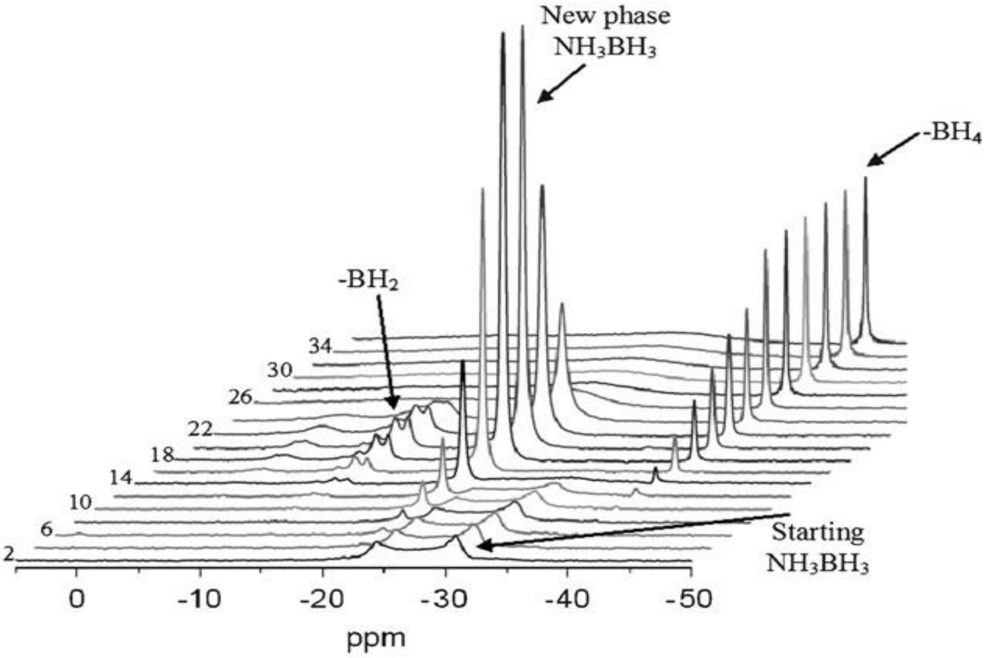

Figure 5.4: Time resolved $^{11}B[^1H]$ MAS-NMR spectra (7.1 T) taken by Stowe *et al.* during thermal dehydrogenation of NH_3BH_3 at 88 °C taken at 2 min intervals from the start of heating. A "new phase" (-23 ppm) is observed just prior to the observation of product $–BH_2$ (-10 to -13 ppm) and $–BH_4$ (-38 ppm) species [191].

Their results suggest that during the induction period, the hydrogen bonding network is disrupted, permitting greater motion of the molecules leading to the formation of a new species containing a BH_3 group resonating at -23 ppm, proposed to be a more mobile phase of AB (AB*). In the subsequent nucleation process, in which hydrogen starts to evolve, diammoniate of diborane (DADB) is generated. DADB then reacts with remaining AB in the growth process to generate $[(NH_3)_2BH_2]+[BH_4]-$, and two BH_2N_2 species, which are thought to emerge from linear ($NH_3BH_2NH_2BH_3$) and the cyclic dimer $(NH_2BH_2)_2$ of aminoborane intermediates, as shown in Figure 5.4. Hydrogen is mostly released through this stepwise bimolecular reaction taking place during the growth process and resulting in the formation of polyaminoborane, as shown in Figure 5.5.

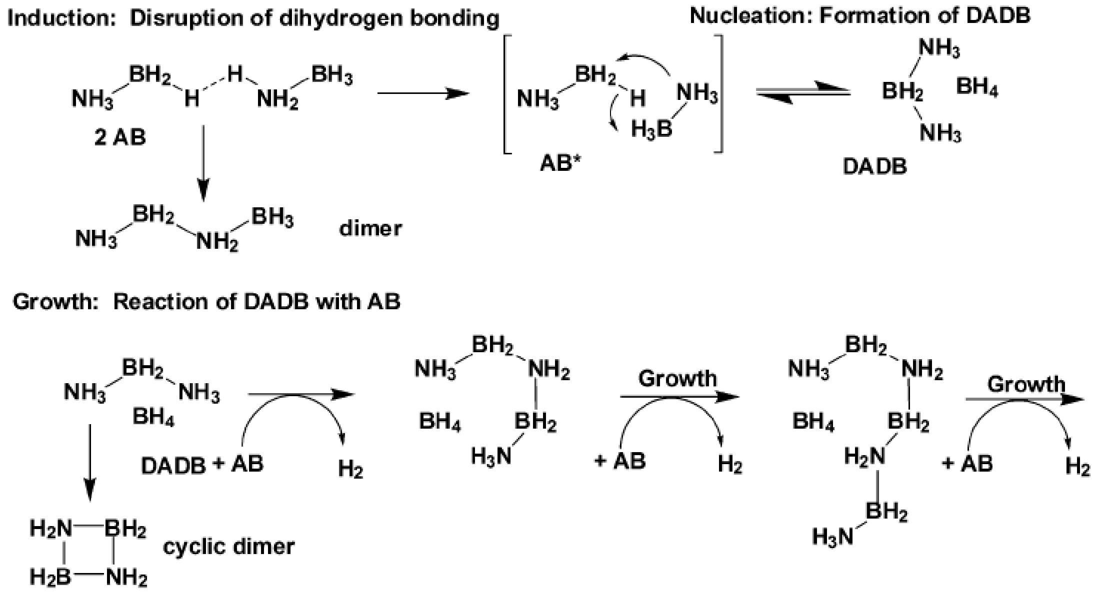

Figure 5.5: The thermal dehydrogenation mechanism of AB (NH_3BH_3) proposed by Stowe *et al.* The induction, nucleation and growth steps leading to hydrogen release are as shown in the reactions [191].

This scheme assumes that the N-H and/or B-H bonds of DADB are more reactive than the corresponding N-H or B-H bonds of ammonia borane. This would thus suggest that the energy barrier for reaction between DADB and AB molecules would be lower than that between two AB molecules. Thus, the addition of DADB to AB should in principle lead to a reduction in the induction period. This was confirmed experimentally by the authors.

Follow up studies using techniques such as TGA/DSC, optical microscopy, and high temperature X-ray powder diffraction, used to examine this process, have provided further evidence in support of this mechanism [192]. In the initial stage, where very little hydrogen was released, an exotherm was observed in the DSC data, at which point it was found that the sample lost crystallinity and birefringence. This was interpreted as a sign for the formation of the new (more mobile) form of AB (*AB) and diammoniate of diborane, $[NH_3BH_2\text{-}NH_3]^+[BH_4]^-$.The phase change was even observed visually when a crystal of ammonia-borane was heated to 90 °C, as shown in see Figure 5.6. From these images, a phase front can clearly be seen traveling through the crystal [193]. When a heated crystal was quench cooled, it was possible to arrest these phases and analyse them by Raman spectroscopy to identify their composition. Before the phase front, the Raman spectrum showed crystalline AB, but closer to the phase front, the peaks broaden significantly, and beyond the phase front a frequency corresponding to a B-H stretching mode was observed which compared well to an authentic sample of DADB. Another insightful observation made in this study was that even under pressures up to 3 GPa, decomposed ammonia borane could not be converted back to neat AB, further highlighting the difficulties in recycling this material.

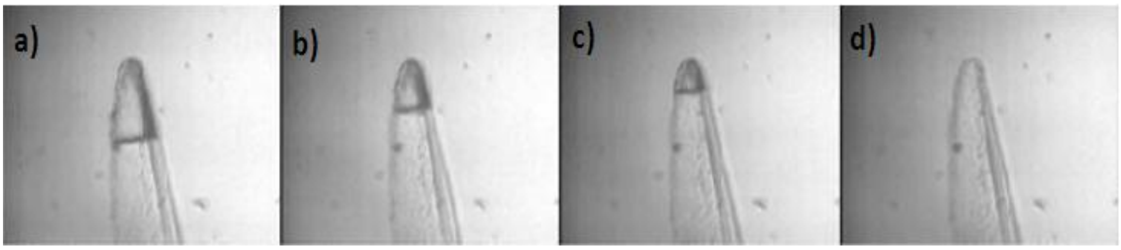

Figure 5.6. Optical micrograph images of a single crystal of NH_3BH_3 heated to 90 °C, images (a) to (e) shows the progression of the phase front in the AB crystal upon the transfer of heat, in (d) the phase transition is complete [193].

5.2.1.4 Hydrogen release from nanophase AB encapsulated in scaffolds

As discussed in §1.5 it has already been demonstrated that in the case of metal hydrides, nanostructuring has the effect of improving (de)hydrogenation kinetics relative to the bulk materials [18]. Gutowska and co-workers [186] have tested this observation in the case of AB, to see if nanostructuring of AB results in improved dehydrogenation characteristics. In respect of this they studied the intercalation of AB in high-surface-area mesoporous silica (SBA-15) scaffold as a model system. For such a nanocomposite of mesoporous silica and ammonia borane in a 1:1 mixture they have made three notable observations. The first of these was the lowering of the activation barrier that resulted in increased H_2 release rates and lowering of the dehydrogenation temperature. This was observed through thermal decomposition of ammonia borane at 50 °C which showed a half-reaction time of 85 min compared 290 min at 80 °C for neat (bulk) AB. This corresponds to a peak dehydrogenation temperature of approximately 98 and 110 °C for AB:SBA-15 and neat AB respectively at a heating rate of 1 °C /min [186].

The second important observation was the reduction in the enthalpy of reaction releasing H_2 ($\Delta H = -1\pm1$ kJ/mol) as measured by the DSC data that showed the loss of hydrogen being significantly less exothermic for the AB:SBA-15 scaffold compared to that of neat AB ($\Delta H =-21\pm1$ kJ/mol). This difference in the enthalpy of dehydrogenation was attributed to a difference in the reaction mechanism that leads to the release of hydrogen and other products. This hypothesis was confirmed by ^{11}B NMR spectra of the volatiles released, which showed only one resonance (at δ=-23ppm) for AB:SBA-15 that was assigned to PAB, but three other boron resonances in addition to PAB was observed in the case of neat AB under the same experimental conditions. The formation of the additional boron-containing products is thought be the reason for higher exothermicity of the dehydrogenation reaction. The reduction in the enthalpy of the hydrogen loss reaction is a very important result in terms of regenerability of AB. As hydrogen loss becomes less exothermic, the reverse reaction; hydrogen uptake, becomes more favourable at a given temperature and pressure. This result has significant implications for the realisation of AB as a regenerable hydrogen source.

The third notable observation in the thermolysis process of AB:SBA-15 was the suppression of borazine release, which was shown by the TPD/MS data to be significantly lower than for neat AB. Solid-state 11B NMR spectroscopy was used to check if the borazine became entrapped within the mesoporous scaffold as a non-volatile product, but no 11B signal was observed for borazine. As borazine is not observed as a volatile or non-volatile product, the authors postulated that the mesoporous scaffold, or the nanostructure, may be affecting the decomposition pathway of AB to suppress borazine production.

In another study, Feaver *et al.* [185] tested the idea of nanoscaffolding of AB in a material with much lower mass and better thermal conductivity than mesoporous silica, carbon cryogel (see Figure 5.7). They have observed an even greater reduction in the decomposition temperature with a 24 wt.% AB encapsulated in carbon cryogel, forming CC-AB composite. It is reported that hydrogen releasing reaction starts at 80 °C, with a broadened decomposition peak centred approximately at 90 °C, with no further decomposition peaks at higher temperatures. Volumetric measurements have shown that approximately 9 wt.% of hydrogen is released from AB in the nanocomposite and no borazine was detected in the mass spectroscopy data. However, the dehydrogenation reaction was found to be significantly more exothermic than neat AB, with an enthalpy of $\Delta H = -120$ kJ/mol.

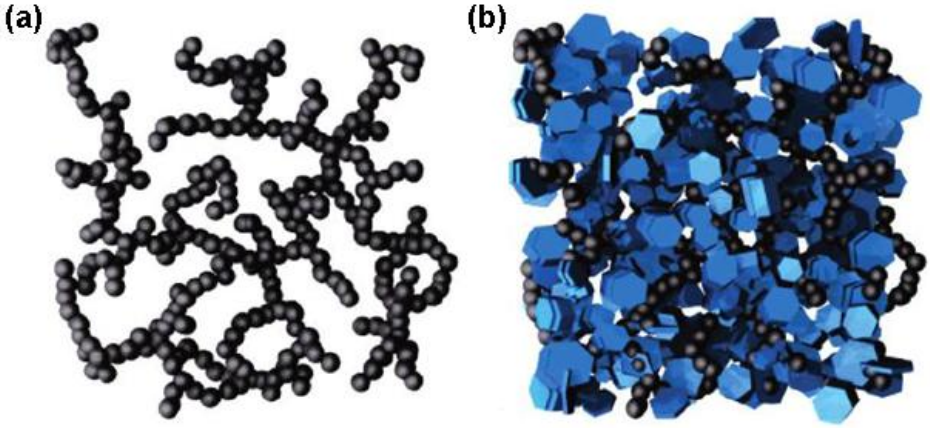

Figure 5.7. Schematic of (a) an unmodified carbon cryogel and (b) a CC-AB nanocomposite as constructed by Feaver *et al*. [185].

The exact mechanism responsible for the observed differences in the dehydrogenation of AB in both mesoporous silica and carbon cryogel is not very clear, but several possible explanations are provided. The observed catalytic effect may be a function of the reduction in AB crystal size, due to nanoscale pores, which is known to lower the phase transition temperature (as discussed below) and thereby presumably the dehydrogenation temperature. The pores in the carbon cryogels range in size from 2 to 20 nm and those in the mesoporous silica have an average diameter of 7.5 nm. Another possible reason for the differences in the dehydrogenation process could be due to the presence of functional groups exposed in the cavities in each material. In the case of AB encapsulated in mesoporous silica, SiO-H groups, and in the case of AB in carbon cryogel, carboxylic acids are considered to have a possible catalytic effect on the dehydrogenation process.

More recent studies have been conducted on materials from the same family with the aim of getting further insight into the decomposition pathways of AB in these particular set of materials. In the case of mesoporous silica, a synchrotron X-ray powder diffraction study on MCM-41 [194] showed suppression of the AB tetragonal-orthorhombic phase transition temperature from 225 K in neat AB to 110 K in MCM-41 [194]. Quasielastic neutron studies looking at the dynamic behaviour of AB in MCM-41 scaffold showed reduced barriers of activation for proton movements, which could possibly contribute to faster dehydrogenation kinetics in the scaffold environment. A later study using ^{129}Xe NMR also suggested possible disturbance of the dihydrogen bonding network in AB at the surface of the mesoporous silica that leads to the formation of diammoniate of diborane [178, 195]. All of which provide further evidence for the manipulative effect of confinement and nanostructuring on the thermolysis behaviour of AB.

In the case of AB incorporated into carbon cryogels, an ^{11}B NMR and FTIR study on the system showed the formation of a new reaction product in the thermal decomposition process of AB in carbon cryogel (CC-AB) nanocomposite [151]. In this case, the new product is thought to have a destabilising effect on AB as a result of the –O–B bond formation, leading to a separate decomposition pathway that is highly exothermic when hydrogen is released. Therefore, even though the exact mechanisms causing the changes seen in the decomposition of AB in these nanocomposites is not directly obvious, encapsulation and nanostructuring of AB in these systems is clearly having an effect on the decomposition pathways and resulting in improved kinetics and reduced decomposition temperatures. However, despite these improvements, it is important to note that these frameworks have high weight density, which means the effective weight % of H_2 stored in them would be lower than desirable. Additionally, regenerability of AB from the decomposition products remains a challenge even in these materials. On the other hand, encapsulation of AB in nanofibres with a light weight polymeric sheath permeable only to hydrogen can enable the decomposition products other than hydrogen to be retained. Therefore, while enabling AB to be nanostructured, the AB-polymer fibres can potentially be reloaded with hydrogen for the regeneration of AB after a thermolysis process. In such a case, the stability and inertness of the polymer sheath will be particularly important for ensuring that no other elements are introduced into the system during the (de)hydrogenation process, or any other point, so that the polymer sheath acts solely as a layer facilitating the regeneration process.

5.2.2 Polystyrene

Polystyrene (PS) is an aromatic polymer, used for many applications due to its low cost, ease of processibility and performance properties. PS was selected as the sheath material for the co-electrospun fibres for a number of reasons. Firstly, the sheath material needs to be a lightweight polymeric material, with a high permselectivity in favour of hydrogen gas, such that all other reaction products are retained in the core while H_2 molecules are released. Secondly it is important for the sheath be stable at temperatures up to ~200 °C, so thermolysis of the AB can take place without decomposition of the sheath. Finally, it is important to use a polymer that is soluble in solvents compatible and immiscible with AB solutions. PS was identified as a suitable polymer on the basis of these requirements, as it has a good H_2 permeability value (23.8 barrer) and a melting point of approximately 240°C [159].

PS is formed of molecular chains of styrene, with strong covalent bonds between the atoms and short range van der Waals attractions between chains. This intermolecular weakness (as opposed to the strong intramolecular bonds) allows the polystyrene chains to slide along each other, rendering the bulk system flexible and stretchable. Malleability of the sheath material is certainly an advantage for ease of shaping the hydrogen storage medium as necessary for the storage system.

Depending on the processing technique polystyrene can come in various different structural forms, the amorphous 'atactic' structure and the crystalline 'isotactic' and 'syndiotactic' molecular structures as determined by ordering of the phenyl groups along the polymer chain; Figure 5.8 compares the molecular structure of these three analogues. In the case of atactic or general purpose polystyrene, the chains form with a random stereochemistry with the large phenyl groups randomly distributed on both sides of the chain. In contrast, the isotactic and syndiotactic forms, which are produced by stereospecific catalysis techniques, have highly ordered structures. This high degree of molecular ordering enables isotactic and syndiotactic PS to crystallise from the melt, with crystalline domains giving rise to a semi-crystalline microstructure [196]. The degree of crystallinity has a large effect on the properties of the polystyrene as in the case of other polymers. Syndiotactic PS, for instance, exhibits performance attributes that are considerably different to the amorphous phase, including higher melting point (~270 °C for syndiotactic-PS compared to ~205 °C for atactic-PS) and much better electrical conductivity [196].

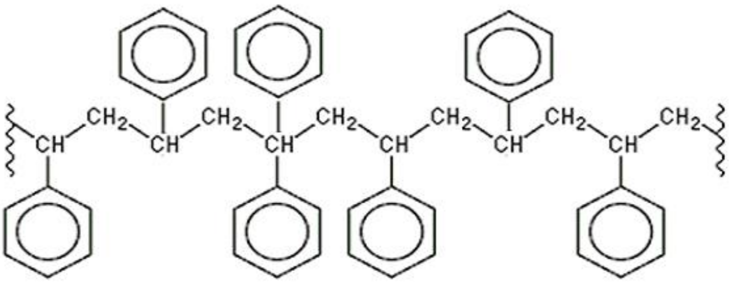

Atactic polystyrene

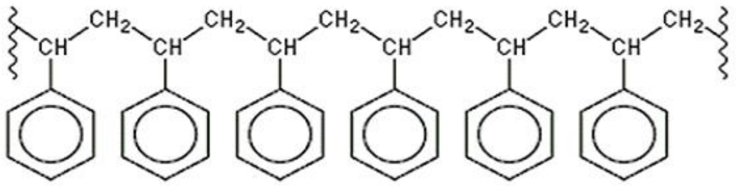

Isotactic polystyrene

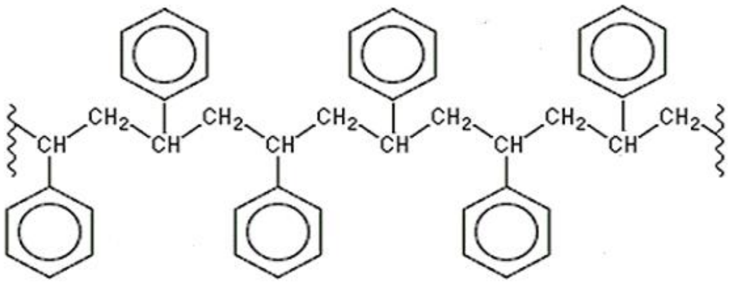

Syndiotactic polystyrene

Figure 5.8: Comparison of chemical structures of atactic, isotactic and syndiotactic polystyrene.

The PS used for this experiment was of general purpose grade obtained from Sigma Aldrich, but other than its molecular weight no information was provided on its structural or physical properties. Powder X-ray diffraction and differential scanning calorimetry (DSC) was used, respectively, to determine its crystallographic composition and melting point prior to and post electrospinning (i.e. that of PS in pellet form and as electrospun fibres). The DSC measurements on the PS pellets and fibres have shown no melting endotherm, a behaviour that is characteristic of amorphous polymers [197]. However, XRD on pure PS and AB-PS fibres have shown the existence of both amorphous and crystalline phases of polystyrene. The crystalline phase was neither identified as isotactic or syndiotactic, but a new crystalline phase was instead found, these results are further discussed in the results section below.

5.3 Experimental Details

5.3.1 Materials: solutes and solvents

Ammonia borane (NH_3BH_3, AB) complex (purity 97%, Sigma Aldrich) was supplied in powder form and polystyrene (PS) (typical $M_w \approx 3.3 \times 10^5$ Daltons, general purpose grade, Sigma Aldrich) was supplied in pellet form. The solvents used were toluene (≥99.5, spectrometric grade, Sigma Aldrich), N,N-dimethylformamide (DMF, 99.0% GC, Riedel-de Haën), dimethyl sulfoxide (DMSO, minimum 99.5%, Sigma Aldrich), 1,2-dichloroethane (DCE, 99+% spectrometric grade, Sigma Aldrich), deionised water and pyridinium formate (PF), an organic salt. PF was prepared by reacting pyridine (99+% spectrometric grade, Sigma Aldrich) and formic acid (99-100%, Riedel-de Haën) in an equimolar amount. All materials detailed were used without further purification.

5.3.2 Solution preparation

The solvent selection process developed (as discussed in §3.3.3) was used for the preparation of the core and shell solutions. The solvents for the core (AB) and shell (PS) solutions were chosen on the basis of creating i) miscible, ii) semi-miscible and iii) immiscible solution combinations. I have specifically tried to optimise the conductivity, viscosity and vapour pressure of the shell solutions as these are parameters that have a strong influence on the success of co-electrospinning and the resultant fibre morphology. However, as it was not always possible to achieve the correct miscibility and the required core and shell solution properties using a single phase solvent in the shell, solvent blends were used to optimise these parameters, as outlined below. The HSPs of selected solvents and their properties controlled for electrospinning are given in Table 4 and Table 5 respectively. A pictorial representation of the HSPs of the solvents and solvent blends is given in the 2-D Hansen solubility plot of PS (Figure 5.9). Both the RED values in Table 4 and Hansen solubility circle in Figure 5.9 was used when determining the degree of miscibility of solvents and solvent blends (as described in §3.3.3)

The electrical conductivity of shell solutions was increased through the addition of salts to solvents with a dielectric constant high enough to allow dissolution of salts. It was discussed in §2.6.1.4 that salt dissolution in solvents decreases with decreasing dielectric constant of solvent, so it is important to select solvents with high dielectric constants if salts are to be used for increasing the electrical conductivity of solutions. Despite all efforts, it was not possible to obtain a shell solution with electrical conductivity higher than that of the core. This is because dissolution of AB, which is highly polar, results in highly conducting solutions. Whereas the addition of PS was found to reduce the conductivity of the selected shell solvent blends, which were mostly composed of low conductivity and low dielectric constant solvents.

Controlling the vapour pressure of the core and shell solution sets was less straightforward, due to the large differences in the vapour pressures of the selected solvents. It was important to use core and shell solvents with similar vapour pressures to prevent fibre buckling (which was discussed in §3.2.3.4). Equalising the vapour pressure of the core and shell solutions was particularly difficult for the preparation of immiscible core-shell solutions due to the limited number of solvents identified as being immiscible as well as compatible (i.e. suitable) as solvents for AB and PS. Nitrobenzene (NB) was identified as the solvent with the highest dielectric constant and boiling point (i.e. lowest vapour pressure) (see Appendix A) of those that reside in the Hansen sphere of PS (Figure 5.9). This solvent enabled the formation of the optimal shell solution for electrospinning non-porous core-shell fibres, as described below.

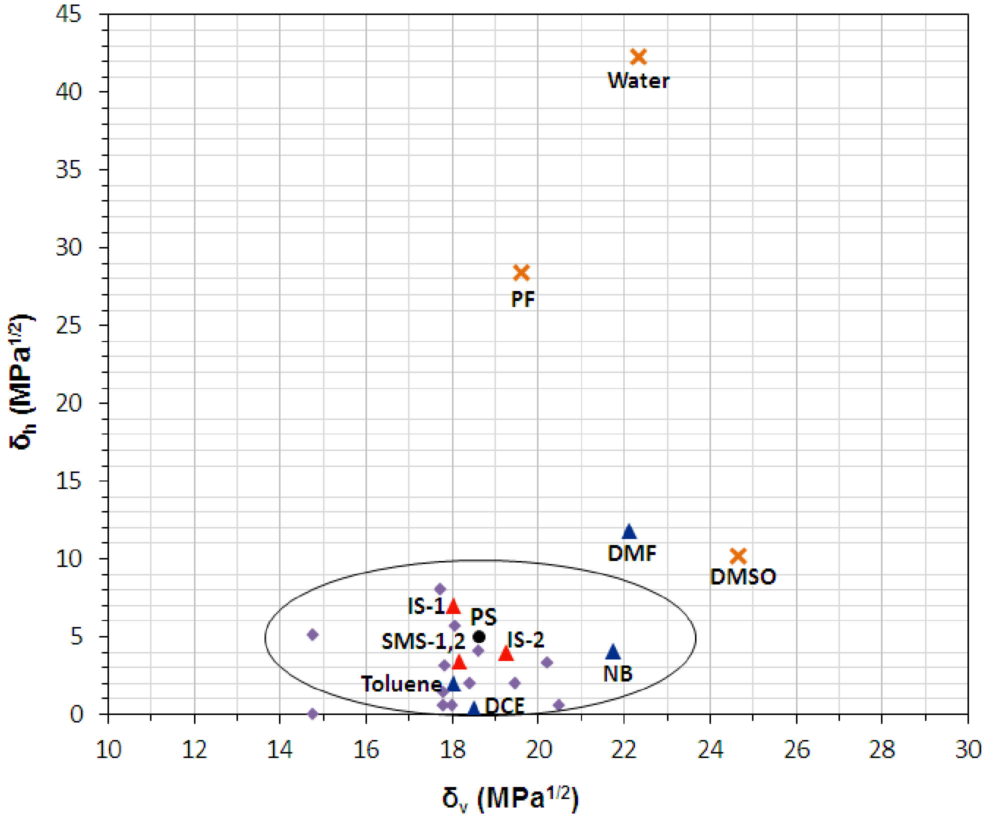

Figure 5.9: Two dimensional (δ_v vs. δ_h) diagram showing extent of solubility of polystyrene (PS) [●] in various solvents. The solvents and solvent blends used in this study are marked with triangles [▲] and [▲] respectively; sMS-1,2=*7:1.2,1 mass ratio of toluene:DMF;* IS-1=*3:1:1 volume ratio of toluene:DCE:PF;* IS-2=*7:2:1 volume ratio DCE:NB:PF*. Those that are non-solvents for PS but good solvents for AB are marked with a cross [✕]. Other good solvents for PS are marked with diamond markers (♦), these include chloroform, diethyl ether, benzene, ethyl benzene, p-diethyl benzene, tetrahydrofuran, styrene, chlorobenzene, o-dichlorobenzene and carbon disulphide.

Table 4. Hansen solubility parameters of solvents and solvent mixtures, with a PS interaction radius of R_0=5 [144] and R_a calculated using Eq.(3.15).

Solvent	δ_d (MPa)	δ_p (MPa)	δ_v (MPa)	δ_h (MPa)	R_a	RED (R_a/R_0)	Miscible with PS?
Polystyrene, PS	17.6	6.1	18.63	5.0	0	0	–
N,N-dimethylformamide, DMF	17.4	13.7	22.15	11.8	10.21	0.8	Yes
dimethyl sulfoxide, DMSO	18.4	16.4	24.65	10.2	11.65	0.92	Yes
Toluene, Tol	18	1.4	18.05	2	5.63	0.44	Yes
1,2-dichloroethane, DCE	16.6	8.2	18.51	0.4	5.44	0.43	Yes
Pyridine	19	8.8	20.94	5.9	3.99	0.31	Yes
Formic acid, FA	14.3	11.9	18.6	16.6	14.55	1.15	No
Water	15.6	16	22.35	42.3	38.8	3.05	No
Pyridium Formate, PF	16.65	10.35	19.6	28.4	23.86	1.88	No
7:1 mass. ratio Tol:DMF	17.91	3.16	18.19	3.4	3.41	0.27	Yes
3:1:1 vol. ratio Tol: DCE:PF	17.45	4.55	18.03	6.96	2.52	0.2	Yes
7:2:1 vol. ratio DCE:NB:PF	17.28	8.49	19.25	3.94	2.69	0.21	Yes

Table 5. Solvent parameters used for solvent selection (solution preparation) for electrospinning.

Solvent/ Solution	Conductivity at RT (S/cm)	Dipole moment (Debye)	Dielectric constant	Boiling Point (°C)	Heat of vaporisati-on (J/mol)	Vapour pressure at 20°C (atm)
Water	5.5 x 10^{-3}	1.87	78.54	100	40790	2.75 x 10^{-2}
DMF	6.0 x 10^{-8}	3.8	36.7	153	47600	2.24 x 10^{-2}
DMSO	2.0 x 10^{-9}	3.96	46.6	189	52900	3.54 x 10^{-4}
Toluene	8.0 x 10^{-16}	0.4	2.4	111	38060	2.46 x 10^{-2}
Nitrobenzene	2 x 10^{-10}	4	34.8	211	40590	1.39 x 10^{-3}
DCE	4.0 x 10^{-11}	1.8	10.42	83.5	33910	8.37 x 10^{-2}
Pyridine	5.0 x 10^{-8}	1.41	12.3	115.2	40200	1.74 x 10^{-2}
Formic acid	5.5 x 10^{-3}	-	58	100	23100	1.31 x 10^{-1}
Pyrdinium formate	1.49 x 10^{-2}	-	27.15	-	-	2.19 x 10^{-2}
7:1 Tol:DMF	6.0 x 10^{-8}	-	6.69	-	-	2.10 x 10^{-2}
3:1:1 Tol:DCE:PF	2.19 x 10^{-4}	-	15.12	-	-	5.22 x 10^{-2}
7:2:1 DCE:NB:PF	4.39 x 10^{-4}	-	8.07	-	-	3.15 x 10^{-2}

Materials were weighed into jars and solvents were added with a syringe while on a balance plate. Mixing was carried out with PTFE-coated magnetic stir bars; polymer solutions were heated at 50 °C until homogenous solutions were obtained. The specific solvent mixtures used to make i) miscible, ii) semi-miscible and iii) immiscible solution sets are as described below, with the exact combinations summarized in Table 6.

Miscible:

Two miscible solution sets were used: the first (MS-1) used dimethylformamide (DMF) for both the core and shell, and the second (MS-2) used dimethyl sulphoxide (DMSO) for the core solvent and DMF for the shell.

Semi-miscible:

The shell solutions were composed of 20 wt.% PS dissolved in 7:1.2 or a 7:1 mass ratio toluene:DMF and were semi-miscible with a core solution composed of 10 or 20 wt.% AB in DMSO (denoted sMS-1 and sMS-2 respectively). The specific shell solvent ratios were chosen to keep the HSPs of the binary mixture within the Hansen sphere. DMF was specifically chosen to increase both the dielectric property and conductivity of the shell solution.

Immiscible:

The immiscible sets were made with a core solution composed of 10 or 20 wt.% AB in water. In a further attempt to improve the conductivity of the shell solutions that needed to be composed mostly of toluene for control of miscibility, pyridinium formate (PF) salt was used. PF, which was made from equimolar amounts of pyridine and formic acid, was dissolved in 1,2-dichloroethane (DCE), a solvent with a high dielectric constant, and added to toluene. This was used to produce the shell solution sets; IS-1, a 3:1:1 volume ratio of toluene:DCE:PF and IS-2, with a 7:2:1 volume ratio of DCE:NB:PF. The latter mixture (IS-2), the last one to be prepared, after all above solutions were tested, was prepared to further optimise the shell solution, i.e. to adjust for the vapour pressure of the shell solvent. Nitrobenzene, which is one of the few PS compatible solvents with a boiling point higher than that of water (see Table 5), was used to reduce the vapour pressure of the shell solvent mixture, such that it was more comparable with that of the core solvent (water) and to make it more suitable for electrospinning.

Experimental verification of miscibility

The degree of miscibility of the core and shell solvent mixtures was checked experimentally by mixing the shell and core solvents in equal proportions and the predictions made using HSPs were found to be correct. Figure 5.10 show the mixtures in bottles; the immiscible solution (IS) set remain phase-separated, the semi-miscible solution (sMS) set creates an opaque solution initially before turning clear over a period of a day; this suggests that solutions eventually mix though it starts off as partially miscible. On the other hand the miscible solution (MS) starts off as a colourless clear mixture and remain clear over time, indicating complete mixing.

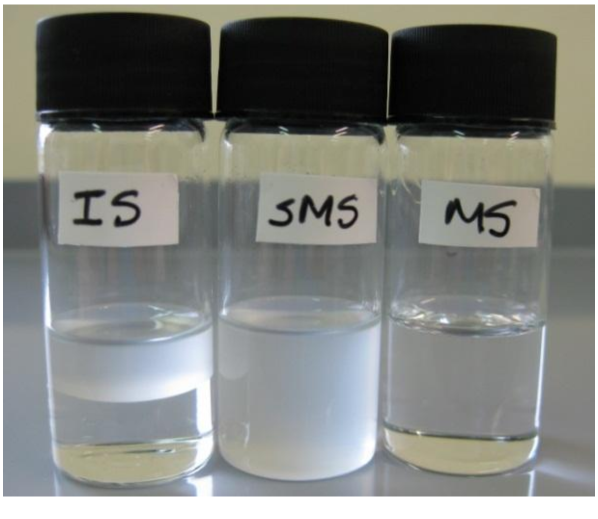

Figure 5.10: Core and shell solvent mixtures showing the difference between the immiscible (IS), semi-miscible (sMS) and miscible (MS) solution sets.

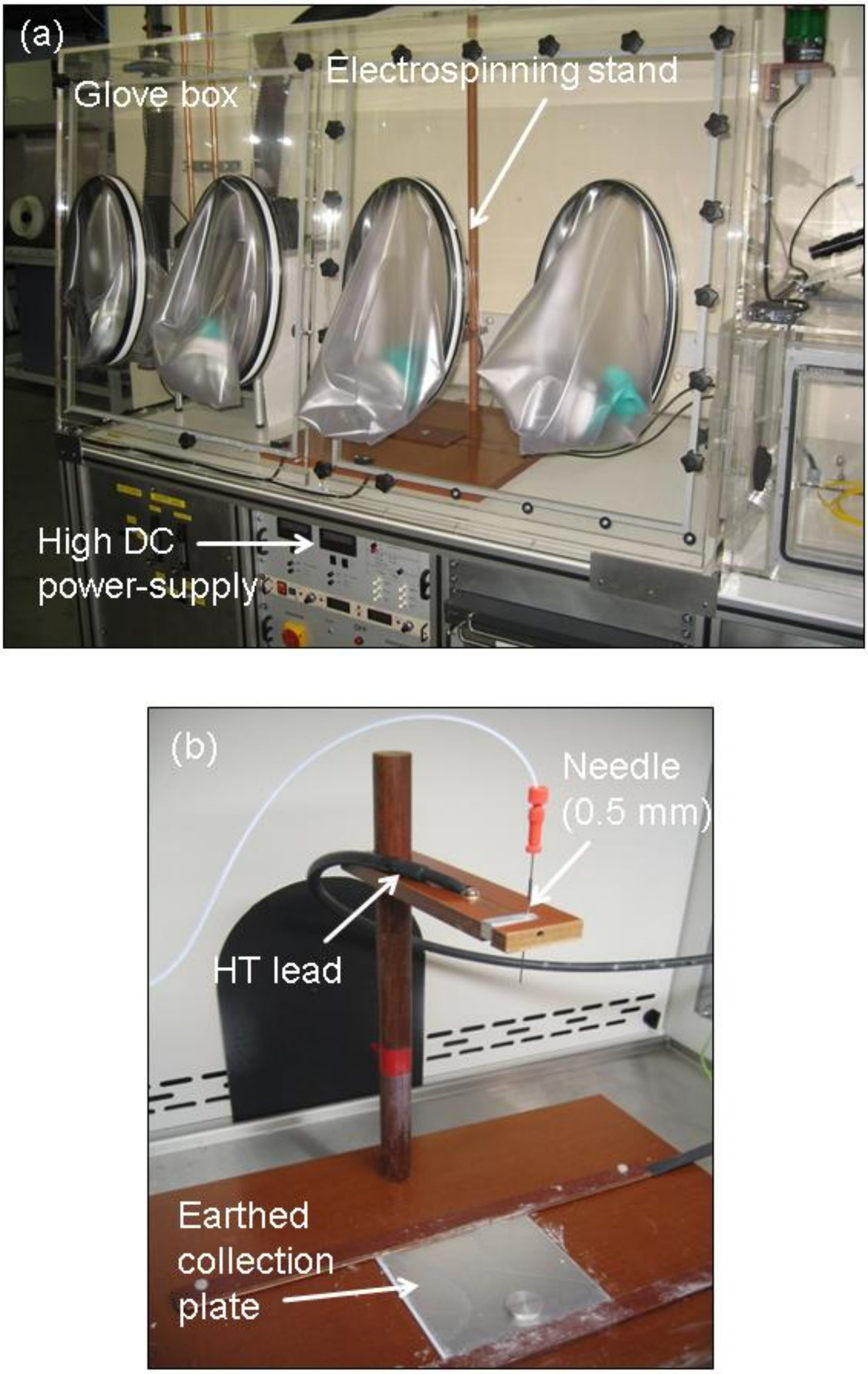

Figure 5.11: Electrospinning apparatus setup a) Glove box with high DC voltage supply, b) The nozzle and collector plate setup placed inside the glove box (note: the nozzle set up here is that for a single nozzle, but this can be exchanged with the co-axial nozzle set up shown in Figure 5.12.

Table 6. Shell and core solution mixtures used to make the immiscible, semi-miscible and miscible core and shell solution combinations. The abbreviations for the solutions are: DMF Dimethylformamide, DMSO Dimethyl sulphoxide, Tol Tolunene, DCE Dichloroethane, PF Pyridinium formate and NB Nitrobenzene

Core-shell solution set		Shell solution			Core solution		
		Composition	**Viscosity at 20-22°C(cP)**	**Conductivity at 20°C (S/cm)**	**Composition**	**Viscosity at 20-22°C (cP)**	**Conductivity at 20°C (S/cm)**
Miscible	MS-1	20 wt.% PS in DMF	281	9.60 x 10^{-7}	10 wt.% AB in DMSO	-	1.00 x 10^{-5}
	MS-2				10 wt.% AB in DMF	-	4.59 x 10^{-5}
Semi-Miscible	sMS-1	18 wt.% PS in 7:1.2 mass ratio Tol:DMF	-	1.00 x 10^{-8}	(b) 20 wt.% AB in DMSO	9.5	5.00 x 10^{-6}
	sMS-2	20 wt.% PS in 7:1 mass ratio Tol:DMF	254	1.00 x 10^{-8}	(a) 10 wt.% AB in DMSO	-	1.00 x 10^{-5}
Immiscible	IS-1	20 wt.% PS in 3:1:1 vol. ratio Tol: DCE:PF	526	4.91 x 10^{-5}	(a) 10 wt.% AB in water	1.5	4.71 x 10^{-4}
					(b) 20 wt.% AB in water	-	1.13 x 10^{-3}
	IS-2	20 wt.% PS in 7:2:1 vol. ratio DCE:NB:PF	1046	1.13 x 10^{-4}	10 wt.% AB in water	1.5	5.72 x 10^{-4}

5.3.3 Electrospinning set-up

The electrospinning set up used for this investigation is shown in Figure 5.11; the single nozzle-head shown in the figure is replaced with the co-axial nozzle-head shown in Figure 5.12. This system was designed and built by the Micro and Nano-Technology Centre at the Rutherford Appleton Laboratory. The inner and outer tubes of the co-axial nozzle were independently connected via tubing to 10 ml syringes that contained the solutions. The flow rates of core and shell solutions were controlled by attaching the syringes to two programmable Harvard- PHD 2000 syringe pumps. The inner diameters of the core and shell nozzles used were 0.45 and 1.01 mm respectively. The flow rate of the core solution was varied between 50 and 500 μl/hr, while that of the shell solution was fixed at 500 μl/hr; this allowed the AB:PS ratio to vary. An aluminium sheet was used as the collector plate, at a distance of 30 cm from the nozzle tip. A Gamma High Voltage power supply was used to generate a high static potential difference across the nozzles (connected to the emitting electrode) and the collector plate (connected to the grounding electrode). The voltages used for the semi-miscible and immiscible solution sets in this study were set at 12 kV and 19 kV respectively. These specific voltages were selected as they yielded the most stable electrospinning. The stability of the spinning process was monitored by a high-speed CCTV camera focused on the nozzle tip.

5.4 Results and Discussion

AB-PS fibres with a range of morphologies and properties were co-electrospun from a set of different solution combinations. Significant differences were observed between fibres electrospun from each solution set; with variation in the fibre morphology, core-shell configuration and the sample mass loss in the thermolysis process. Although solvent mixing was found to be a highly useful way of optimising solvent parameters for electrospinning, maintaining the delicate balance between all solvent variables to ensure success of electrospinning was found to be rather difficult, as discussed further in §5.3.2.

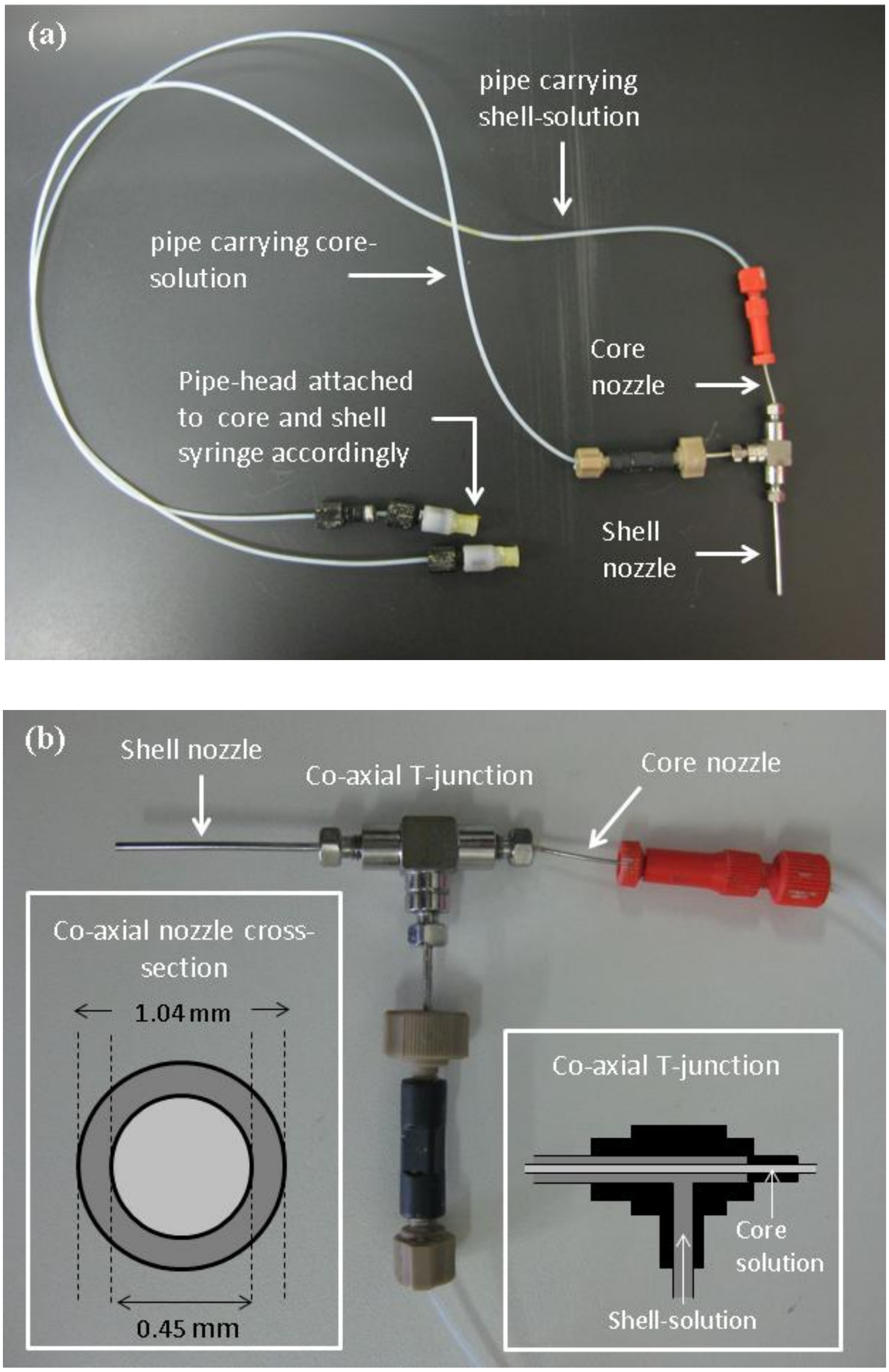

Figure 5.12: Co-axial nozzle setup used in experiments: (a) co-axial nozzle with pipe connections for the flow of core and shell solutions, (b) a close up of the co-axial nozzle with insets showing a schematic of its cross-section and a schematic of the T-junction connecting the core and shell nozzle pipes together.

In this section the results of co-electrospinning for each solution set, the differences in the obtained fibre morphologies, their chemical and crystallographic structure and their thermal decomposition properties will be presented and discussed with respect to the parameters of core-shell solution combinations. In order to gain a better understanding of how the properties of each solution control the morphology and structure of the co-electrospun fibres, where possible, the fibres electrospun in the single phase (those solely from the core or shell solutions) are also analysed.

5.4.1 Co-electrospinning of AB-PS fibres

The miscible, semi-miscible and immiscible AB-PS solution combinations used in co-electrospinning are shown in Table 6. The minimum polystyrene concentration in DMF that yielded non-beaded continuous PS fibres was 20 wt.% for the PS molecular weight used (330,000 Daltons); this was the highest molecular weight PS available from the manufacturer. For the purpose of maintaining consistency the same PS concentration was used throughout for all but one solution set (sMS-1), as shown in Table 6. The effect of polymer concentration on fibre morphology could not be measured in the case of PS-toluene solutions, as these solutions could not be electrospun in the single phase at any of the PS concentrations tested (10-30 wt.% PS in toluene). As for the core solutions, both 10 and 20 wt.% AB concentrations were used; the later value was found to be close to the point of solubility saturation in both core solvents used (water and DMSO), as measured by the opacity of the solutions with any additional amounts of AB.

Fibres were co-electrospun from both semi-miscible and immiscible solution sets; however, neither of the miscible solution sets (MS-1 and MS-2) yielded any fibres. Although the outer shell solution (*20 wt.% PS in DMF*) can be electrospun successfully on its own, introducing the core solution (*10 wt.% AB in DMSO or DMF*) caused the polymer to precipitate out of solution at the nozzle orifice, preventing spinning from taking place. Polymer precipitation resulted in the formation of an elastic gel-like material at the tip of the nozzle, with the droplet insufficiently liquid to precipitate a jet. This result, replicated *in vitro* away from the electrospinning apparatus, is attributed to the differing compatibility and miscibility of the solutes and solvents. In the case of MS-1, although the core solvent, DMSO, is a non-solvent for PS, it is highly miscible with DMF, the shell solvent. It is likely that the two solvents mix to produce a combination which can no longer dissolve PS, causing it to aggregate and precipitate out [198]. In an attempt to overcome this I have used DMF as the solvent in both the core and shell solutions, as it readily dissolves both AB and PS. However, the same problem was encountered once again, although PS precipitated out of the solution at a slower rate, perhaps owing to the presence of the AB.

In the case of semi-miscible and immiscible solution sets composite fibres of AB and PS were successfully electrospun. However, the optimisation of the solution parameters through blending of solvents with specific proportions was vital for the success of the process, so that a compound jet could be initiated and fibres could be electrospun. Nevertheless, problems in the continuity of the electrospinning process were still encountered at times. Nozzle blockage, in the case of highly volatile solutions, or electrostatic charging of fibres that caused the electrospinning jet to lose its stability, were two specific issues we had to watch out for during the spinning process.

Fibre samples were collected over a period of minutes to hours on plastic rods lying on the collection plate, before being removed for analysis. The resulting fibre-mats, which resembled cotton wool or tissue paper (see figure Figure 5.13), were dried at ambient temperature under dynamic vacuum of at least 2×10^{-2} mbar for 4 hours or until no further weight loss owing to evaporation of solvents was observed. The incorporated AB proportion was calculated as a fraction of the total remaining sample mass, assuming complete evaporation of all the solvents from core and shell.

Prior to co-axial tests, single phase electrospinning of individual core and shell solutions were tested using the inner nozzle. AB solutions electrospray rather than spin as there is no polymer (or viscoelastic) component. The AB proportion in the resulting fibres ranged from 0 for the PS solution spun alone, through to 44 wt.%. This gives a nominal total accessible hydrogen content ($2H_2$/AB molecule) of 5.8 wt.% (to 150 °C).

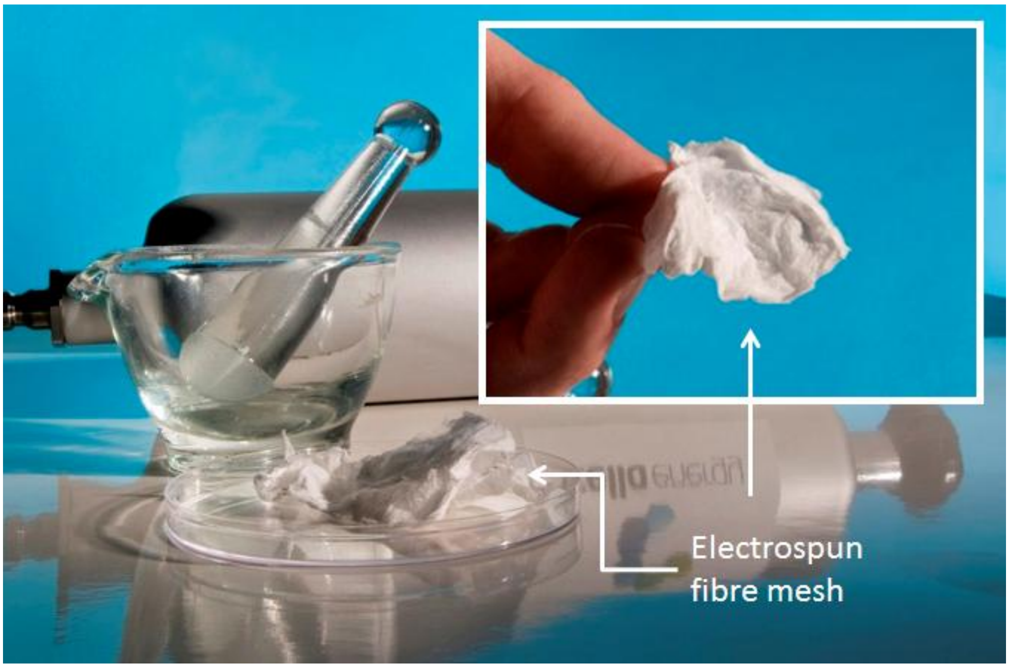

Figure 5.13: Electrospun fibre mesh (fibre mat) collected off the collection plate. The fibre-mesh resembles cotton wool or tissue paper, depending on how aligned and flattened the fibres are.

Samples obtained from each spinning session were numbered uniquely and separated into portions for each characterisation technique. Sample masses spun per session ranged from ~10 to 500 mg prior to drying depending on the combined flow rate and the length of the stable spinning period. In the drying process samples lost typically 30-50 % of their as-spun mass, indicating the removal of a significant fraction of the remaining solvent.

The reported AB content was obtained from the set flow rate (FR) for each solution into the spinning nozzle, as given by:

$$AB\ proportion = \frac{(AB\ wt.\%\ in\ core\ sol.\ \times\ core\ FR)}{(AB\ wt.\%\ in\ core\ sol.\ \times\ core\ FR\ +\ PS\ wt.\%\ in\ shell\ sol.\ \times\ shell\ FR)}$$

Although the target was to maintain a consistent flow of both core and shell solutions, at the set flow rates, it was not always possible to do so due to factors that could not be easily controlled. Bubbles were often observed in the core solution which went into the flow line creating air gaps in the line. Occasionally the solution in the core nozzle was found to deplete at a faster rate than that set on the syringe pump, as observed through formation of a large air gap in the syringe. This suggested that the core solution was experiencing capillary flow under the influence of the electric field, sometimes at a rate greater than the set flow rate. Thus, uncertainties exist in the actual core/shell flow rate ratio, which appear to be semi-systematic but are difficult to determine quantitatively. A core flow rate error range of 5-30 % was measured in some cases. Also unknown was the quantity of solvent remaining in the fibres even after the drying period. The fibres analysed here are ordered by nominal AB content as calculated by the core-shell flow rate ratios and concentrations (assuming equal core and shell solutions densities, a parameter not quantitatively determined). Where a difference was recorded in the flow rate and actual amount of solution used in the production of a given fibre sample notes are made.

5.4.2 Morphological characterisation of fibres: SEM and TEM

5.4.2.1 Semi-miscible solution set

The semi-miscible solution sets (sMS-1 and sMS-2) were successfully co-electrospun with both *10* and *20 wt. % AB in DMSO* as the core solution. Figure 5.14 (a-d) shows SEM and TEM micrographs of fibres co-electrospun using sMS-1 and sMS-2 solution sets; these fibres are highly porous, with the degree of porosity and extent of core-shell configuration changing depending on the particular shell solution concentration and flow rate ratio selected. Fibres produced using sMS-1, with *18 wt.% PS in 1:1.2 mass ratio Toluene: DMF* as shell solution, have a high degree of porosity extending through the bulk of the fibre, i.e. lacking a core-shell structure (Figure 5.14 (a) and (b)).

On the other hand, fibres produced using the second semi-miscible solution set (sMS-2) with a slightly higher PS concentration in the shell, *20 wt.% in 7:1 volume ratio Toluene:DMF*, maintain a core-shell configuration with a porous sheath structure (Figure 5.14 (c) and (d)). It is important to note that while this shell solution does not electrospin on its own, due to its low conductivity (charge density) and dielectric constant, it does when spun co-axially with the highly conducting core solution. Thus, in this case it is likely that the charge that collects on the interface between the core and shell solutions drives the electrospinning of the compound jet. As discussed in §3.2.3.3, theoretical studies suggest that the component driving the compound jet is the one that is the conductor because under the influence of the electrical field the electrical relaxation time of charges in a conducting solution is much smaller than that in a dielectric (insulating) solution. Thus, in this case the charges from the AB-DMSO solution migrate to the liquid-liquid interface when a potential difference is applied, and the electrical stresses acting at the apex of the Taylor cone cause the viscoelastic stretching of the compound jet, enabling fibres to form.

Formation of fibres from co-electrospinning of a core-shell system, composed of core and shell solutions non-spinnable in the single phase, is an important result for electrospinning of polymeric solutions that cannot be electrospun on their own. This finding, which has not been reported previously, suggests that if two solutions with the correct properties are combined (even if neither one of them have all its properties optimised for electrospinning) then it can be possible to initiate co-axial electrospinning even if it is not possible to spin either solution individually. Furthermore, I demonstrate experimentally that it is possible to initiate electrospinning using just a conducting core-solution and a non-conducting shell solution, in contrast to what is reported in the review by Moghe and Gupta [72]. Here it is important to note that though Loscertales and co-workers have demonstrated the possibility of using non-spinnable solutions for initiating co-axial jets with only the core solution conducting [123, 124], co-electrospinning of fibres from two non-electrospinnable solutions, to my knowledge, has not been reported before.

Lopez-Herrera *et al.* [124] report on the variation of droplet diameters depending on whether the driving liquid is flowing inside or outside the core, while Li *et al.* [129] report, based on calculations, variation in the jet instability modes for core and shell liquids with different electrical properties. These observations can be used to explain some of the differences we see in our fibre sets, which were made from solutions with different relative core-shell conductivities. It is possible that in the case of a compound jet formed of a highly conducting core fluid of low viscosity and a shell fluid with no conductivity (but relatively high viscosity), as in the case of our sMS set, that the build-up of charge on the core-shell interface drives the mixing of the two phases under the influence of the electric field that causes instability or perturbations. Incorporation of the core phase into the shell phase through such a mechanism will form core-solvent rich regions in the spinning jet, which will yield highly porous fibres once all the solvent has evaporated, possibly like those shown in Figure 5.14 (a) and (b). This type of porosity, which extends from the core to the surface of the fibres, is different from the surface porosity typically observed in fibres, which is normally attributed to humidity of the spinning environment. Based on theoretical data on the instability theory of the spinning jet, we have developed a theory to explain a mechanism that can possibly lead to the kind of porosity seen in sMS-1 fibres (Figure 5.14 (a) and (b)). This theory, which can be used to control the degree of porosity in electrospun fibres, is outlined in §5.4.4.

On a further note, to illustrate the effect of core flow rate and AB concentration on the jet conductivity, we look at the variation of fibre morphology of those fibres produced using solution set sMS-1, which had a reduced PS concentration of *18 wt.% in 7:1.2 mass ratio of toluene:DMF*. SEM images of these fibres (Figure 5.15) show that, in the case of *10 wt.% AB in DMSO* as the core solution, at low core flow rates the fibres are highly beaded (Figure 5.15 (a)), but when the flow rate is increased the beads elongate along the fibre axis (Figure 5.15 (b)), and when a higher AB concentration solution (*20wt% AB in DMSO*) is used the beads are almost completely removed (Figure 5.15 (c)).

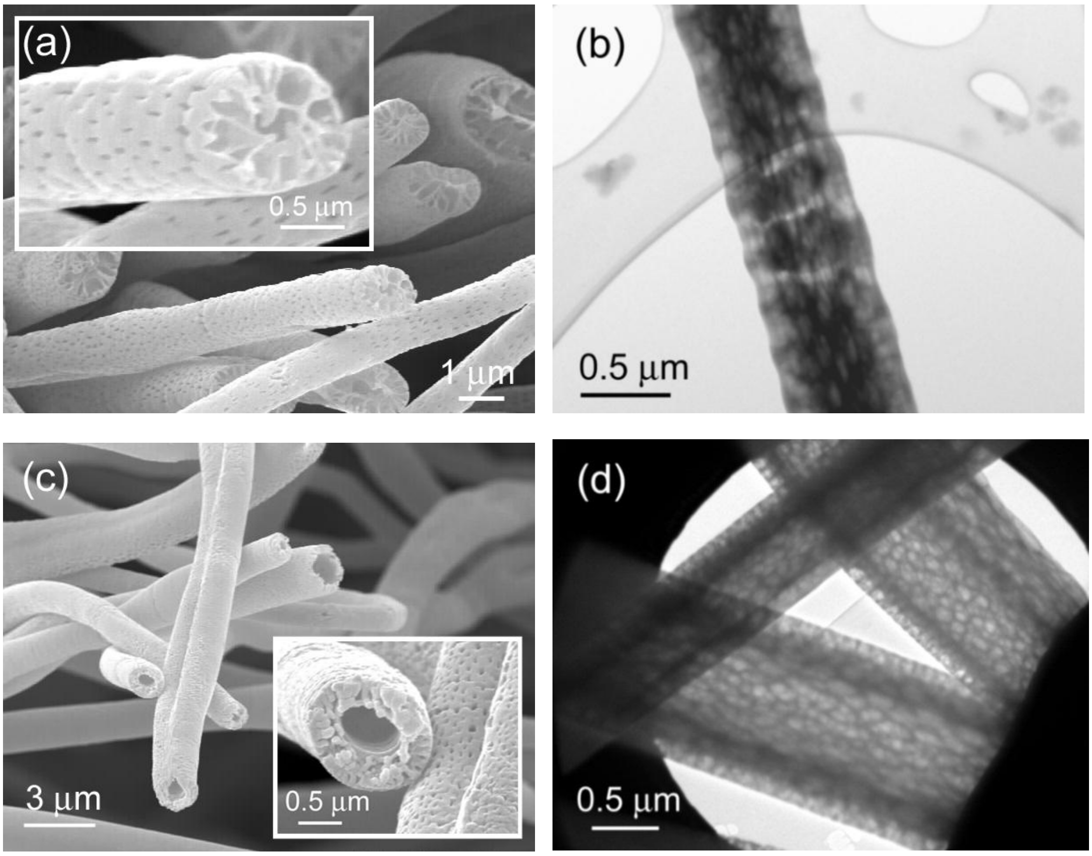

Figure 5.14: (a) SEM and (b) TEM micrograph of fibres produced from semi-miscible solution set-1, sMS-1, with *10 wt.% AB in DMSO* as core solution (electrospun with shell-core flow rate of 500:250 µl/hr, voltage 12 kV, temperature 18°C, humidity 50 %), (c) SEM micrograph of fibres from semi-miscible solution set-2, sMS-2, (electrospun with shell:core flow rate 500: 250 µl/hr, voltage 12 kV, temperature 21°C, humidity 27 %, (d) TEM micrograph of fibres from sMS-2 (electrospun with shell-core flow rate 450:200 µl/hr, voltage 12 kV. The morphological variation between the two sets of fibres (produced from sMS-1 and sMS-2) is illustrated; while sMS-1 fibres have no core-shell structure and high density of pores, sMS-2 fibres have core-shell morphology with much smaller and lower density of pores.

Fibre beading, which is attributed to the effect of surface tension, is typically removed by increasing the conductivity of the solution (as discussed in §2.6.1.3). Thus, it appears that the total conductivity of the compound jet is increased with increasing AB-solution flow rate and AB concentration (i.e with increasing charge density in the compound jet). While we have no direct measure of the conductivity of the compound jet, this hypothesis is in agreement with the results reported by Lopez-Herrera *et al.* [124], who have found that the electrical current transported by co-axial jets of conducting-insulator liquids is dependent on the conducting fluid's flow rate.

5.4.2.2 Immiscible solution sets

The first immiscible solution set (IS-1) resulted in the formation of fibres most of which are collapsed, as shown in Figure 5.16 (a)-(c). These fibres have some porosity but with pore size and density significantly lower than that in the fibres produced from sMS sets discussed above. Fibre buckling (collapsing) is attributed to the difference in evaporation rates of the core and the shell solvents during the formation of the fibres [116] (as discussed in §3.2.3.4). The vapour pressure of the shell solvent blend used for making the IS-1 fibres is approximately 50% higher than that of the core solvent (Table 5), so the shell solvent will be expected to evaporate first leaving a semi-dry shell layer for the core solvent to diffuse through. The dry skin (shell) layer collapses under atmospheric pressure to form elliptical or flat fibres [128], the extent of which depends on the diffusion rate of the core solvent through the shell [116, 128].

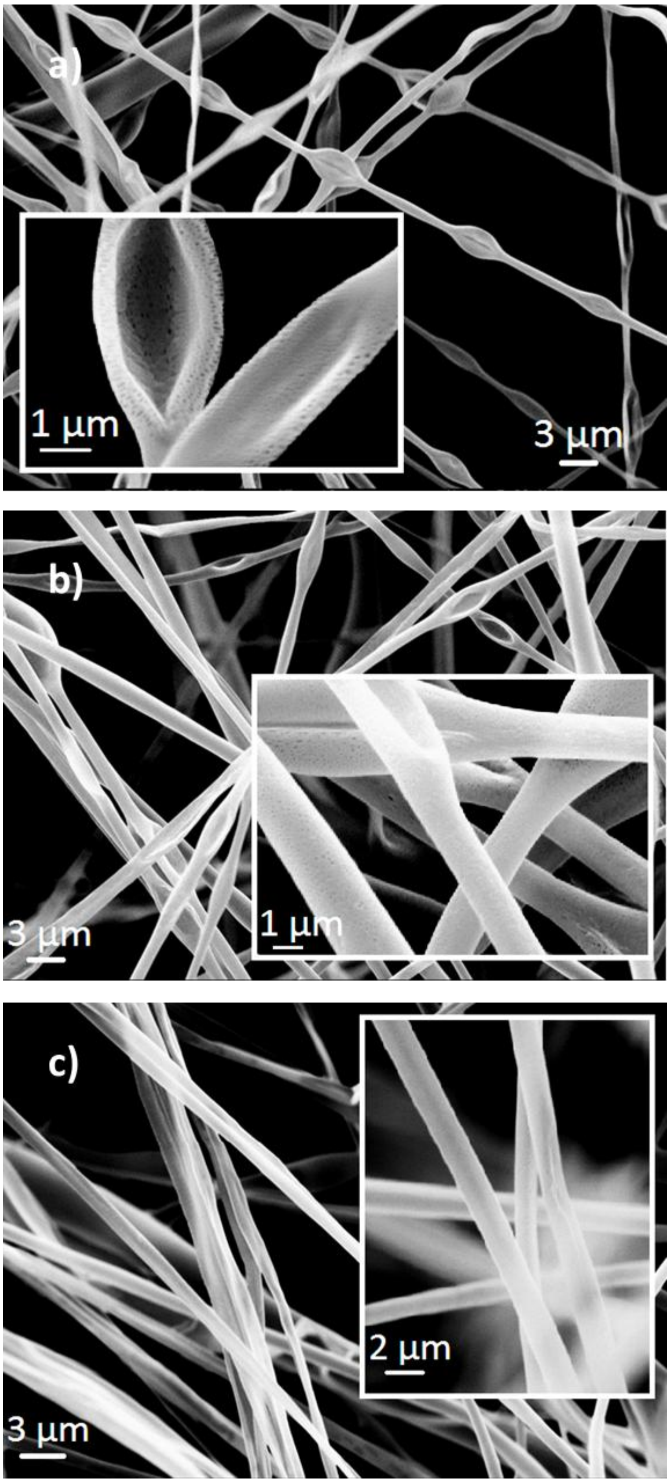

Figure 5.15: Fibres co-electrospun with solution set sMS-2 showing reduction in beading with increasing core (AB) solution quantity (flow rate and concentration) a) core: *10 wt.% AB in DMSO*, shell:core flow rate = 400:150, b) core: *10 wt.% AB in DMSO*, shell:core flow rate = 400:250, V=12, T=18, H=39 %) core: *20 wt.% AB in DMSO*, shell:core flow rate= 400:250. The temperature and humidity in all cases is 17-18 °C and 39-40% respectively.

We find that the degree of collapsing decreases as the core solution flow rate increases for a fixed shell flow rate (500 µl/hr). This is illustrated in Figure 5.16 (a)-(c), which shows SEM micrographs of fibres co-electrospun with increasing core flow rates respectively (150, 250 and 500 µl/hr for fixed shell flow rate of 500 µl/hr). This suggests that the presence of a greater solution (or solvent) volume in the core, as well as reduction of fibre diameters, can reduce the degree of fibre collapse. The low vapour pressure of the shell solvent blend also caused the droplet at the tip of the nozzle to dry up, causing intermittent electrospinning; the jet was sustained only during the time the droplet was sufficiently fluid to form a compound jet. When the droplet dried up, it grew in size and detached from the nozzle as fresh solution emerged from the top, enabling electrospinning to ensue.

Despite much effort to optimise the properties of the shell solution used to make IS-1, it was not possible to match the vapour pressure of the solvent mixture with that of the core solvent (water) by simply varying the proportion of each solvent, as none of the solvents in the blend had a vapour pressure lower than that of water. Thus, it was necessary to make an alternative shell solvent blend composed of PS-compatible solvents with lower vapour pressures without compromising the conductivity and dielectric constant, while retaining immiscibility of the core and the shell solutions. Immiscible solution set-2 (IS-2) was prepared with this in mind using nitrobenzene (NB), a low vapour pressure solvent, as an alternative to the main solvent, toluene, in IS-1. This solution set (IS-2), which had the most compatible core and shell solution combination and the most optimal properties for co-electrospinning of all the solutions tested, resulted in non-porous cylindrical fibres with a core-shell configuration and a smooth surface morphology (Figure 5.17). Thus, the solution selection method developed was found to provide a successful approach to step-wise optimisation of solution properties and control of fibre morphology. It is important to note once more that our aim was to produce co-axial nanofibres with AB encapsulated in a thin polymer sheath permeable only to hydrogen. Fibre porosity is therefore a highly undesirable characteristic for core-shell fibres prepared to retain all reaction products of a hydrogen storage material (other than hydrogen) in the core of the fibres. Nevertheless, the know how developed for understanding the factors leading to pore formation can be extremely useful for making porous fibres or vesicles in a controlled manner for other applications, such as controlled drug delivery systems, as discussed in §5.4.4 below.

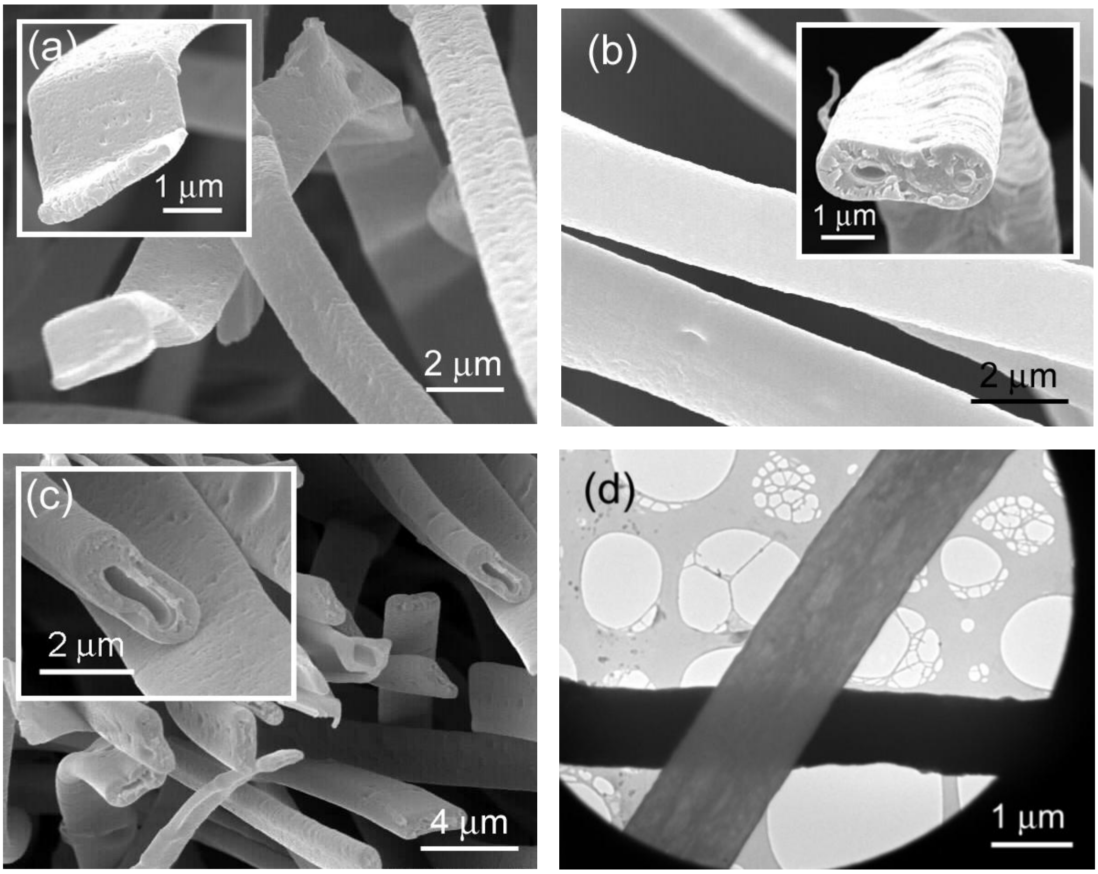

Figure 5.16: (a)-(d) SEM micrographs of fibres produced from immiscible solution set-1, IS-1, with *20 wt.% AB in water* as core solution illustrating the change in degree of collapsing and core-shell morphology with increasing core flow rate, a) Flow rate 500:150 ul/hr; b) Flow rate 500:250 ul/hr, c) Flow rate 500:350 ul/hr, conditions: voltage 18 kV, temperature 23°C, humidity 28 %; (d) TEM micrograph of a fibre filament produced under same conditions as fibres in (b).

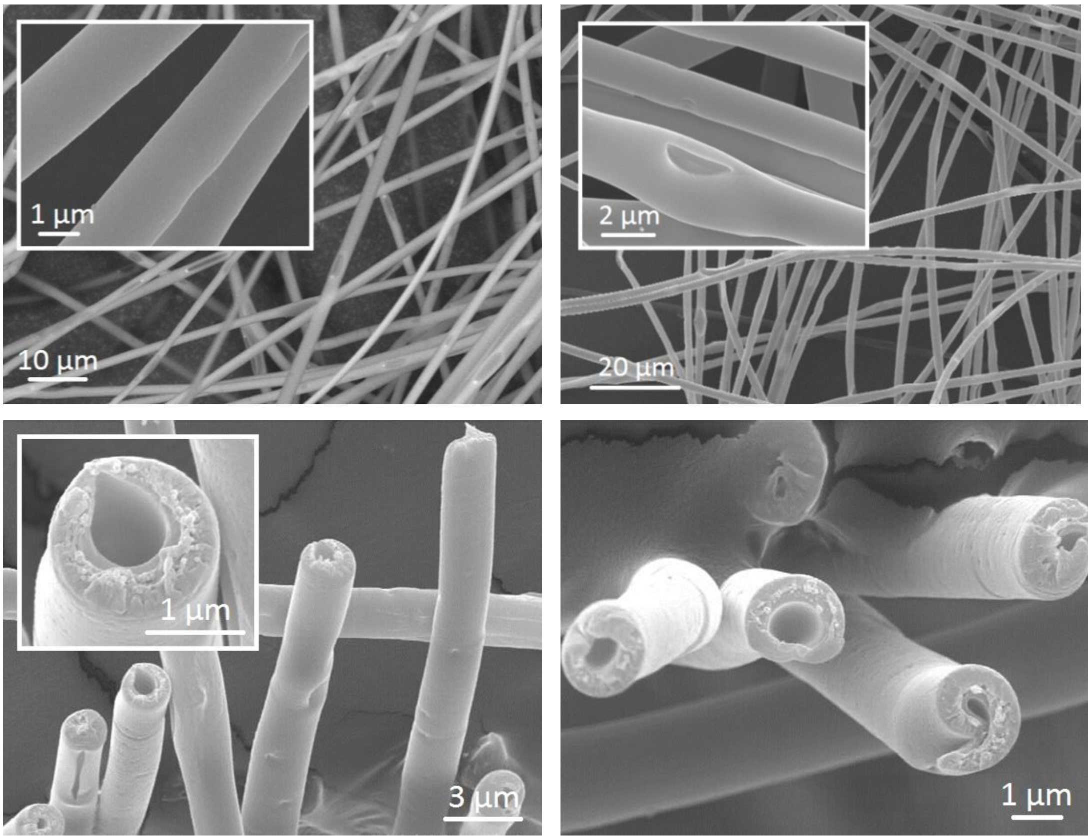

Figure 5.17: Fibres produced from immiscible solution set-2 (IS-2) with *20 wt.% AB in water* as core solution, showing smooth (non-porous) and cylindrical (non-collapsed) fibres.

5.4.2.3 Effect of increasing core solution viscosity

In the case of all co-electrospun fibres described above, the core solution was composed solely of AB dissolved in a single solvent and due to dissociation of AB (NH_3BH_3) molecules in the solvent, the core solution had very low viscosity compared to that of the polymeric shell which is viscoelastic. This satisfies the higher-shell-viscosity condition considered necessary for co-electrospinning. To test the effect of increasing core viscosity on fibre morphology, without exceeding the viscosity value for shell, a small fraction (3 wt.%) of high molecular weight poly(ethylene oxide) (PEO, Mw=900,000 Da) was added to the 10 wt.% AB-water solution to make the core solution viscous. The shell solution used was the same as that used for IS-1 (*20 wt. % PS in 3:1:1 Tol:DCE:PF* mixture).

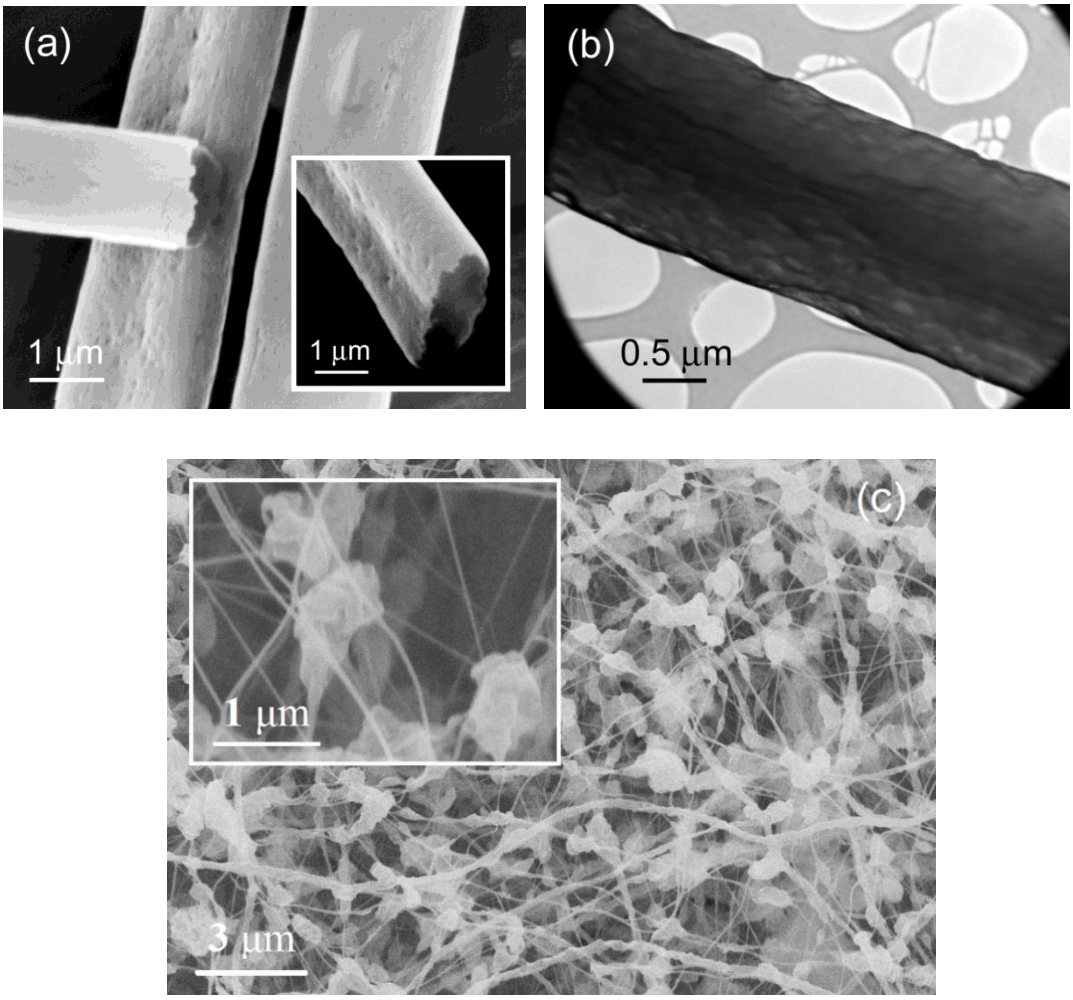

Figure 5.18: (a) SEM and (b) TEM micrograph of fibres co-electrospun from IS-1, *20 wt.% PS in 3:1:1 volume ratio Tol-DCE-PF (shell)* & *20 wt.% AB in water + 3 wt.% PEO (core)* (FR=500:200 µl/hr, voltage 19 kV, temperature 21°C, humidity 40%), showing collapsed bulk fibres with very little porosity; (c) SEM micrograph of fibres obtained with the core solution (*20 wt.% AB in water + 3 wt.% PEO*) electrospun on its own, AB has formed crystallites attached to the fine PEO fibres.

Co-electrospinning of this core-shell solution set resulted in the formation of solid fibres with significantly reduced porosity and degree of collapsing, as illustrated by the SEM and TEM micrographs in Figure 5.18 (a) and (b) respectively. Dror *et al.* [199] reported seeing similar effects due to the polymer precipitating out onto the inner wall of the shell, stiffening the fibres and suppressing the collapse. Figure 5.18 (c) shows the core solution (*20 wt.% AB in water + 3 wt.% PEO*) electrospun on its own through the core nozzle (i.e. without the shell solution running through the annulus of the co-axial nozzle). The core was electrospun to test the process parameters required for electrospinning of the core solution, which was considered as the driver of the compound jet. The PEO fibres formed are very fine (<100 nm) due to low concentration of PEO with AB crystallites (with crystal sizes ranging between 0.2-2 μm). Although this is a very good way of obtaining high density of nano- and micro-structured AB crystals attached to polymeric fibres, the electrospinning process was very unstable due to the difficulty of maintaining continuous electrospinning. The process was not investigated any further since the AB was not encapsulated as required for this study.

5.4.3 Fibre diameters and core structure

A relatively high degree of variation was observed in the core shell morphology and fibre diameters in fibres co-electrospun from both sMS-1,2 and IS-1 fibre sets as shown in SEM and TEM images in Figure 5.19 and Figure 5.20, and the mean fibre diameter plot in Figure 5.21. Fibres with larger diameters have larger pores (as shown in Figure 5.19 (b)) and appear to have collapsed at the tips, most probably as a result of pressure exerted on them in preparation of fibres for SEM imaging, which requires cutting the fibres encased in sticky tape to expose the ends. Fibre variation could be attributed to the instability in the electrospinning process or the particular voltage used (12 kV), as studies have shown lower spinning voltages yield fibres with a greater diameter distribution (this was discussed in §2.6.2.1). However, the large difference between the fibres electrospun from solutions made on different days or the fibres electrospun from a given solution on different days was suggestive of a time-varying effect. There are many variables that can of course vary with time; these are the ambient conditions (i.e. the temperature and humidity of the atmosphere) as well as solution properties such as viscosity and conductivity. Having tested for the latter we have found a large variation over time in the conductivity of the core solutions containing AB, as shown in Figure 5.22. This observation is a very good example of how strictly all the parameters have to be controlled in electrospinning and shows how important it is to identify and control those variables that vary over time. Unfortunately, the variation in conductivity was only discovered in latter stages of the study and hence was not properly controlled for in earlier studies. Fresh AB solutions were made and used on the same day in most cases.

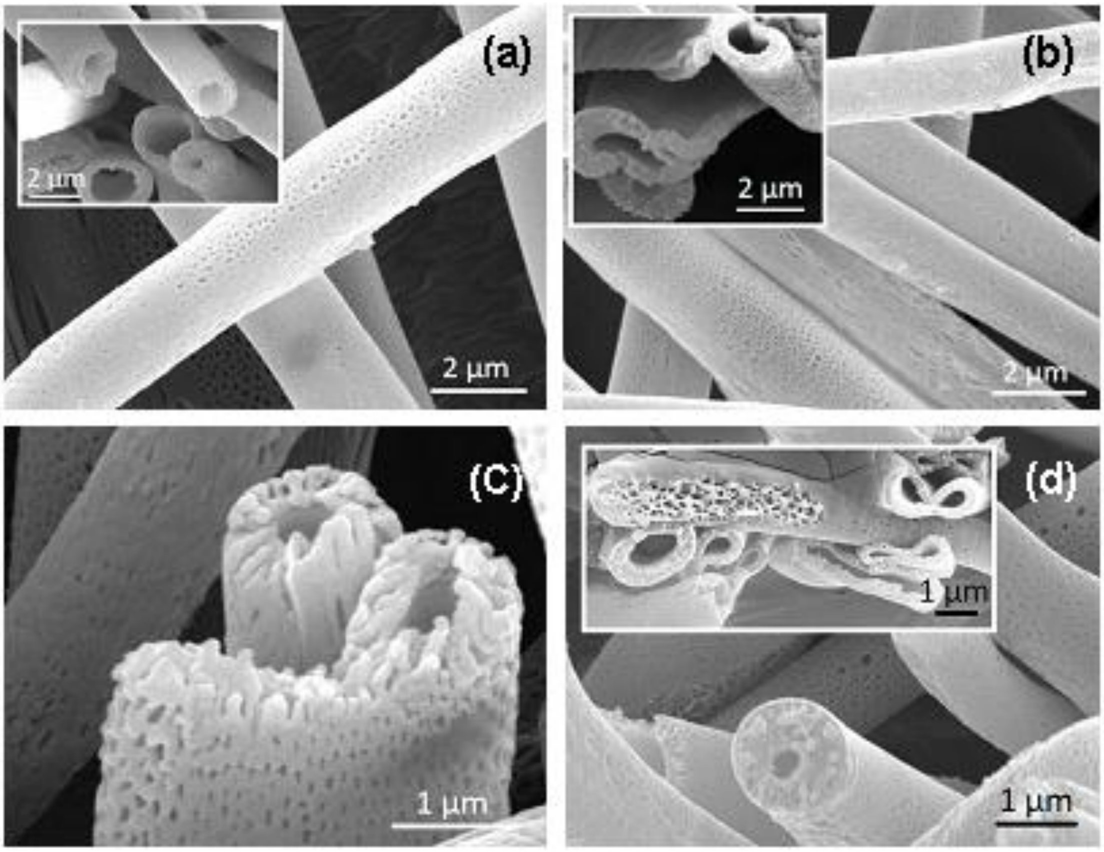

Figure 5.19: Fibres co-electrospun from solution set sMS-2 with 10wt% AB in DMSO as the core solution, showing the variation in fibre diameter and the degree of porosity along the fibre axis in one fibre set. Larger fibres collapsed at the fibre ends due to pressure applied when cutting the ends for SEM analysis; a) shell:core flow rate 500:250, V=12, T=21, H=27 b), c) shell:core flow rate 500:500, V=12, T=20, H=33 d) shell:core flow rate 500:200, V=12, T=21, H=32.

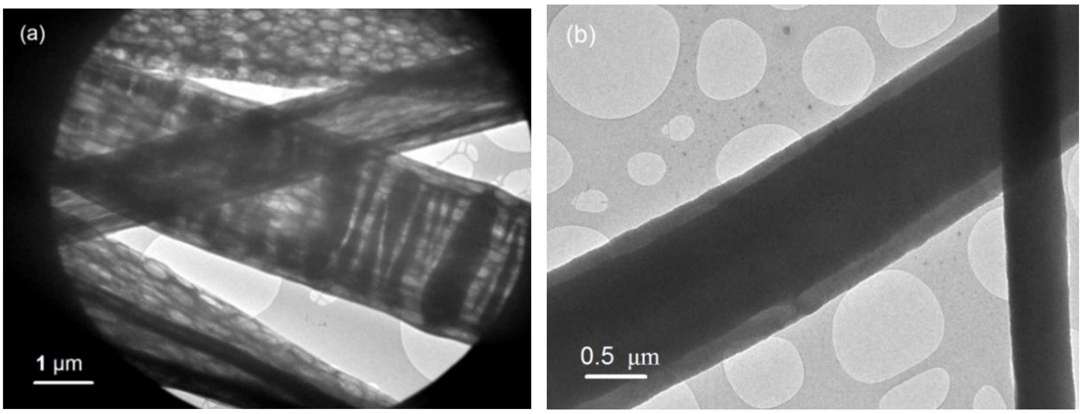

Figure 5.20: TEM images of fibres electrospun from (a) sMS-2 solutions set (with *10 wt.% AB in DMSO* (core); (b) IS-1 solutions set with *10 wt.% AB in water*, showing the variation between the two fibre sets and the difference in the fibre morphology and diameters within each fibre set.

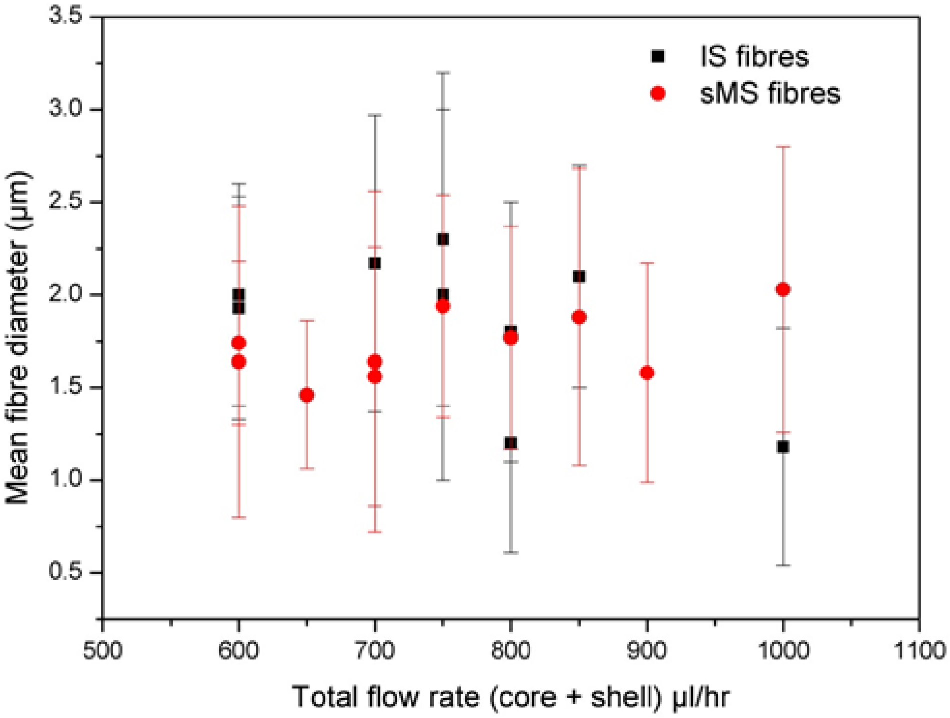

Figure 5.21: Mean diameters of fibres electrospun from semi-miscible (sMS-2) and immiscible (IS-1) solutions sets; error bars represent the standard deviation on sample of ~100 fibres.

The fibres produced have diameters typically in the range 1-2.5 µm as shown in the plot of mean fibre diameters as a function of total flow rate for sMS-2 and IS-1 (Figure 5.21). These diameters are unfortunately not in the nanometre range we were aiming to get. Fibre diameters can typically be reduced by reducing polymer concentration, while using a higher molecular weight polymer to maintain a specific viscosity for chain entanglement, and by increasing electrical conductivity of the diluted solution to prevent beading. It was not possible to obtain a higher molecular weight general grade PS from the manufacturers, and reducing the PS concentration even a small amount resulted in beaded fibres for the molecular weight used (M_w = 350,000 Daltons), as shown by fibres electrospun from sMS-1 (Figure 5.15). Increasing the electrical conductivity of the shell solution further was very difficult using the selected PS-compatible solvents. However, the main reason for the lack of focus on lowering the fibre diameters further was because the porous fibres, with pores tens of nanometres across, were considered to be nanostructured based on the initial dehydrogenation data obtained using coupled TGA-mass spectroscopy techniques are discussed (as discussed below in §5.4.6).

It is possible to observe some discontinuity in the core-shell configuration in some of the fibres in all sample sets, sMS1,2 and IS-1,2 (as shown in Figure 5.14, Figure 5.16, Figure 5.17 and Figure 5.19); there appears to be some variation in the wall thickness and while some fibres have a hollow core structure, some do not. In the case of these fibres the hollowness of fibres is attributed to evaporation of the core solvent after the shell has hardened; the core solution will take up more space than the AB can fill after the core solvent has evaporated and hence fibres with hollow cores are formed with AB presumably deposited on the inner walls. Hollow fibre structures were observed by Dror *et al.* [199] and Arinstein *et al.* [200] even in the case where the core solution was polymeric like the shell solution. In these studies, based on both experimental and theoretical findings, the formation of the hollow fibre structure is attributed to a mechanism whereby the shell forms a hardened skin layer due to initial evaporation of the shell solvent, which results in the formation of microtubes that contain many slugs of entrapped core solvent that are bound by a vapour phase [199, 200]. As the remaining core solvent evaporates the slugs shorten from each end in the tubes, leaving a thin but macroscopic layer of core solute behind [199]. Depending on the rate of evaporation of core solvent through the shell layer the core of the fibres can result in being either hollow or compact. If the AB is retained on the inner surface of the pores in a similar manner in the case of porous sMS fibres, then the AB encased in the pores may well be formed of nano-AB layers or crystallites. This is a possible reason for the observed reduction in desorption temperature in the sMS fibres but not the IS ones (as discussed in 5.4.6). However, it is important to note that, continuity of the core flow and phenomena such as bubbles in the core solution during electrospinning of the fibres could also potentially influence the core structure (i.e. hollowness) of the fibres.

Further analysis of the internal structure of the fibres are needed to more conclusively determine how AB is deposited in the core of the fibres and whether AB is nanostructured in some of the fibres. Unfortunately the TEM images of the fibres (see examples in Figure 5.14(b) and (d) and Figure 5.20(a)) do not conclusively show how AB is encapsulated in the fibres, mostly because AB crystals are not visibly obvious in the images. TEM diffraction was used to see if AB crystals were present in certain segments of the fibres imaged, but no diffraction data was obtained in the few tests done. Further research is needed using the TEM to determine how AB is deposited or encapsulated in the fibres (both along the fibre axis and its cross-section). Also, if AB is deposited on the inner core of the fibres as particles, the particle dimensions have to be determined; if it is deposited as a film then the film thickness will have to be determined, though this could be less straightforward. In the case of porous fibres, it is important to determine if the AB is embedded in the pores of the fibres along their cross-section or purely in the hollow core of the fibres. The high density, crack like core structures, as observed in Figure 5.20(a), have to be further investigated to determine if these are due to AB coagulation, etc. These variations can explain some of the differences measured in the thermolysis experiments as discussed later.

a)

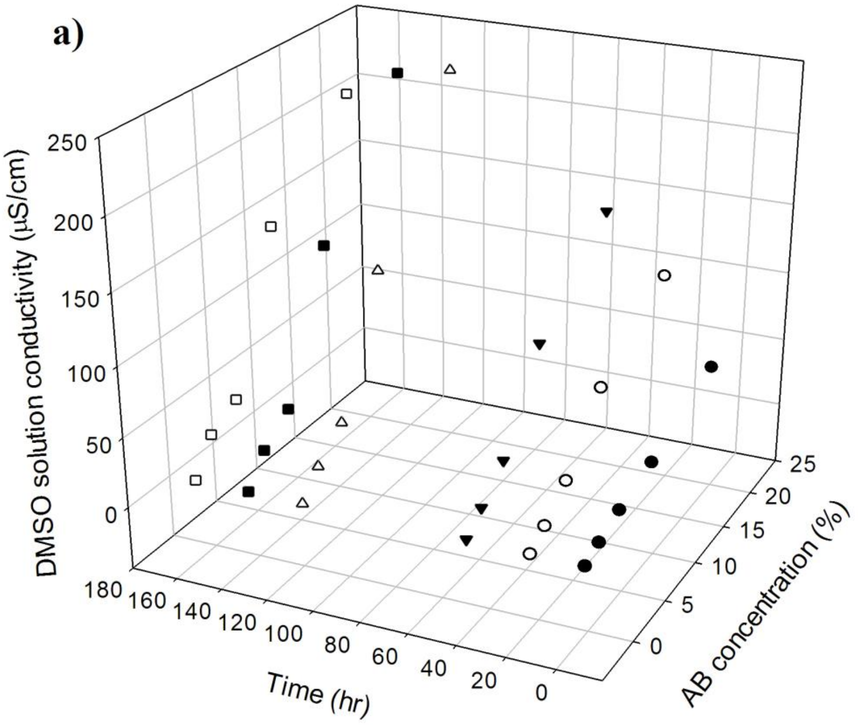

b)

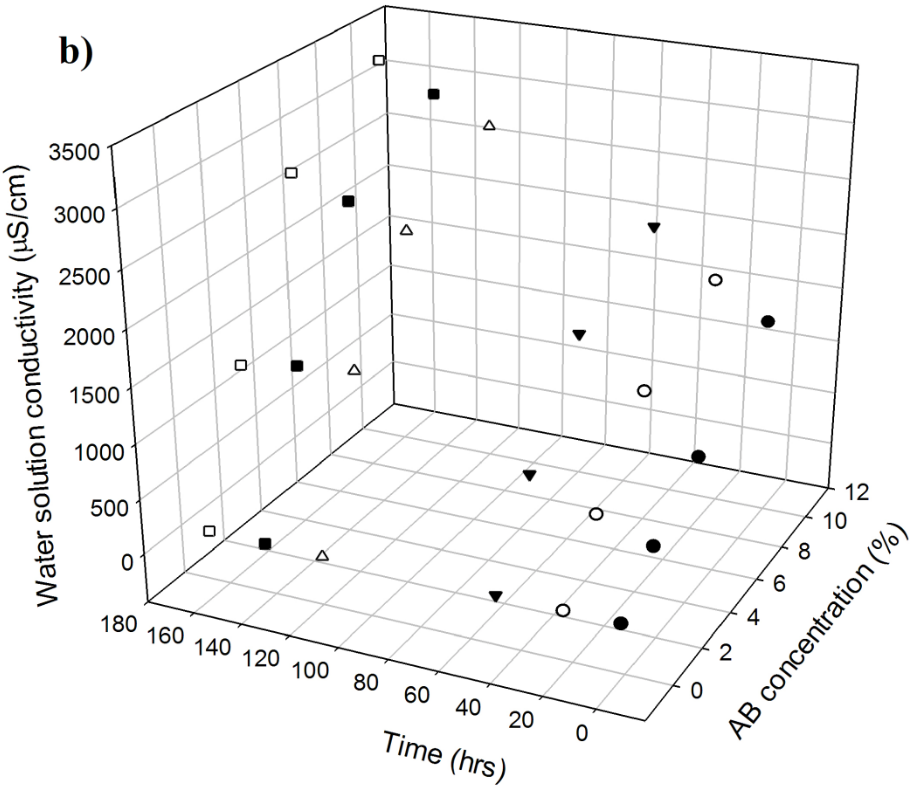

Figure 5.22: Graphs showing the variation of AB solution conductivity over time for different AB concentration in (a) DMSO and (b) in water.

5.4.4 Fibre Porosity

Porosity in the co-electrospun fibres was a phenomenon we had not initially anticipated at the beginning of this study, at least to the extent we have seen in the fibres. Since porosity was initially considered as an undesirable characteristic of AB-PS fibres, attaining an understanding of the factors that lead to porosity and removal of the pores from the fibres was crucial for this investigation. However, upon conducting thermolysis studies on the electrospun fibres, more interesting results were obtained in the case of fibres with the greatest degree of porosity, which indicated possible nanostructuring of AB in the highly porous fibres (as discussed in §5.4.6 below). This in return made fibre porosity and the mechanisms that lead to porosity more interesting to investigate. In this section I will look at the factors that are thought to lead to porosity, as outlined in literature, and discuss why these do not provide sufficient justification for the kind of porosity seen in the co-electrospun fibres discussed. I will then make references to the jet instability model discussed in §3.2.2.1, to explain how it could possibly be used to explain the extent of porosity we see in our fibres. This theoretical model, which needs to be tested more thoroughly on other solution systems, can be very powerful for gaining control of the porosity in fibres and vesicles, opening up many potential applications for engineered porous fibres besides biomedical uses.

5.4.4.1 Creating porous fibres

In literature, fibre porosity is attributed to a thermodynamic instability driven either by cooling, the loss of solvent or the increase in the concentration of a non-solvent such as water that drives the phase separation during the electrospinning process [201-204]. Volatile solvents such as THF can cause significant evaporative cooling. If this takes the system below its upper critical solution temperature (UCST) then the system will become unstable and separate into a solvent-rich phase and a solvent-poor phase, the solvent-rich phase results in the formation of pores as the solution evaporates. This is known as thermally induced phase separation (TIPS). A related effect known as vapour-induced phase separation (VIPS) is also thought to occur when the atmospheric humidity is high. As the water concentration increases in the solution, it can also drive the system into the unstable region of the tertiary phase diagram. In principle both effects could occur simultaneously.

PS in water-soluble solvents such THF [205, 206] or DMF [201, 202, 206, 207] shows porosity at relative humidities of above 25-30% as would be expected via VIPS. However, porosity has also been observed with PS dissolved in water-insoluble solvents such as toluene at similar values of relative humidity [206]. In our investigation all the fibres were electrospun in an atmosphere with a humidity greater than 25% (typically between 30-50%) and as reported elsewhere [119, 208] there appears to be some increase in porosity with atmospheric humidity, but only in fibres produced from the semi-miscible solutions. However, the large variation in porosity between fibres produced from each solution set (sMS-1, sMS-2, IS-1 and IS-2), despite being electrospun in an environment with the same atmospheric conditions, suggest additional factors are influencing the porosity of these fibres. This is clearly illustrated by the fibres electrospun from IS-2 set (Figure 5.17), which have no porosity despite being electrospun in an atmosphere with a relatively high humidity (50%).

Toluene and PS are completely miscible at room temperature and below; because of the nature of the interaction between solvent and polymer it is a system which does not have UCST but a lower critical solution temperature, LCST, of around 550 K [209], making it necessary to heat the solution to initiate phase separation. This and the fact that toluene and water are immiscible imply that neither VIPS nor TIPS should occur. Even though our semi-miscible solutions contain a small proportion of DMF (a 7:1 or 7:1.2 ratio of toluene and DMF), this mixture is still largely immiscible with water. However, it is not clear if the mixing of the shell solution with the core solution (AB-DMSO) at the nozzle orifice would introduce a UCST that could initiate thermodynamic instability and yield porous fibres.

By engineering a solution or pair of solutions, which phase separate reliably, vapour- or thermally induced phase separation could be exploited in a more controlled manner to form porous fibres with the desired size of pores (important for nanostructuring) rather than just relying on environmental parameters such as temperature or humidity. It is possible to use the Hansen parameters to obtain an estimate of the Flory-Huggins interaction parameter [142] and hence some idea of the nature of the binary phase diagram. The process is complex and much also depends on factors such as the volatility of the solvent. High evaporation rates cause significant cooling which makes both VIPS and TIPS more likely, but if the polymer drying time is too fast then it can solidify before significant water can be absorbed [207].

Although vapour or thermally induced phase separation can lead to pores in fibres, the kind of pores seen in semi-miscible solutions (sMS) are of a different character than those which would be expected by VIPS or TIPS, which would produce pores more like the ones seen in immiscible-solution (IS) fibres. In the sMS fibres there are a large number of regularly spaced pores with smaller surface openings, extending frequently through the entire fibre cross-section (as in Figure 5.14 (a)), and sometimes co-existing with a larger core section (as in Figure 5.14 (c)). For a given fibre the pores are all of roughly equal size, whereas in the porous IS fibres, the pores are shallow, sparse, and distributed less evenly (as shown in Figure 5.16). Therefore, it appears that another mechanism is controlling fibre porosity and we think this is the electrohydrodynamic instability experienced by the electrospinning compound jet. This instability mechanism and the justification for why we think it may play a role in shaping fibre porosity are discussed below.

5.4.4.2 Core-shell instability

The idea that porosity is driven by a thermodynamic instability is compelling, but it must also be remembered that there may well be effects due to the large electrostatic fields. In the semi-miscible solution combination, the conductivity of the core solution is 2 to 3 orders of magnitude higher than that of the shell solution, so charge will collect on the core-shell interface rather than on the outside of the fibre. This is predicted to create an instability driven by the axial component of the electrostatic field, which can induce fibre porosity in addition to phase separation or even if there is no phase separation; a mechanism that can also be effective during melt electrospinning.

Most theoretical work on the electro-hydrodynamics of electrospinning has focused on the axisymmetric instability modes which drive the helical motion of the fibres and the breakup of the fibres into droplets [210, 211]. These works show that the viscosity, as characterized by the Reynolds number, controls the growth of these instability modes; and higher viscosity will suppress the Rayleigh-type modes that cause the break-up of the jet into droplets i.e. electro-spraying. But they also show that as the Weber number, which is proportional to the inverse of the surface tension, increases, the higher wavenumber modes become unstable.

Calculations by Li *et al.* [212] show that these non-axisymmetric modes can also be driven unstable in a radial electric field as the Weber number becomes sufficiently large. Because these modes are actually on the core-shell interface in our system, it is the interfacial surface tension resulting from the difference in cohesion energy between the two liquids which is relevant in this case. It is intuitively obvious that as two liquids become miscible, their mutual interaction becomes as strong as their self-cohesion, and the interfacial surface tension will tend to zero.

It was described in §3.2.2.1 that using a normal mode it is possible to decompose the capillary waves on a cylindrical surface into modes characterized by an azimuthal number n.

$$f(r,\theta,z,t) = \hat{f}(r)e^{wt+i(kz+n\theta)} \tag{5.5}$$

where k is the wavenumber along the fibre axis. The axisymmetric modes are all $n=0$ and the helical mode is $n=1$ (as discussed in §3.2.2.1). These modes are shown for three values of *m* for a co-axial fibre in Figure 5.23 (a). The amplitude for a capillary wave for a given energy is proportional to one over the square-root of the surface tension (from Eq. 3.3), so the capillary waves on the interface between the inner and outer solutions will be controlled by the interfacial surface tension.

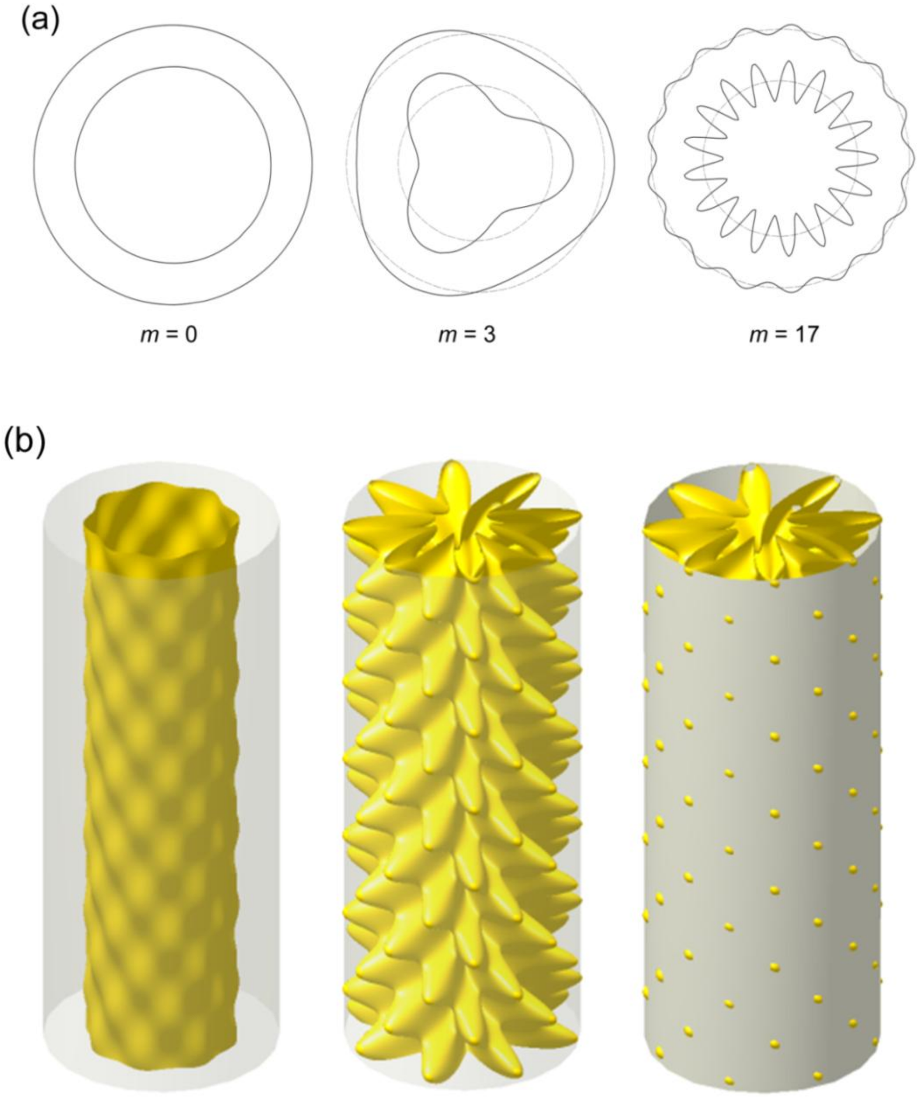

Figure 5.23: a) A series of cross-section of some non-axisymmetric modes for a coaxial fibre. b) A representation of an m=8 non-axisymmetric mode on the core shell interface with different amplitudes showing the formation of the porous fibres.

For a wide range of solvents Beerbower [213] showed that there is a correlation between the surface tension and the Hansen parameters:

$$\gamma_1 = 0.0715V^{1/3}\left[\delta_d^2 + 0.632(\delta_p^2 + \delta_H^2)\right] \tag{5.6}$$

where γ_1 is the surface tension in air for material 1; suggesting that the surface tensions of two solutions would become the same as R_a tends to zero.

For a liquid on a solid surface the cosine of the contact angle decreases with increasing Hansen radius $R_{a.}$ (Eq. 3.15)[214]. When R_a is sufficiently small the contact angle goes to zero as the liquid spreads out to form a thin film. Assuming no mixing, the same trend should be true of two liquids. The contact angle between a liquid and a solid, or in our case two liquids, is given by

$$\gamma_1 cos\theta_c = \gamma_2 - \gamma_{12} \tag{5.7}$$

for liquid 1 on liquid 2, where γ_{12} is the interfacial surface tension. A contact angle of zero would occur if γ_1 and γ_2 are the same and γ_{12} is zero; i.e. the solutions are miscible and R_a is zero. As R_a increases, γ_1 and γ_2 will diverge, and γ_{12} will become non-zero and the contact angle will get larger. We can therefore control the interfacial surface tension by controlling R_a. As we make our solutions more miscible we reduce our interfacial surface tension. Figure 5.23 (b) shows the resulting growth of instability of an m = 8 azimuthal capillary wave, forming intrusions of core solution into the shell and penetrating the fibre surface to leave a regular pattern of porous inclusions similar to that seen in SEM images of sMS fibres (e.g. Figure 5.14(a)).

In co-axial spinning cases where the charge lies on the core-shell interface, therefore, it may be possible to drive interfacial instabilities if the solutions are sufficiently miscible and the interfacial surface tension is sufficiently small. We propose that these instabilities are likely to produce highly porous fibres and can be suppressed either by making the solutions less miscible, as with the IS fibres, or by increasing the viscosity of both shell and core.

In those fibres produced from the semi-miscible solution set sMS-1, the pores are spaced approximately 200 nm apart and have an approximately 50 nm opening on the surface of the fibre. It is interesting to note that the spacing of the pores is roughly the same parallel and perpendicular to the fibre axis, indicating that the same wavenumber is unstable in both directions. Therefore, by controlling the core-shell conductivities, the interfacial surface tension and the viscosities accordingly, it should be possible induce porosity in the fibres in a controlled manner.

There are indications from X-ray and FTIR results that porous fibres spun from semi-miscible solutions may lose some or all of their AB during the spinning process. In the most extreme case, sMS fibres with a nominal AB proportion of 38 wt.% did not show any AB content at all. AB is reported to sublime at higher temperatures [215] but not at room temperature; however, it is possible that AB solution is lost through the pores during the spinning process. Under the strong radial fields and mechanical forces present during spinning, any core solution that penetrates the shell outer surface may be electrostatically sprayed from the fibre.

In the application for hydrogen storage we were interested in reducing the surface porosity to a minimum for successful encapsulation, but the solution selection method I have formulated (as discussed in §3.3.3) could also be used to select solutions with the required properties for controlling fibre porosity in co-axially spun fibres, for nanostructuring hydrides in these fibres (though without encapsulation) and for other applications. In biomedical applications by controlling the size of the pores in co-axial fibres that contains a drug in the core, the release rate of a drug through the porous sheath can be controlled, for example, to make active wound dressings. It is also possible to make structured nanofibres through templating: e.g. if a sol-gel material is spun down the centre of the fibre and then the composite fibre is heated to drive off the polymer and set to oxide it, it would be possible to make highly structured oxide fibres for sensors or catalyst applications.

5.4.5 Structural characterisation: X-ray diffraction

Figure 5.24 and Figure 5.26 show XRD patterns as a function of nominal AB content for sMS-2 fibres and IS-1 fibres respectively. AB/PS fibre patterns show mixed phases of pure tetragonal AB and electrospun PS. It is notable that in most cases there is no sign of a mixed or intercalated phase and that the AB/PS fibres therefore consist of regions of oriented tetragonal AB intermingled with crystalline PS.

While PS pellets consist purely of an amorphous phase, pure electrospun PS consists of some portion of amorphous PS identified as a broad peak with a width of 8° centred around 19° and a smaller peak around 9°, and a crystalline phase superposed on this pattern with a primary peak at 18°, two large sub-peaks at 20 and 22°, and smaller peaks at 28, 29, 38, 41 and 47° (Figure 5.24 to Figure 5.26). This phase has some features which make it distinct from crystallised isotactic or syndiotactic PS [216]: all the peaks are of similar width (~0.8°) and none are present at angles below 18° (d-spacing 2.49 Å), suggesting a lack of long-range order coupled with strain broadening. The influence of solvent evaporation on the formation of semi-crystalline PS after electrospinning can be compared with solution casting, as both cases occur below the PS glass transition temperature. However the strong tensile forces acting during the electrospinning process and subsequent stretching of the PS polymer chains are likely to lead to a strong preferred orientation.

AB incorporated in the fibres, for both semi-miscible (sMS-2) and immiscible (IS-1) solution combinations, is generally in the tetragonal phase (t-AB), but there is greater variance in the intensity of the AB peaks across the sMS-2 fibres, with some samples lacking AB diffraction signal entirely. Interestingly, some of the fibres appear to undergo a change in crystalline structure over a period of time, as observed by the variation in the XRD patterns of the same samples after a period of ~3 months. Though it is not known at which stage the crystalline transition was complete, it is clear that a new AB phase appears in the fibres as the sample ages (see Figure 5.25).

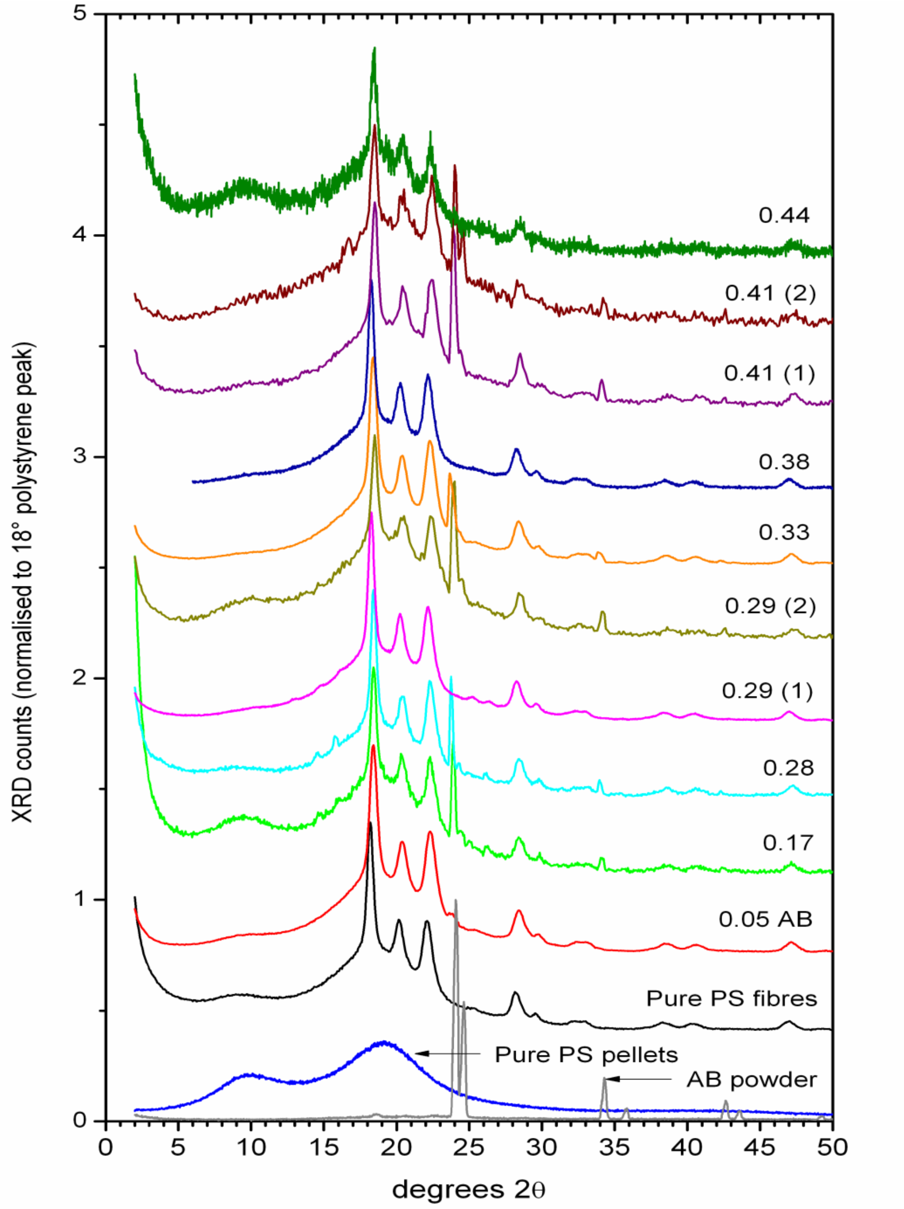

Figure 5.24: XRD patterns of fibres produced from semi-miscible solutions (sMS-2), ordered by nominal AB content (labelled as weighted proportion of whole sample). The X-ray wavelength is 1.5402 Å (Cu Kα). The patterns are normalised to the height of the PS peak at 18°. Also included are pure AB powder diffraction and pure PS fibres from 20% PS in DMF solution.

Omitting these exceptions, there is a trend to more AB diffraction as the nominal AB fraction spun in the sample increases. The XRD measurements are taken from a macroscopic area of sample and with a penetration depth of at least 1 mm and so the variation in AB peak intensity probably reflects variations in the AB content of samples accurately. The ratio of crystalline to amorphous PS varies slightly, as can be seen by the variation in intensity of the 9° peak and the relative intensities of the crystalline and principal amorphous peaks (see Figure 5.25 and Figure 5.27). It is interesting that the crystalline portion of PS disappears in IS-1 fibres containing above a certain portion of AB (≥ 0.33) as shown in Figure 5.26. The reason for this is not immediately obvious looking at the morphological (SEM) data, especially since the crystalline portion of PS is unchanged in sMS-2 fibres containing even higher amounts of AB (as shown in Figure 5.24)

Preferred orientation in the encapsulated AB is evident from the change in intensity ratios of the two most intense peaks, the (1 1 0) at 23.8° and the (1 0 1) at 24.4° 2θ, from bulk powder AB. The powder averaged intensity ratio is given to be 3:2 for (1 1 0) to (1 0 1), but in bulk AB this ratio appears closer to 2:1. In the fibres, the (1 0 1) peak is in many cases <1/10 the intensity of the (1 1 0) peak. For a (1 1 0) preferred orientation plane, the March-Dollase parameter [217], which represents the effective sample compression or extension due to the preferred orientation effect, is 0.8 for bulk AB (as determined by data fitting in the PowderCell program). However, the range of preferred orientations evident in sMS fibre diffraction patterns have March-Dollase parameters from 0.5-0.7. This suggests that a higher degree of preferred orientation is present in the AB in electrospun fibres. As the fibres are flattened lengthwise onto the XRD sample platform, this orientation indicates that the AB is preferentially aligned with the crystallographic c-axis parallel to the fibre axis.

Small variations in the peak positions for both AB and PS suggest that there is slight variation in the unit cell dimensions, which may arise from an interaction between core and shell material where they mix. These do not vary consistently with AB content. PS in single phase fibres appears to have a slightly larger unit cell than in the co-axially spun fibres. In the case of fibres from IS-1, this pattern is clearer. The ratio of the AB (1 1 0) at 23.7° to the (1 0 1) peak at 24.5° is changed in both cases from bulk AB. In most cases (for both sMS-2 and IS-1 fibres) the peak widths of both crystalline PS and AB are not significantly changed within the resolution of the instrument, implying that no reduction in crystal dimensions from the bulk occurs. While morphological differences are observed between the two AB-PS fibre sets, the XRD is not particularly sensitive to the differing morphologies in the fibres (see Figure 5.27 for a comparative XRD plot of the two fibre sets, AB and pure PS fibres).

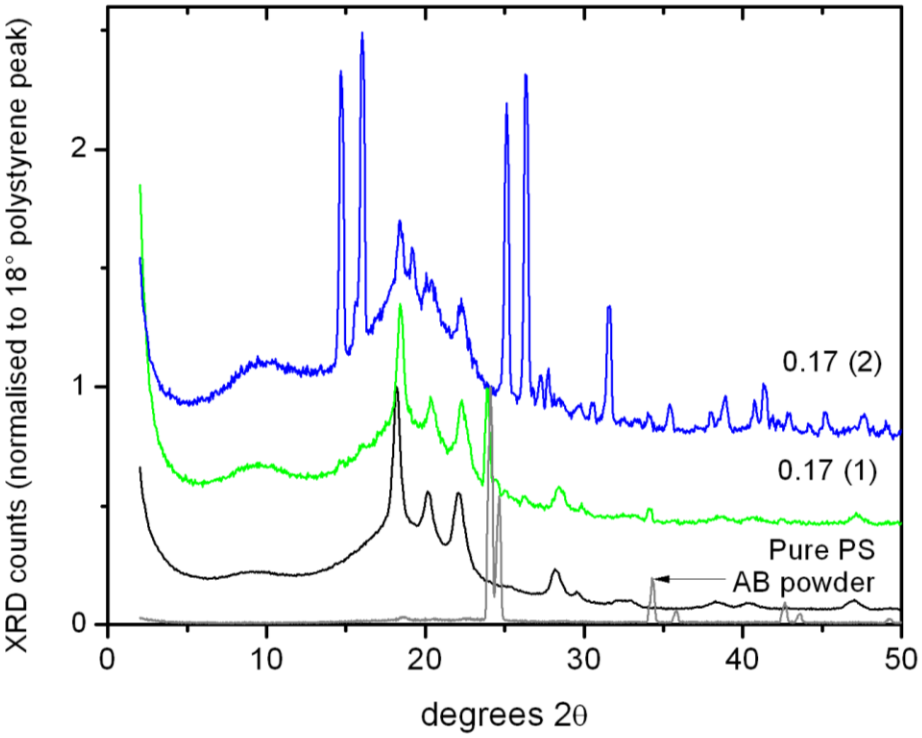

Figure 5.25: XRD patterns of fibres produced from semi-miscible solutions (sMS-2), showing anomalous phase of AB compared with typical pattern of fibres with the same nominal AB content. The X-ray wavelength is 1.5402 Å (Cu Kα). The patterns are normalised to the height of the PS peak at 18°. Also included are pure AB powder diffraction and pure PS fibres from 20% PS in DMF solution.

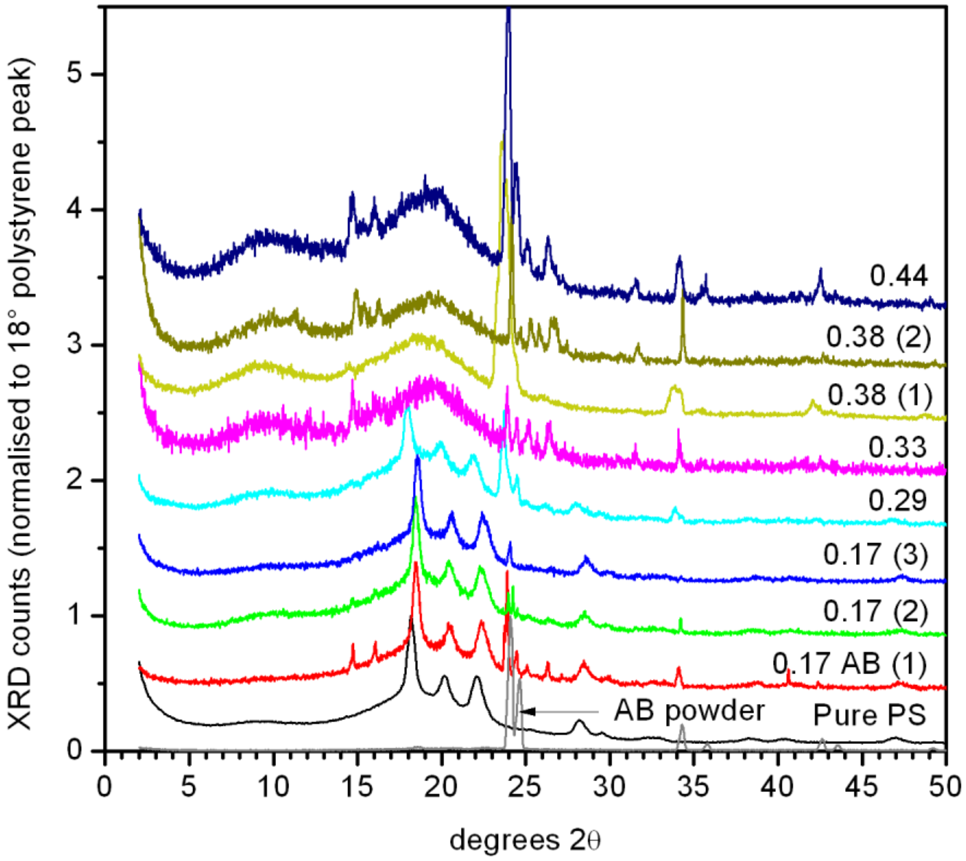

Figure 5.26: XRD patterns of fibres produced from immiscible solutions (IS-1), ordered by nominal AB content (labelled as weighted proportion of whole sample). The X-ray wavelength is 1.5402 Å (Cu Kα). The patterns are normalised to the height of the PS peak at 18°. Also included are pure AB powder diffraction and pure PS fibres from 20% PS in DMF solution.

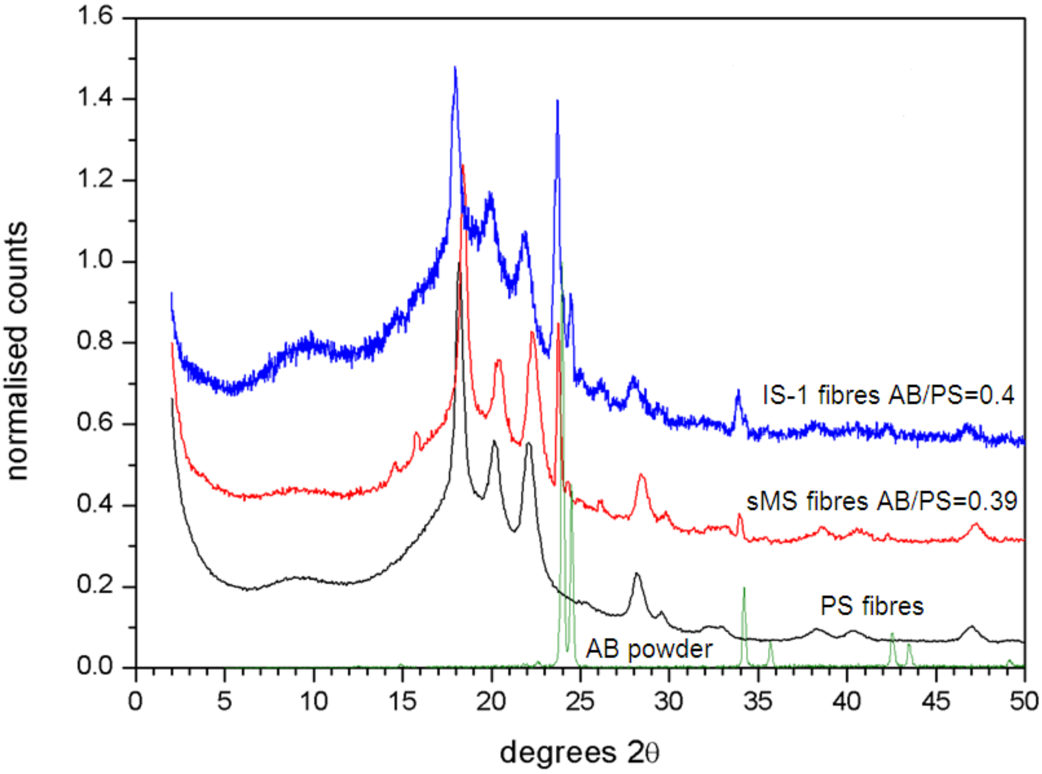

Figure 5.27: X-ray diffraction patterns of AB powder, electrospun PS fibres, electrospun AB-PS fibres spun using miscible and immiscible core-shell solution combinations. X-ray wavelength 1.5402 Å (Cu Kα). Patterns are normalised to the height of the PS peak at 18° and offset for clarity.

5.4.6 Thermolysis properties of AB-PS fibres: DSC, TGA and mass spectroscopy analysis

5.4.6.1 Differential scanning calorimetry

From DSC measurements the fibres show a mixture of thermolysis characteristics. Figure 5.28 shows DSC measurements on neat AB (at a heating rate of 1 and 5 °C/min). As characteristic of AB decomposition, a melt endotherm precedes the first decomposition exotherm, which starts before the melting is complete. At a heating rate of 1 °/min the exothermic peak, which commences during melting (between 95 and 100 °C) peaks at ~105 °C. The second reaction is not very visible, but appears to take place between 130 and 150 °C. At a heating rate of 5 °/min the reaction temperatures for neat AB are shifted up in temperature by ~ 8-10 °C; first reaction commences at ~ 115 °C and peaks at ~120 °C, the second peak is not visible but the first has a long tail up to approximately 150 °C, which indicates a reaction is still commencing up to this point.[1] This data compares well to that reported by Wolf *et al.*, as discussed in §5.2.1.3 and reproduced in

Figure 5.2; the only exception being that they have observed a strong signal for the second reaction at around 140 °C, whereas we see this peak to be suppressed significantly.

The DSC data for pure PS fibres (PS post-spinning) and pellets (PS prior to spinning) is shown in Figure 5.29. While the PS pellets only show a glass transition at ~100 °C, the PS fibres show no transition up until the end point of the measurements (300 °C). A thermogravimetric analysis on the PF fibres has shown the fibres to decompose at ~ 350 °C. According to these results, which show no melt endotherm, the electrospun PS fibres are non-crystalline. These results show some inconsistency with the XRD data on PS fibres, which showed (see Figure 5.24) the electrospun fibres to have some

---

[1] The sloping background seen in the data collected for the run at 1 °/min is due to an instrumental problem in the DSC, which has been calibrated out to ensure the actual measurements are corrected.

crystalline structure. Thus, further analysis is needed to determine why the DSC and XRD data do not match.

The DSC measurements on the AB-PS fibres (all of which were taken at a heating rate of 1 °C/min) show differing results between different fibre sets. While the data have shown some inconsistency between different fibre sets depending on the AB proportion in them and the day they were electrospun, there appears to be a sharp difference between some sMS-2 and IS-1 fibres. In sMS fibres the decomposition temperature of AB is generally lowered while in IS-1 fibres the decomposition is more bulk like, as shown in Figure 5.30 and Figure 5.31 respectively. In some sMS fibres where the decomposition of AB takes place at a temperature below the melting temperature (112-114 °C), no melting endotherm is observed (Figure 5.30).

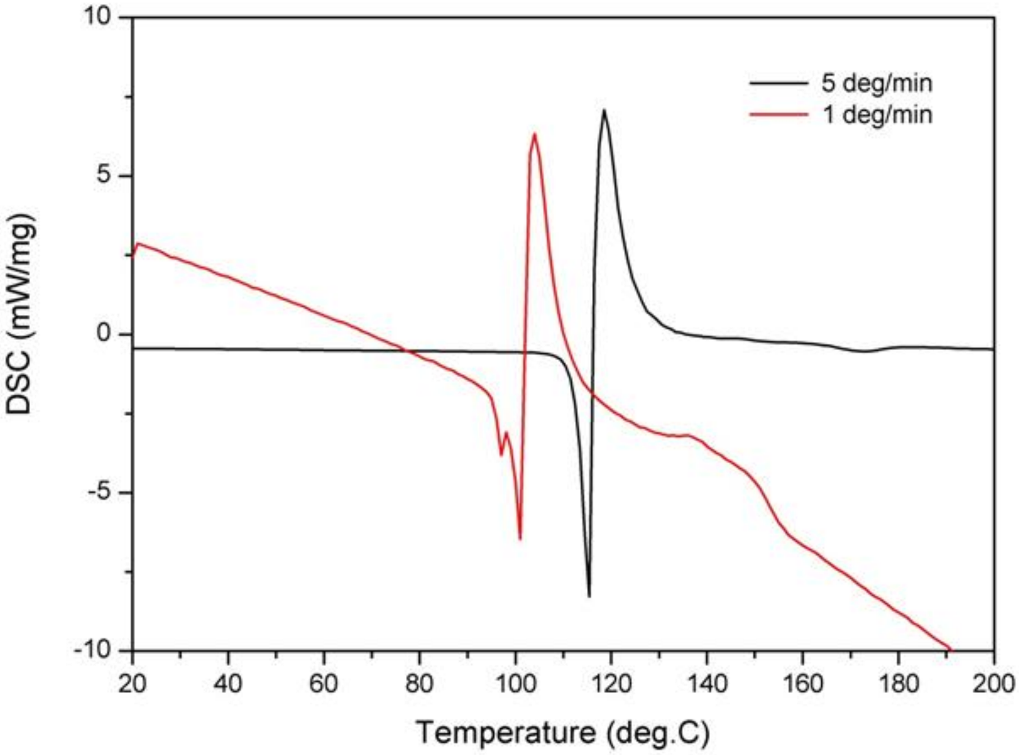

Figure 5.28: DSC measurements of neat AB at heating rates of 5 and 1 °/min. The peak corresponds to the first exothermic reaction that realises the first H_2 molecule in the decomposition of AB and the troth corresponds to the melting of AB, which coincides with the start of the reaction.

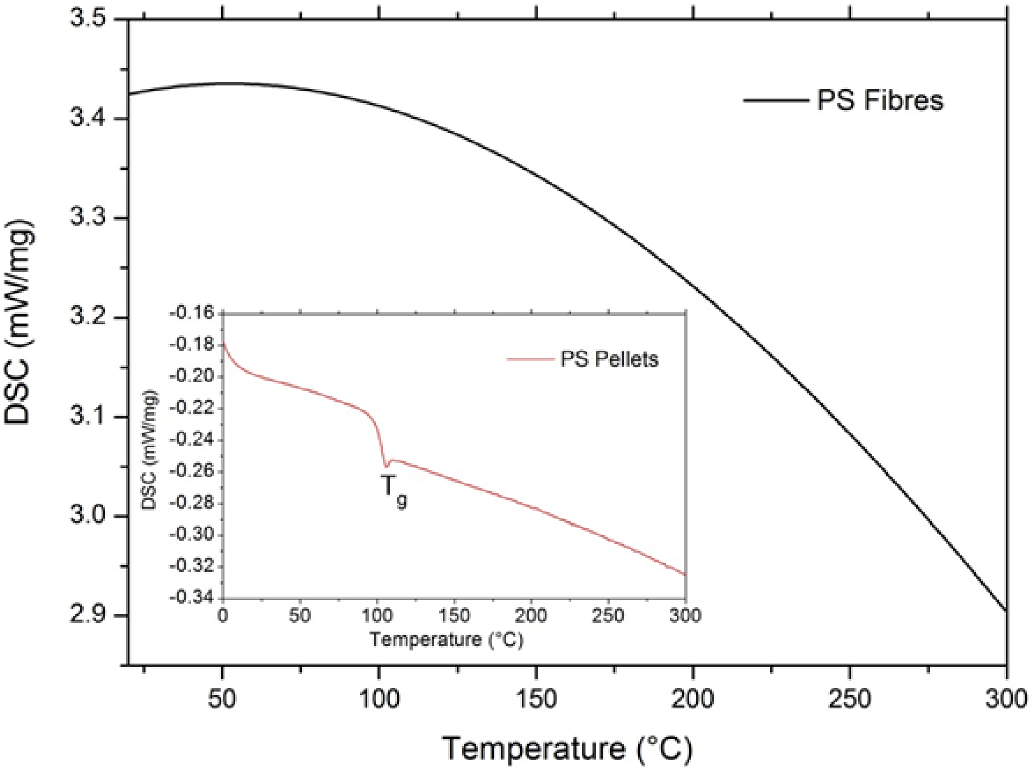

Figure 5.29: DSC measurements of pure Polystyrene (PS) fibres (post electrospinning) and PS pellets (prior to electrospinning) as show in the inset.

In the case of fibres obtained from sMS-2 with 10 wt.% AB in the core, the decomposition temperature is lowered significantly, down to ~94 °C in some samples (as shown in Figure 5.32) and no discernable trend is seen with AB proportion in the fibres. However, with 20 wt.% AB in the core of these fibres, the decomposition behaviour is more bulk-like, and the decomposition temperature appears to increase slightly with AB proportion in the fibres. Likewise, the fibres obtained from IS-1 appear to show a bulk like decomposition behaviour, with both 10 and 20 wt.% AB in the core. Analysis of the SEM images of each fibre sets show that sMS-2 fibres with 10 wt.% AB (the only ones to show reduced decomposition temperatures in this particular set) are the only fibres with significant porosity, see Figure 5.33. Thus, porosity clearly has the effect of reducing the decomposition temperature, indicating nanostructuring of AB in the porous fibre sets.

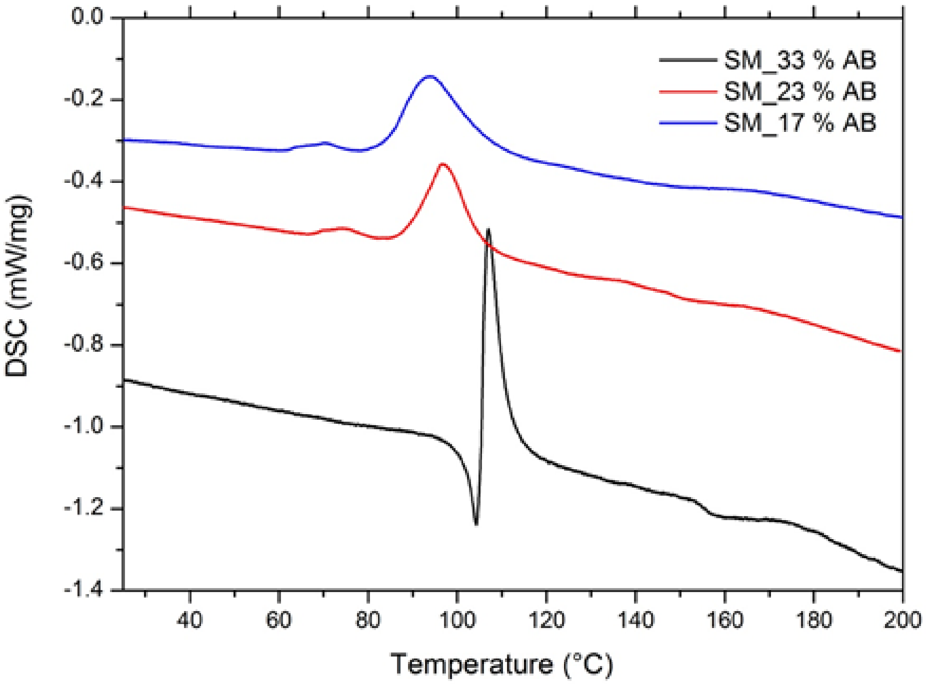

Figure 5.30: DSC measurements of sMS-2 fibres electrospin with 10 wt.% AB in core, measured at a heating rate of 1°/min (plotted as black squares in Figure 5.32; note AB proportions for comparison).

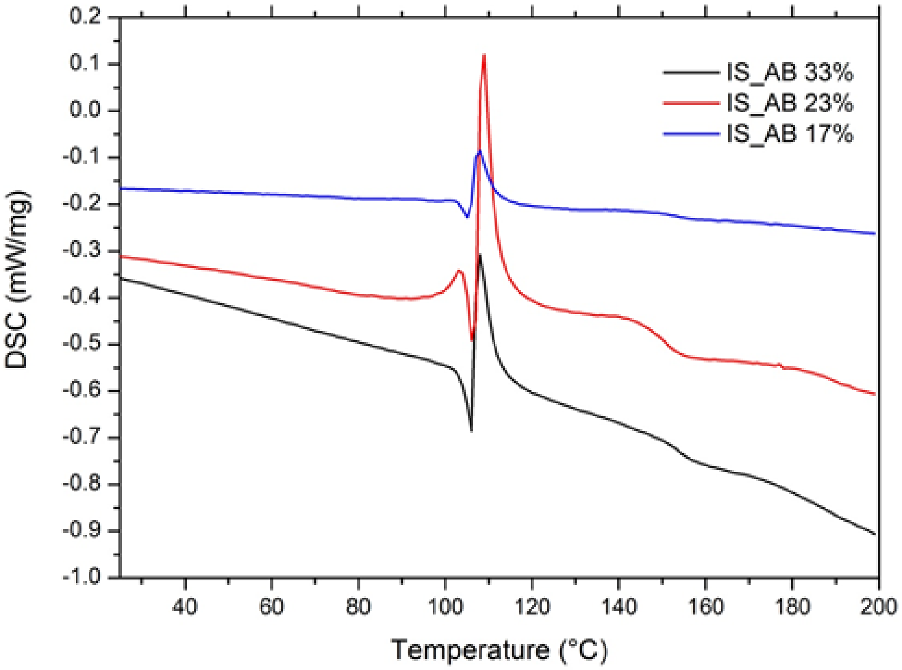

Figure 5.31: DSC measurements of IS-1 fibres electrospun with 10 wt.% AB in core, heating rate of 1°/min (plotted as green triangles in Figure 5.32).

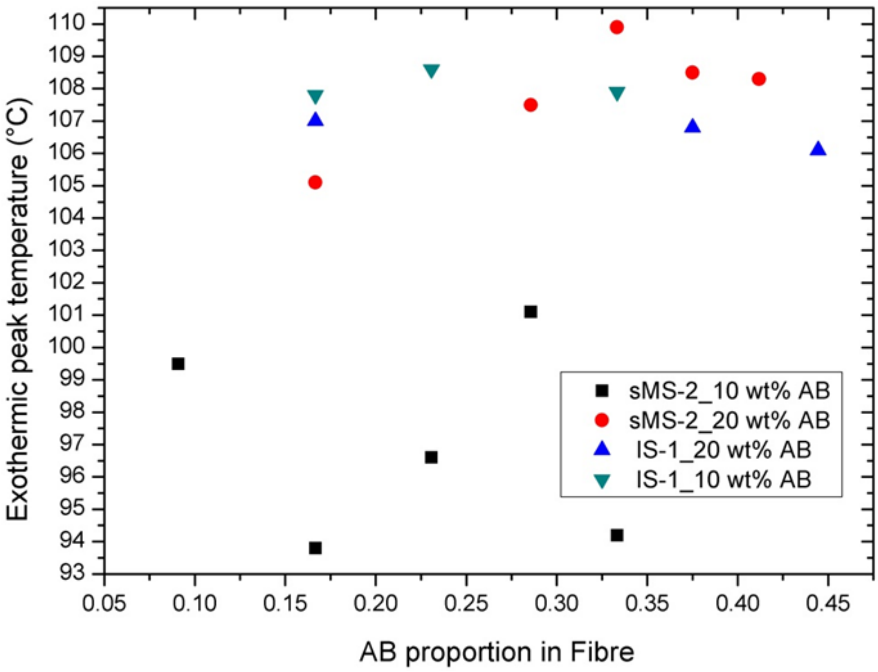

Figure 5.32: AB decomposition temperature vs. AB proportion in the fibres.

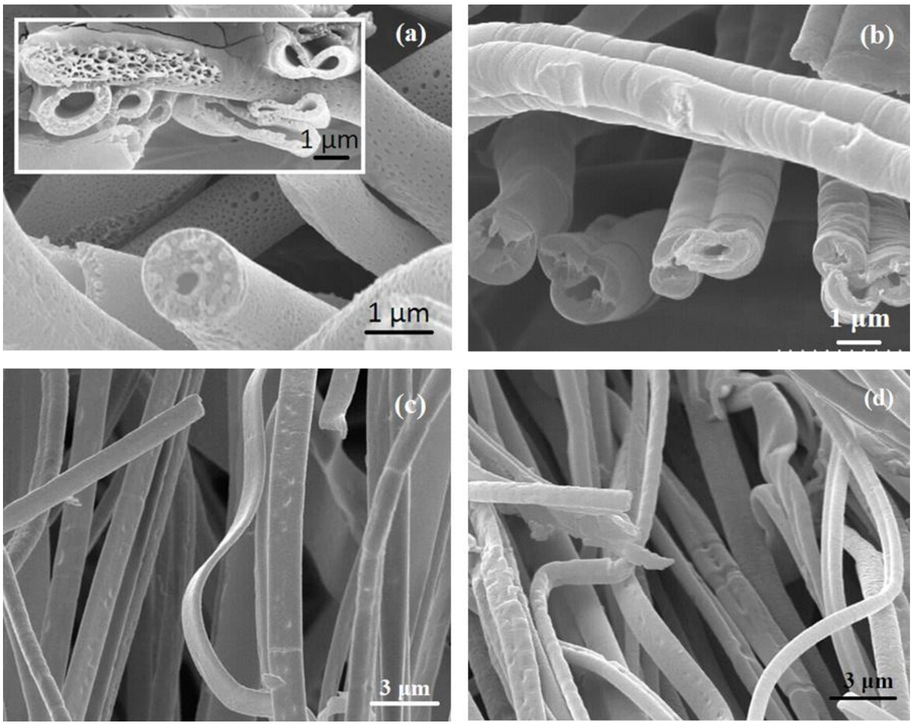

Figure 5.33: SEM images of fibres corresponding to the DSC data in Figure 5.32; a) sMS-2 fibres with 10% AB, b) sMS-2 fibres with 20% AB, c) IS-1 fibres with 10% AB, d) IS-1 fibres with 20% AB.

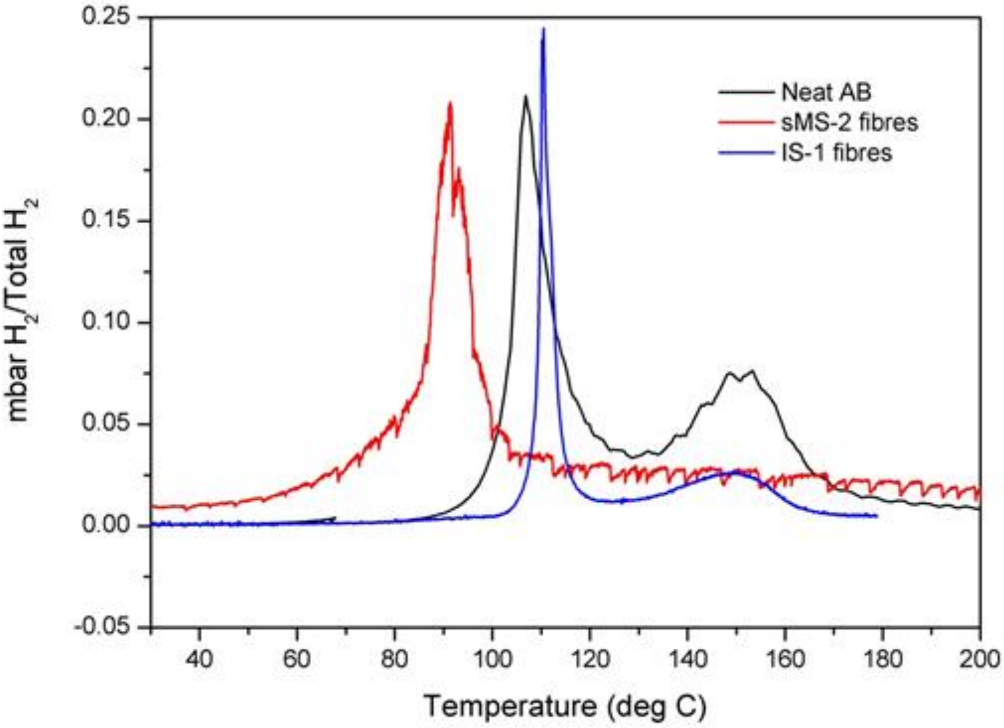

Figure 5.34: Hydrogen mass spectrometry measurements of hydrogen from thermolysed neat AB and sMFs fibres into 1.0 bar Ar carrier gas, and IS-1 fibres into He carrier gas stream. Heating rate = 1°C min^{-1}.

5.4.6.2 Thermogravimetric analysis

Thermogravimetric data obtained using the IGA (as detailed in §4.2), during the thermolysis of the fibres, show results in agreement with the DSC data discussed above. However once again, while there is a particular trend in the thermolysis behaviour of a given fibre set, the results can show small variations between samples made from a given solution set made and electrospun on different days. For example the decomposition temperature of AB in the fibres can differ a few degrees between samples made of solutions with the same formula. While the exact reasons for these variations in the fibres were not determined during the time of this PhD project (mostly due to the vast number of variables that have to be controlled), it is thought that factors such as the variation in solution conductivity over time (as discussed in §5.4.3), viscosity and even the actual core solution flow rate, which at times appeared not to match the set flow rate (as determined by the air gap in the syringe) are all possible factors for the small variations between a given fibre set. Due to the availability of a large amount of data obtained from many different fibre samples, the data discussed here is only representative of the thermolysis behaviour of a given sample set; neat AB, sMS and IS fibres. In the case of sMS-2 fibres the hydrogen releasing reaction was initiated at around 60 °C, reduced significantly from the value of ~95 °C in neat AB, with the peak hydrogenation temperature reduced to 90°C from the value of 110° in neat AB (as shown by the red peak in Figure 5.34). However, in the case of IS-1 fibres, in accordance with the DSC measurements, the decomposition was more bulk-like (as shown by the blue peak in Figure 5.34)[2]. In the SMS-2 sample the second hydrogenation reaction observed at around 150 °C for neat AB is either suppressed or lowered down in temperatures (i.e. starting before the first is complete) and hence not clearly visible as a separate peak, or it does not take place at all. In the case of IS-1 fibres, the second reaction peak is present but suppressed.

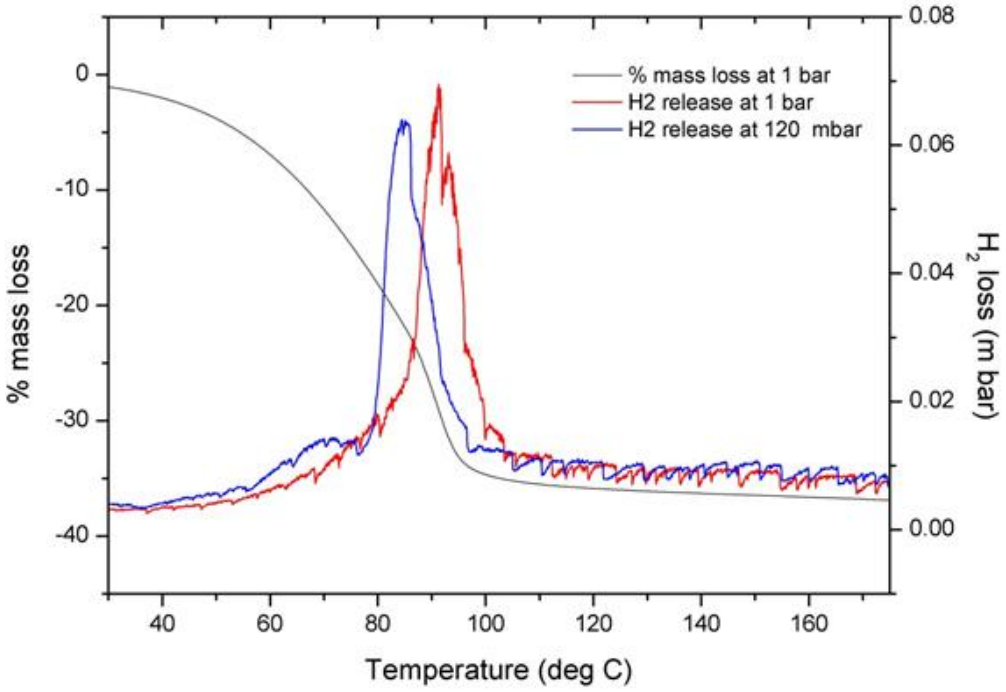

Figure 5.35: Hydrogen mass spectrometry measurements of hydrogen from thermolysed sMS fibres into 0.12 bar Ar carrier gas (blue line) compared to that

---

[2] A different IGA-MS set-up (set-2 of the same model) was used to obtain the H_2 loss data from IS-1 sample in Figure 5.34.

taken at ambient pressure (1 bar, red line). Heating rate = 1°C min^{-1}. Mass loss data for sample at 1 bar (black line) shown for comparison with mass spec data.

Furthermore, little or no borazine and diborane emission was observed in sMS-2 fibres. These differences between the decomposition of neat AB and sMS fibres suggest a different decomposition pathway of AB in sMS fibres, possibly due to nanostructuring of AB in the porous fibres produced from semi-miscible solutions. The peak temperature of the first hydrogenation reaction was found to be reduced even further with the pressure around the sample lowered from ambient (1 bar) to 0.12 bars, as illustrated in Figure 5.35. The influence if sub-ambient pressure on the isothermally induced decomposition of AB is reported in a recently published study [138] (after the measurements in Figure 5.35 were taken). The authors of the study report that at pressures below 800 mbar the induction period is appreciably reduced, leading to the release of the first equivalent of hydrogen from AB at shorter reaction times. A possible cause for the reduction in the induction time, as we have observed (Figure 5.35) is attributed to the observed sublimation of AB at lowered pressures, which apparently can cause disruption of the dihydrogen bonding network in the AB crystals as a result of defects that occur during the physical sublimation. Since previous studies have shown that disruption of dihydrogen bonds in AB facilitates the isomerisation of AB to the diammoniate of diborane (DADB), followed immediately by the release of molecular hydrogen, sublimation of AB is provided as the possible reason.

The difference between the semi-miscible and immiscible fibre sets is further highlighted in Figure 5.36 which shows a typical series of thermogravimetric mass loss measurements from both fibre sets as a function of temperature. To 200 °C, with AB/PS ratios as a comparative indicator, more mass is lost from sMS fibres – up to 30% in samples shown in Figure 5.36 , but as much as 50% in some cases (as shown in Figure 5.37). The characteristic mass loss curve suggests that desorption for sMS fibres begins at temperatures significantly below 110 °C, although the amount of mass lost is far greater than the value of 12 wt.% [174] expected for the desorption of $2H_2$ per entrained NH_3BH_3 molecule below 150 °C. In the case of IS fibres, the trend in mass loss more closely follows that predicted by desorption of only hydrogen from the entrained AB, being <10 wt.% in general, and the temperature of greatest mass loss rate (i.e. the peak temperature) is approximately 110 °C.

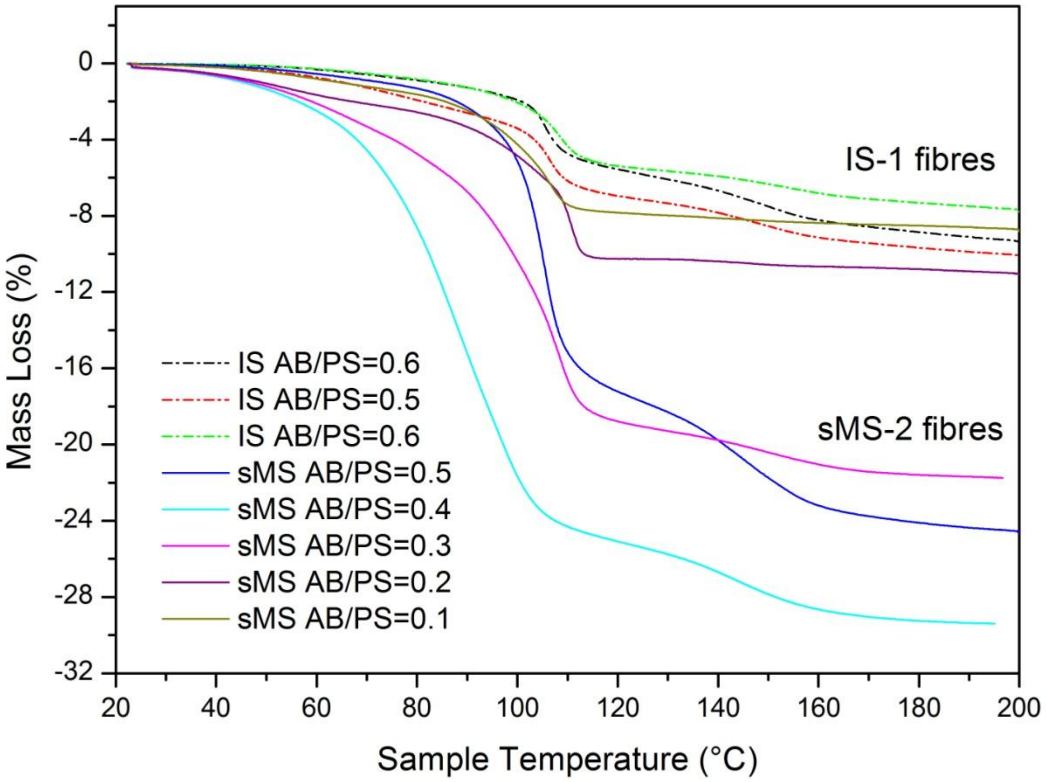

Figure 5.36: Thermogravimetric mass loss as a function of temperature for fibres obtained from immiscible (IS-1) and semi-miscible (sMS-2) solution sets, at a heating rate of 1 °/min.

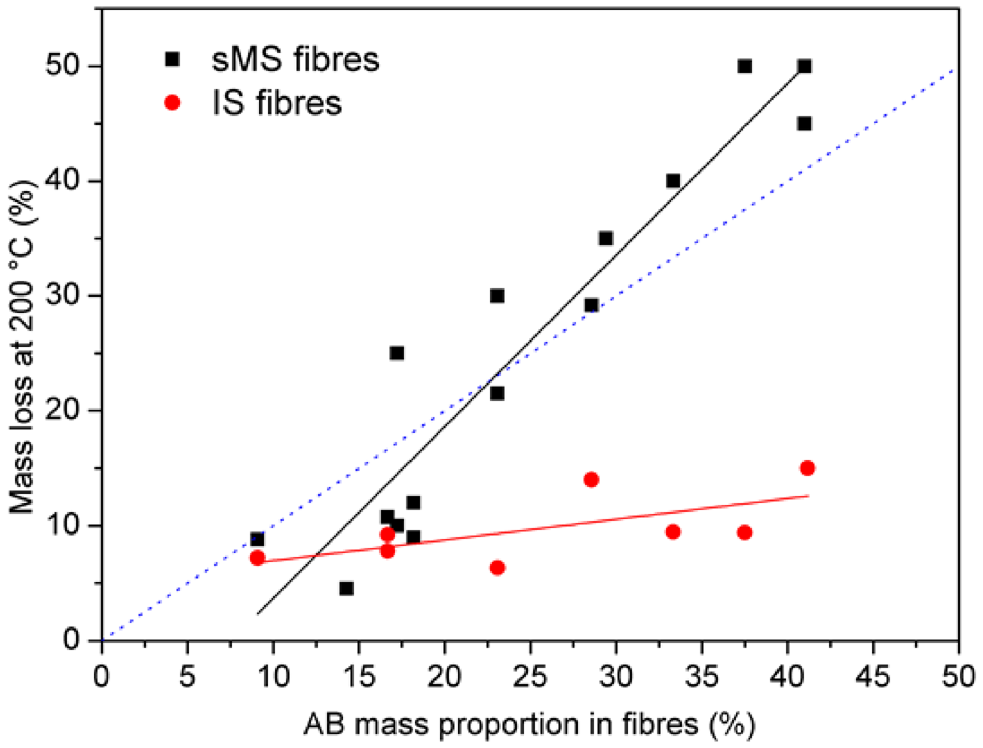

Figure 5.37: Thermogravimetric mass loss on heating at 1°/min to 200 °C immiscible (IS-1) and semi-miscible (sMS-2) samples, as a function of sample nominal wt.% AB, with linear fits. The dashed line represents x=y.

The marked difference between the sMS-2 and IS-1 fibres is more obvious with the plot of fibre mass loss to 200 °C as a function of nominal AB content of fibres (expressed as a percentage of total fibre mass), as shown in Figure 5.37. Immiscible solution-based fibres show mass loss on heating that scales weakly with AB proportion, from 7 to 12 wt.% across a 40 wt.% range of AB. The fibres from sMS set show a much greater mass loss as shown in Figure 5.36 , which fits closely with the starting AB wt.%.

The total mass loss measured for neat AB heated up to 200 °C at 1°/min was also found to be excessively high, with up 50% mass loss found in some thermogravimetric measurements. While a mass loss of 35% is reported in literature for neat AB heated at 5°/min up to 200 °C [187], such a large reduction in mass is puzzling. The amount of mass loss in the samples raises questions as to what is differing in the decomposition processes between the volatiles released, or even if the mass loss is purely due to the release of volatiles in the case of neat AB. The problem with AB is that it tends to foam and expand out of its container due to the release of volatiles when heated. For this reason the large mass loss seen in the thermogravimetric data was initially not just attributed to the release of volatiles, but to the physical loss of AB from the container. But even with controlled measurements of small amounts of AB, which did not overflow out of the container, such high mass losses were observed. The high mass loss seen in the AB-PS fibres, however, was clearly due to the loss of volatiles and not physical mass loss, since these samples were retrieved as hardened nuggets of brittle and crumbly material, fully entrained in the sample container post heating, no sample loss was possible.

Thus, the mass spectroscopy measurements taken in conjunction with the thermogravimetric data was rigorously analysed for clues for the volatiles causing the large mass loss during heating. Figure 5.38, Figure 5.39 and Figure 5.40 show the mass spectra of AB, sMS-2 and IS-1 samples, respectively, taken while the samples are incubated at 88 °C (the samples are raised to 88 °C in less than 10 minutes). The background species/fragments (i.e. those detected with an empty can run) are annotated with horizontal lines on the red bars). These species/fragments are thought to be H (AMU=1), H_2O(AMU=18), $^{40}Ar^{2+}$ (AMU=20) and ^{36}Ar(AMU=36) and appear to saturate the spectra. The spectra for all samples are rather similar. There is a trace amount of a species with AMU=28, which could be diborane. However it should be noted that diborane was not seen in the spectra when the samples were heated at 1 °C/min up to 200 °C. Unfortunately, volatiles with AMU>50 could not be detected with the mass spectrometer used to look at these specific samples. Thus, tracing borazine (AMU=81) was not possible. However, the mass spectra from another mass spectrometer[3], which had an AMU range of $1 \leq AMU \geq 100$, showed no signs of borazine in neither of the sMS or IS samples. This second data set is not presented here as the instrument background spectrum was not available, and thus, a reliable comparison cannot be made between the samples.

---

[3] This mass spectrometer is located at the Chemistry department of University of Oxford, and access to it was limited.

This data (Figure 5.39 and Figure 5.40) however, does not explain the large difference in the mass loss seen in thermolysis of sMS-2 and IS-1 fibres. Since the mass loss cannot be explained by a normal loss of H_2 gas, it is likely that heavier fragments that are not detected by the mass spectrometer cause the difference in the mass loss. However, it is also possible that the difference in mass loss between the sMS-2 and IS-1 samples is attributed to the morphology of the fibres rather than the difference in the volatiles emitted. In the sMS-2 fibres the volatiles will be released more easily through the pores or the hollow core of the fibres. But in the case of IS-1 fibres, which are mostly collapsed and non-porous, some volatiles may be trapped in the core (or released at lower quantities). More detailed analysis of the mass spectra data is required to determine the kind of reactions taking place along with normalisation for sample mass and full calibration of the mass spectrometer.

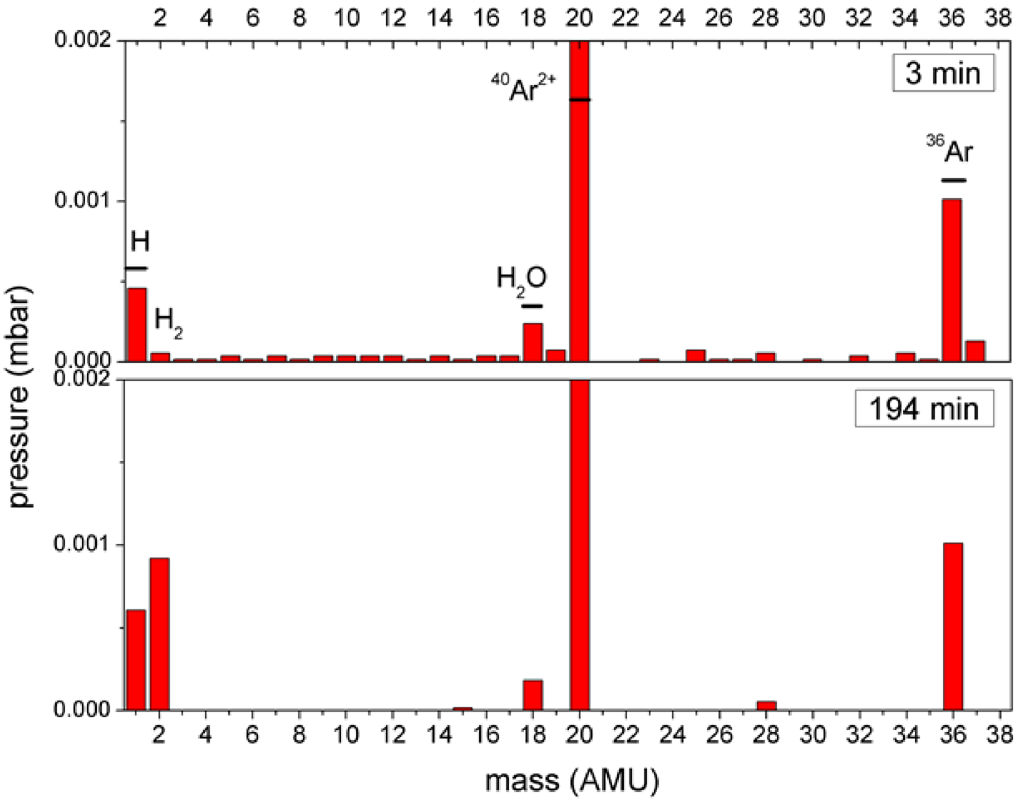

Figure 5.38: Mass spectra of neat AB rapidly heated to and incubated at 88 °C for 4 hours, partial pressure of fragments detected under Ar carrier gas.

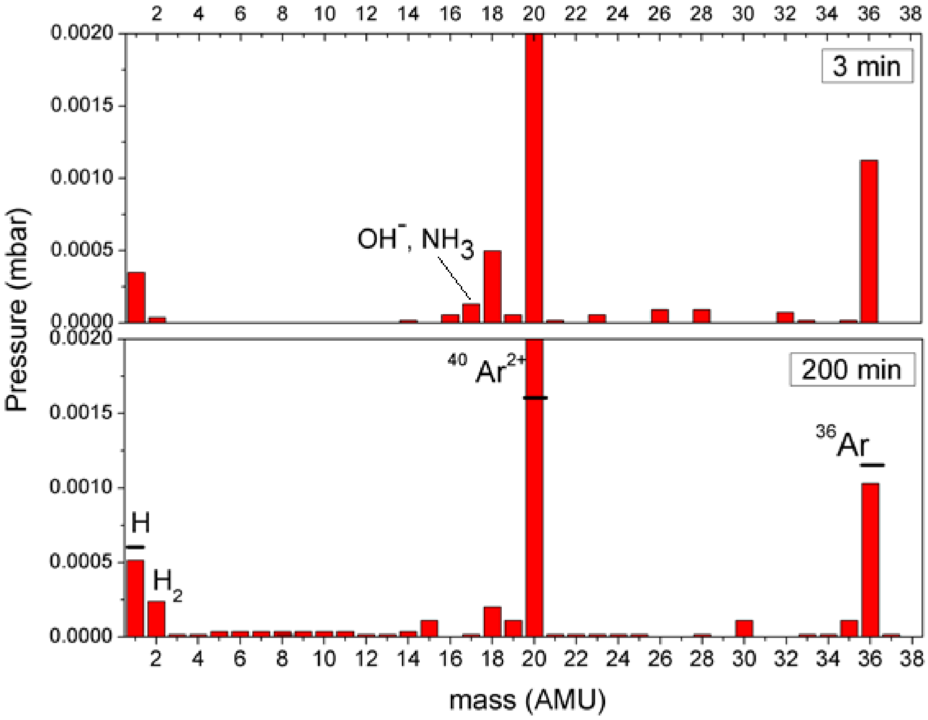

Figure 5.39: Mass spectra of a sMS sample rapidly heated to and incubated at 88°C for 4 hours, partial pressure detected under Ar carrier gas.

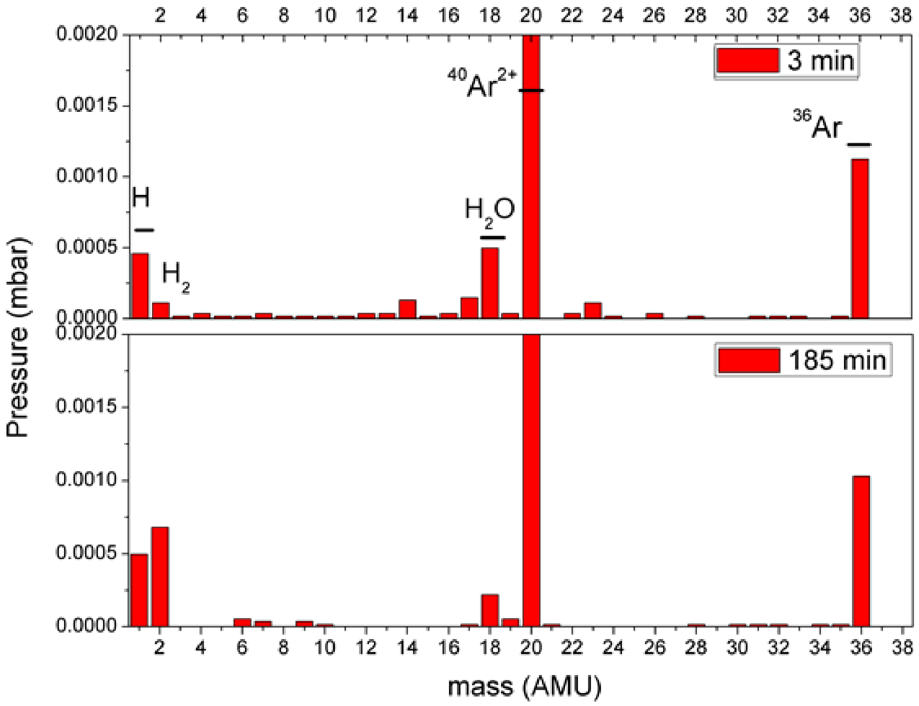

Figure 5.40: Mass spectra of an IS sample rapidly heated to and incubated at 88 °C for 4 hours, relative partial pressure detected under Ar carrier gas.

Another important point to note is that on fast heating to 200 °C (>10°/min.) under dynamic vacuum, AB is found to evaporate and reform on cooler surfaces inside the furnace tube (the 'fingerprinting' of the deposited AB was carried out using FTIR spectroscopy). Sublimation of AB, though not commonly reported, has been observed in other experiments [138, 187] at sub-ambient pressures. It is therefore possible that the large mass loss observed in the sMS-2 fibres is partly due to sublimation of the encapsulated AB through the porous structure to the fibre surface and out of the fibres, a route largely inaccessible in the IS-1 fibres, where the AB core is physically separated from the fibre surface by the polymer sheath which has a lower degree of porosity. The slow heating rate and ambient pressure of the TGA carrier gas should preclude this possibility in the case of bulk AB, but the nanostructured mixed-phase sMS-2 fibres may conceivably increase the thermodynamic selectivity of this route. On the other hand, there is no sign of gaseous molecular AB (30-31 AMU) in sMS-2 sample's mass spectroscopy data so if this is occurring the AB must condense out of vapour phase or decompose further, long before it is carried to the mass detector. Investigation into identifying all the thermolysis molecules released and the difference in the mass loss seen between different fibre sets continues beyond the study discussed in this thesis.

Isothermal thermogravimetric studies have been performed on AB-PS fibres made from semi-miscible solution sets (sMS) with the fibre samples incubated at a temperature of 85 °C for a period of time.[4] While the data produced were variant between fibre sets made from different AB-PS ratios, the general trend has been in the lowering of the peak induction time of the decomposition reaction in the AB-PS. A comparison between thermolysis results of neat AB (Figure 5.41) and sMS fibres (Figure 5.42) shows that the peak induction time of the hydrogenation reaction is lowered by an order of magnitude for the fibres as compared to the time taken for neat AB; in the

---

[4] TGA isothermal measurements on AB-PS fibres were taken by my colleagues as part of the work following on from that reported here and I have selected only an example to report on.

case of sMS fibres the reaction is complete in 15 minutes whereas for neat AB it takes ~150 minutes (as deduced from the width of the H_2 release peaks). This is a clear indication for improved reaction kinetics in the sMS fibres. These results, in addition to the DSC and TGA thermolysis data at 1 °C/min heating rates, suggest the nanostructuring of AB in the sMS fibres. Taking a look at the evolution of the species detected through mass spectroscopy over time (Figure 5.44), it appears that NH_3 and B_2H_6 (or N_2) evolves at the point the hydrogenation reaction takes place.

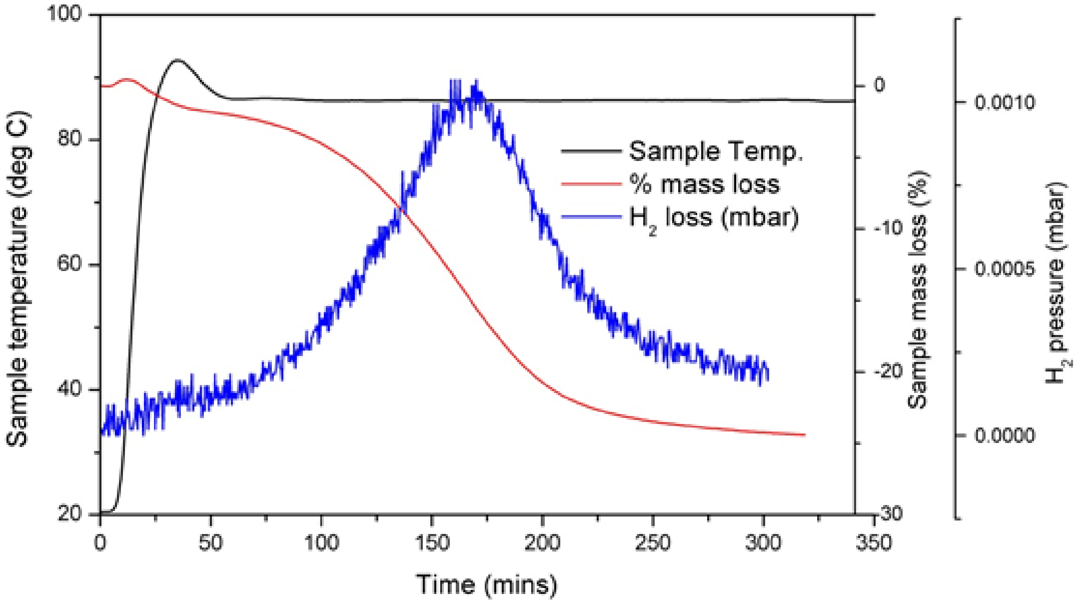

Figure 5.41: Thermogravimetric and mass spectrometry measurements of hydrogen from neat AB into 1 bar He carrier gas with the sample rapidly heated to and incubated at 85 °C. Sample mass loss data from IGA (red line) compared to H_2 loss (pressure) data from mass spec (blue line), with the corresponding sample temperature shown (black line).

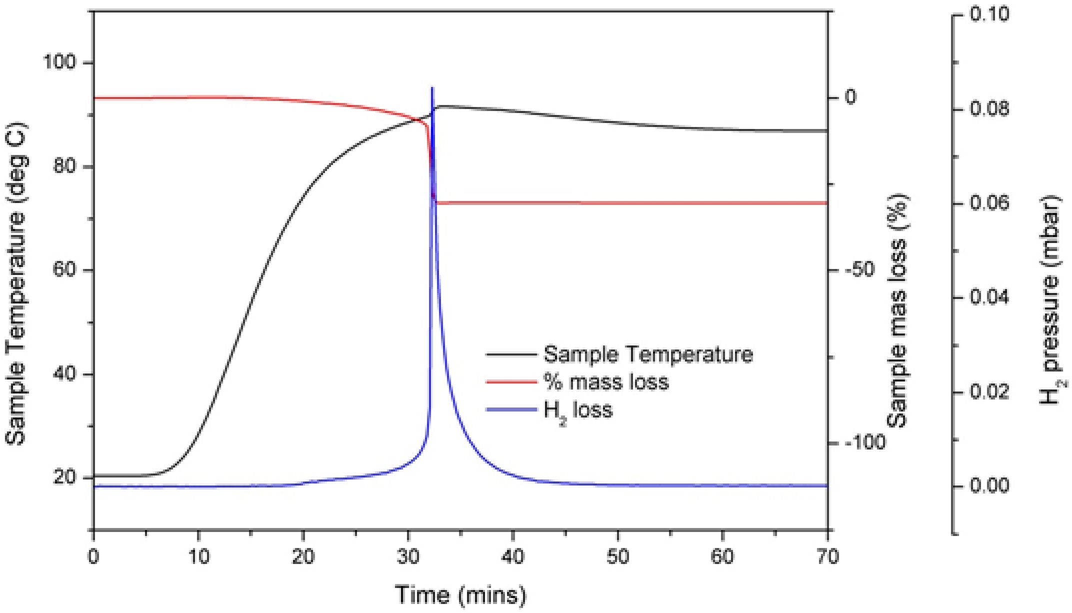

Figure 5.42: Thermogravimetric and mass spectrometry measurements of hydrogen from a set of sMS fibres (made from *15 wt.% PS in 5:1 Tol: DMF (shell) and 10 wt.% AB in DMSO* (core) at shell-core flow rate ratio of 1000:750 ul/hr) into 1 bar He carrier gas with the fibres rapidly heated to and incubated at 85 °C. Sample mass loss data from IGA (red line) compared to H_2 loss (pressure) data from mass spec (blue line), with the corresponding sample temperature shown (black line).

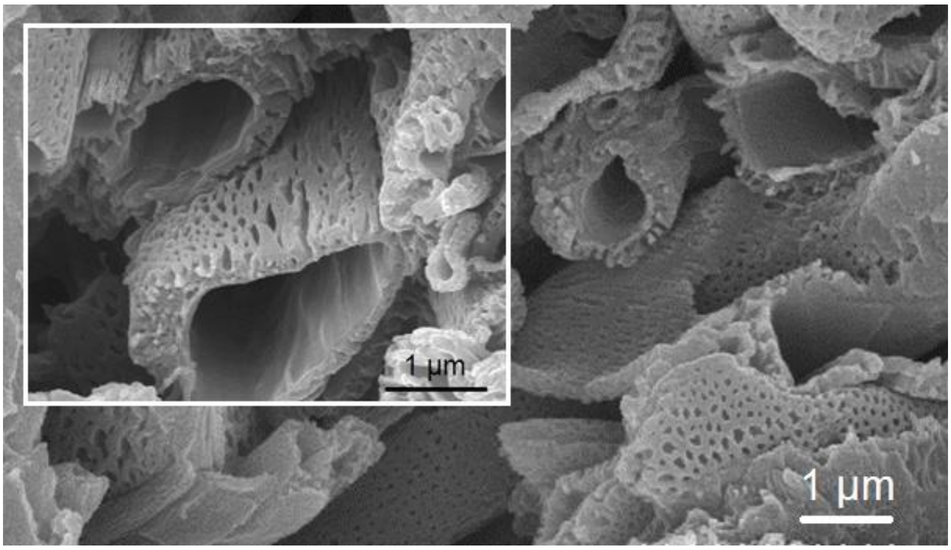

Figure 5.43: SEM image of sMS fibres prior to being incubated at 85 °C.

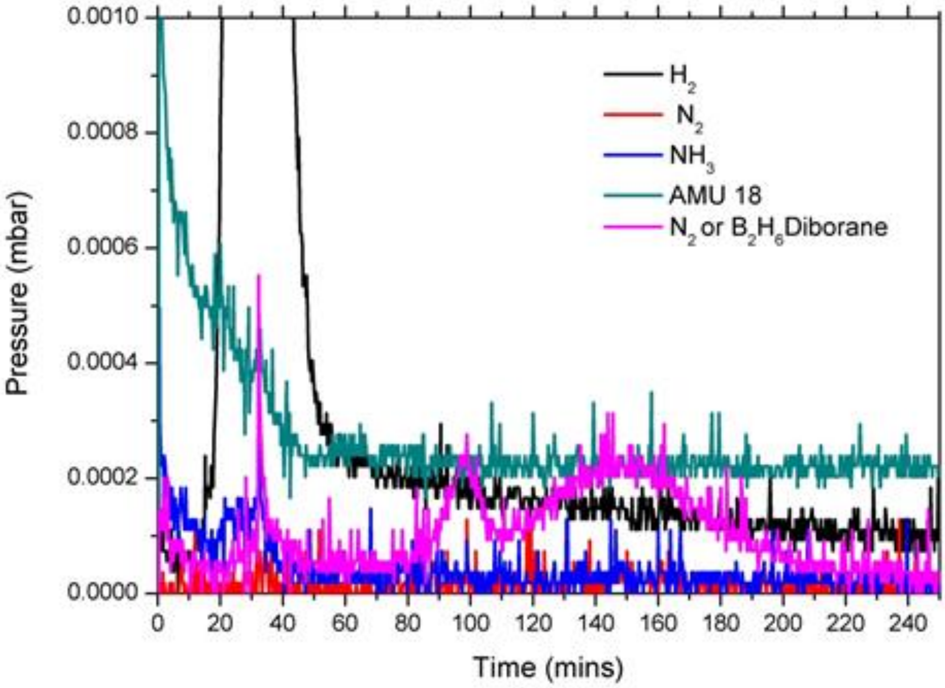

Figure 5.44: Mass spectrometry data from sMS fibres (made from *15 wt.% PS in 5:1 Tol: DMF* (shell) and *10 wt.% AB in DMSO* (core) at shell-core flow rate ratio of 1000:750 ul/hr) into 1 bar He carrier gas with the fibres rapidly heated to and incubated at 85 °C.

5.4.7 ATR-Fourier transform infrared spectroscopy

FTIR data showing the spectra of as-received AB, electrospun single-phase PS fibres and typical sMS and IS AB-PS fibre samples are shown in Figure 5.45. The PS-containing samples are normalized to the highest-intensity PS peak at 700 cm^{-1}, and the pure AB spectrum is normalized to the intensity of the B-H stretching mode in the IS fibre spectrum at 2300 cm^{-1}. The AB-PS spectra are very similar and consist principally of a linear combination of the pure PS and pure AB modes. There is minimal interaction between the AB and the PS modes, though two modes are shifted or created (marked •). The marked mode at 1020 cm^{-1} shows a significant exchange of intensity with the B-H_2 torsional mode at 1055 cm^{-1} in pure AB between the IS and sMS fibre spectra, relative to the other AB modes. As there is little or no change in recorded mode widths for AB in the AB-PS fibres, the vibrational environment of the AB seem to remain essentially unchanged in the fibres.

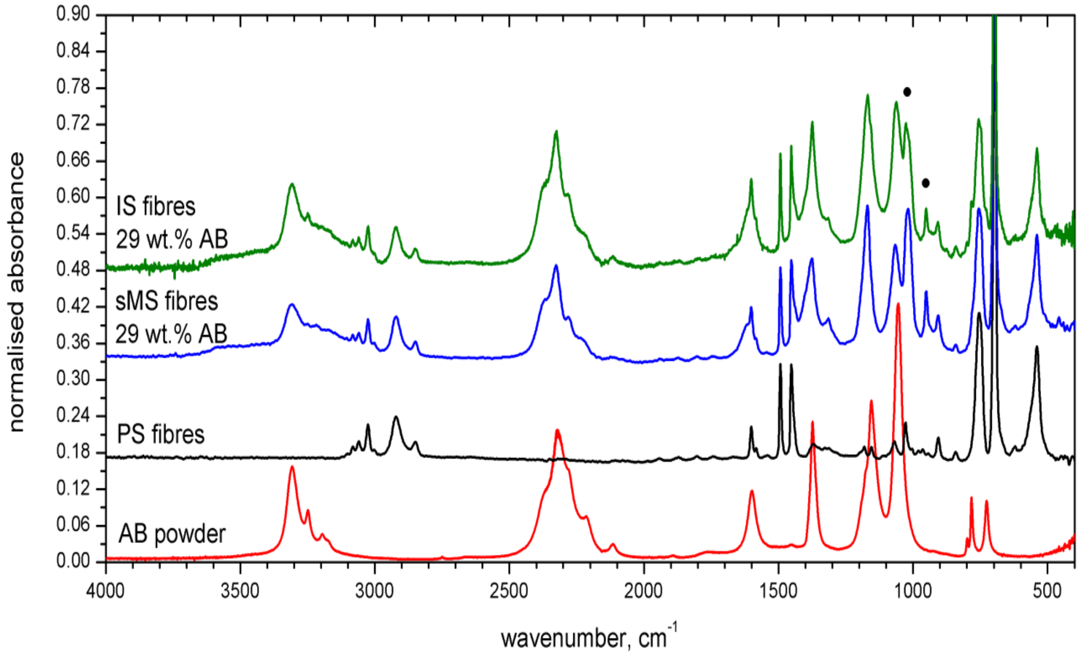

Figure 5.45: FTIR spectra of AB powder, electrospun PS fibres, electrospun AB-PS fibres spun using semi-miscible and immiscible solution combinations. The PS-containing spectra are normalized to the height of the PS CH ring bending mode at 700 cm-1; the AB spectra is normalized to the B-H stretching mode in the IS fibre spectrum at 2300 cm-1. Shifted or new modes in the composite fibres are marked (•).

5.5 Summary and Conclusions

Co-axial electrospinning has been successfully used to make composite AB-PS fibres with a core-shell and/or amorphous morphologies with a total accessible hydrogen content of up to 5.8 wt.% (to 150 °C) in some fibres, opening the way for further research on encapsulating chemical hydrides in polymeric fibres for hydrogen storage applications. The success of the process is achieved through the development of a new method for determining the compatibility and miscibility of co-electrospinning solutions using the Hansen solubility parameters. This model was used to select mixtures of solvents with optimised properties and varying degrees of miscibilities to form core-shell solution combinations that were miscible, semi-miscible and immiscible. While fibres were co-electrospun with an AB core from the latter two sets, no fibres were obtained from the first (miscible) set due to incompatibility of the miscible solutions. Thus, we have not been able to definitively resolve the uncertainty in literature with regards to the inconsistent reports on the requirements of core-shell solution miscibility in co-electrospinning. However, it is clear that the use of immiscible solutions is desirable for ensuring success of co-axial spinning. Due to AB solutions being highly conducting (with greater electrical conductivities than that of shell solutions) the core solution is found to have a greater response to the electric field than the shell and appears to act as the driver of the coaxial jet. This disproves the reports in literature regarding the requirement of higher shell solution conductivity for the success of co-electrospinning.

Many different techniques (SEM, TEM, XRD, FTIR, DSC, TGA and mass spec) have been employed to investigate the structural and thermolysis properties of the fibres. It is found that different solution sets yield different fibre morphologies; those made from semi-miscible solution (sMS) set are mostly porous, while those made from the first immiscible solutions (IS-1) are mostly non-porous and collapsed. These fibres, differing in morphology, display different thermolysis characteristics (as measured by the TGA and DSC). The porous fibres co-electrospun from sMS sets appear to contain a nanostructure that enables three notable improvements in the dehydrogenation properties of AB, these are:

1) lowering of the first dehydrogenation temperature of AB by 15-20 °C,

2) the improvement of the dehydrogenation kinetics with the reaction time reduced by an order of magnitude from ~150 minutes to as low as 15 minutes in some sMS fibres sets, and
3) absence of the poisonous species borazine from the reactions,

all of which are effects observed in other nanostructured AB systems. On the other hand, the fibres analysed from the IS set, which were mostly collapsed, did not show any sign of nanostructure neither in the SEM images or the thermolysis results, which were similar to that of bulk AB. Borazine, however, was not seen in the thermolysis of IS fibres either. This may be because the encapsulation of the hydride in the polymer sheath results in trapping the impurities. The sMS-2 samples, however, show a large mass loss, which increases with AB proportion in the fibres, with up to 50% mass loss in fibres containing 40% AB. This compares to a maximum mass loss of 15% in IS-1 fibres containing ~40% AB.

The marked difference observed in the thermolysis measurements of AB in sMS-2 fibres is attributed to nanostructure of AB in the fibres on the basis of the SEM and TEM images that show pore diameters of tens of nanometres across. Unfortunately, direct measurements of the AB particle size in the fibres are not yet available for verification of this assumption. Thus, further structural and morphological characterisation, such as TEM measurements, are needed to verify the particle size of AB crystals and how they are embedded into the structure of the fibres. To ensure that the AB particles are traceable in the TEM images, a chemical marker can be used to look at AB embedded in the polymer. Further XRD analysis of crystal dimensions and SEM imaging with Energy Dispersive Spectroscopy (EDAX) can also be carried out to obtain an idea of the dimensions of the AB particles/crystals.

The FTIR measurements from the as spun fibres have not produced any conclusive results that point to any phase change that may be prevalent in the fibres. More FTIR measurements of the fibres are needed look at any possible phase change in the fibres as different stages of the thermolysis process.

As this was the first study of its kind, a major part of this thesis was devoted to formulating ways of successfully co-electrospinning AB encapsulated fibres as well as finding the best ways to analyse the as spun fibres. As a result, the study was not conducted as systematically as it could have been to identify the variables that make a difference to the solution properties, the morphology and the chemical decomposition of the AB-PS fibres. The dependence of co-axial electrospinning on many inter-related variables made the systemisation process much more difficult, since changing one variable often resulted in change in another. Also, at different stages of the study the area of focus varied depending on the kind of information that needed to be extracted from the fibres using a given technique, and thus, parallel measurements using the other techniques were not always done. This is why it has been specifically challenging to extract consistent information from the measurements that were made.

It is very important to note that none of the fibres electrospun were synthesised in the structure initially envisioned; this was the production of nano-diameter fibres with AB encapsulated in a non-porous polymer sheath. I have got close to making fibres with properties closer to that idealised using the IS-2 solution set, which was developed using the solution selection model formulated. The IS-2 fibres produced had a well-defined core-shell structure with non-porous shell. However, the solution properties required further optimisation to reduce their diameters to tens of nano-metres instead of the 1-2 μm measured. Unfortunately, due to the lack of time the thermolysis properties of these fibres were not investigated during the duration of this PhD project.

Finally, though some of the AB-PS fibres (i.e. porous sMS-2 fibres) appear to be nanostructured by showing improved dehydrogenation properties compared to bulk AB, regenerability of hydrogen is still an issue in these fibres. The porosity, which seems to enable nanostructure, also appears to allow permeation of all the reaction products of AB from the core. Thus, in order to ensure regenerability of these materials, further work is needed to induce nanostructure in the non-porous core-shell fibres (i.e. those produced from the immiscible solution sets, IS-1,2.

5.6 Prospects and Future Work

This study, based on the use of co-electrospinning to manufacture fibres of encapsulated and nanostructured complex hydrides, initiates another field of interest for this versatile technique. I have shown that an electrospun polymer can act as a scaffold, protective sheath and impurity filter for a hydrogen storage material. With further work it can be possible to increase the maximum hydrogen storage capacity in excess of 5.8.wt.% obtained for some of the fibre. For improving the decomposition rates of AB it is important to understand the factors that have led to increased decomposition kinetics in some of the SM-2 fibres. For mass production of fibres it is important to find compatible core-shell solution sets that co-electrospin easily without frequent breakup. Thus, continuing the solution optimisation process started in this study, by using the solution selection model as a guide to selecting different polymers and solvents, is critical to the advancement of this research. With further work, the co-axial electrospining method can potentially be used as a scalable, one-step production process for a lightweight nanostructured hydrogen store. This could be done with any hydride that can be dissolved or suspended in compatible solvents. Also, with effective choice of hydride and the synthesis of a non-porous polymer sheath this composite store could be made reversible by re-pressurising with H_2.

Further work is needed to determine the exact reasons for some of the observations made on the morphology and the thermolysis process of the fibres, or more specifically if the improvements seen in the decomposition process of the sMS-2 fibres are due to the nanostructuring of AB: These include:

- Determining the average size and morphological distribution of AB particles in the fires and hence whether the AB is nanostructured in the PS fibre matrix.
- Identifying all the decomposition products of AB using the mass spec data and accounting for the large mass loss seen in the TGA measurements of sMS-2 fibres.
- The verification of the reason(s) for the porosity seen in the fibres.
- Identification of any phase change that may be taking place in AB or PS during the decomposition process of the fibres (i.e. further FTIR analysis is required).
- Resolving the discrepancy between XRD and DSC measurements on the crystallinity of the PS fibres, as the former showed the fibres to be semi-crystalline while the latter gives results suggesting a solely amorphous structure.
- Identification of any time dependent changes (e.g. changes in viscosity and conductivity) or any reactions that may be taking place in the solutions prepared for electrospinning.

Further work also needs to be carried out on the thermolysis properties of the fibres produced from the second immiscible solutions (IS-2). As these fibres have the desired morphology for regeneration of AB in the core of the fibres, further optimisation of the solution properties is necessary to reduce their diameters and induce nanostructure in them.

While this specific study has to be concluded for AB and PS solutions used in this study, the solution selection formula needs to be used to select and test other compatible core-shell solution combinations to electrospin AB-Polymer fibres with the objective of producing. nano-structured non-porous co-axial fibres, with further improved hydrogenation properties. Increasing the mass density of AB in the fibres beyond 5.8 wt.% is also very important. Extending this study to other chemical hydride materials, such as MgH and $NaBH_4$, is important for understanding the prospects of this novel study for hydrogen research.

Chapter 6

KC_{24} nanofibres and Hydrogen

6.1 Introduction

One of the main aims of this investigation was to study the hydrogenation properties of doped graphitic nanofibres (GNFs) produced using the electrospinning technique. In §1.5 I have discussed how (de)-hydrogenation properties of materials can be heavily influenced by nanostructure, and how this is likely to be a key factor in improving the performance of many functional materials. In the study outlined in this chapter we have looked at whether similar improvements can be made to physisorption of H_2 in potassium doped graphitic nano-fibres (GNFs).

As discussed in §1.4.5.1 carbon materials having slit-pore structures with opening distances slightly higher than the kinetic diameter of hydrogen (2.89 Å) are considered most ideal for physisorption of hydrogen. Graphitic nanofibres, which have a unique crystalline arrangement consisting of graphitic layers with an interplanar distance of 3.37 Å, have this slit pore structure over a long range, making it an interesting material to explore for hydrogen storage applications. I have already discussed in §1.4.5.1 that graphite on its own has a very low adsorption enthalpy (4 kJ mol^{-1}), which needs to be increased to within 15 – 24 kJ mol^{-1} range before it can have any practical use. Intercalating graphite with metal species on the other hand can dramatically increase the interaction potential between the graphite sheets as a result of charge transfer from the metal ion to graphite and the hydrogen molecule, making it possible to 'tune' the formation enthalpy into the desired range. Nanostructuring the graphite host is also expected to enable faster hydriding kinetics, as a result of shortened diffusion paths of hydrogen. Investigating the hydrogenation properties of intercalated GNFs is therefore important for determining the hydrogen storage potential of these compounds.

While many groups have already looked at the hydrogen adsorption characteristic of graphite (§1.4.5.1) and their intercalates (as discussed in the next section), no studies on the hydrogenation properties of intercalated GNFs are reported. Graphitic nanofibres, depending on the precursor material and the synthesis process can have the graphene sheets arranged in a parallel, perpendicular, or angular orientation with respect to the fiber axis, with only the graphene edges exposed and often with an amorphous component. The particular orientation of the graphite planes or increased density of edge states may influence the ease of intercalation as well as the hydrogen adsorption potential. For example, zig-zag graphite edges are known to have unusual electronic and even magnetic properties near the Fermi surface due to the presence of unbonded π-bonds: these appear to enhance the electron transfer from the donor atoms making it possible to intercalate many species that are not possible in bulk graphite.

We were specifically interested in investigating the intercalation of graphitic nanofibres obtained from electrospun polymeric fibres (made from carbonisable precursors) and their hydrogen adsorption properties. Electrospinning has the advantage of being a scalable method for large-scale polymer nanofibre production and is a more efficient method than the traditional techniques used for the production of carbon fibres, such as chemical vapour deposition, plasma-enhanced chemical vapour deposition methods or wet spinning and stretching methods.

Of the existing alkali metal GICs only K, Rb, and Cs compounds are known to adsorb hydrogen. Even though the adsorption capacity of these materials is no more than 2 wt.%, their high degree of structural ordering makes them a model system for studying hydrogen adsorption in carbon nanostructures [218]. In this investigation we have looked at hydrogen storage properties of K intercalated graphitic nanofibres. The potassium-graphite system was selected as the initial GIC due to its relative ease of synthesis and its attractiveness as a lightweight dopant; the reversible hydrogen uptake of up to $2H_2$ per K ion in the second stage graphite intercalation compound (GIC) KC_{24} [219-221] was what made this stoichiometry specifically interesting. The improvement in enthalpy of adsorption in KC_{24} to 9 kJ mol^{-1} [48] from that in graphite (4 kJ mol^{-1}) is another important factor taken into consideration in selection of this compound. We were interested in seeing how nanostructuring affects the physics of the intercalation and hence enthalpy of sorption of hydrogen, and if the adsorption/desorption kinetics will be improved as expected for a nanostructured material.

This particular investigation is split into two sections: 1) Synthesis of polymer nanofibres using electrospinning and their subsequent carbonisation to obtain graphitic fibres, 2) Potassium intercalation of the GNFs to obtain KC_{24} nanofibres and their hydrogen adsorption properties as investigated by neutron scattering measurements. Our objective in the first part was to understand the mechanisms that control fibre diameters and use these in the right way to obtain uniform polymer nanofibres with the lowest possible diameters achievable for the selected polymer-solvent system. Furthermore, we were interested in understanding the effects of the heat treatment process on the carbonisation and subsequent graphitisation of the electrospun polymer fibres in order to deduce a method for obtaining reproducible graphitic nanofibres, which could then be used to make alkali-intercalated fibres for hydrogen adsorption investigations. Our principle objective in the second part was to investigate the structure and dynamics of hydrogen in our first nanostructured GIC (KC_{24} nanofibres) using neutron scattering techniques.

The work undertaken in this investigation will be presented in the following order. In the first section I will be reporting on the work done for quantitatively tuning fibre diameters and morphology through the addition of an anionic surfactant, higher-conductivity polymer, and NaCl salt to the PAN-DMSO solutions used to electrospin the polymer fibres. I will also describe the heat treatment processes used for carbonisation and graphitisation of the electrospun fibres and provide the results for their structural analysis (i.e. SEM, TEM and XRD data). In the second part I will discuss the intercalation process of the GNFs to make KC_{24} nanofibres and present the neutron diffraction and spectroscopy data for hydrogenation studies on the KC_{24} nanofibres. In order to elucidate the effect of nanostructuring on the adsorption properties of hydrogen, I will be providing a comparative analysis between the neutron data of nanostructured KC_{24} (GNFs) and bulk KC_{24} GICs using results from a previous study by this group.

6.2 Graphite and hydrogen

Graphite is an ordered allotrope of carbon constructed from stacked layers of sp2 bonded trigonal planer sheets, known as graphene sheets. In each layer, the carbon atoms are arranged in a hexagonal lattice, so each carbon has three bonds separated by 120°, with a separation distance of 0.142 nm. The neighbouring planes have an interlayer spacing of 0.335 nm [221] and experience week van der Waals interactions, 1/300th of C−C bond strength experienced by the intraplanar carbon atoms in the sheets. The basal planes register in a –ABA– sequence along the c-axis (hexagonal) or more rarely in a –ABCA– sequence (rhombehedral). The crystal structure of the former, which has group geometry P63mmc, is shown in Figure 6.1.

The electronic shell configuration of a carbon atom ($1s2\ 2s2\ 2p2$) results in each carbon atom forming a covalent π-bond with its three nearest neighbours, giving rise to the *sp*2 hybridisation, with the fourth electron forming a delocalised σ-bond. In the basal plane (i.e. graphene layers) the binding energy is 7 eV/atom [221]. The weak overlapping of the π-bands leads to a 0.02 eV/atom binding energy between the planes, giving rise to a semi-metallic nature in three-dimensionally ordered graphite.

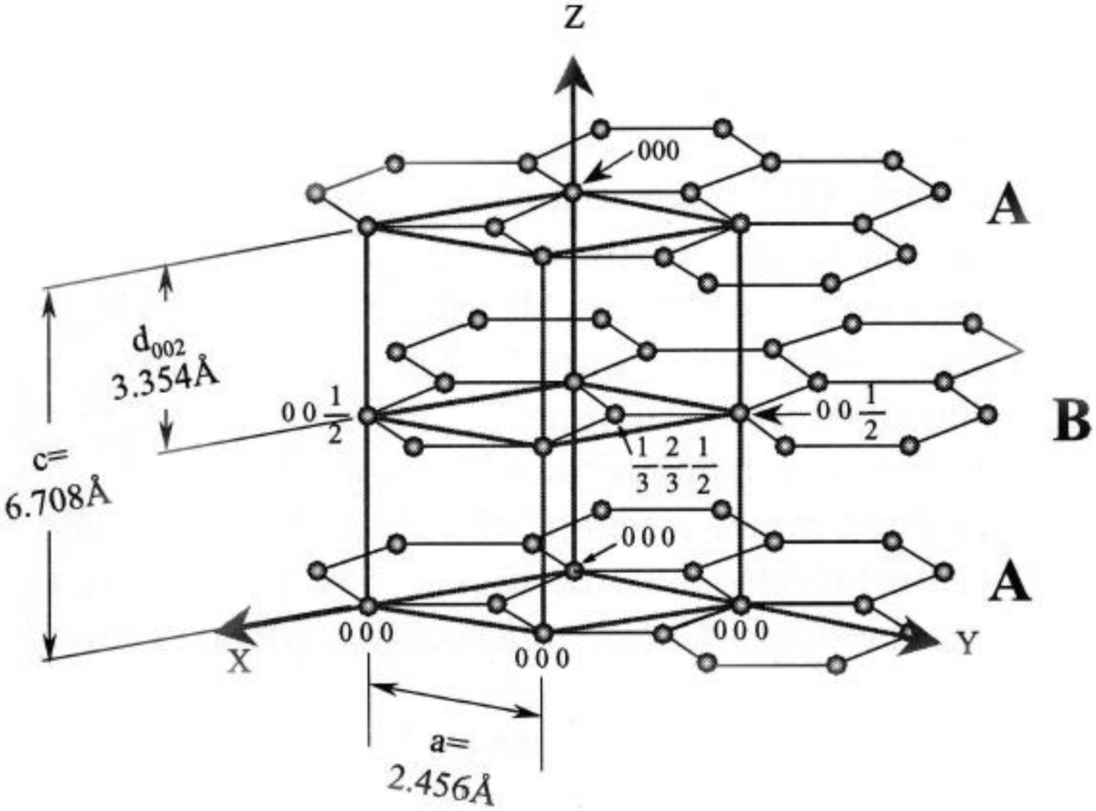

Figure 6.1: Structure and unit cell of graphite showing the stacking sequence of the basal planes along the c-axis following a staggered -ABA- pattern; half of the carbon atoms in a given plane sit between the hexagon centres of the layers above and below it [221].

It is this difference between the intra-planar and inter-planar interaction that cause the large anisotropic properties characteristic of graphite. One manifestation of this anisotropic geometry is unidirectional electrical conductivity; the free electrons within the carbon layers have a much greater mobility within the plane than across the planes such that the electrical resistivity of pure graphite is approximately one thousand times greater across the interlayer spacing than it is in any direction in the graphene planes [221]. The weak van der Waals interaction between the basal planes allows for the planes to slip along one another under a small force, enabling graphite to be used for lubrication purposes, the reason for why layers of graphite are easily transferred from a pencil 'lead' on to a sheet of paper.

Graphitic carbons have very low surface areas due to the lack of porosity, with specific surface areas a(ssa) typically under 20 m^2g^{-1} , and as a result have a very small hydrogen uptake (< 0.5 wt.%) at low temperatures [222]. The measured adsorption enthalpy of hydrogen on Graphon, a material closely approaching the characteristics of graphite, was found to be 3.8 kJ mol^{-1} [223], well below the targeted value.

Various hypothetical structures, such as slit pore structures [43, 198] or pillared graphite layers [224, 225] have been the subject of computational studies for investigating the scope for increasing the binding energy of hydrogen. When the graphitic layers (walls) have a width not exceeding a few molecular diameters the potential fields from opposing slit-pore walls overlap, leading to an enhancement of the heat of adsorption as attractive force acting on adsorbate molecules increases [14]. Increasing the space between the graphene sheets to accommodate for two H_2 monolayers on each slit-pore wall also increases uptake. Nevertheless, the general consensus is that the gravimetric density is intrinsically low in graphite due to the geometry. Assuming condensation of a monolayer of H_2 molecules on a graphene sheet with a specific surface area of S = 1315m^2g^{-1} and using liquid H_2 density at boiling point, the amaximum concentration of hydrogen on carbon is calculated to be 2.28×10^{-3} wt.% S[m^2g^{-1}] = 3.0 wt.% (H/C= 0.18). The details of this calculation can be found in reference [14]. So the theoretically maximum possible concentration of hydrogen in graphitic carbon with hydrogen adsorption on both sides of a graphene layer is approximately 6 wt.%. Even if this value was attainable in practice, though it is not, the binding energy of hydrogen is still too low for practical applications of graphitic carbon as a hydrogen storage medium. On the other hand, intercalation of metallic species in between the layers (galleries) provides the scope for increasing the binding energy further, as discussed in the next section.

6.3 Graphite intercalation compounds

6.3.1 Graphite intercalates and hydrogen storage

Graphite intercalation compounds (GICs) are a unique class of lamellar materials formed by the intercalation (insertion) of atomic or molecular 'guest' species between the graphene layers of 'host' graphite. Since graphite is an amphoteric material it can accept both positively and negatively charged intercalant species that form donor or acceptor compounds depending on the charge on the guest species. The most widely known and studied donor compounds are alkali metal e.g. K, Rb, Cs and Li GICs, although other donor intercalants, such as alkaline earth metals and lanthanides also exist. Acceptor compounds are often based on Lewis acid intercalants such as the halogen Br_2 or halogen mixtures, metal chlorides, bromides, fluorides and oxyhalides [221].

In the intecalation process the guest species usually remain molecular and cause the graphite galleries to expand along the c-axis; the expansion being proportional to the size of the intercalated molecules. The readily charged guest materials exchange charge with the π-bands in the graphene sheets, enabling controlled variation of physical properties of the graphite host, such as its electrical, thermal and magnetic properties. The free carrier concentration of graphite is very low (10^{-4} free carriers/atom at room temperature) but through intercalation of different species at different concentrations it is possible to vary it's electrical conductivity behaviour from almost insulating for c-axis conductivity in certain acceptor compounds to superconducting in-plane below 1.0 K for the first stage alkali metal donor compounds, e.g. KC_8 [221]. In the case of KC_{24}, the electrical conductivity along the c-axis is about 24 times larger than that for pristine graphite, the anisotropy factor σ_c/σ_a being around 860 [226].

The particular change induced in the graphite host is largely dependent on the type of species intercalated and their specific concentration. The amount of intercalant used determines the staging sequence of the intercalant between graphite galleries, denoted as stage-*n*, *n* being an integer corresponding to the number of graphene planes between each intercalate layer. For example, a stage-1 GIC such as KC_8 (Figure 6.2) contains metal ions between every graphene layer, making it the most densely intercalated compound. The density of the intercalant in the graphite galleries can also change between different stages, for example the stage-2 potassium GIC KC_{24} is only 2/3 as densely populated with K as its stage-1 counterpart (Figure 6.2).

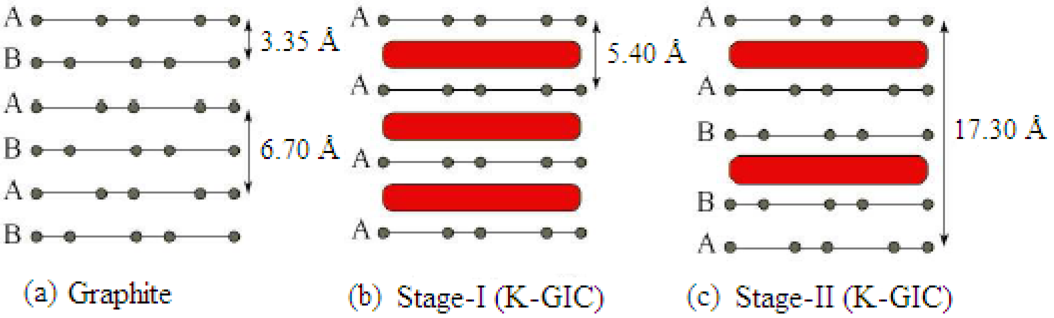

Figure 6.2: Graphite stacking and interlayer spacings for pure graphite, stage-1 and stage-2 potassium graphite intercalation compounds. Roman numerals mark graphene layer arrangement and red bars represent metal layers [48].

The simple relationship between the staging and the c-axis lattice spacing *Ic* is given by the following equation:

$$I_c(\text{Å}) = d_s + 3.35(n-1) \tag{6.1}$$

where n is the stage number and d_s *is* the interlayer distance of a fully-intercalated gallery.

In the case of alkali-metal GICs it is thought that in the process of transferring charge to the graphite lattice the alkali-metal ions are pulled into the galleries and hence diffuse through along them. It is interesting that these GICs can easily undergo transition between different stages, e.g. from stage-1 to stage-2 under the right conditions. The exact mechanism for this transition is difficult to explain, especially since the metal atoms are unable to cross between the planes through the graphene sheets. In the standard staging model outlined by Daumas and Hérold [227] the mechanism for staging is explained by shifting of domains of intercalate in between the layers periodically until the minimum energy configuration is reached.

The induced polarity of the intercalate and the expansion between the graphene layers increases the interaction potential between the graphite and a second intercalant, such that the uptake of a second species e.g. hydrogen, can be more energetically favourable in GICs than in pure graphite. This interaction potential varies between different GICs [228] and in fact only K, Rb, and Cs compounds are known to adsorb hydrogen. Of the first stage compounds only RbC_8 is known to adsorb small proportions of hydrogen, to give $RbC_8H_{0.05}$ [48]. The hydrogen uptake is more promising in stage-2 compounds. In the case of MC_{24} GICs, where M=K, Rb, Cs, it has been reported in several studies that they reversibly adsorb ~$2H_2$ per metal ion at temperatures below 200 K [219, 220, 229].

Although the maximum reported hydrogen uptake in GICs is no more than 2 wt.%, their high degree of structural ordering and potential to be chemically modified make them a model system for studying hydrogen adsorption in a carbon nanostructure. Also, more recent studies on GIC based structures [230, 231] have raised the possibility of obtaining high-density storage at near ambient temperatures and pressures with their physical properties tuned to optimise hydrogen uptake. Yet, research on the hydrogenation properties of GICs is currently limited and the understanding of the exact effects of chemical modification on hydrogen adsorption is incomplete. One of the main reasons for this is because the interaction of the hydrogen with the host is through dispersion forces, which are extremely difficult to calculate using first principle methods. Therefore, despite the low hydrogen uptakes, investigating the thermodynamics and kinetics of H_2 in these materials is specifically important for developing an understanding of the hydrogen storage potential of these materials. Furthermore, we expect nanostructuring to lead to some improvement in the hydrogen adsorption properties as described in §1.5. A brief description of potassium doped graphite, more specifically KC_{24} (the GIC we've chosen to study), is given in the next section.

6.3.2 Structure of potassium-intercalated graphite

Potassium GICs are formed by intercalation of potassium atoms in between the graphitic galleries; the compounds known to form are KC_8, KC_{24} and KC_{36}. There are two competing forces in the system upon insertion of K atoms into the galleries. The first is due to the host graphite planes wanting to form a staggered sequence, ABAB stacking (as shown in Figure 6.2 (a)), in which half the carbon atoms in a given plane sit over the hexagon centres of the adjacent planes. The second is due to the arrangement of K atoms that want to sit at the hexagon centres due to the strong graphite corrugation potential, forcing the graphite planes into an AA stacking geometry (as shown in Figure 6.2 (b)). It is the competition between these two forces that gives rise to discrete GIC stages [8]. The stoichemetry and hence the staging of the final compound depends on the concentration of the potassium i.e. the amount of K used in the intercalation process or the chemical potential gradient across the intercalated and the vapour phase (as described in §6.3.5 below).

The stacking sequence of KC_{24} is not known for sure and in fact the in plane geometry of the stage-2 GICs is not yet fully characterised. For a stage-2 compound Nixon and Perry [232] suggest an AB|BC|CA|A stacking, which means that the graphite layers (denoted by Roman letters) on either side of the intercalate layer (denoted by the vertical bar) are aligned while the empty galleries maintain a graphite layering structure [8]. It is known that upon intercalation of the K atoms the filled layer expands from 3.35 Å to 5.4 Å, while the unfilled layers maintain the same c-axis dimensions [232].

The in-plane geometry of KC_{24} (or other stage-2 compounds) is not conclusively determined either, but since graphite has a hexagonal honeycomb lattice structure, the minimum energy configuration would result in K atoms sitting at the centre of the hexagons forming a triangular lattice. The KC_{24} (or K:C = 1:24) stoichiometry is expected to result in a $(\sqrt{12}\,x\,\sqrt{12})$ R30 geometry, as in the structure illustrated in Figure 6.3 (a). However this structure is inconsistent with XRD results. In fact at room temperature the potassium atoms are disordered, they diffuse through the layers like a two dimensional liquid [233]. Upon cooling the structure is found to undergo a series of phase transformations in which both the in-plane structure and the stacking sequence assume long-range order [234, 235].

Two other geometries are proposed as shown in Figure 6.3 (b) and (c). The first of these (Figure 6.3 (b)) is based on a domain structure model used to explain the conformation of Cs in the CsC_{24} structure, in which a $(\sqrt{7}\,x\,\sqrt{7})$ R19.11 commensurate structure is surrounded by domain walls (as shown in Figure 6.4) [8]. Even though the $(\sqrt{7}\,x\,\sqrt{7})$ structure has a stoichiometry of KC_{28}, taking account of the greater alkali metal density in the domain walls can give a KC_{24} stoichiometry. The last proposed structure, and probably the most likely one is the incommensurate close-packed potassium structure with a liquid-like separation of roughly 6 Å [8]. This structure is thought to result from the rotation of the K-monolayer about the c-axis by an arbitrary angle, followed by the relaxation of the potassium atoms into the nearest hexagon centres [236]. This relaxed close-packed structure, which has the closest agreement with single-crystal X-ray data

[237] has nearest-neighbour distances of 2a, $\sqrt{7}a$, and 3a (as shown in Figure 6.3 (c)).

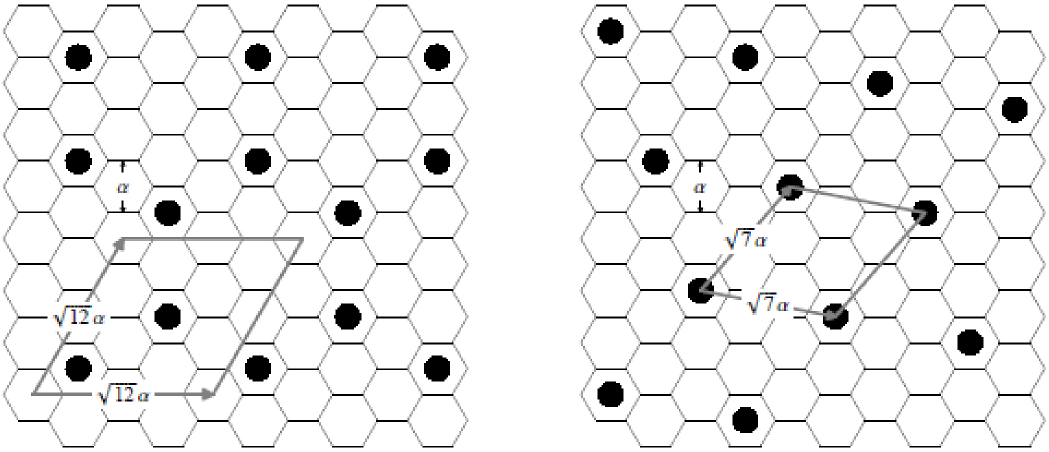

(a) $(\sqrt{12} \times \sqrt{12})\ R\,30^\circ$ structure **(b)** $(\sqrt{7} \times \sqrt{7})\ R\,19.11^\circ$ structure

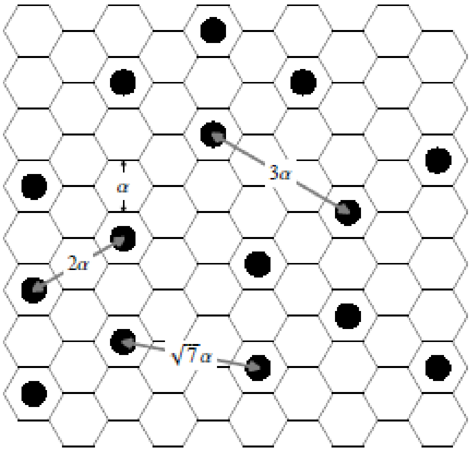

(c) Relaxed Close-Packed

Figure 6.3: Proposed in-plane potassium structures for K-GIC showing K registry with the graphite host. (a) The $(\sqrt{\mathbf{12}}\ \boldsymbol{x}\ \sqrt{\mathbf{12}})$ structure corresponds to a KC_{24} stoichiometry. (b) The $(\sqrt{\mathbf{7}}\ \boldsymbol{x}\ \sqrt{\mathbf{7}})$ corresponds to a KC_{28} stoichiometry. (c) The relaxed close-packed structure which consists of a close-packed potassium layer rotated in-plane and relaxed into the nearest hexagon centres [8].

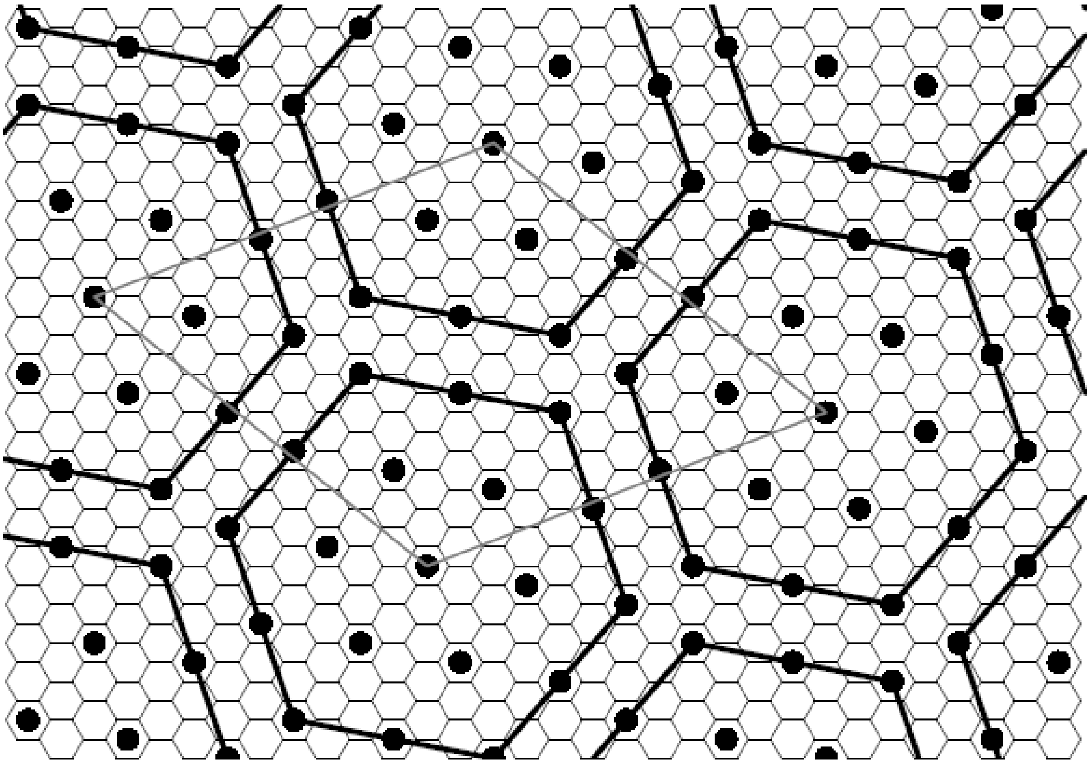

Figure 6.4: Domain model for CsC_{24} in which ($\sqrt{7}\ x\ \sqrt{7}$) islands are separated by domain walls, or discommensurations [8].

6.3.3 Hydrogen Storage in KC_{24}

Hydrogen physisorption in stage-2 compounds KC_{24}, RbC_{24}, and CsC_{24} was initially investigated by Watanabe *et al.* in the early 70s [219, 220]. The maximum H_2 uptake in KC_{24} was reported to be ~2.1 H_2 molecules/K ion. The hydrogen is adsorbed into the metal containing layers and causes these galleries to expand by ~5% along the c-axis (from 5.4 Å to 5.6 Å). This expansion, which indicates a monolayer mixing of H_2 and K atoms, is also true for RbC_{24}, though not for CsK_{24}. The expansion is thought to be just enough to overcome the hindering potential for hydrogen entry [228]. It is also found that due to quantum sieving effects D_2 adsorbs preferentially over H_2 [238]. The H_2 appears to stay molecular as no evidence exists for H_2 dissociation upon intercalation. Thus, the interaction between H_2 and KC_{24}

is thought to be composed of just dispersive and electrostatic components. Charge transfer from potassium to graphite induces a strongly polarized potential field, which is thought to enhance the interaction of the adsorbed H_2 molecules with the system through charge-quadrupole and charge-induced dipole forces. It is also possible that an increase in the charge density around the potassium atoms and the graphene layers enhances the dispersion interaction with the H_2 molecule. In fact computational studies [239, 240] appear to suggest the increase in the electron density around the alkali ions is the main cause of the enhanced H_2 interaction potential in these systems. The isosteric heat of H_2 adsorption for KC_{24} is reported to be 8.4 kJ/mol, approximately double that for pristine graphite.

6.3.4 Inelastic neutron scattering from KC_{24}

As described in §4.6, neutron scattering is the most powerful tool for investigating the structure and dynamics of H_2 bound systems. Inelastic neutron scattering has been specifically used to investigate the excitation characteristics of H_2 in GICs. Beaufils *et al.* [46], in the early 80s, have looked at $RbC_{24}(H_2)_x$ with x in the range 0.5 to 2.1, the upper value corresponding to H_2 saturation at 30 K. The data produced in the energy range $100\ \mu eV < \Delta E < 1400\ \mu eV$ ($0.8\ cm^{-1} \sim 11\ cm^{-1}$) showed an excitation peak at 1.34 meV, and as H_2 loading increased from $x = 1.5$ to $x = 2.1$, this peak acquired a growing shoulder at 1.17 meV while another excitation appeared and grew at 0.60 meV (Figure 6.5). These peaks were thought to be the result of H_2 molecules undergoing quantum tunnelling in a hindering potential and they proposed a two site model *A* and *B* for H_2 in this GIC system below 77 K; site-*A* representing an tetrahedral crystal field and the double peak site-*B* representing an octahedral one. While tests with methane and HD were carried out to verify this model the resolution of the peaks is not good enough to deduce a finer structure at the specific energy modes. Furthermore, the data suggests that the hydrogen was not entirely converted to para-H_2 as intensity appears on the neutron energy gain side.

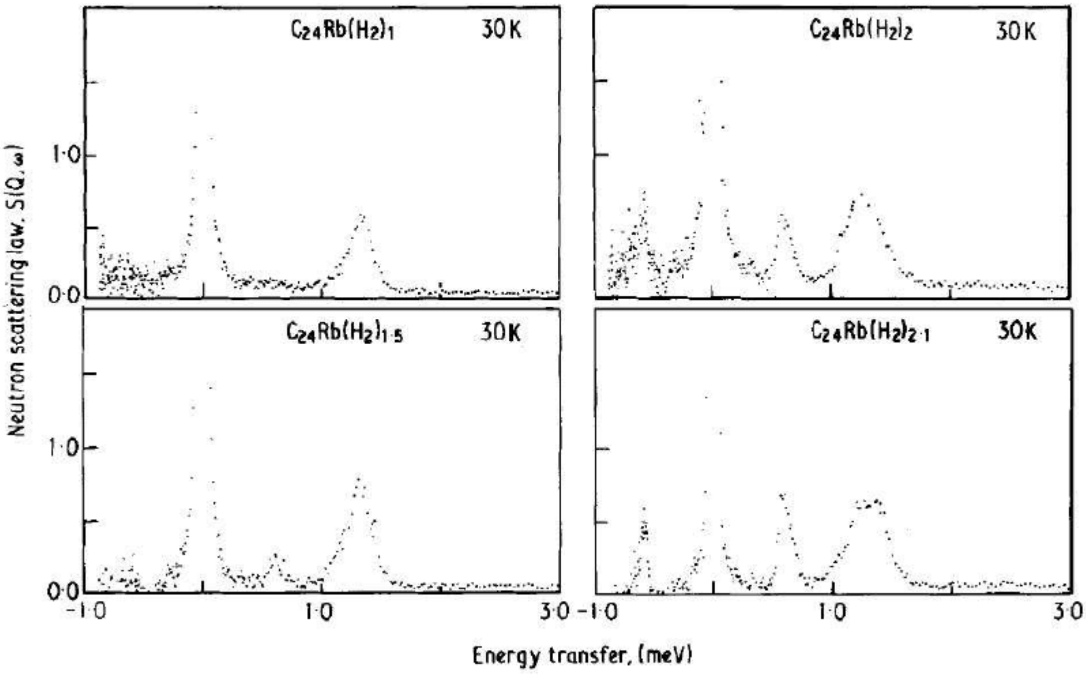

Figure 6.5: INS spectra of $RbC_{24}(H_2)_x$ for x = 1:0, 1.5, 2.0, 2.1 (Beaufils *et al.*) [46].

Stead *et al.* [241] used inelastic neutron scattering to look at the H_2 excitations in $CsC_{24}(H_2)_{1,2}$ in the librational energy region ΔE=10 to 200 meV (80-1600 cm^{-1}). The tunnelling and librational transitions of the H_2 molecules in a bound system are used to obtain the strength and symmetry of the molecular barrier to rotation. Hence, the data obtained was used to calculate the molecular barrier to rotation in the $CsC_{24}(H_2)_{1,2}$ compound with the use of a H_2 librational splitting model for H_2 in a $\cos^2\theta$ potential outlined by Silvera [242]. The tunnelling data is reported to be consistent with the two site model (site A and B) mentioned above. These site occupancies are thought to occur as a result of metal-ion superlattices with the H_2 molecules centred in the plane of the metal ions, but oriented perpendicularly to the graphite plane, which suggests the energy of the H_2 molecules to be independent of the in-plane orientation (i.e. cylindrical symmetry). Assuming this geometry the data is said to indicate a sinusoidal potential as given by

$$V = V_0(1 - cos2\theta) \tag{6.2}$$

where $2V_0$ is the barrier constant and θ is the angle to the preferred orientation. Using this potential model with the data (details given in ref. [241]), they have calculated the transition energies from the ground state as a function of the hindering potential, as shown in Figure 6.7. This splitting diagram, which allows for the predicted tunnelling and librational modes to be read off directly, suggest the presence of a strong hindering potential that causes the splitting of the first hydrogen J = 1 rotational level into two: the singly-degenerate M = 0 level, and the doubly degenerate M = ±1 level, as shown in Figure 6.7. According to their model, the "A" site in $CsC_{24}(H_2)$ has a potential barrier of $2V_0$=13B, which predicts the tunnelling mode seen at 1.55 meV and a corresponding librational line seen at 39 meV (as verified by their experimental data showing 1.0-1.2 and 35-38 meV, respectively). The "B" site is said to have the same symmetry but a stronger potential with $2V_0$ = 18B, predicting tunnelling at 0.65 meV and a fundamental libration at 50 meV (with observed values of 0.67 and 49-51 meV). These are seen to shift in energy as a function of coverage: the principal line from 37 meV in $CsC_{24}(H_2)_1$ to 35 meV in $CsC_{24}(H_2)_2$.

This two-site model, as described for $CsC_{24}(H_2)_x$ and later used for $BeC_{24}(H_2)_x$ was subject to scrutiny by Lovell *et al.* and co-workers [48, 218] with new (more refined) INS data collected from $KC_{24}(H_2)_x$. The authors argue that the data (from the low-energy spectra) presented above by Beaufils *et al.* (Figure 6.5), showed additional complexity (multiplet structure) which was not accounted for in detail. The new data on KC_{24}, as discussed in §6.5.4.1, shows that there are no clear differences in the coverage dependence of the two tunneling bands at 0.6 and 1.5 meV and the peak at each band are formed of three triplets (i.e. each band has three band heads). Thus, the presence of two distinct sites with their own librational energy level structure is said to be questionable. The authors propose that the multiplet structure seen at 0.6 meV indicates the existence of multiple sites with an almost identical librational energy barrier and that the band at 1.5 meV, which is also formed of a triplet with the same symmetry to that in 0.6 meV, is related to this multiplicity of sites. This hypothesis was supported by theoretical work using PW-DFT code CASTEP, which showed good agreement with INS data when the structure was modelled with H_2 delocalised in three neighboring sites located 1.1 Å away from the centre of the trigonal subunit cell (as shown in Figure 6.6). On the basis of these results the authors conclude that there is a quantum mechanical delocalization (QD) of the H_2 centre of mass across these three sites. Further details of this calculation are given in ref [218].

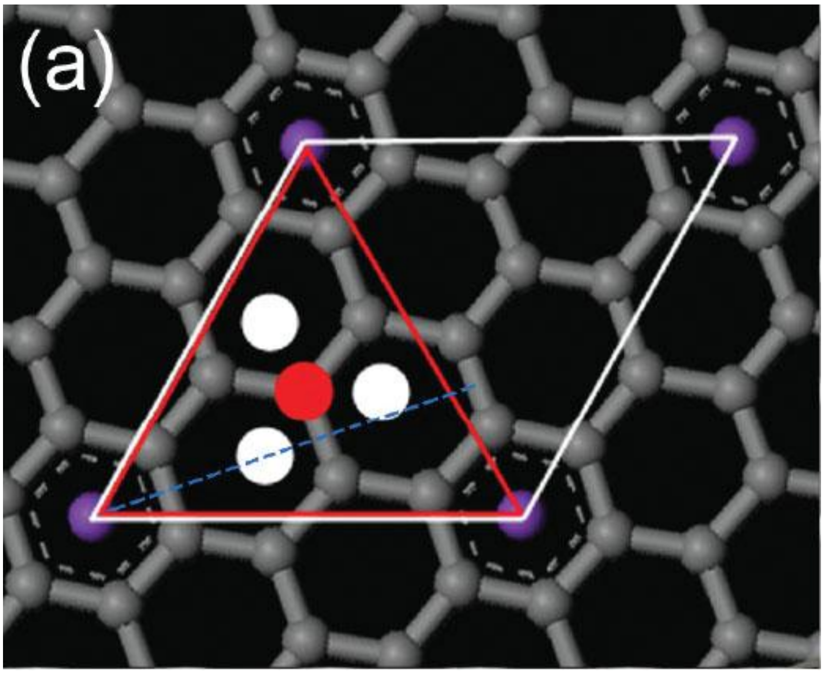

Figure 6.6: View along the *c* axis (white lines define the unit cell). The trigonal subunit cell and its centre are shown in red. White circles denote three adjacent H_2 sites [218].

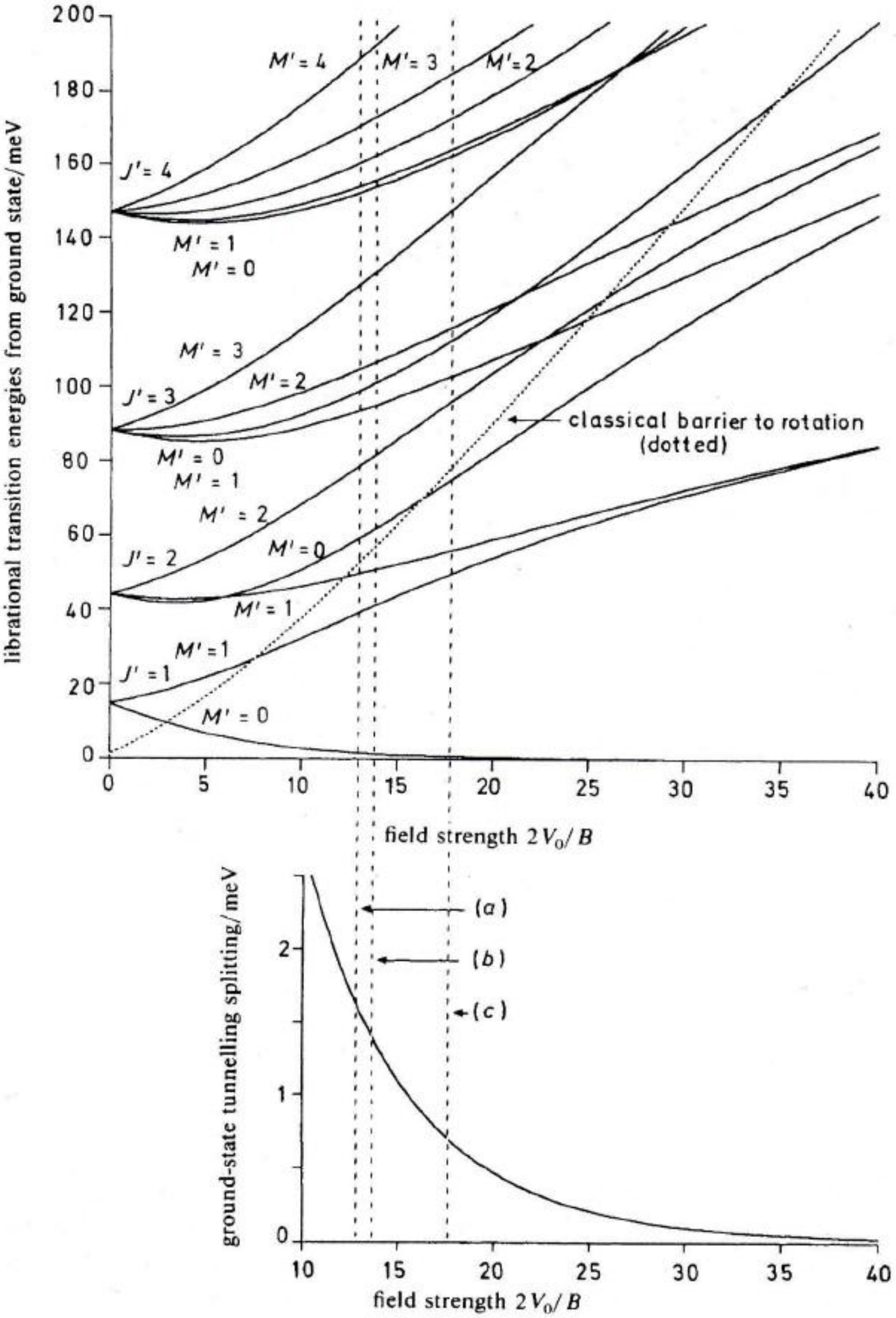

Figure 6.7: Splitting pattern for the rotational energy levels of a hydrogen molecule in a cylindrically symmetric cos$^2\theta$ potential showing transition energies from the ground state in meV. Rotational transitions are depicted up to $J_0 = 4$. (a) is the 'A' site in CsC$_{24}$(H$_2$)$_x$, (b) is the 'A' site in RbC$_{24}$(H$_2$)$_x$, (c) is the 'B' site in both compounds. Reproduced from Stead *et al.* [241].

6.3.5 Intercalation methods

A number of general techniques exist for the preparation of graphite intercalation compounds, these include the two-zone vapour transport, the liquid intercalation and co-intercalation techniques [221]. The main parameters taken into consideration are temperature, vapour pressure, the chemical and physical properties of the intercalant. The prime objective is to get the intercalant (guest) species to mobilise and enter the graphite (host) galleries. Although any one of the above techniques can in principle be used, the physical and chemical properties of the intercalant generally favours one technique over another in terms of the ease of intercalation. The nature of the graphite sample, e.g. size and crystallinity, also effects the ease of intercalation, with small and thin samples yielding more homogeneous and better staged compounds than larger ones. In this section I will only describe the vapour pressure method, since this was the method we have used for the intercalation of potassium in to our graphitic nanofibres. Further details on this and all other methods can be found in the review by Ebert in ref. [243].

In the vapour transport method, the intercalant and the graphite host are placed in a sealed, typically evacuated, container and heated to a specific temperature to vaporise the intercalant, which gets taken up by the graphite sample. The intercalation temperature is determined according to the intercalant used. Two variants of this technique exist, the first known as one-zone vapour transport (1ZVT), the second is the two-zone vapour transport (2ZVT) method (see Figure 6.8).

In the 1ZVT method the intercalant metal and the graphite host are placed in a sealed container in near contact, with both samples being exposed to the same temperature T1Z. The staging of the intercalation is controlled by using the correct stoichiometric amount of the intercalant metal plus a small excess (Figure 6.8 (b)). In the two-zone vapour transport method, the intercalant and the graphite are placed a distance apart and the intercalant (metal) is heated to temperature T_i while the graphite is maintained at a higher temperature T_g (Figure 6.8 (b)). The desired staging is obtained by controlling the thermal gradient between the intercalant and the graphite, a smaller difference in T_i and T_g yields GIC with lower stages. The correct T_i and T_g temperatures are listed for many metals and are available in literature; for K T_i=250 °C, and T_g (°C) = 225-320 (stage-1), 350-400 (stage-2) and 450-280 (stage-3) [221]. The region of stability for a given stage decreases with increasing difference in T_i and T_g, i.e. higher stages have a smaller T_g-T_i temperature range over which they are stable. Excess amounts of metal can be used since the intercalation is controlled by the chemical potential. The time taken for the completion of the intercalation is highly dependent on the intercalant species and the size and structure of the graphite host. It can vary between a few seconds for an easily intercalated species such as potassium to many weeks for metals more difficult to intercalate such as Ytterbium in HOPG (highly ordered pyrolytic graphite).

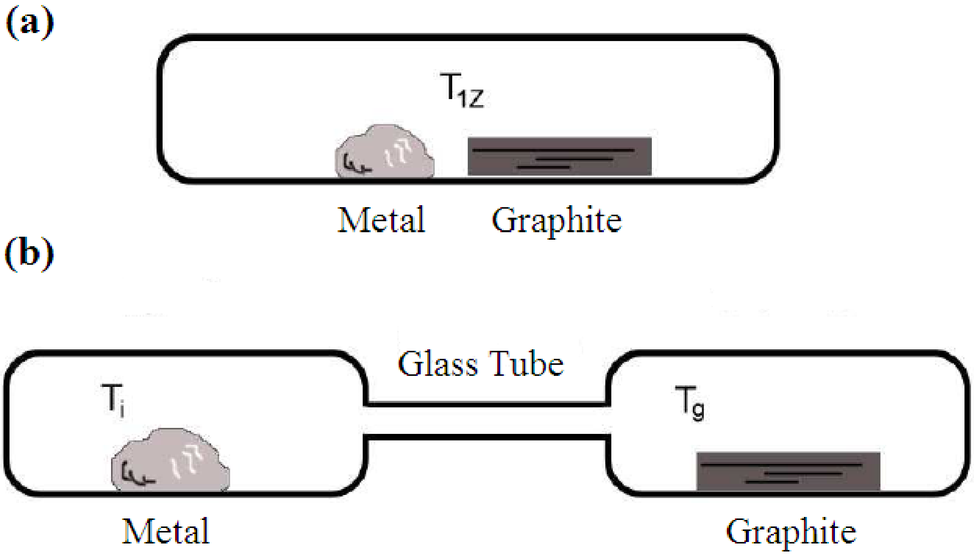

Figure 6.8: Schematic diagram of (a) one-zone transport method with accurate stoichiometric amount of metal at the same temperature, and (b) two-zone vapour transport method where T_g and T_i indicate the temperature of the graphite and intercalant respectively [48].

Upon intercalation the charge transfer to the graphite results in the compound having a unique colour, characterised by type of species and the intercalation stage. Thus, the staging of the compounds can be monitored through observation of the colour change during the intercalation process and the purity of the resultant sample can be assessed from the sample colour. Pure KC_8, like RbC_8 and CsC_8, is a golden-orange colour and KC_{24} a metallic blue [48], but the tones and intensity of the colours can change depending on the mosaicity of the graphitic sample.

6.3.6 Carbon fibres and their synthesis

Carbon fibres have historically gained great commercial interest with applications ranging from sports equipment to the aerospace industry. Their high tensile strength [244, 245], large length-to-diameter ratio [246], high specific surface area [247] and high thermal and electrical conductivity [248, 249] have ensured that they have an increasing number of applications. As production methods improved, nanoscale carbon fibres have found increasing numbers of applications including their use as templates for nanotubes [250], filters [251], supercapacitors [104], batteries [105], and bottom-up assembly in nanoelectronics [104] and photonics [106]. Conventionally nanofibres are prepared using techniques such as chemical vapour deposition [252], plasma-enhanced chemical vapour deposition[253] or wet spinning and stretching methods. However, electrospinning has the advantage of being a far more efficient way of producing carbonisable fibres than these particular methods.

Carbon fibres are considerably less ordered than highly oriented pyrolytic graphite (HOPG), even though the degree of ordering is strongly dependent on the precursor fibre being graphitised as well as the heat treatment temperature. Since the graphitic structure of the nanofibres are highly important for both intercalation and hydrogen adsorption purposes, understanding the graphitisation process and the structure of the resultant fibres formed a significantly large part of this study.

Most common carbon fibre precursors are polyacrylonitrile (PAN), pitch or rayon fibres. PAN was initially used in this study as it was more easily attainable than both pitch and rayon. While the precursor material plays the determining role in shaping the microstructure, increasing the heat treatment temperature results in: (i) an increase in the mean crystallite size and (ii) increased degree of alignment of the basal planes along the fibre axis. Generally heat treatment temperatures >2500 °C yield fibres that have a greater degree of ordering.

In the PAN-based fibres the graphitic structure forms through the growth of graphite ribbons that tend to be aligned along the fibre axis. The degree of alignment generally is highest near the outer skin, decreasing towards the core of the fibre (as illustrated in Figure 6.9 (a)). In contrast the basal planes in Pitch tend to form in a radial direction along the fibre cross-section (as shown by Figure 6.9 (b)). The microfibril structure of PAN based carbon fibres are illustrated in Figure 6.10 and Figure 6.11 showing depiction of the fibre structure in 2D (side view) and 3D (crossection and side view). The ordering in the fibres is typically characterised by the length (L_c) and with (L_a) of the ordered ribbon regions.

Polymer fibres pyrolysed for carbonisation are generally subjected to a stabilisation step in which they are heated in the presence of oxygen, which apparently changes the carbonisation steps to yield stronger fibres. To investigate the effect of oxidisation on the development of graphitic structure in the fibres and whether it was a necessary step, we have looked at fibres pyrolysed with and without this step. The stabilisation mechanism and its possible effects on the fibre structure are discussed in the next section.

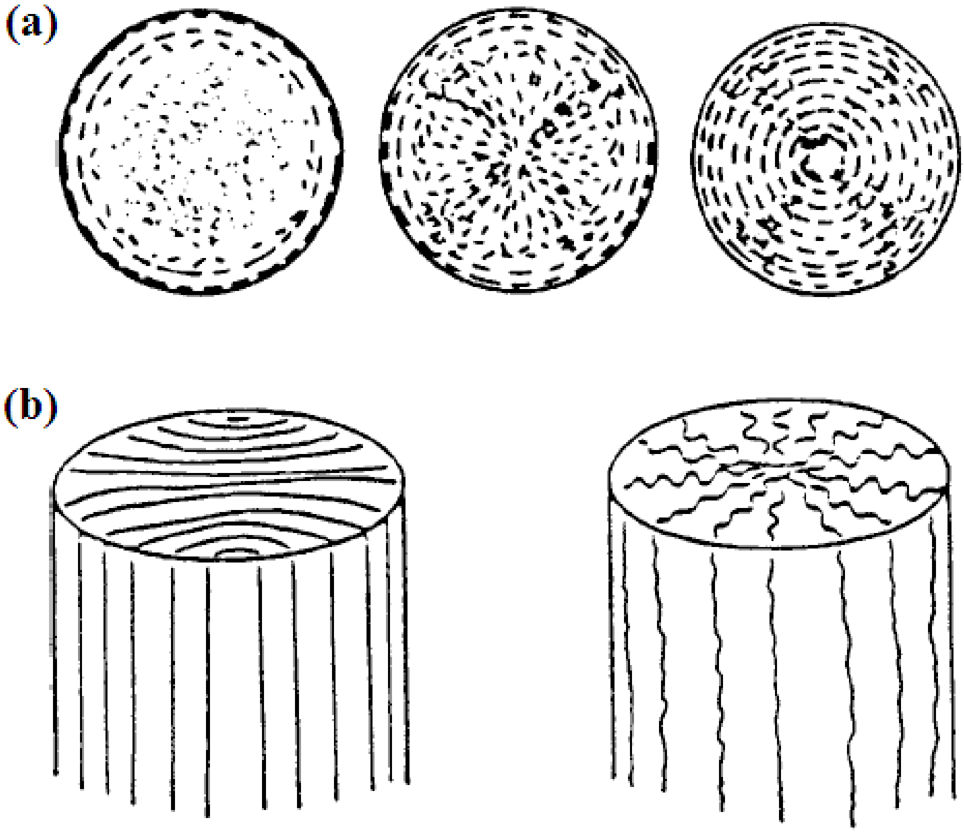

Figure 6.9: (a) Knibbs' identified three different types of structures for PAN based carbon fibres prepared under different processing conditions (b) Endo's proposed structure for two different pitch-based carbon fibres [254].

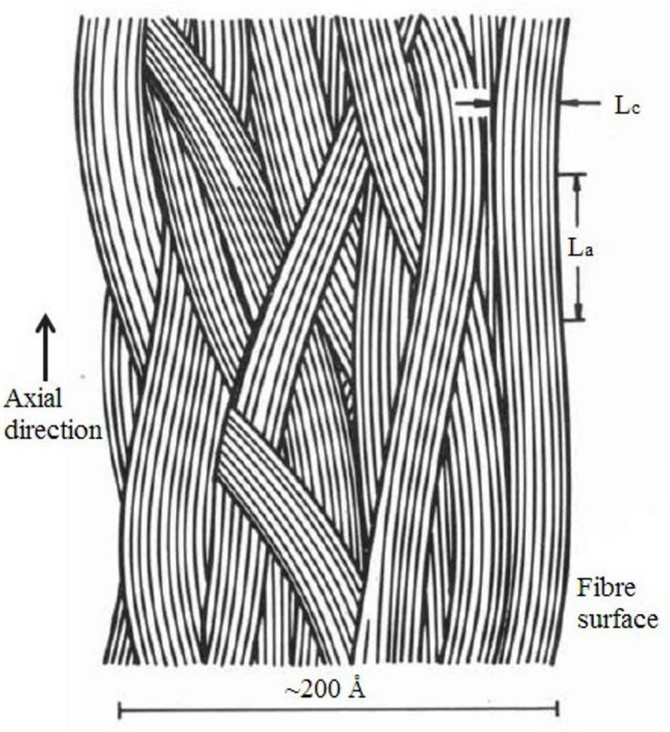

Figure 6.10: Structural model of carbon fibres from PAN precursor as suggested by Diefendorf and Tokarsky [255] showing microfibrils.

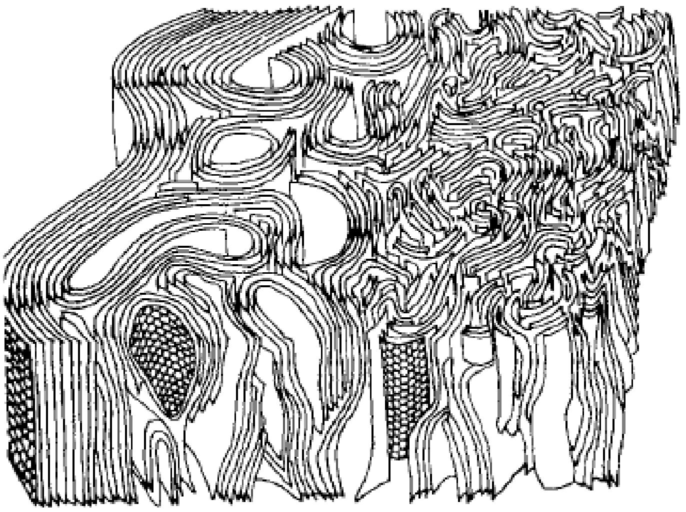

Figure 6.11: A schematic 3D representation of the structure of a PAN based carbon fibre showing irregular space filling and the distortion of the carbon layers [256].

6.3.6.1 Thermal treatment of polymer fibres for carbonisation

In order to develop an understanding of the carbonisation and the subsequent graphitization process it was important to gain knowledge on the possible reaction mechanisms during the pyrolysis process and the effect of stabilization (oxidation) on the graphitic structure of fibres. The stabilisation of fibres is accepted as an important step for obtaining high strength stable carbon fibres [257]. In spite of the numerous studies that have been done to understand the reaction steps involved in this particular process the chemistry of the stabilisation step remains complicated and not well understood.

Chain scission and loss of molecular alignment are two processes that take place during carbonisation leading to a loss in a significant mass [258]. Heating the fibres in an oxidising atmosphere while under mechanical restraint appears to prevent this from happening to a large degree. Grassie *et al.* [259] has shown the occurrence of an exothermic reaction at around 300 °C when PAN fibres are heated in an inert atmosphere. The exotherm is shown to correspond to a significant weight loss as a result of the rapid increase in sample temperature, with the release of volatile products such as CO_2, N_2, NH_3, HCN [257-259]. The process causing the exotherm is believed to be the polymerization of nitrile groups to give conjugated carbon-nitrogen sequences, which inhibit the cyclisation process and result in a chain scission reaction. From 350 °C to 700°C, the cyclized structure loses hydrogen and become more aromatic in character. At around 900 °C, the chain begins to lose nitrogen, indicating breakdown of the heterocyclic rings in PAN and rearrangement to give pure carbon. A detailed explanation of this work is given in [259]. On the other hand the oxidative stabilisation treatment of polymers, before this exotherm occurs, appears to stop this chain scission effect, preventing mass loss and fusion of polymers. During the oxidative thermal treatment of PAN fibres, dehydrogenation and oxidation reactions take place, as well as ‘nitrile cyclization reactions’ that produce a stabilised (more rigid) ladder polymer as illustrated in Figure 6.12 [259-262]. Nitrile cyclisation involve the conversion of the nitrile groups

(−C≡N) into >C=N-which is highly exothermic, leading to the formation of heteroaromatic rings. The oxygen that is added during stabilisation is thought to result in formation of −OH, =CO and (=N−O) which promotes cross linking as shown in Figure 6.12 [262]. During subsequent carbonization in a non-oxidizing atmosphere, oxygen and the heterocyclic nitrogen are split off and planar polyaromatics are formed. All nitrogen incorporated into the ladder structure is eliminated by at 1700 °C [263].

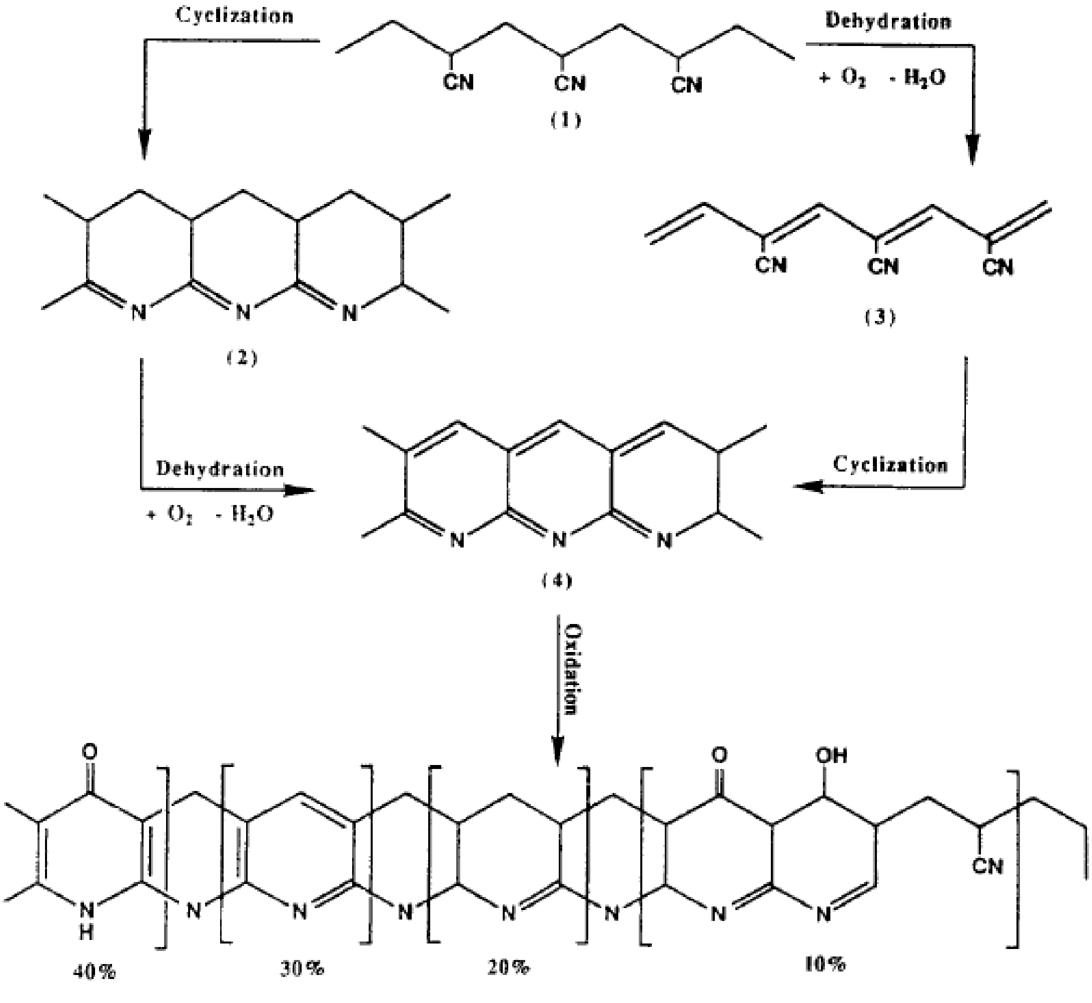

Figure 6.12: Mechanistic pathways for the thermal degradation of polyacrylonitrile according to Keller *et al.* [262].

Although numerous studies have looked at how the stabilisation process improves the mechanical properties of the carbon fibres by improving cross-linking and retaining higher carbon content, the difference in the development of graphitic structure in the fibres between the oxidised and non-oxidised has not been discussed. We were interested in establishing the difference between the development of the graphitic structure, e.g. rate of formation and orientation of graphite crystals, between oxidised and non-oxidised carbon fibres. This detail is important for controlling the carbonisation process to yield fibres that are most suitable for intercalation and hydrogen adsorption.

Typical conditions for preparation of carbon fibres are oxidation in air at 200-300 °C for 2-10 hours, preferably under mechanical restraint for optimised mechanical properties, followed by carbonization in vacuum or inert atmosphere. These fibres can then be graphitized by heating at temperatures ranging from 1500 to 3000 °C in an inert atmosphere or vacuum for 1-2 hours.

6.4 Experimental details

6.4.1 Solution preparation

Polymer solutions were made by mixing polyacrylonitrile, PAN, powder (150,000 gmol^{-1}) in >99.5 % purity Dimethyl sulfoxide, DMSO, (both from Sigma Aldrich). PAN was selected as the carbon precursor as it was the most easily obtainable polymeric carbon precursor. DMSO was used because it is a highly compatible solvent with PAN (i.e. it has matching solubility parameters) and because it is a more benign solvent, both environmentally and physiologically, than N,N-Dimethylformamide, DMF, which is typically used for electrospinning PAN. Since our main aim was to minimise the fibre diameters we have modified the solution concentrations and chemistry through the use of additives to find the composition that yielded uniform fibres with the lowest diameters. For this reason we have prepared solutions with a range of concentrations, 2-10 wt.% PAN. These solutions took approximately a day to achieve a clear-coloured homogeneous state, but this time could be reduced by immersion of the solution contained in bottles in an ultrasonic bath heated to 40-50 °C.

Sodium chloride (NaCl) and the anionic surfactant 4-styrenesulphonic acid, sodium salt hydrate (SASH) (Sigma-Aldrich), were added to some solutions at concentrations of 1 mg ml^{-1} and 5 mg ml^{-1} respectively. Salts increase the conductivity of the solution without largely varying the viscosity, while surfactants have the effect of reducing the solution surface tension and increasing the conductivity. Both additives when balanced in the right direction (to allow for the columbic force to overcome surface tension) enable the production of low diameter uniform fibres from low polymer concentration solutions that otherwise have the tendency to yield beaded fibres.

Solution viscosity and conductivity was determined using a Brookfield (Programmable –II+) viscometer and a Jenway 4510 conductivity meter respectively, at room temperature (~ 21°C) prior to electrospinning. The viscosity curves obtained as a function of spindle rotational frequency were fitted to obtain the high shear limit of viscosity.

6.4.2 Electrospinning of PAN fibres: Set up and process parameters

The same in-house-built electrospinning rig (as detailed in §5.3.3) was used to electrospin the PAN solutions, except with a single nozzle set as opposed to a co-axial nozzle. The solution feed rate was controlled using a programmable Harvard- PHD 2000 syringe pump. The inner diameter of the nozzle used was 0.45 mm and its height from the aluminium collection plate was set as high as possible within our equipment, to 30±1 cm. This height was maximised to allow for fibres with smaller diameters to be electrospun (as explained in §2.6.2.2). The voltage was adjusted between 5-10 kV for each solution until a stable jet was emitted from the Taylor cone, but once this stability voltage was found it was generally kept fixed at that value. The flow rate was selected once the flow rate dependence of the fibre diameters was determined. The rate selected was 200 μl hr^{-1}, which was the most stable rate that produced fibres with the lowest diameters. The electrospun fibres were either collected on small aluminium stubs (for microscopy studies) or graphite discs (for heat treatment) Figure 6.13.

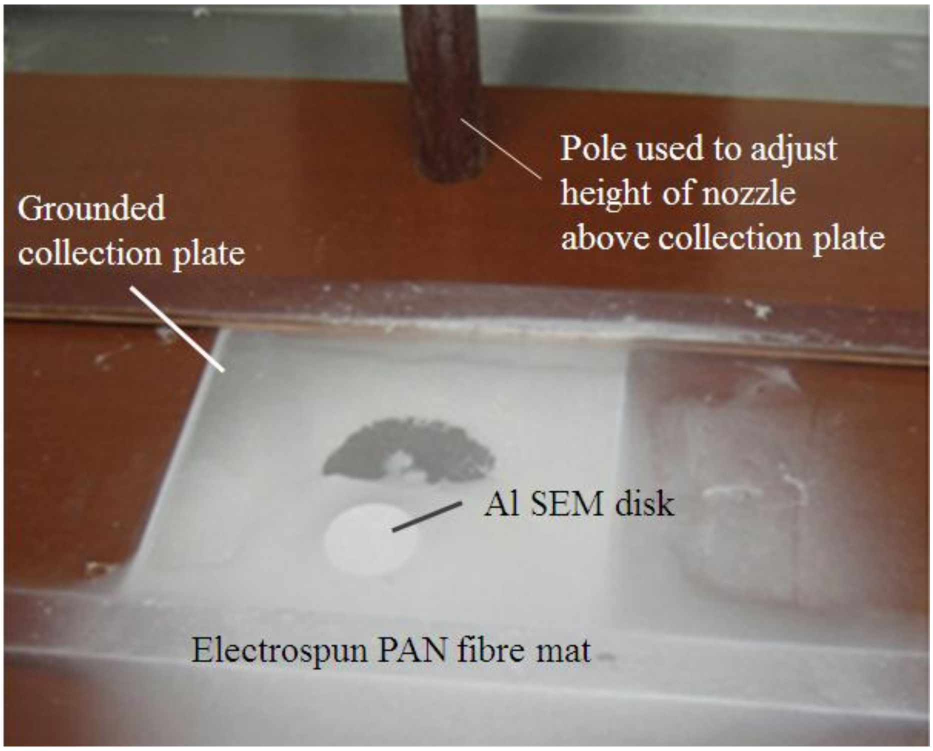

Figure 6.13: Electrospun PAN fibres (white coating) on grounded collection plate.

6.4.3 Thermal treatment of as-spun PAN fibres

The electrospun PAN fibres were heat treated in a series of steps to yield graphitic nanofibres. As discussed earlier in §6.3.6.1 the synthesis of carbon fibres from polymer fibres involves three steps: i) stabilization, ii) carbonization and iii) graphitization. Although we were not initially concerned about maximizing the tensile strength, which is why the stabilisation step is usually used, we were interested in investigating the effect of oxidation on the structure of our fibres, primarily because it reduces the mass loss during graphitization. Thus two sets of CNFs were prepared; a non-oxidised set and an oxidised set.

The non-oxidised (non-stabilised) set were obtained by heating the PAN fibres in a tube furnace at a heating rate of 3° min^{-1} to 500 °C, where the temperature was retained for one hour. During this time the system was kept under a dynamic vacuum to remove the volatiles. The stabilised CNF set was obtained by initially heating the PAN fibres in air at 250 °C for six hours, (using the same ramp rates of 3° min^{-1}) followed by the same carbonization procedure of the non-oxidised set up to 500 °C. To graphitise these CNFs they were then further heated in a high temperature furnace at a set of temperatures ranging from 1500 to 3000°C, again at a heating rate of 3° min^{-1}. The heat treatment temperature (HTT), the polymer used and the process condition employed in making the fibres are the most influential factors affecting the development of the structure. Since our main aim was to develop carbon fibres of sufficient crystallinity to enable alkali-metal intercalation, we looked at the change in the crystallinity of the fibres at a range of temperatures to monitor the development of the graphitic structure from the amorphous CNFs. From X-ray diffraction and TEM results we found that the out-of-plane crystallinity in the fibres increased with heat treatment temperature (HTT), as discussed in the results section below. It should be noted that every graphitized fibre sample in this study was spun using polymer solutions of 6.8 % PAN in DMSO or higher. Although this did not produce the finest fibres it did rapidly produce sufficient quantity of material for characterisation and neutron studies without much compromise for the fibre diameters.

6.4.4 Characterising fibre morphology and crystal structure

The fibres were imaged using a FE-SEM (Carl Zeiss XB1540) to determine the morphological appearance of the as-spun fibres. These SEM micrographs, taken from various regions on the SEM stub, were then used to determine average fibre diameters, using the image processing program *ImageJ* [264]. For each spinning condition the arithmetic mean and standard deviation were measured for the fibre diameters from at least 100, and more typically around 300 fibre measurements.

The structure of the nanofibres was examined by X-ray diffraction (XRD), using a Philips X-Pert theta-theta X-ray diffractometer with Cu-Kα source, to determine the degree of crystallinity. A background obtained from an empty glass slide was subtracted from each pattern, and the intensities were normalised to the (100) peak. High magnification images of the fibres were obtained using a TEM (JEOL JEM 2010) at an accelerating voltage of 200 kV, which also enabled a qualitative comparison with XRD of the extent of graphitization of the fibres.

6.4.5 Synthesis of KC_{24} nanofibres

The KC_{24} fibre samples were prepared primarily for neutron scattering experiments. Prior to intercalation the graphitised fibres (~1g) were weighed and outgassed (pumped on) for more than 24 hours to remove all trapped gas and impurities. This was done with the samples placed in a quartz tube sealed with a valve that can be connected to a turbomolecular pump (see

Figure 6.14). In order to ensure that all the volatiles on the sample were removed the outgassing was carried out with the GNF sample heated to 500 °C with the quartz tube placed in a tube furnace, the release of volatiles was monitored through the pump pressure reading. When the pump reading was low and stable ($1\text{-}1.5\text{x}10^{-6}$ mbar was considered sufficiently low) the furnace was turned off and the valve on the tube was firmly shut once the tube had cooled. The quartz tube that was tightly sealed at one end was removed from the cooled furnace and placed into an argon glove box. At this point onwards it was critical not to let the sample to be exposed to air, moisture or any other reactants, for this reason the glove box used was a high purity one with H_2O and O_2 concentrations of less than 10 ppm (the ideal value was less than 1 ppm). The GNF sample was then removed from the tube in the glove box and weighed once again to determine the weight loss during outgassing. This outgassed sample was then ready to be intercalated with potassium.

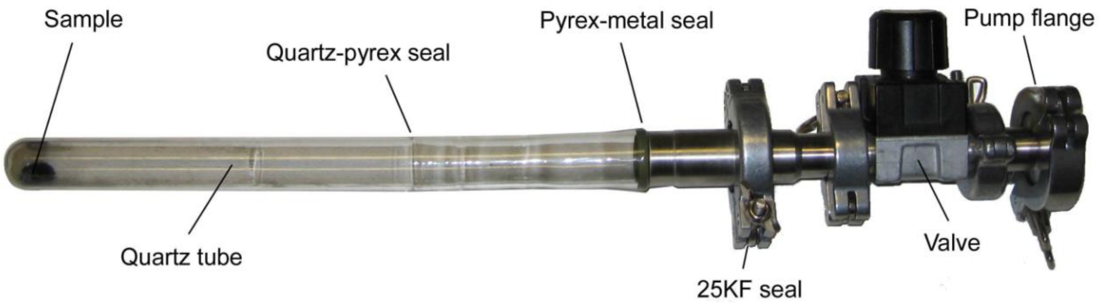

Figure 6.14: Quartz sample tube with valve for vapour transport synthesis.

The intercalation process was carried out using one-zone vapour transport method, which involves heating the intercalant (potassium in this case) above its melting point in the vicinity of the graphitic sample placed inside a glass tube (heated in a furnace) and waiting for the intercalant to vaporise and intercalate into the graphite over a period of time (as discussed in §6.3.5). For this intercalation step the graphitic sample was placed back into the quartz tube inside the glove box with the correct stoichiometric weight of potassium + 20 wt.% excess placed close to it. While the stoichiometric amount of potassium was calculated on the basis of making KC_{24} with the available mass of carbon sample, the excess was added to account for potassium that got trapped inside the quartz tube during the intercalation process. From previous intercalation experiments (using the same method) it was found that a mirror layer of solidified potassium formed inside the cooler end of the quartz tube, at the point close to the valve, where the intercalant vapour condensed and solidified. Evidently, a proportion of the intercalant vapour did not enter the graphite even if there was room for it; thus, to ensure the end result was close to a stoichiometrically-desired stage-2 potassium GIC, excess potassium was added to account for the loss of the intercalant.

The tube containing the potassium (intercalant) and the graphitic fibres was then sealed (with the valve closed), removed from the glove-box and placed inside a tube furnace that was not yet turned on. The glass tube was then reconnected to the turbo-molecular pump and pumped on with the valve open to remove the Ar gas, until the pressure reading was as low as $5x10^{-5}$ mbar. The valve was closed off once again and the furnace temperature was set to 300 °C for 1 hour period, during which time the potassium melted, vaporised and intercalated into the graphitic fibres, with the fibre colour changing from a dark blue-to-bronze colour (as shown in Figure 6.15). This contrasts with the bright blue-to-gold shade obtained for intercalated Papyex strips. This is thought to be due to diffuse reflection of light from the GNF sample surface, which is much rougher than the Papyex carbon strips used as a result of the random orientation of the fibres in the sample. Once the quartz tube had cooled after the intercalation it was returned back to glove box, where the sample was retrieved, weighed and stored in an air tight container, ready to use for experimentation. Besides the colour of the resultant GIC sample (which is a direct indicator of its stage as discussed in §6.3.1) the new mass of the sample (i.e. mass uptake) was also used to check if stoichiometric composition was that of KC_{24}. XRD was also used to check that it had the correct stoichiometry as well to make sure that the samples were fully intercalated. However, since X-ray diffraction only gives information about the surface layers of the sample, the bulk intercalation of the fibre samples was only verified through the use of neutron diffraction prior to hydrogenation studies (as discussed in §6.5.5.1).

Figure 6.15: Graphitic nanofibres during the intercalation process of potassium, (left) shows the fibres at a point near the beginning and (right) towards the end of the intercalation.

6.5 Results and Discussion

6.5.1 Minimising fibre diameters

As outlined earlier our main objective in the synthesis of the PAN nanofibres was to determine the electrospinning conditions (i.e. process and solution parameters) that yielded fibres with the lowest attainable diameters from a PAN-DMSO solution system. Since the main solution parameters that control fibre diameters are polymer concentration (or viscosity), conductivity and surface tension (as discussed in §2.6.1), we have initially looked at the effect of varying these parameters.

Figure 6.16 shows the variation of viscosity with PAN concentration and the respective change in diameters with viscosity (as shown by the inset). If the fibre diameter were a simple function of the polymer content of the solution then it should increase as a square root of the PAN concentration. However, the solution viscosity, which increases exponentially with concentration (Figure 6.16), also has an effect on the diameter. As the viscosity increases, the extent to which the spinning jet can be stretched at a given voltage will decrease, resulting in an increase in fibre diameters. However, when the viscosity is too low, the Rayleigh instability and the increased surface tension cause the jet to break up into droplets, causing electrospraying of the jet. For pure PAN/DMSO solutions this point was established for solutions with PAN concentration of around 3.8 wt.%.

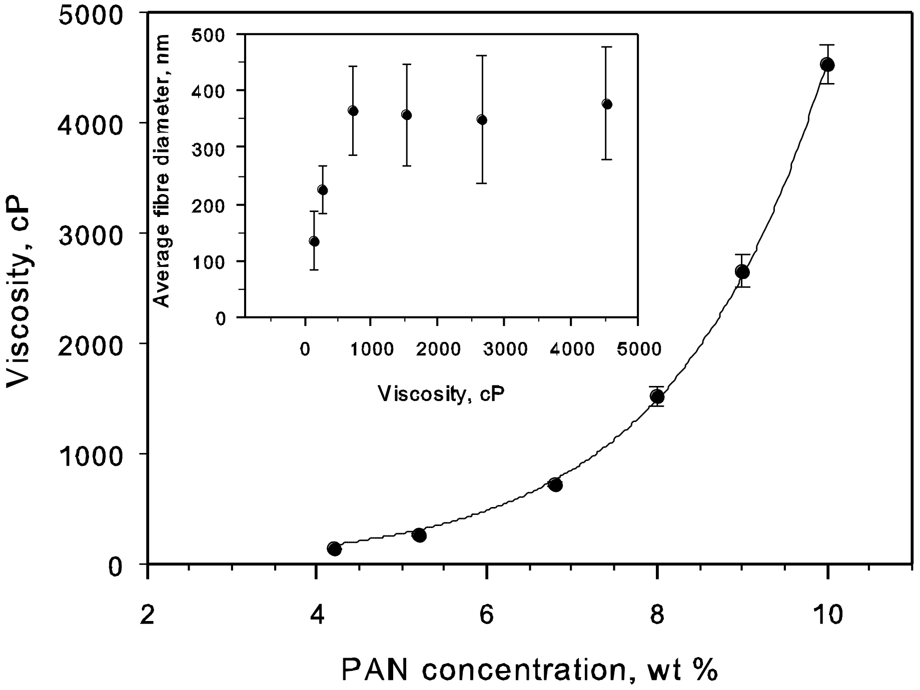

Figure 6.16: Viscosity of PAN solutions in DMSO, the inset shows the fibre diameter as a function of viscosity

Below this concentration it was no longer possible to produce fibres. Above this concentration the diameter does appear to grow approximately as the square root of the PAN concentration (Figure 6.17). However, above 6 wt.% PAN the fibre diameter no longer increases. The reason for this is not clear; however, in order to maintain the stability of the spinning process the voltage was adjusted to obtain a stable Taylor cone. Although the voltage variation was only within the range 7.7 to 9.8 kV, it is probable that this variation caused the small reduction in fibre diameters between 6 and 10 wt.% PAN concentration.

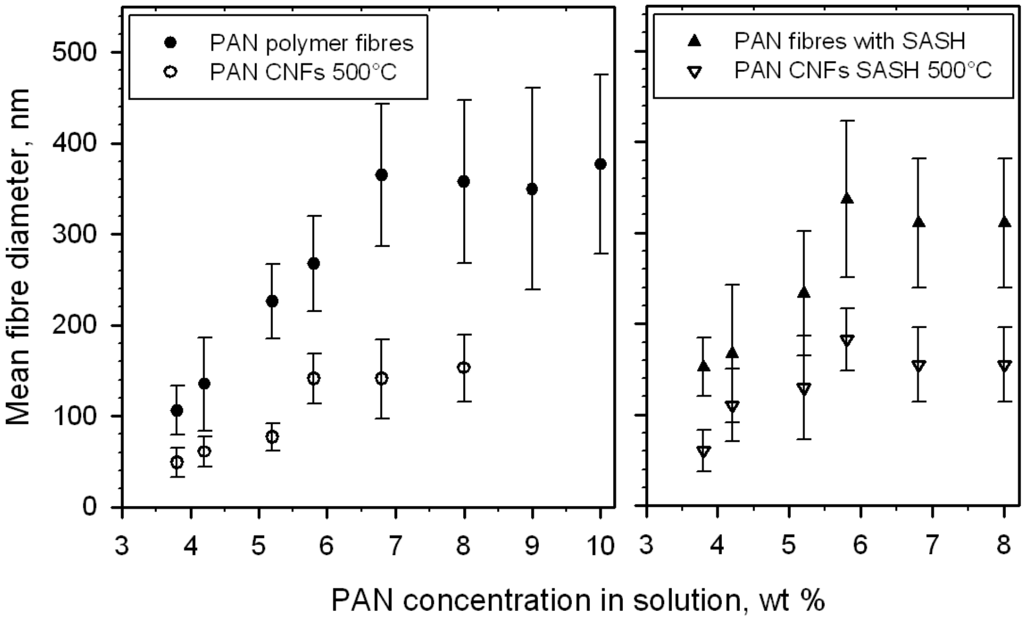

Figure 6.17: Polymer and 500 °C pyrolysed (CNF) fibre diameters as a function of concentration of PAN in DMSO solution, without (left) and with (right) added SASH surfactant. The error in the readings is taken as the standard deviation of the normal distribution of fibres measured from the SEM images.

The variation in electrical conductivity of PAN/DMSO solutions (with and without SASH surfactant or NaCl salt additives) is shown in Figure 6.18. Conductivity increases linearly with increased PAN concentration in the pure solution. Adding NaCl increases conductivity 20-fold up to 2 wt.% PAN. Even though the solution conductivity increases with the addition of SASH, the increase is reduced with PAN concentration. This is probably due to the reduced mobility of the ions in more concentrated solutions.

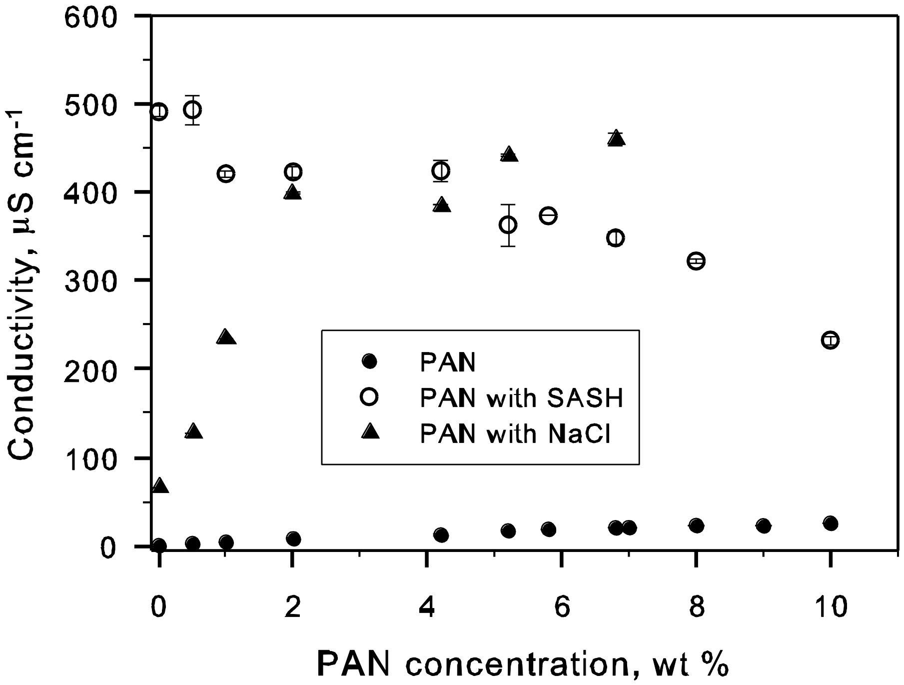

Figure 6.18: Conductivity of PAN solutions in DMSO: (Closed circles) PAN in DMSO; (open circles) PAN in DMSO with 5 mgml^{-1} 4-styrenesulphonic acid, sodium salt hydrate (SASH) surfactant; (triangles) PAN in DMSO with 1 mgml^{-1} NaCl.

Without any additives the PAN/DMSO solutions produced beaded fibres below PAN concentrations of 5.2 wt.% PAN (see Figure 6.19 (a)), but of course beading occurred down to the point when beading converted to electrospraying below 3.8 wt.%. For beaded fibres the measured fibre diameters are from the inter-bead regions which are narrowed as the surface tension draws polymer from the fibres into the beads. Beading is known to occur as a result of the competition between the electrostatic forces and the surface tension (as discussed in 2.6), and we found that using a saturated solution of NaCl was effective at reducing the beading. NaCl only really changes the conductivity (increasing it from less than 50 µS cm^{-1} to around 400 µS cm^{-1}) with little effect on the viscosity and surface tension. Addition of an anionic surfactant (5 mg ml^{-1} SASH) was also effective at controlling the beading, as shown in Figure 6.19 (b), although it is not clear whether this is due to the increased conductivity (also to around 400 μS cm^{-1}) or due to a decrease in surface tension.

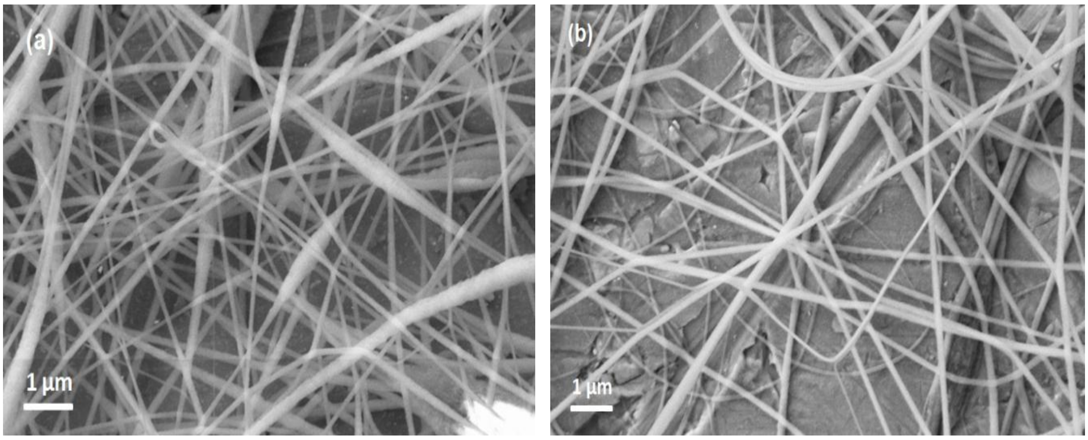

Figure 6.19: SEM images of fibres electrospun from 4.2 wt.% PAN/DMSO solution; a) fibres without SASH b) fibres with SASH

When investigating the effect of additives on the polymer fibre diameters, the variation in the diameters of the same fibres when carbonised at 500 °C was also studied. Thus, it was be possible to obtain an idea of the final diameters once the fibres were carbonised. Table 7 shows the variation in the diameters of the fibres produced from 4.2 wt.% PAN in DMSO solution. The lowest diameter is obtained without any additives. Although the additives remove the beading it also causes the polymer mass to be more evenly distributed along the fibre axis. In the beaded fibres the polymer density is greater in the beads and the fibre between the beads is stretched more to give finer fibres. The lower SASH concentration (5 mg ml^{-1}) solution bizarrely results in lower diameter fibres than that with the higher concentration (10 mgml^{-1}). Likewise with NaCl and SASH combined. It is possible that adding saturation amounts of additives cause ions in the solution to coalesce and result in reduced conductivities, which will lead to increased fibre diameters. As shown in the table, the standard deviation of the data is relatively large; this is due to the large variation in the fibre diameters for a given sample set. Although these particular diameters are on the low end of the diameter range, the smallest fibre diameters (with an average of 106 nm for polymer fibres and 49 nm for the same fibres carbonised at 500 °C) were obtained through the electrospinning of 3.8 wt.% PAN/DMSO + SASH solution.

Once the effect of NaCl and SASH on fibre diameters was established and the optimal process parameters were determined, one solution concentration had to be chosen to be used for making large quantities of fibres for graphitisation. The selected solution was 6.8 wt.% PAN in DMSO; even though this solution did not necessarily produce fibres with the lowest diameters, we used a solution concentration in the mid-range as a compromise between fibre diameter and the rate of fibre production. All the heat treatments processes described below were carried out with these fibres.

Table 7. Average fibre diameters for 4.2% PAN in DMSO with NaCl and SASH additives, as-spun polymer and after carbonisation at 500 °C under vacuum.

	Polymer		Carbonised at 500°C	
	Fibre diameter [nm]	Standard deviation [nm]	Fibre diameter [nm]	Standard deviation [nm]
4.2% PAN in DMSO	130	50	60	20
plus 5mg/ml SASH	170	80	110	40
plus 10mg/ml SASH	290	60	200	60
plus 1mg/ml NaCl	160	50	90	40
plus 1mg/ml NaCl and 5 mg/ml SASH	200	70	140	60

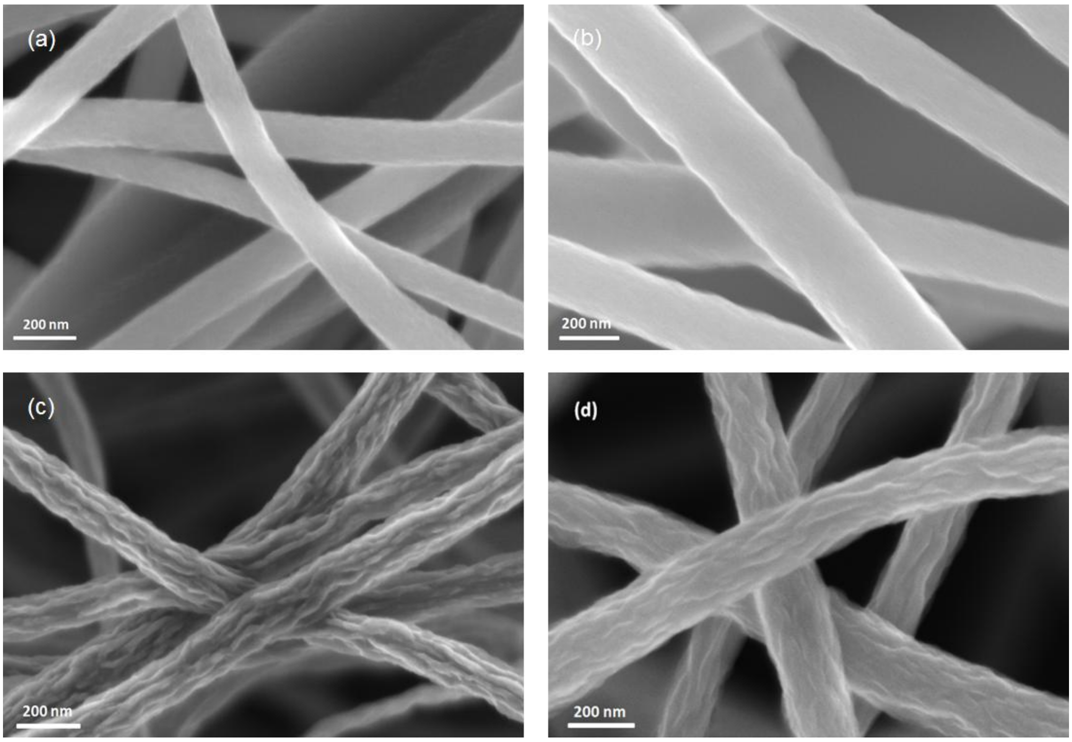

Figure 6.20: SEM images of heat treated non-oxidised fibres: a) HTT=1500°C, b) HTT=2800°C, and oxidised fibres c) HTT= 1500°C and d) HTT= 2800°C.

6.5.2 Carbonised fibres: SEM & TEM analysis

SEM images of fibres from 6.8% PAN in DMSO solution after heat treatment (Figure 6.20 (a)-(d)) show how the surface morphology of the fibres changes with increasing temperature. While the fibres heat treated at lower temperatures (<1500 °C, Figure 6.20 (a) and (b)) have a smooth surface, those at higher temperatures (e.g. 2800°C, Figure 6.20 (c) and (d)) develop a rougher and more ridged morphology with increasing temperature. As shown in Figure 6.21 the fibre diameters and sample mass decrease with increasing heat treatment temperature. Oxidized fibres retain a greater proportion of their diameter and overall mass loss to 1500 °C is approximately 70% of the starting polymer mass, which remains constant to 3000 °C. Non-oxidized fibres lose upwards of 90% mass to 3000 °C. This may be a result of the mass loss on heating, and of the transformation of an amorphous carbon structure to a more crystalline graphitic structure. The non-oxidized fibres, as well as having a smaller average fibre diameter, have a more uneven morphology along the fibre axis than the oxidized fibres, probably due to the fact that they are prone to a greater loss of carbon in the heating process as a result of greater evaporation of volatiles [245, 265]. The development of the graphitic structure with increasing heat treatment temperature (HTT) is clearly visible in Figure 6.22 through the formation of graphitic ribbons (called fibrils in literature). Both the fibril depths, which correspond to layers of graphite basal planes in c-direction, and lengths increase with temperature. The orientation of (002) planes along the fibre axis also increases with heat treatment temperature, in agreement with previous work [255].

Higher magnification TEM images of the fibres heated treated at 2800°C are shown in Figure 6.23; (a) and (b) are images of a non-oxidised fibre, (c) is that of an oxidised fibre at the same magnification as (b) (400K). Though it is difficult to make a generalised comparison between the structure of oxidised and non-oxidised fibres with just an observation of part of the fibre, graphitic structure appears to be similar in both fibres (treated under oxidised and non-oxides conditions) as confirmed by XRD spectroscopy discussed below. Both oxidised and non-oxidised fibres have an entangled ribbon structure formed of micro-fibril layers of graphite basal planes (sp^2 type carbon). The average layer spacing measured from the images is 3.34Å. These ribbons appear to pass smoothly from one domain of stacking to the other, with a general orientation along the fibre axis. This observation is in agreement with the 'ribbon structure model' suggested by Diefendorf and Tokarsky [255] for formation of graphitic structure in carbon fibres (as discussed in §6.3.6.1). It is however not clear how the ribbons interact in three dimensions to give the undulations and entanglement seen in the TEM images. The 3D structure proposed by Bennett and Johnson, as shown Figure 6.11, show a possible way in which the graphite layer planes interlink both longitudinally and laterally. Although such a structure results in some two-dimensional (2D) ordering, three-dimensional (3D) ordering is not attained. Thus, it appears that the graphitic structure obtained from carbonisation of the PAN fibres results only in 2D ordering of the graphite planes, in the presence of an amorphous component as discussed below.

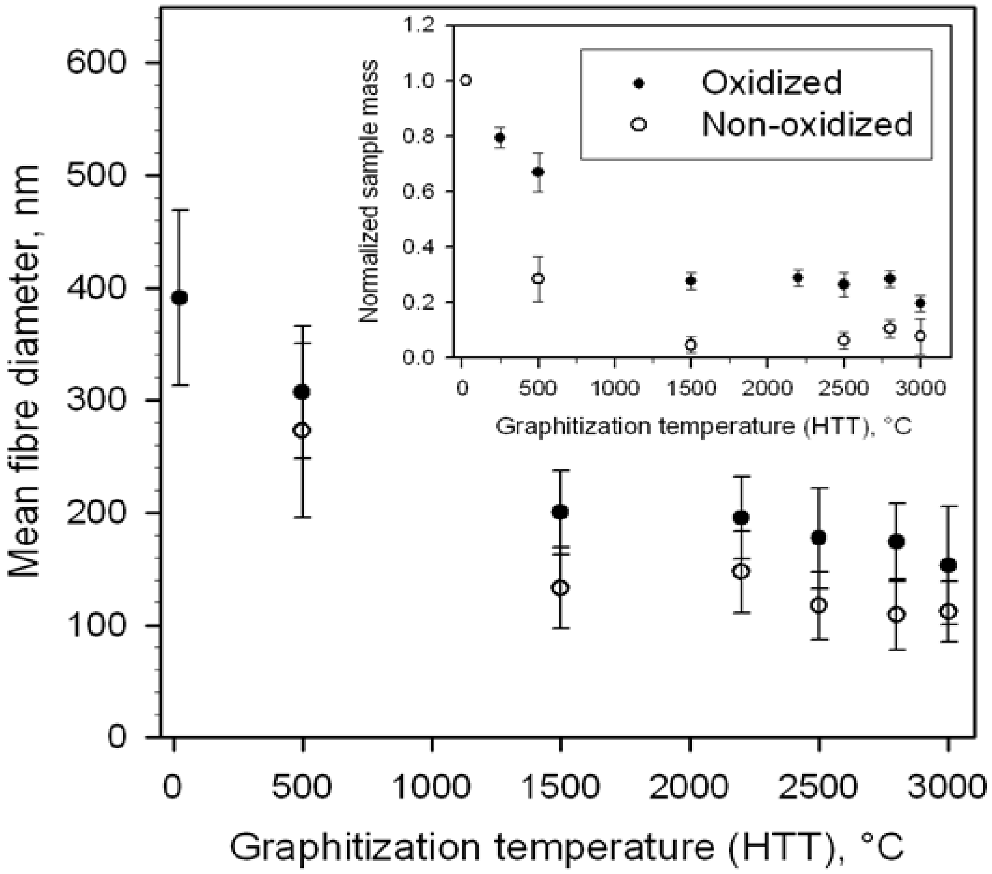

Figure 6.21: Fibre diameters and normalized mass (inset) of fibres from 6.8wt.% PAN in DMSO solution as a function of HTT. Closed circles = oxidized fibres, open circles = non-oxidized fibres. Mass is normalized to the pre-heat treatment polymer mass for each sample.

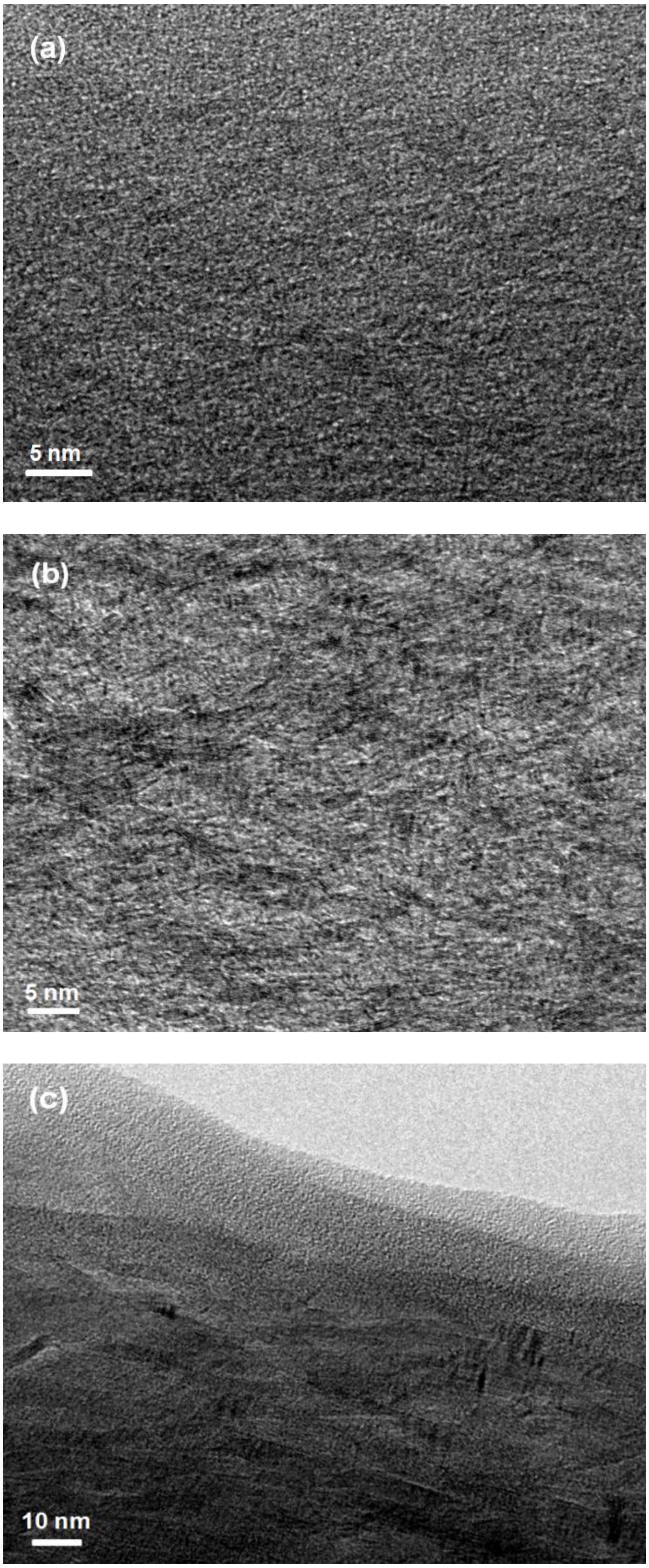

Figure 6.22: TEM images of fibres at a) HTT = 1500, b) HTT= 2200, and c) HTT = 2800 °C.

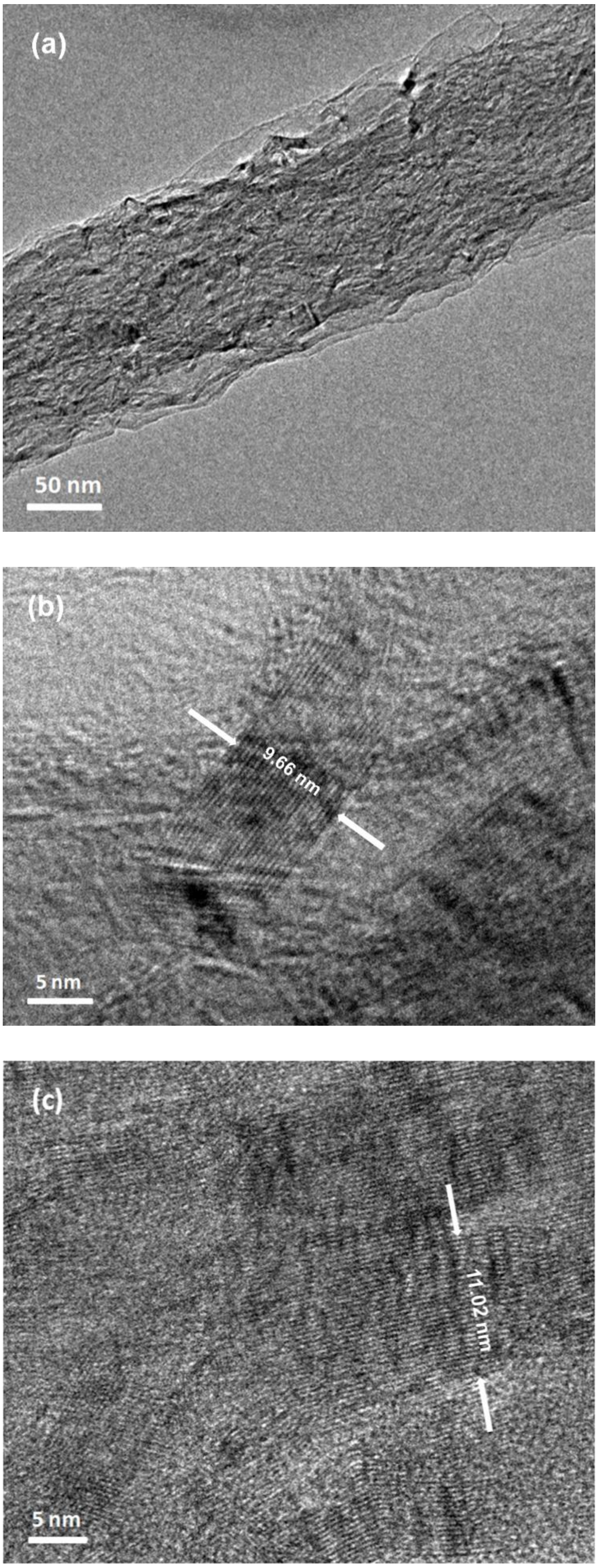

Figure 6.23: TEM images of fibres heat treated at 2800C; Non-Oxidised fibres (a) and (b) and Oxidised fibre (c) ((b) and (c) magnification 400K).

6.5.3 XRD Analysis of GNFs

The background-subtracted X-ray diffraction data are presented in Figure 6.24. The principal graphite diffraction peaks seen for high HTT are the (002), (100), (004), (110) and (006). There is no evidence for the presence of peaks combining in-plane (*hk*0) and out-of-plane (00*l*) indices (*h*, *k*, *l* >0), and so the graphitic nanofibres do not appear to contain 3D ordering. Thus the local structure of the graphitic fibrils appears to be unregistered, or turbostratically disordered, stacked graphene planes. This result is expected, as PAN is not a precursor of crystalline graphite.

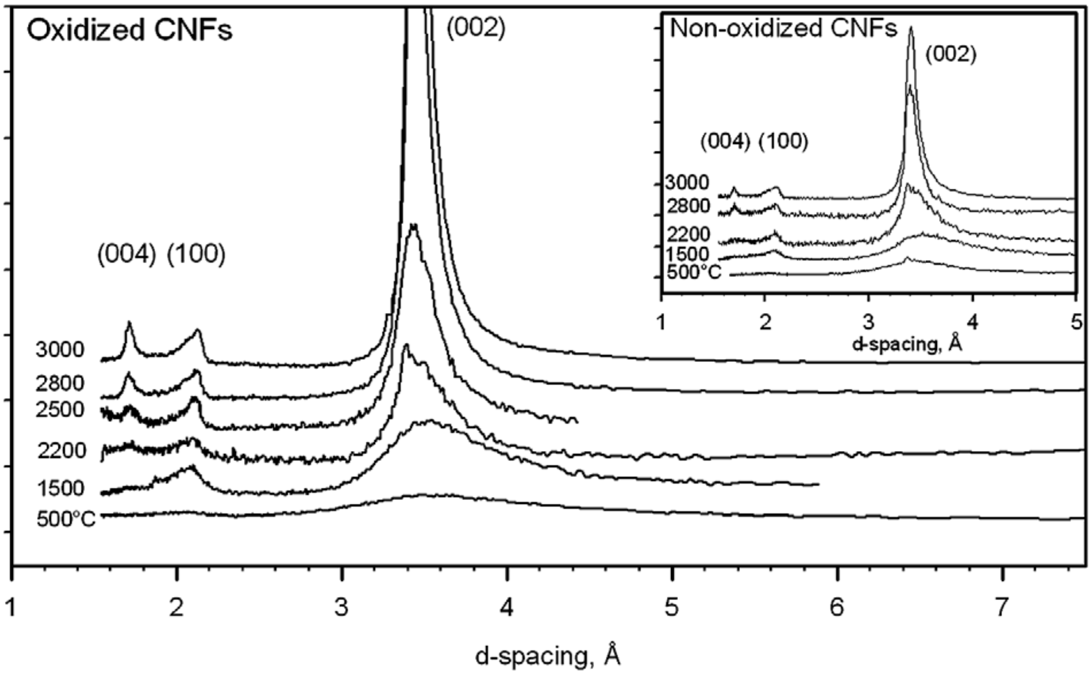

Figure 6.24: X-ray diffraction data from oxidised and (inset) non-oxidised fibres at HTT from 500 to 3000°C using Cu Kα source. The background from the glass slide has been subtracted from each pattern.

The data show a strong signature of developing graphitization in the *c*-axis direction. For both oxidized and non-oxidized fibres the graphitic structure increases with temperature, as is evident from the growing intensity of the (002) peak at 3.3 Å and the (004) at 1.7 Å. The asymmetry of the (100) peak at 2.1 Å, with a tail to the low-d side, is typical of turbostratic graphite [266]; but the (002) peak is asymmetric with a tail in the opposite direction. This is unexpected for a single phase peak; however, theory shows that when there are very few graphene layers the (002) peak is shifted towards lower d-spacings even though the interlayer spacing is unaltered. So we believe that the tail is actually due to the presence of only a few graphitic layers. Using the theory developed by Fujimoto [266], it is possible to fit to a model containing a percentage of graphene bilayers, tri-layers etc. However, it was not possible to get a stable fit using this method since above 3 or 4 layers the peaks are too similar in width and position. We chose a simplified model where we fitted the (002) peak to two Lorentzians: a broad one at low d-spacings to represent the fraction of the graphite with only 2 or 3 layers and one at higher d-spacings to represent 4-layers and above. Although not strictly accurate this model produces a stable fit and gives a good indication of the development of the c-axis stacking as a function of heat treatment temperature.

The areas of the peaks are expressed as a proportion of the overall fitted peak area at each temperature in Figure 6.25. As the HTT increases, the proportion of two and three-layer graphitic material falls and many-layer turbostratic graphite increases, above 80% for oxidized fibres and 60% for non-oxidized fibres. The fitted peak width reduces slightly between 2200 and 3000 °C, although the intensity grows for both oxidized and non-oxidized fibres, suggesting that the many-layer c-axis crystallite nucleates at or below 2200°C and further increase in layer stacking scales only weakly with temperature. However at these temperatures the (002) peak is now sufficiently symmetric to reliably extract the number of graphite layers from the Scherrer equation:

$$\tau = \frac{K\lambda}{\beta cos\theta} \tag{6.3}$$

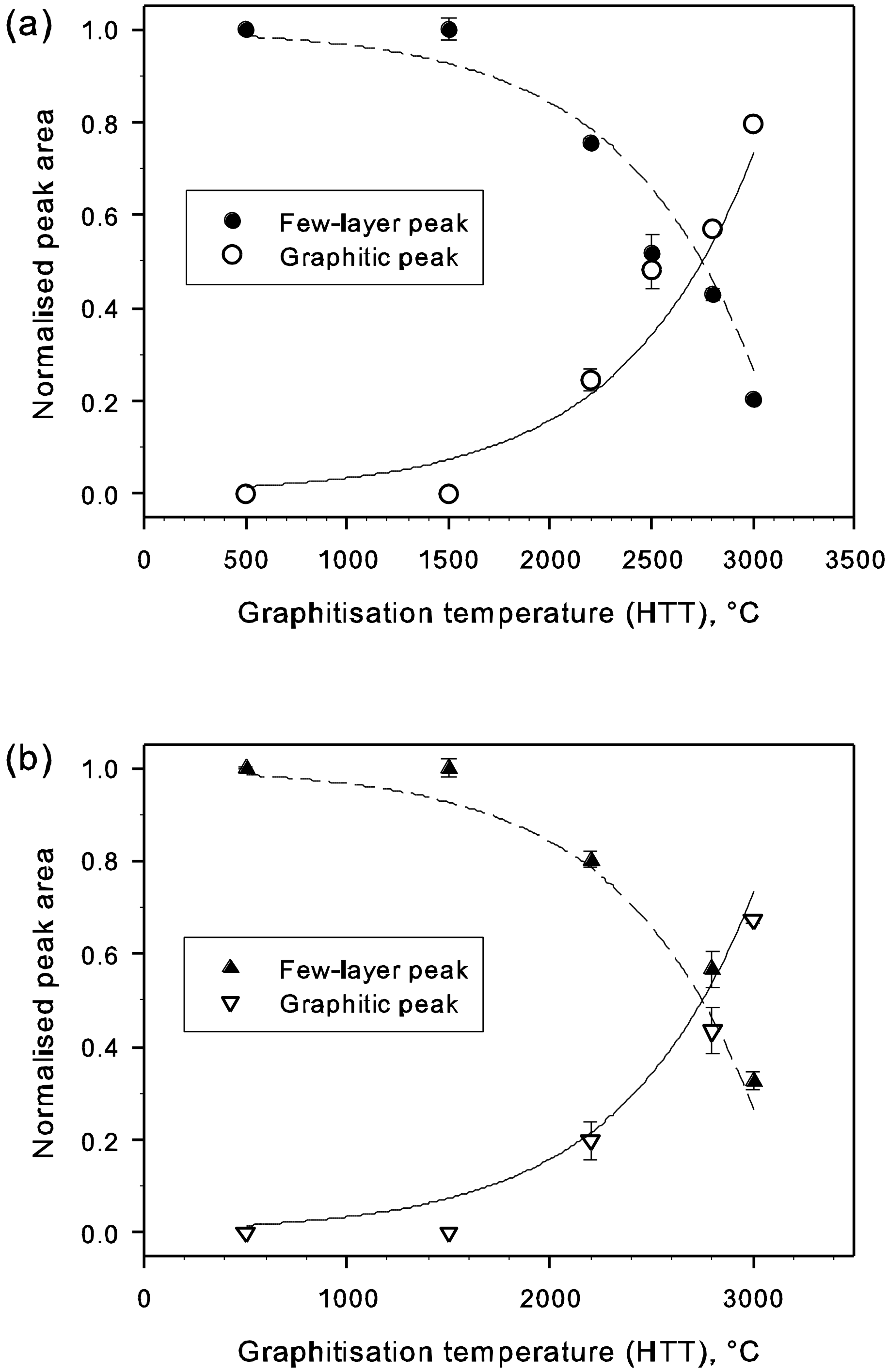

Figure 6.25: Proportional sub-peak fits to the (002) peak showing the growth of the graphitic phase from a phase consisting of few-layer (1- and 2-layer stacked) graphite with increase in HTT; (a) for oxidised and (b) non-oxidised GNF. Exponential fits are provided as a guide to the eye.

with a pre-factor of K=0.9 [266] , X-ray wavelength λ=0.15418 nm, ß, the line broadening at half the maximum intensity (FWHM) in radians, and θ, the Bragg angle. At a HTT of 2800 °C and above, the c-axis crystallite dimension is ~30 graphene layers for oxidized GNFs (corresponding to 7.3±0.2nm lattice dimension), which compares well with what we observe in the TEM images (e.g. Figure 6.23 (c)) where up to 30 graphene layers can be counted in visible crystallite fibrils.

Table 8: The resulting c-axis crystallite dimensions for graphitic component of (002) peak fit at the specific HTTs.

	Oxidised	Non-oxidised
Temperature (°C)	No. of layers	No. of layers
2200	27±3	29±4
2500	19±2	--
2800	29±1	39±4
3000	28±3	36±1

For assessing the in-plane graphite lattice dimension, the (100) peak width was measured, and the pre-factor to Scherrer's equation, which depends on crystallite size, was obtained from [266]. For oxidized GNFs with a HTT of 3000°C, the in-plane dimension was found to be 5.8±0.2 nm, using a pre-factor of 1.70. For non-oxidized GNFs with the same HTT, the equivalent dimension was 4.5±0.1 nm, using a pre-factor of 1.55. This is almost certainly not a reflection of the ribbon width, but an indication of the length scale over which they are flat [267].

Thus, as indicated by the TEM micrographs earlier (Figure 6.23) and the XRD results above the fibres are not fully graphitised and 3-D ordering is not attained. The entanglement of the ribbons in 3-D is not clear and further work is needed to see how these ribbons are formed and ordered across the cross-section of the fibres. TEM imaging of the fibre cross-sections must be done. Additionally, Raman spectroscopy could be used to look at the crystallographic structure in 3-D. The degree of graphitisation and the configuration of the graphitic planes is important for intercalation of species into the fibres. The ideal configuration for ease and speed if intercalation would be to have the graphene planes ordered either perpendicularly to the fibre axis (i.e. basal planes being stacked like discs along the fibre axis) or to have the basal planes ordered radially along the fibre axis, as in the case of pitch fibres (shown in Figure 6.9 (b)). Both these configurations give greater exposure of the graphite edges for intercalation of species. Unfortunately, neither of these configurations was observed in the case of CNFs made from PAN. Other precursor materials such as pitch or rayon, which yield greater degree of graphitic ordering, could be used as alternatives to PAN.

6.5.4 Neutron scattering measurements on H_2-KC_{24}

6.5.4.1 Inelastic neutron scattering

In the neutron scattering studies we were interested in investigating the effect of nanostructuring on the hydrogenation/dehydrogenation behaviour of hydrogen in KC_{24}. Inelastic neutron scattering (INS) provides direct information on the nature and strength of the hydrogen bonding, making it one of the most effective methods for studying hydrogen in materials. INS measurements on hydrogenated KC_{24} nanofibres were carried out using the IRIS time-of-flight inelastic neutron spectrometer (§4.6.3.1), at the ISIS pulsed neutron source. The IRIS spectrometer was specifically selected to perform low-energy inelastic neutron scattering (INS) and quasi-elastic neutron scattering (QENS), so that we could study both the dynamics and diffusion properties of hydrogen adsorbed in KC_{24} nanofibres. Good resolution close to the elastic line and sensitivity to hydrogen made IRIS a natural choice for this work. The data obtained from this study is compared to that from a previous study on bulk-KC_{24} (prepared using Papyex exfoliated graphite)[48, 218], so that any variation in the dynamical behaviour of hydrogen in the KC_{24} nanofibres, as opposed bulk KC_{24}, can be deduced and the possible effects of nanostructuring determined. The details of this earlier study on bulk-KC_{24}, conducted by the same group, also on IRIS, prior to the start of this PhD project, can be found in the following references [48, 218].

This neutron experiment was designed to be the same as the previous study on bulk KC_{24} [48, 218], so that a direct comparison can be made between the two studies. The KC_{24} fibre sample was prepared as discussed in §6.4.5. The hydrogen concentration was measured volumetrically in situ. Para-H_2 was required to simplify the observed spectrum, thus measurements were conducted at the cryostat base temperature (1.5 K), to enable ortho-hydrogen (the triplet state of H_2 with a molecular spin quantum number J=1 (½+½)); to convert to para-hydrogen (the singlet state of H_2 with a molecular spin quantum number J=0 (½–½)), which took approximately 10 hours to be complete. The sample of mass 0.7552 g was loaded in to the hollow annulus of a cylindrical aluminium can (with an annulus thickness of 1.5 mm) as shown in Figure 6.26 and attached to the instrument sample stick (Figure 6.27) to be inserted in to the instrument. The sample stick had valves for controlled release of gasses into the sample volume. Sample heating was controlled through the copper elements attached to the top and bottom of the sample can. All INS measurements were taken at the cryostat base temperature (1.5 K) across both energy windows on IRIS: the first being the -0.8–2.0 meV energy window, selected through the use of the PG 002 analyser and a chopper frequency of 25 Hz, which has an energy resolution of 15μeV close to the elastic line, and the second being 0 – 20 meV energy window. Concentrations of high-purity para-hydrogen were measured from a gas handling rig by volume at 55 K. The following hydrogen concentrations were studied: $KC_{24}(H_2)_x$, x=0 (background), 0.25 (0.27), 0.5 (0.49), 1 (2.02), 1.5 (1.6), 2 (1.87), and saturation; the values in brackets are the actual experimental values calculated after recalibration of the dosing volume. It should be noted that the saturation value is lower than the $2H_2$/K expected, this is probably due to the GNFs having an amorphous component, or the possibility of overfilling with K. For each additional loading of hydrogen, the cryostat temperature had to be raised to 55 K before being cooled back down to 1.5 K to take the measurements. The IRIS INS data was analysed using the software package MODES [268].

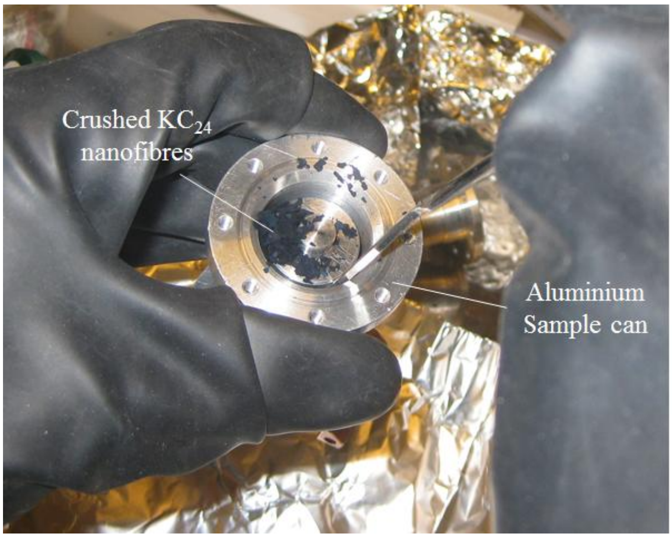

Figure 6.26: KC_{24} nanofibre sample being loaded into the IRIS sample can.

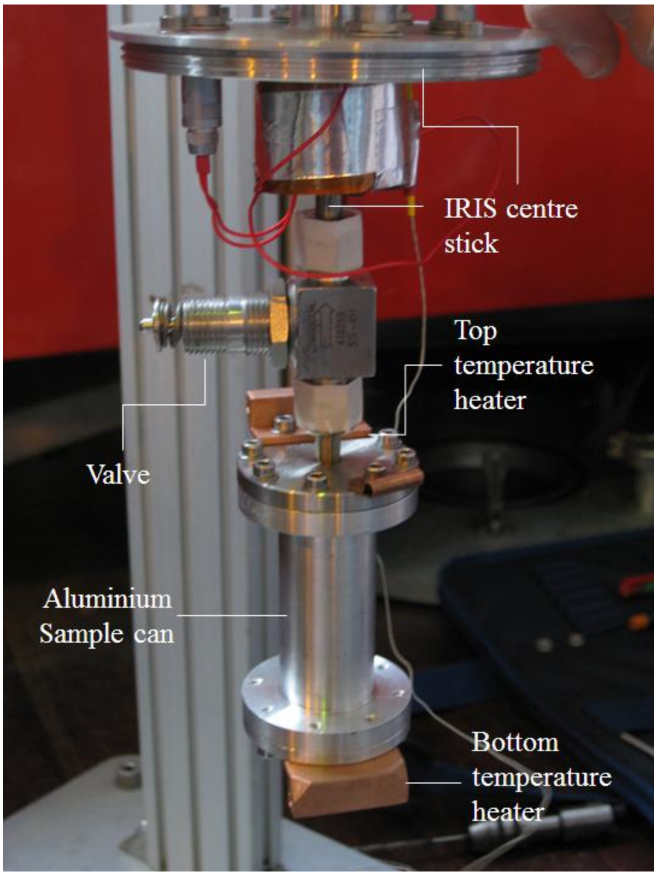

Figure 6.27: The IRIS sample can attached to the cryostat centre stick.

6.5.4.2 INS results

Figure 6.28 shows the spectra of the hydrogen excitations in KC_{24} in the -0.8 to 2.0 meV energy window (a) for bulk KC_{24} synthesised from Papyex exfoliated graphite (from previous study)[48, 218] and (b) for the nanostructured KC_{24} synthesised from graphitic nanofibres (GNFs, from this study). The instrument and sample-can background has been subtracted from the spectrum of pure KC_{24}. In the INS data from the previous sample (Figure 6.28 (a)) two sets of excitations are prominent; one centred around 0.6 meV, and one around 1.5 meV, which shift very slightly towards lower energies with coverage. The band at 0.6 meV arises from tunnel splitting and has a librational counterpart at 48 meV (expected at 51 meV), as shown in the TOSCA data (Figure 6.29 (a)). With the high resolution attainable on IRIS, it was possible to detect a further splitting of this band into a triplet, which was attributed to the existence of three distinct sites for the binding of molecular hydrogen in bulk-KC_{24} [218]. This tunnelling peak is predicted by the librational splitting model [242] discussed in §6.3.4, for H_2 in a $\cos^2\theta$ potential. The second doublet peak centred around 1.5 meV, which was not predicted by librational splitting model, was thought to arise from a combination band involving tunnel splitting and translational motions of the H_2 centre of mass. The observation of three distinct peaks reinforces the notion of three different adsorption sites in KC_{24} (discussed further in [218]]. This assignment was validated by the absence of librational features at 39 meV (see Figure 6.31), which is expected if the features in the tunnelling region were to originate from the presence of orientational forces alone. However, more recent analysis based on new fitting data suggests a different phenomenon. The fittings (see Figure 6.29) show that there is a 2:1 intensity ratio between the outer and inner INS features and a rough 2:1 width change in the bulk GIC system, with the fine structure features more- or-less mirrored in each part. This second tunnelling peak at the higher energy is now attributed to dimerization of H_2 (i.e. H_2-H_2 interactions in the system).

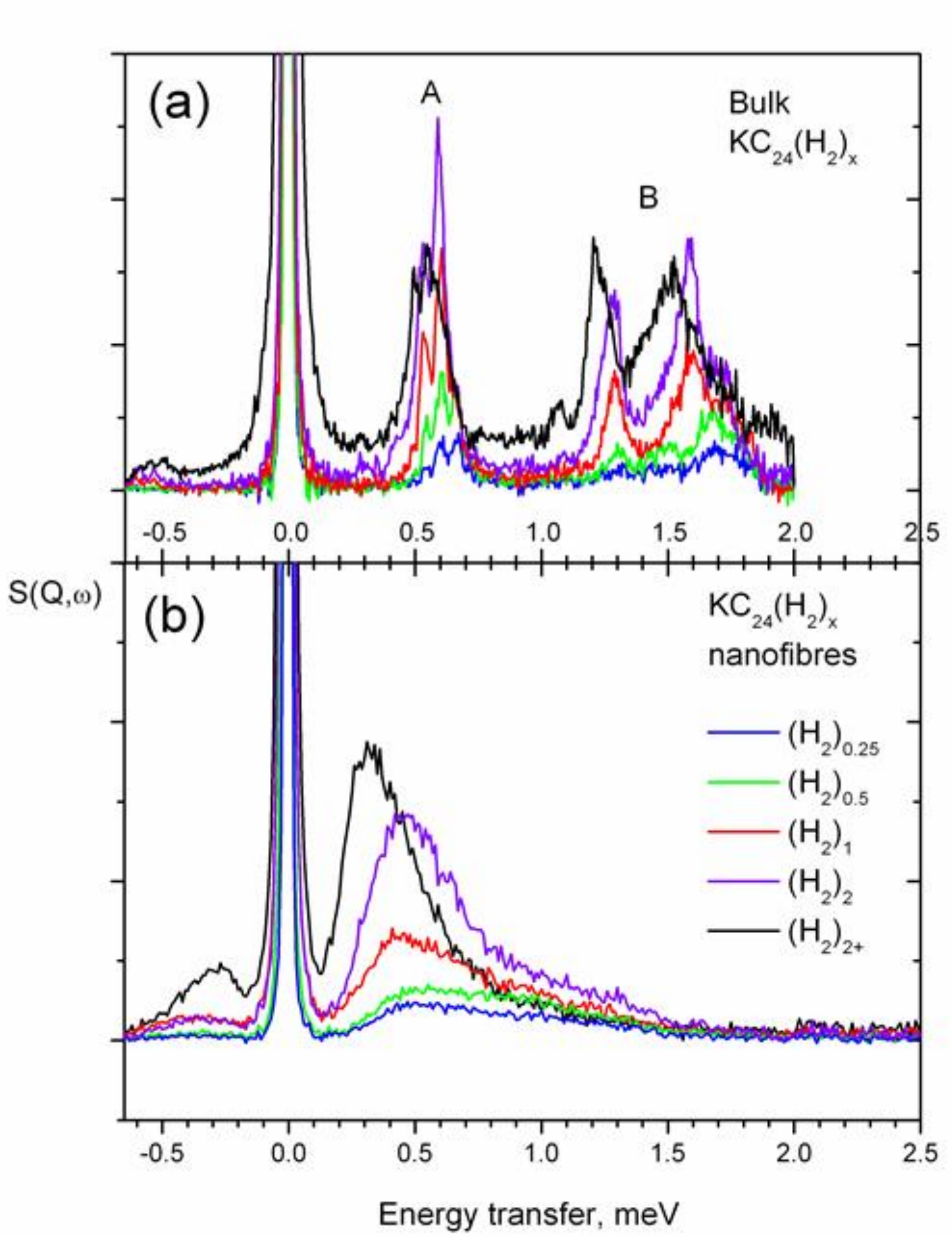

Figure 6.28: INS spectra of $KC_{24}(H_2)x$ using 25 Hz -0.8 to 2.0 meV energy window of IRIS. (a) Bulk KC_{24} sample, data from previous study [1, 13]; two sets of peaks are seen, one around 0.6 meV and the other around 1.5 meV. (b) Data from KC_{24} nanofibres, from this study; the first peak is shifted to the lower energy end by ~0.15 meV, while the second peak associated with H_2-librations appears to be suppressed. *Note: the key is the same for both graphs.*

The INS spectra taken from hydrogen in KC_{24} nanofibres (as shown in Figure 6.28 (b)) show some variation from the data obtained for the bulk (Figure 6.28 (a)). In the nanofibres the spectra take the form of a broad peak which grows with hydrogen coverage, centred on 0.45±0.05 meV in neutron energy loss for $0.25<x<1.5$, and softened to 0.32 meV for saturation $x=1.87$ ($x= 2+$ nominal loading). The principal peak at each coverage has a wide shoulder suggestive of a broader excitation partly covered by the principal but centred higher in energy transfer. By taking each spectrum between 0.15 and 2.0 meV to be a conflation of these two peaks, each with Gaussian lineshape, a fit was performed and the resulting peak centres are plotted in Figure 6.30 with the full-width half maxima represented by the error bars. For coverage of $0.25<x<1.5$, the fitted peak positions are constant to within ~1/5 of the fitted peaks' full-width half maxima. Thus, the site model has the same energy independent of coverage. The reason for the shift in energy of the excitations at $x=1.87$ ($x=2+$ nominal) to a slightly lower value (~0.3 meV) is not very clear but is thought to be due to the saturation of hydrogen sites; another indication of excess K in the GNFs (i.e. slightly more than 1 K per 24 C atoms).

The greater width of features in the nanofibre system is consistent with the lack of long-range order and implies that the fine structure is smeared out with a continuous variation in site energies, i.e. the sites are less distinct and the fine structure, as seen for the bulk, is smeared out. The lack of long range order, or the difference between the crystal sizes between the two samples is discussed further below (§6.5.5.1). What is not so obvious is whether there are two overlapping features in the KC_{24} nanofibre spectra. When fitted as two Lorentzians and two Gaussians the 2:1 ratio is not so clearly marked in the case of nanofibres. This may be because the peaks overlap too much for the fit. This broadening and shift in energy of the higher energy peak (peak B in Figure 6.28) is further suggestive of this peak being a manifestation of the H_2 dimer (i.e. H_2-H_2 interactions in the system). This is because the disorder in the GNFs is likely to result in disordered intercalation of K and hence removal of H_2 dimerization that exists in a more ordered adsorption configuration, which could explain the absence of the higher energy peak that was present in the bulk sample. Figure 6.28 (b) also shows significant intensity on the neutron energy gain side of the window, implying that the hydrogen was not fully converted into the ground state while scattering was taking place. The tunnelling transitions (as shown in the neutron energy loss side of the window) are detected through incoherent scattering of neutrons from H_2 as a result of the nuclear-spin-flip through para-to-ortho conversion of H_2. This is due to the length of time in which the ortho-para conversion took to complete, which was ~10 hrs despite the reported catalytic effect of the intercalate [48]. Time constraints for the experiment meant that a complete transition was not attainable.

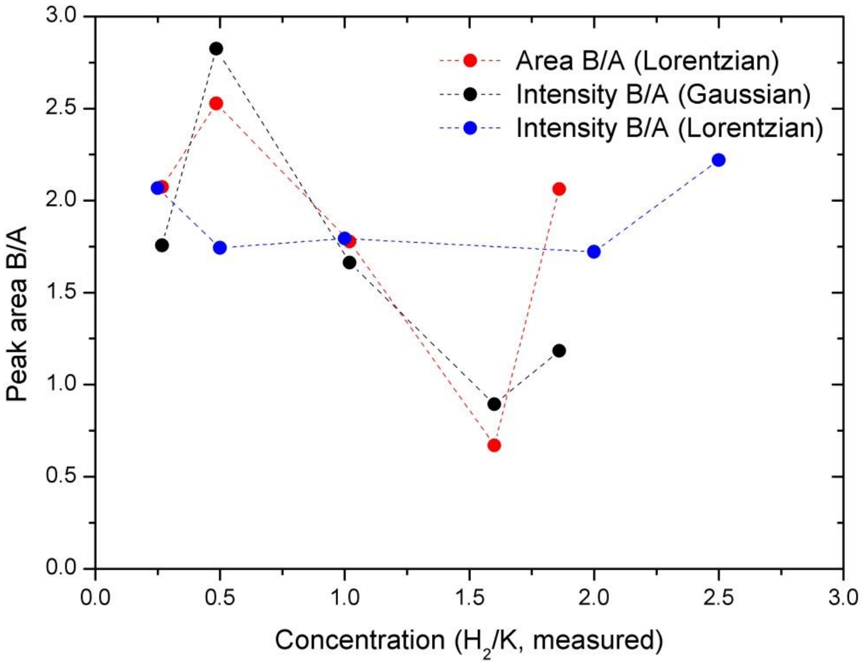

Figure 6.29: Ratio of peak areas obtained using two-peak Gaussian or Lorentzian fits to bulk-KC_{24} data shown in Figure 6.28 (a).

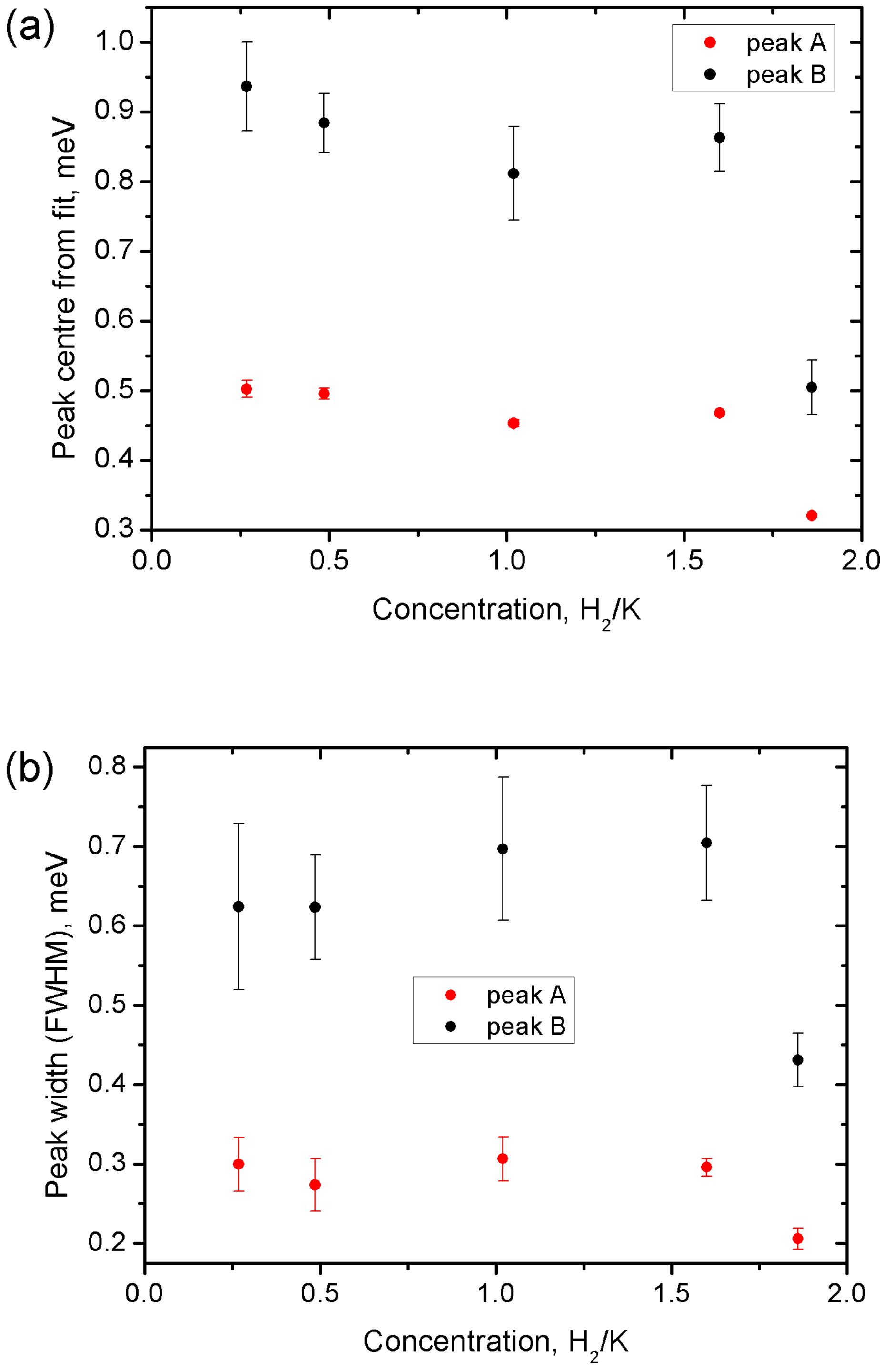

Figure 6.30: (a) Peak centres and (b) peak full-width half maxima derived from two-peak Gaussian fits to bulk-KC24 data shown in Figure 6.28 (a).

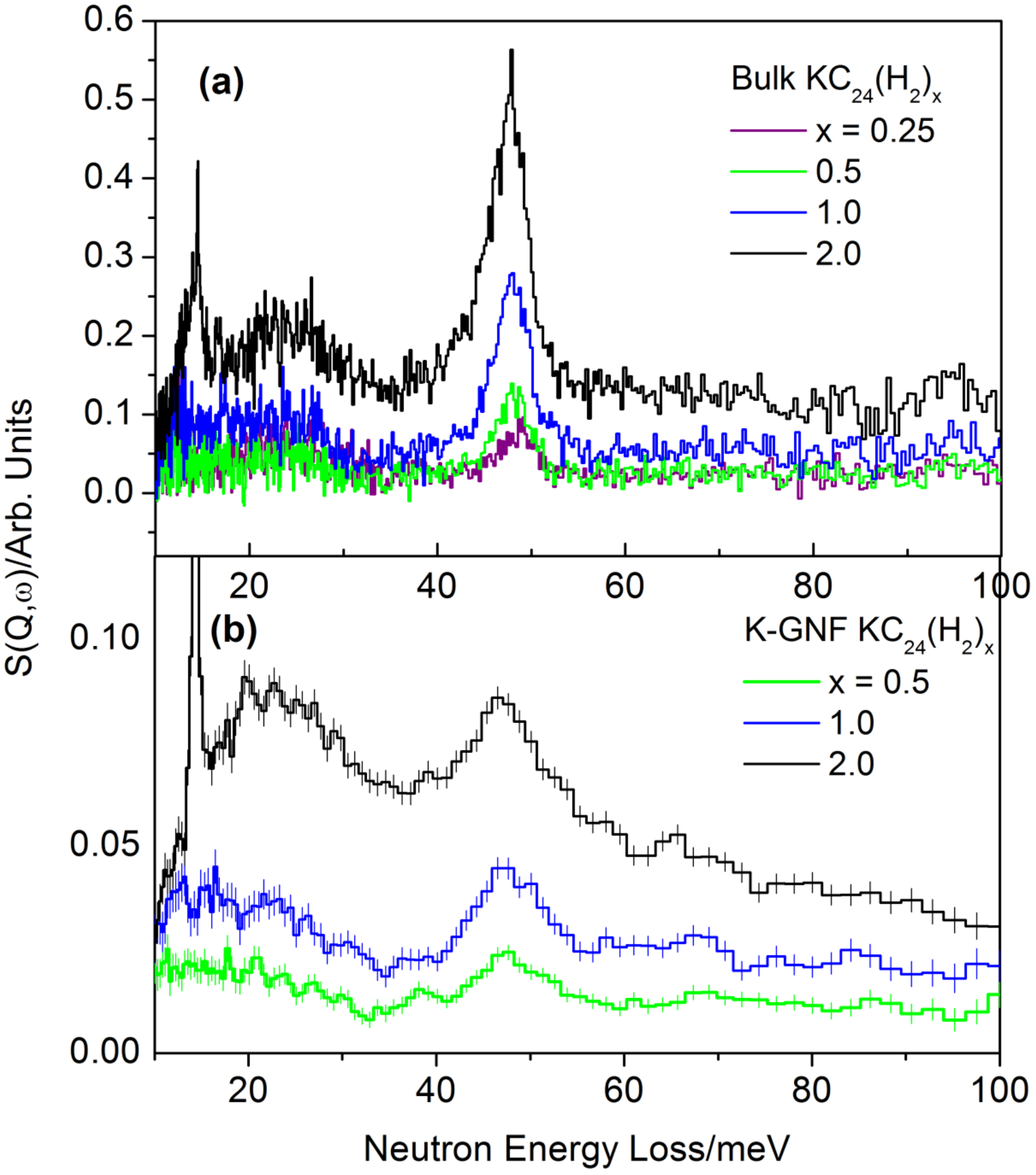

Figure 6.31: INS spectra of $KC_{24}(H_2)x$ nanofibres on TOSCA from forward-scattering banks; (a) data collected on bulk KC_{24} (from previous study) [48], (b) data collected on KC24 nanofibres (from this study).

The higher librational states at 39 and 51 meV, as predicted by the tunnelling model discussed in §6.3.4, were looked at using the TOSCA instrument which cover this energy range. The presence of these states, along with the lower energy states seen in the IRIS data, supports the theory on the tunnelling of Hydrogen in a $\cos^2\theta$ potential, as discussed in §6.3.4.

While the first transition is neither seen in the bulk KC_{24} (Figure 6.31 (a)) or KC_{24} nanofibre (Figure 6.31 (b)) data, a peak is observed at 48 meV in both cases for all coverages (corresponding to 51 meV predicted by the $\cos^2\theta$ potential model). While this peak is well defined for the bulk samples it is broadened in energy in the case of the nanofibres, in accordance with the IRIS data. No other difference is observed in the two data sets obtained from the forward scattering banks of TOSCA.

6.5.5 Neutron diffraction

Neutron diffraction measurements were conducted to look at the structural changes that take place in KC_{24} nanofibres upon hydrogenation and to see how this compares to the changes observed in the bulk KC_{24} samples. The diffraction studies were carried out on the high neutron flux GEM diffractometer at ISIS. For this diffraction experiment deuterium was used instead of hydrogen. This is because although hydrogen is highly useful for dynamical studies it is not very suitable for diffraction experiments due to its high incoherent scattering cross-section. Deuterium, on the other hand, is a better coherent scatterer and is therefore generally used in diffraction experiments instead of hydrogen to improve the quality of the diffraction data.

Besides looking at any structural changes in the fibres, we were also interested at looking at the hydrogenation kinetics as determined by time-resolved diffraction data during deuterium loading of the sample. For this reason it was important to use a high neutron flux diffractometer such as GEM. In graphite based compounds (e.g. GICs) the ease of structural changes such as intercalation of hydrogen is thought to be regulated by the elastic constraints of long range order; this is what leads to orderly staging in GICs. This elastic constraint is also thought to affect the kinetics of hydrogen adsorption. For this reason we expected the hydrogenation kinetics to be substantially different in nano-graphites, in which the size reduction is expected to lower the elastic strain and hence the ease of intercalation as well as lowering the diffusion distances. Once again for a comparative analysis between nanostructured and bulk KC_{24}, the results from this experiment were compared to those obtained for bulk KC_{24} from a separate study conducted previously on the POLARIS diffractometer at ISIS [48].

The 0.7552 g KC_{24} nanofibre sample used on IRIS and TOSCA was loaded (within the same annular aluminium container) into the GEM neutron diffractometer (§4.6.4), where diffraction measurements were carried out at 50 K on the following nominal D_2/KC_{24} compositions, measured as pressures in a calibrated volume: 0, 0.25, 0.5, 0.75, 1.0, 1.5, 1.75 and 2.0. As the sample was saturated at 1.22 D_2/K, it appeared that significant degradation in the uptake capacity had occurred. A new sample consisting of 0.3952 g of KC_{24} nanofibres from the same synthesis batch, but unused, was loaded into the same annular aluminium container. Since no difference was observed in the diffraction results of the both samples, I have chosen to report on the diffraction measurements on this second sample.

Firstly, the sample was saturated with D_2, to a maximum uptake of 1.64 D_2/K. This was then evacuated by warming the sample to 170 K under dynamic vacuum. Following this, the sample was reloaded with several different compositions in steps, with diffraction data recorded at each loading at 50 K as before: x=0 (background), 0.25 (0.235), 0.5 (0.47), 0.75 (0.72), 1.0 (0.96), 1.25 (1.19), 1.5(1.43), 1.75(1.60) and saturation (1.67) D_2/K.

6.5.5.1 Diffraction results

Figure 6.32 shows the time resolved diffraction patterns for (a) bulk KC_{24} sample from previous study on POLARIS and (b) KC_{24} nanofibres from this study on GEM, taken during D_2 loading up to the saturation point at 50 K. Since both the Papyex-based sample (bulk KC_{24}) and the sample made from graphitic nanofibres (nanostructured KC_{24}) are turbostratic they have a preferred orientation in one direction; the small crystallites in the Papyex-based sample are mostly arranged with the c-axis perpendicular to the plane of the sheet, and the fibres even when crushed have the tendency to align in one direction with the crystallite c-axis mostly aligned perpendicular to the fibre axis. Despite both GEM and POLARIS having detectors with a Q-vector range covering the scattering angles from both c-axis stacking and a-b plane stacking, the in-plane geometry is not easy to resolve due the lack of long-range order in either of the samples. For this reason the data range selected for comparison between the bulk and nanostructured KC_{24} is the data showing the out-of-plane geometry of the samples, as shown by the (002) and the (003) peaks in Figure 6.32. From this data we can clearly see that the GNF sample is fully intercalated to yield KC_{24} as no sign of pure graphite is detected; otherwise graphite (002) peak would be present at 3.34 Å, as measure by XRD on the GNFs (§6.5.3).

It must be noted that despite the lack of long range order in both graphitic samples, Papyex is locally more like single crystal; the flakes that make it are aligned turbostratically but there is reasonable long range order in the c-axis within each flake, whereas the GNFs are highly turbostratic. The average crystalline dimensions in Papyex is reported to be $L_a \approx 600$ Å (in-plane) and $L_c \approx 300$ Å (out-of-plane) [269], for the GNFs used in the neutron scattering experiments these values were calculated to be $L_a \approx 58$ Å (in-plane) and $L_c \approx 73$ Å (out-of-plane), as discussed in §6.5.3 above. This greater disorder in the GNFs is one reason for the broader spectrum (peak width) seen in the neutron scattering measurements, as discussed above in the INS data and as shown below for the diffraction data (Figure 6.32 and Figure 6.33)

One obvious difference we found between the nanostructured and the bulk sample is the rate of D_2 adsorption. The rate is significantly faster for KC_{24} nanofibres for the same mass of sample. It can be seen from both (003) and (002) peaks in the bulk sample (Figure 6.32 (a)) as deuterium is put on the sample, the KC_{24} peaks diminish and hydrogenated peaks appear and increase at a slightly expanded *d*-spacing. By the time the full amount of D_2 is present, the original peaks are less than a faint shoulder on the new ones.

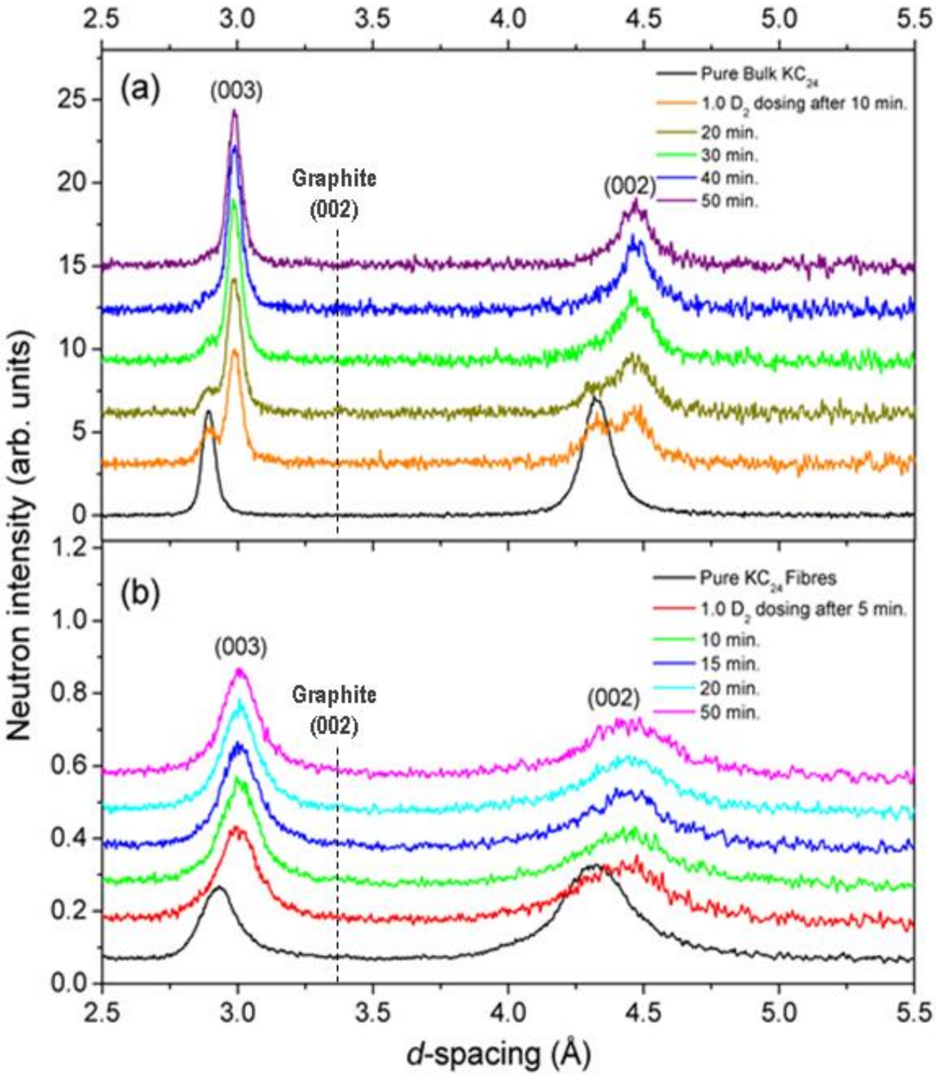

Figure 6.32: Time-resolved diffraction patterns of (a) bulk KC_{24} sample from previous study on POLARIS [48] and (b) KC_{24} nanofibres from this study on GEM, taken during D_2 loading up to the saturation point at 50 K. Both data sets show c-axis expansion with 1 D_2 loading per KC_{24} (offset for clarity). The time resolution is 10 minutes in (a) and 5 minutes in (b).

The c-axis repeat distance increases from 8.66 ± 0.03 Å to 8.94 Å. Considering that the empty gallery spacing in the KC_{24} unit cell does not change significantly, then the results can be quantified by a change in the filled layer spacing from 5.35 to 5.63 Å, corresponding to a gallery expansion of 5.1%. This value is the same for the nanostructured KC_{24} sample with an increase in the filled layer spacing from 5.30 to 5.57 Å. While it takes 40-50 minutes for the phase change from KC_{24} to $1D_2$-KC_{24} to complete in the bulk sample, it takes less than five minutes in the case of the nanofibres. Though this is as expected for a sample with reduced domain dimensions, which provides reduced diffusion distances for the deuterium (hydrogen), the increase in the speed of hydrogen adsorption is significant for the same mass of sample.

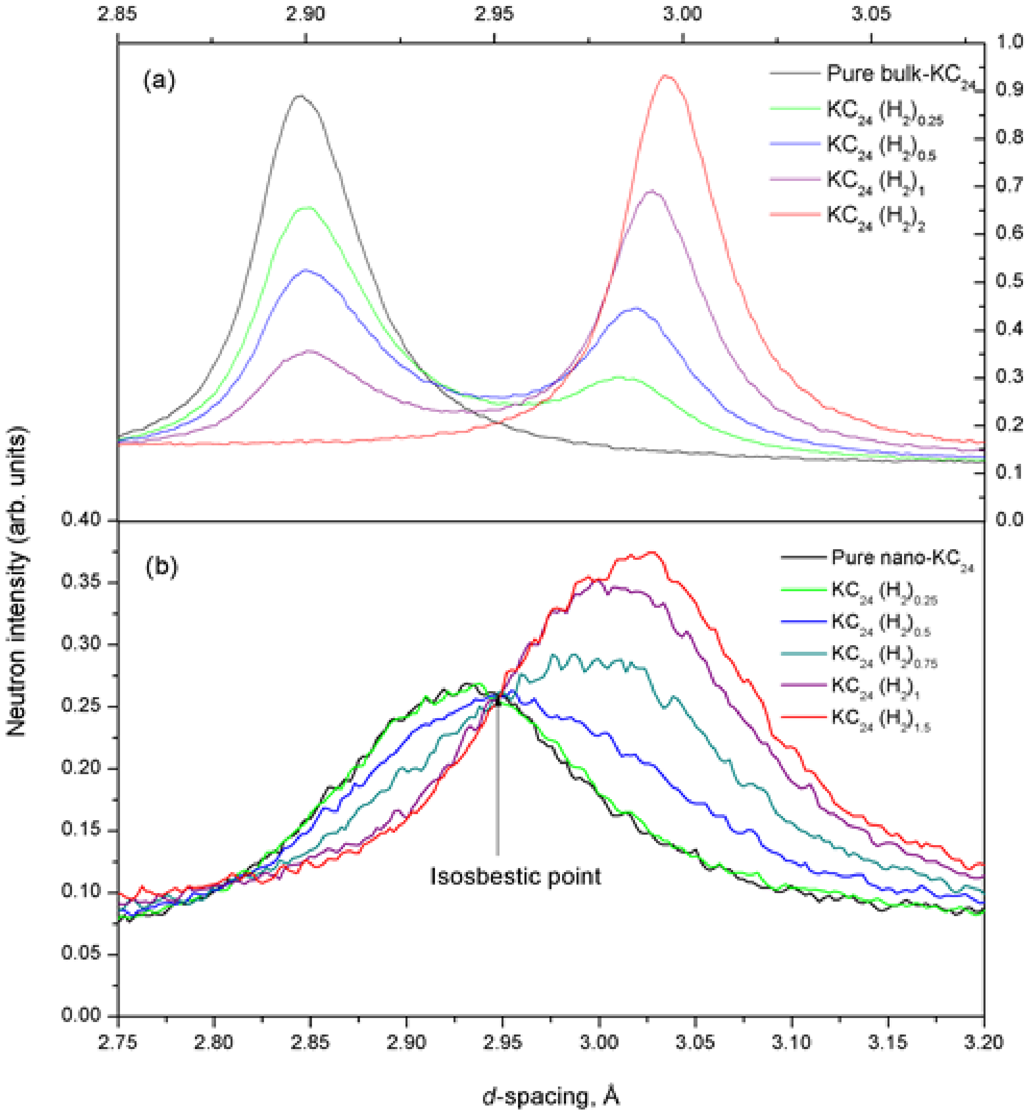

Figure 6.33: The evolution of the (003) diffraction peak of (a) bulk and (b) nanostructured KC_{24} with increasing concentration. Data in (a) obtained from previous diffraction study on IRIS [48].

To look at the cause of this difference in the kinetics of adsorption, it is important to take a closer look at the data and the way in which the transition from the non-deuterated phase to the deuterated phase differs between the two samples. Figure 6.33 (a) shows the evolution of the (003) peak with increasing hydrogen concentrations. This is the diffraction data taken on IRIS in the previous experiment [48] and was the only one available for comparison with the GEM diffraction data on the nanofibres at different hydrogen loadings (Figure 6.33 (b)). As the hydrogen content of bulk sample increases, the intensity of the original peak (the un-hydrogenated phase) diminishes and that of the hydrogenated peak increases. The peaks remain discrete, but coexist, which suggests that domains of hydrogenated and pure KC_{24} are prevalent in the sample during H_2 loading [48]. The peak positions also shift slightly to higher d-spacing with uptake. However, what is interesting is that we do not see such a heterogeneous transition with the nanofibres (Figure 6.33 (b)). At first sight the peak, which is very broad, appears to show a homogeneous transition from the non-deuterated phase to a deuterated phase, as opposed to the clear heterogeneous phase change seen for the bulk sample. Due to the breadth of the peak, even a more quantitative analysis of this peak does not give a clear indication of whether this is a homogeneous or a heterogeneous phase transition taking place. ARIEL, a data reduction/visualisation package developed for handling crystallographic data on GEM, was used to fit the data in order to determine if the (002) and (003) peaks were undergoing a heterogeneous or homogeneous transition. The fitting function, which was a convolution of a Lorentzian and Gaussian function, incorporating the instrument resolution parameters, struggled to fit two peaks to the both (002) and (003) peaks. The two peak fittings, with the peak centres set to be that of the deuterated and the non-deuterated phase as in bulk KC_{24}, which were not-fixed, collapsed in to a single peak when fitted. The χ^2 values and the peak widths and intensities did not give conclusive results as to whether a heterogeneous or a homogeneous transition was taking place. However, the presence of an isosbestic point (as shown in Figure 6.33 (b)) indicate that the two phases co-exist at once in the nanostructured KC_{24} sample; an isosbestic point typically arises as a result of two inter-converting species having a well-defined, fixed, spectral response mutually [270]. Thus, at this stage with the data available and the level of analysis done, it is not conclusive whether the phase transition is homogeneous or heterogeneous (i.e. filled by growth of hydrogenated domains in the sample) as postulated for the Papyex based GIC in the previous study [48].

6.5.6 Enthalpy of adsorption

The enthalpy of adsorption of hydrogen is one of the key parameters of interest to us, as it gives an indication of how strongly the hydrogen is bound to the system. I have discussed in §1.4.5 and §1.5.2 respectively that the enthalpy of adsorption (in the case of physisorption based materials) or the enthalpy of absorption (in the case of metal hydrides) is usually determined through the use of Langmuir isotherms or a Van't Hoff plot. In this study, since desorption data was collected in situ on IRIS, an alternative method developed by Fernandez-Alonso and co-workers [TIDES] was used to determine the desorption enthalpy of KC_{24} nanofibres. As described in more detail in Ref. [TIDES], this method involved an isochoric temperature programmed desorption run of the KC_{24} sample, with a specific H_2 coverage, and the measurement of pressure as a function of temperature. The experimental details are summarised as follows:

1) The sample is dosed with H_2 at 50 K to specific coverage; I report the results for $1H_2/KC_{24}$ below.
2) The sample is then isolated from the gas manifold and cooled to the base temperature, 5 K.
3) Once at base temperature, the sample is again opened to the rest of the gas manifold to allow desorption of H_2 in to the known manifold volume by heating the sample at set temperature steps (2 °C steps were used in this case). The pressure (P) in volume (V) is then

recorded as a function of temperature (T) with the temperature increased up to a point beyond complete desorption of H_2 from the sample (>150 K in this case). For these measurements it is important that the pressure equilibrates at each temperature step, thus, a dwell time of 5 minutes was used to ensure this.

The pressure desorption curve obtained from these measurement, which is normalised to the maximum pressure (P_{max}, as determined by the manifold volume), shown in Figure 6.34, was used to fit the data and to extract the hydrogen desorption energy, E_{des}, using the following equation [TIDES]:

$$P = P_{max}\left[\frac{1}{1+\left[\frac{P_{max}}{AT}\right]e^{E_{des}/_{KT}}}\right] \tag{6.4}$$

where A is a fitting parameter, which is said to be related to the change of entropy between gaseous and adsorbed phases and k is Boltzmann constant (1.38×10^{-23} m^2 kg s^{-2} K^{-1}). This equation provides an alternative way of extracting pressure dependent parameters using the method described above. It is to be noted that Equation (6.4) assumes a single adsorption site and no adsorbate-adsorbate interactions.

As shown in Figure 6.34, the fitting obtained using the function (Eq. (6.4)) (red line), fits very well to the measured data. Using this fit desorption energy of hydrogen from the KC_{24} nanofibres is calculated to be 4.39 kJmol^{-1}. This is half the value 10.1 kJmol^{-1} for the Papyex based bulk-KC_{24} sample in a previous study by Fernandez-Alonso and co-workers [TIDES] using the same method described above. This is a significant change in the desorption energy, though it is in line with what is observed with nanostructuring of the metal hydrides (§1.5.2) which show a reduction in enthalpy through nanostructuring, it is greater than expected. Most importantly, this reduction is an unfavourable result for GICs which store hydrogen through physisorption. Since binding energy is weak in the physisorption regime, the adsorption/desorption energy needs to be increased rather than lowered. The exact reasons for the reduction in the desorption energy is not known, however, it is highly likely that the surface energy contribution to the Gibbs free energy is increased as discussed for metal hydrides in §1.5.2. In this earlier section, looking at thermodynamic effects of nanostructuring metal hydrides, I had discussed that in reducing the size of the particles, the surface area, and thus, the surface energy contribution to the Gibbs free energy becomes important. It was discussed that if the surface energy term is larger for the hydrogenated phase than the pure adsorbate phase then some of the heat of formation energy will be stored as the surface energy, which will reduce the enthalpy of absorption/desorption (see §1.5.2 for further details and calculations).

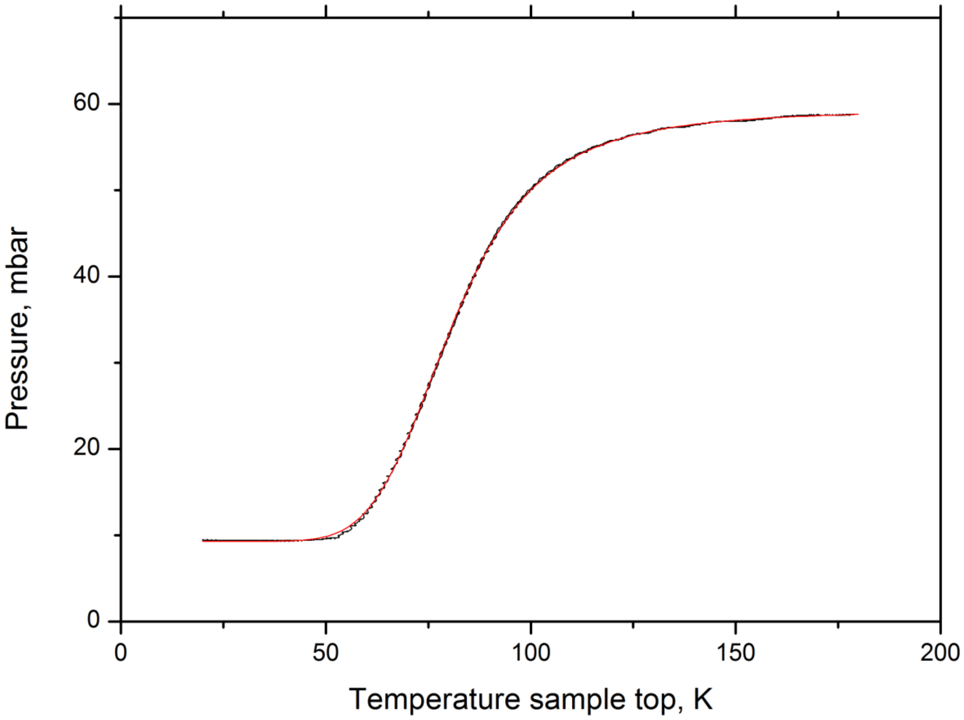

Figure 6.34: The pressure desorption curve of KC_{24} nanofibres with H_2 coverage of $1H_2/KC_{24}$, black line correspond to the original data and red line is that fitting obtained using Eq.(6.4)

6.6 Summary and Conclusions

The electrospinning method was successfully used for the synthesis polymeric nanofibres from PAN in DMSO which were then heat treated for the production of carbon and graphitic nanofibres (CNFs and GNFs). As our main aim in the first part of this study was to lower the diameters of the electrospun fibres to as low as possible with the available PAN solutions, as well as to make them as highly graphitic as possible, both the electrospinning and the carbonisation processes were subject to thorough analysis through modification of the solution parameters and measurements of the morphological and structural characteristics of the polymeric and carbonised fibres.

Addition of surfactant and salt to polymeric solutions was found to lower the fibre diameters as well as removing or reducing beading found at low polymer concentrations. While fibre diameters as low as 130nm was achieved for polymer fibres electrospun with low polymer concentration solutions (4.2 wt.% PAN in DMSO), these diameters were lowered to as low as 60 nm in CNFs (polymer fibres heat treated up to 500 °C). With further heat treatment, up to 2800 °C, these fibres were converted to graphitic nanofibres (turbostratic nanofibres, GNFs). The stabilisation step in the heat treatment process was found to be important for maintaining fibre mass during the pyrolysis process. The structure of the graphitised fibres, which also have an amorphous component as shown by the XRD results, is found to be of fibrils of graphite running along the length of the fibres with c-axis graphite staking varying from bilayers to ~40 layers depending on the heat treatment temperature. The way in which the ribbons are entangled in three dimensions is not clear, but the XRD measurements show that 3-D ordering of the graphitic planes is not fully attained.

The synthesised GNFs were then intercalated with potassium to yield KC_{24}-nanofibres, which were then used for hydrogenation studies through the use of neutron scattering techniques. The INS neutron data on the K-intercalated nanofibres, which is compared to previous data on bulk-KC_{24}

gives us no new information about the interaction dynamics of hydrogen in the K-GIC system, though differences are seen as a result of differences in the long range order of potassium intercalation (arising from the disorder in the nanofibres). As a result, the fine detail seen in the bulk-KC_{24} resulting from the local interaction of hydrogen in the potential is not visible and, in fact, the H_2 dimerization seen in the bulk KC_{24} system is lost or suppressed in the nanofibres.

Two important observations have been made with regards to the (de)hydrogenation process of hydrogen in these fibres:

1) The speed of hydrogenation in the nanofibres is greatly improved with hydrogenation times reduced to <5 min in the nanofibres compared to the 40-50 minutes seen in the bulk-sample, for the dosing of $1D_2/K$.
2) The enthalpy of adsorption/desorption is lowered by more than 50% in the nanofibres from 10.1 $kJmol^{-1}$ in the bulk sample to 4.39 $kJmol^{-1}$ in the nanofibres.

The first observation shows a substantial change in the dehydrogenation speed of hydrogen, thus, a significant improvement is made through nanostructuring. The second observation, though an expected consequence of nanostructuring, is however a change in the wrong direction for physisorption based materials like graphite compounds, which require their enthalpy of adsorption to be increased for more practical hydrogen storage applications.

6.7 Future Work

Future work should be initially focussed on further investigating the hydrogenation properties of the K intercalated GNFs to verify the results above and to further understand the effect of nanostructuring and disorder on the breakdown of hydrogen dimerization in intercalated graphite fibres. It is worth investigating if hydrogen dimerization affects the speed of hydrogenenation by testing graphites of varying degrees of ordering. DFT calculations looking at the potential energy surface of the K-H_2 in the graphite to investigate where the dimerization breaks down can give further information about the way H_2 is intercalated in KC_{24} GICs.

This investigation should be extended to CNFs made from other precursors, which may yield a greater degree of structural ordering, such as pitch, rayon and cellulose. The ideal configuration for ease and speed if intercalation would be to have the graphene planes ordered either perpendicularly to the fibre axis (i.e. basal planes being stacked like discs along the fibre axis) or to have the basal planes ordered radially along the fibre axis, as in the case of CNFs made from pitch. Both these configurations give greater exposure of the graphite edges for intercalation of species. Thus, investigating other precursors of carbon fibres in the search for such a structure is certainly worthwhile for hydrogen storage investigations. It is very important that electrospinning efforts of fibres from other carbon precursors should continue to focus on further reducing the fibre diameters.

Appendix A Polymer and solvent data sheet (solvent matrix)

Polymer (PS)	Molecular weight (g/mol)	Solubility radius R	δ_d	δ_p	δ_h	δv	Solubility in water (g/100g)	Solubility in water (% w/w)	Melting point	Hydrogen permeability
Polystyrene	variant, used 350, 000	12.7	21.3	5.8	4.3	22.1	insoluble	insoluble	240 °C	23.8 barrers

Selected solvents for AB	Molecular weight (g/mol)	δ_{total}	δ_d	δ_p	δ_h	δv	Solubility in water (g/100g)	Solubility in water (% w/w)	Boiling point (°C)	Dielectric constant at 20C	Dipole Moment (D)	Polarity	Electrical Conductivity (S/cm)
Water	18	47.8	15.6	16	42.3	22.3	N/A	N/A	100	78.54	1.87	100	5.50E-06
Dimethylformamide	73	24.8	17.4	13.7	11.3	22.1	–	Total	153	36.7	3.8	40.4	6.00E-08
Dimethyl sulfoxid	78	26.7	18.4	16.4	10.2	24.6	–	–	189	46.6	3.96	44.4	2.00E-09

Solvents PS but not for AB	Molecular weight (g/mol)	δ_{total}	δ_d	δ_p	δ_h	δv	Solubility in water (g/100g)	Solubility in water (% w/w)	Boiling point (°C)	Dielectric constant at 20C	Dipole Moment (D)	Polarity	Electrical Conductivity (S/cm)
Chloroform	119	19	17.8	3.1	5.7	18.1	0.795	0.82	61	4.8	1.1	25.9	<1.0E-10
Cyclohexane	84	16.8	16.8	0	0.2	16.8	<0.1	0.0055	81	2.02	0.3	0.6	7.00E-18
1,2-Dichloroethane	99	18.5	16.6	8.2	0.4	18.5	0.861	0.81	83.5	10.42	1.8	32.7	4.00E-11
Dichloromethane	84.93	11.09	5.62	8.21	4.99	9.9	1.3	–	40	9.1	–	–	–
Diethyl ether	74	15.8	14.5	2.9	5.1	14.8	7.5	6.9	35	4.3	1.3	11.7	3.00E-16
Ethyl acetate	88.10	18.1	15.8	5.3	7.2	16.7	8.7	–	77	6	–	–	–
Heptane	100.21	15.3	15.3	0	0	15.3	0.01	3.00E-04	98	1.92	0	1.2	1.00E-16
Hexane	86.18	14.9	14.9	0	0	14.9	0.014	9.50E-04	69	1.89 - 2	0	0.9	1.00E-16

Solvents PS but not for AB	Molecular weight (g/mol)	δ_{total}	δ_d	δ_p	δ_h	δv	Solubility in water (g/100g)	Solubility in water (% w/w)	Boiling point (°C)	Dielectric constant at 20C	Dipole Moment (D)	Polarity	Electrical Conductivity (S/cm)
Pentane	72	14.5	14.5	0	0	14.5	0.04	3.80E-03	36.1	1.84	0	0.9	2.00E-10
Toluene	92	18.2	18	1.4	2	18.1	0.05	0.052	111	2.4	0.4	9.9	8.00E-16
Chlorobenzene	112.56	19.6	19	4.3	2	19.5	0.05	–	131.7	5.69	–	–	–
o-dichlorobenzene	147	20.5	19.2	6.3	3.3	20.2	–	–	180	–	–	–	–
Nitrobenzene	123	22.2	20	8.6	4.1	21.8	–	0.19	211	34.8	4	32.4	2.00E-10
1,4 Dioxane	88.11	20.5	19	1.8	7.4	19.1	miscible	–	101.1	2.21	–	–	–
Styrene	104.15	19	18.6	1	4.1	18.6	–	–	145	–	–	–	–
Xylene mixtures	–	18	17.8	1	3.1	17.8	Insoluble	0.02	136	2.3	1.3	7.4	8.00E-16
Benzene	78	18.6	18.4	0	2	18.4	insoluble	0.18	144	2.28	0	11.1	4.40E-17
Carbon Tetrachloride	154	17.8	17.8	0	0.6	17.8	0.08	0.077	76.7	2.24	0	5.2	4.00E-18
1,1,2 Trichlorotrifluoro-ethane	133	14.7	14.7	1.6	0	14.8	–	0.13	74	7.2	1.7	17	7.30E-09
Tetrahyrofuron	72	19.4	16.8	5.7	8	17.7	–	Total	66	7.6	1.75	21	4.5 E-5
Acetone	58	20	15.5	10.4	7	18.7	–	Total	56	20.6	2.9	35.5	5.00E-09
Methylethylketone (MEK)	72.1	19	16	9	5.1	18.4	27.5	–	79.9	–	2.76	–	4.41E-06
Pyridine	79.1	21.8	19	8.8	5.9	20.9	Miscible	–	115.2	12.3(25)	–	–	–
Formic Acid	46.03	24.9	14.3	11.9	16.6	18.6	Miscible	–	100 °C	58	1.41	–	–
Dimethylacetamide	87.82	22.7	16.8	11.5	10.2	20.4	Miscible	–	166	37.8	3.79E-29 @20C	–	–
Dimethylformamide	73	24.8	17.4	13.7	11.3	22.1	–	Total	153	36.7	3.8	40.4	6.00E-08

Key:

🟧	Solvents that are immiscible or have very low miscibility with water
🟪	Solvents with high boiling point and hence low vapour pressure
🟦	Solvents with high dielectric constant which are likely to dissolve salts
🟥	Solvents with high dipole moment which are likely to dissolve salts
🟩	Solvents with high Conductivity

Appendix B Permeability of selected polymers to selected gasses

1 barrer = 3.348 x 10^{-19} kmol m / (m^2 s Pa)		Melting Temperature, °C	Permeability (at 30°C, 30psi feed pressure)					
	polymer		H_2 (barrers)	N_2 (barrers)	O_2 (barrers)	CH_4 (barrers)	CO_2 (barrers)	H_2/CO_2
Ref: Orme *et al.*[159]	polysulphone [PSU]	190	12.1	0.8	1.7	0.4	6.1	2
	polystyrene [PS] (Mw=280, 000)	240	23.8	0.6	2.4	0.8	10.4	2.3
	Poly(benzyl methacrylate)	200	11			1.4	7.9	1.4
	Poly(methyl methacrylate) [PMMA]	130	2.4	1.2	3.3	0.6	0.6	4
	co-polymer of poly(ethylene) and polyvinyl alcohol		0.5	0.3	0.2	0.2	0.2	2.5
	PVDF kynar	160	2.4	0.7	1.3	1.3	1.2	2
	Poly(dimethyl siloxane)		375	299	540	600	1300	0.3
	Poly(ethylene) low density film	110	17.3	4.2	6.3	7.7	17.9	0.9
	Poly(vinyl acetate)		15.1	1.3	2.3	0.9	13.1	1.2
	Poly(styrene co-butadiene)		7.9	1.8	0.6	2.5	15.3	0.5
	Poly(propylene) - in mixed gas stream	160	3.5					
	Poly(ether ether ketone)	334						
	Polycarbonate	225						

Bibliography

1. Züttel, A., et al., *Hydrogen: the future energy carrier*. Philosophical Transactions of the Royal Society A 2010. **368**: p. 3329–3342.

2. Satyapal, S., et al., *The U.S. Department of Energy's National Hydrogen Storage Project: Progress towards meeting hydrogen-powered vehicle requirements.* Catalysis Today, 2007. **120**(3-4): p. 246-256.

3. US-DOE. *Status of Hydrogen Storage Technologies*. 2010 [cited 2010; Available from: http://www1.eere.energy.gov/hydrogenandfuelcells/storage/tech_status.html.

4. Schlapbach, L. and A. Zuttel, *Hydrogen-storage materials for mobile applications.* Nature, 2001. **414**(6861): p. 353-358.

5. Carrette, L., K.A. Friedrich, and U. Stimming, *Fuel Cells – Fundamentals and Applications.* Fuel Cells, 2001. **1**(1): p. 5-39.

6. Mandal, T.K. and D.H. Gregory, *Hydrogen: a future energy vector for sustainable development.* Proceedings of the Institution of Mechanical Engineers Part C-Journal of Mechanical Engineering Science, 2010. **224**(C3): p. 539-558.

7. Dillich, S., *FY 2009 Annual Progress Report*, H. US Department of Energy, Fuel Cells & Infrastructure Technologies, Editor. 2009. p. 388-397.

8. Purewal, J., *Hydrogen Adsorption by Alkali Metal Graphite Intercalation Compounds*. 2010, California Institute of Technology , Pasadena, California. p. 1-194.

9. Pritchard, D.K., M. Royle, and D. Willoughby, *Installation permitting guidance for hydrogen and fuel cell stationary applications: UK version* H.a.S. Executive, Editor. 2009: Buxton, Derbyshire

10. Hu, J., et al., *Analysis of composite hydrogen storage cylinders subjected to localized flame impingements.* International Journal of Hydrogen Energy, 2008. **33**(11): p.2738-2746.

11. Motyka, T., R. Zidan, and W.A. Summers *Hydrogen Storage: The Key Challenge Facing a Hydrogen Economy*, S.R.T. Center, Editor: Aiken, South Carolina.

12. Sirosh, N., *"Hydrogen composite tank project" FY2003 progress report*, U.S. Department of Energy, Editor. 2003: Irvine, California.

13. *Technical Assessment: Cryo-Compressed Hydrogen Storage for Vehicular Applications*, U.S. Department of Energy, Editor. 2006 (revised 2008).

14. Züttel, A., et al., *Model for the hydrogen adsorption on carbon nanostructures.* Applied Physics A: Materials Science & Processing, 2004. **78**(7): p. 941-946.

15. Sakintuna, B., F. Lamari-Darkrim, and M. Hirscher, *Metal hydride materials for solid hydrogen storage: A review.* International Journal of Hydrogen Energy, 2007. **32**(9): p. 1121-1140.

16. Jain, I.P., P. Jain, and A. Jain, *Novel hydrogen storage materials: A review of lightweight complex hydrides.* Journal of Alloys and Compounds, 2010. **503**(2): p.303-339.

17. Züttel, A., *Hydrogen storage and distribution systems.* Mitigation and Adaptation Strategies for Global Change, 2007. **12**(3): p. 343-365.

18. Bérubé, V., et al., *Size effects on the hydrogen storage properties of nanostructured metal hydrides: A review.* International Journal of Energy Research, 2007. **31**(6-7): p.637-663.

19. Heung, L.K., *Using Metal Hydride to Store Hydrogen*, U.S. Department of Energy, Editor. 2003.

20. Baldé, C.P., et al., *Sodium Alanate Nanoparticles − Linking Size to Hydrogen Storage Properties.* Journal of the American Chemical Society, 2008. **130**(21): p. 6761-6765.

21. Ströbel, R., et al., *Hydrogen storage by carbon materials.* Journal of Power Sources, 2006. **159**(2): p. 781-801.

22. Bhatia, S.K. and A.L. Myers, *Optimum Conditions for Adsorptive Storage.* Langmuir, 2006. **22**(4): p. 1688-1700.

23. Dillon, A.C., et al., *Storage of hydrogen in single-walled carbon nanotubes* Nature, 1997. **386**: p. 377– 379.

24. Ansón, A., et al., *Hydrogen adsorption studies on single wall carbon nanotubes.* Carbon, 2004. **42**(7): p. 1243-1248.

25. Texier-Mandoki, N., et al., *Hydrogen storage in activated carbon materials: Role of the nanoporous texture.* Carbon, 2004. **42**(12-13): p. 2744-2747.

26. Blackman, J.M., et al., *Activation of carbon nanofibres for hydrogen storage.* Carbon, 2006. **44**(8): p. 1376-1385.

27. Marella, M. and Tomaselli, M. *Synthesis of carbon nanofibers and measurements of hydrogen storage.* Carbon, 2006.

28. Huang, C.-W., H.-C. Wu, and Y.-Y. Li, *Hydrogen storage in platelet graphite nanofibers.* Separation and Purification Technology, 2007. **58**(1): p. 219-223.

29. Danilov, M.O., A.V. Melezhyk, and G.Y. Kolbasov, *Carbon nanofibers as hydrogen adsorbing materials for power sources.* Journal of Power Sources, 2008. **176**(1): p. 320-324.

30. Hong, S.E., et al., *Graphite nanofibers prepared from catalytic graphitization of electrospun poly(vinylidene fluoride) nanofibers and their hydrogen storage capacity.* Catalysis Today, 2007. **120**(3-4): p. 413-419.

31. Tian, H.Y., et al., *Enhanced hydrogen storage capacity in carbon aerogels treated with KOH.* Carbon, 2009. **47**(8): p. 2128-2130.

32. Murray, L.J., M. Dinca, and J.R. Long, *Hydrogen storage in metal-organic frameworks.* Chemical Society Reviews, 2009. **38**(5): p. 1294-1314.

33. Wong-Foy, A.G., A.J. Matzger, and O.M. Yaghi, *Exceptional H_2 Saturation Uptake in Microporous Metal−Organic Frameworks.* Journal of the American Chemical Society, 2006. **128**(11): p. 3494-3495.

34. Langmi, H.W., et al., *Hydrogen storage in ion-exchanged zeolites.* Journal of Alloys and Compounds, 2005. **404-406**: p. 637-642.

35. Xiao-ming, D. and W. Er-dong, Chinese Journal of Chemical Physics, 2006. **19**: p. 457-462.

36. Bénard, P. and R. Chahine, *Storage of hydrogen by physisorption on carbon and nanostructured materials.* Scripta Materialia, 2007. **56**(10): p. 803-808.

37. Ross, D.K., *Hydrogen storage: The major technological barrier to the development of hydrogen fuel cell cars.* Vacuum 2006. **80**: p. 1084–1089.

38. Chambers, A., et al., *Hydrogen Storage in Graphite Nanofibers.* The Journal of Physical Chemistry B, 1998. **102**(22): p. 4253-4256.

39. Dillon, A.C. and M.J. Heben, *Hydrogen storage using carbon adsorbents: past, present and future.* Applied Physics A: Materials Science & Processing, 2001. **72**(2): p. 133-142.

40. Jordá-Beneyto, M., et al., *Hydrogen storage on chemically activated carbons and carbon nanomaterials at high pressures.* Carbon, 2007. **45**(2): p. 293-303.

41. Gogotsi, Y., et al., *Importance of pore size in high-pressure hydrogen storage by porous carbons.* International Journal of Hydrogen Energy, 2009. **34**(15): p. 6314-6319.

42. Wang, Q. and J.K. Johnson, *Molecular simulation of hydrogen adsorption in single-walled carbon nanotubes and idealized carbon slit pores.* The Journal of Chemical Physics, 1999. **110**(1): p. 577-586.

43. Aga, R.S., et al., *Theoretical investigation of the effect of graphite interlayer spacing on hydrogen absorption.* Physical Review B, 2007. **76**(16): p. 165404.

44. Okamoto, Y. and Y. Miyamoto, *Ab Initio Investigation of Physisorption of Molecular Hydrogen on Planar and Curved Graphenes.* The Journal of Physical Chemistry B, 2001. **105**(17): p. 3470-3474.

45. Park, C., et al., *Further Studies of the Interaction of Hydrogen with Graphite Nanofibers.* The Journal of Physical Chemistry B, 1999. **103**(48): p. 10572-10581.

46. Beaufils, J.P., et al., *Tunnelling of hydrogen in alkali metal intercalation compounds.* Molecular Physics: An International Journal at the Interface Between Chemistry and Physics, 1981. **44**(6): p. 1257-1269.

47. Kojima, Y. and N. Suzuki, *Hydrogen adsorption and desorption by potassium-doped superactivated carbon.* Applied Physics Letters, 2004. **84**(20): p. 4113-4115.

48. Lovell, A., *Tuneable graphite intercalates for hydrogen storage*, in *Physics and Astronomy*. 2007, University College London: London. p. 1-326.

49. Yoon, M., et al., *Charged Fullerenes as High-Capacity Hydrogen Storage Media.* Nano Letters, 2007. **7**(9): p. 2578-2583.

50. Li, M., et al., *Ca-Coated Boron Fullerenes and Nanotubes as Superior Hydrogen Storage Materials.* Nano Letters, 2009. **9**(5): p. 1944-1948.

51. Lee, H., et al., *Ab initio study of beryllium-decorated fullerenes for hydrogen storage.* Journal of Applied Physics, 2010. **107**(8): p. 084304-084304-4.

52. Whitney, E., et al., *Synthesis of novel metal-coordinated fullerenes for vehicular hydrogen storage* Materials Issues in a Hydrogen Economy, ed. P. Jena, A. Kandalam, and Q. Sun. 2009, Singapore: World Scientific Publ Co Pte Ltd. 155-172.

53. Yan, Y., et al., *Exceptionally high* H_2 *storage by a metal-organic polyhedral framework.* Chemical Communications, 2009(9): p. 1025-1027.

54. Lim, K.L., et al., *Solid-state Materials and Methods for Hydrogen Storage: A Critical Review.* Chemical Engineering & Technology, 2010. **33**(2): p. 213-226.

55. Zaluska, A., L. Zaluski, and J.O. Ström-Olsen, *Structure, catalysis and atomic reactions on the nano-scale: a systematic approach to metal hydrides for hydrogen storage.* Applied Physics A: Materials Science & Processing, 2001. **72**(2): p. 157-165.

56. Fichtner, M., et al., *Nanocrystalline aluminium hydrides for hydrogen storage.* Materials Science and Engineering B, 2004. **108**(1-2): p. 42-47.

57. Imamura, H., et al., *High hydrogen storage capacity of nanosized magnesium synthesized by high energy ball-milling.* Journal of Alloys and Compounds, 2005. **386**(1-2): p. 211-216.

58. Wan, X., et al., *Nanoengineering-Enabled Solid-State Hydrogen Uptake and Release in the LiBH4 Plus MgH2 System.* The Journal of Physical Chemistry C, 2008. **112**(46): p. 18232-18243.

59. Leonard, A.D., et al., *Nanoengineered Carbon Scaffolds for Hydrogen Storage.* Journal of the American Chemical Society, 2008. **131**(2): p. 723-728.

60. Aguey-Zinsou, K.-F. and J.-R. Ares-Fernández, *Synthesis of Colloidal Magnesium: A Near Room Temperature Store for Hydrogen.* Chemistry of Materials, 2007. **20**(2): p. 376-378.

61. Vajo, J.J. and G.L. Olson, *Hydrogen storage in destabilized chemical systems.* Scripta Materialia, 2007. **56**(10): p. 829-834.

62. Dornheim, M., et al., *Hydrogen storage in magnesium-based hydrides and hydride composites.* Scripta Materialia, 2007. **56**(10): p. 841-846.

63. He, T., et al., *Nanosized Co- and Ni-Catalyzed Ammonia Borane for Hydrogen Storage.* Chemistry of Materials, 2009. **21**(11): p. 2315-2318.

64. Siegel, D.J., C. Wolverton, and V. Ozolincedilscaron, *Thermodynamic guidelines for the prediction of hydrogen storage reactions and their application to destabilized hydride mixtures.* Physical Review B, 2007. **76**(13): p. 134102.

65. Chronakis, I.S., *Novel nanocomposites and nanoceramics based on polymer nanofibers using electrospinning process--A review.* Journal of Materials Processing Technology, 2005. **167**(2-3): p. 283-293.

66. Ramakrishna, S., et al., *Electrospun nanofibers: solving global issues.* Materials Today, 2006. **9**(3): p. 40-50.

67. Reneker, D.H. and A.L. Yarin, *Electrospinning jets and polymer nanofibers.* Polymer, 2008. **49**(10): p. 2387-2425.

68. Teo, W.E. and S. Ramakrishna, *A review on electrospinning design and nanofibre assemblies.* Nanotechnology 2006. **17**: p. R89–R106.

69. Jingwei, X., L. Xiaoran, and X. Younan, *Putting Electrospun Nanofibers to Work for Biomedical Research.* Macromolecular Rapid Communications, 2008. **29**(22): p. 1775-1792.

70. Moghe, A.K. and B.S. Gupta, *Hybrid Nanofiber Structures for Tissue Engineering.* Aatcc Review, 2009. **9**(10): p. 43-47.

71. Huang, Z.M., et al., *Encapsulating drugs in biodegradable ultrafine fibers through co-axial electrospinning.* Journal of Biomedical Materials Research Part A, 2006. **77A**(1): p. 169-179.

72. Moghe, A.K. and B.S. Gupta, *Co-axial Electrospinning for Nanofiber Structures: Preparation and Applications.* Polymer Reviews, 2008. **48**(2): p. 353 - 377.

73. Ramakrishna, S., et al., *An introduction to Electrospinning and Nanofibres*. 2005: World Scientific Publishing Co. Pte. Ltd. 381.

74. Bhardwaj, N. and S.C. Kundu, *Electrospinning: A fascinating fiber fabrication technique.* Biotechnology Advances 2010. **28**: p. 325–347.

75. Gilbert, W., *On the Magnet and Magnetic Bodies, and on That Great Magnet the Earth*, ed. P. Short. 1628, London.

76. Larmor, J., *Note on the complete scheme of electrodynamic equations of a moving material medium, and on electrostriction.* Proceedings of the Royal Society of London. Series A, Mathematical and Physical Sciences, 1898. **63**: p. 365.

77. Cooley, J.F., *Apparatus for Electrically Dispersing Fluids*. 1902: U.S. Patent 692,631.

78. Morton, W.J., *Method of dispersing fluids*. 1902: U.S. Patent 0705691.

79. Teo, W.E. and S. Ramakrishna, *A reviewon electrospinning design and anofibre assemblies.* Nanotechnology 2006. **17**: p. R89–R106.

80. Formhals, A., *Method and apparatus for the production of fibers*. 1938: United States of America.

81. Formhals, A., *A Method and apparatus for the production of artificial fibers* 1939: U.S.A.

82. Formhals, A., *Method and apparatus for spinning* 1939.

83. Zeleny, J., *Instability of electrified liquid surfaces* Physical review, 1917. **10**: p. 1.

84. Taylor, G., *Disintegration of water drops in an electric field* Proceedings of the Royal Society A: Mathematical, Physical and Engineering Sciences, 1964. **280** p. 383.

85. Taylor, G., *Studies in electrohydrodynamics: I. The circulation produced in a drop by electrical field* Proceedings of the Royal Society A: Mathematical, Physical and Engineering Sciences, 1966 **291**: p. 145.

86. Taylor, G., *Electrically driven jets* Proceedings of the Royal Society A: Mathematical, Physical and Engineering Sciences, 1969. **313**: p. 453

87. Simons, H.L., *Process and Apparatus for Producing Patterned Nonwoven Fabrics.,* 1966: US Patent 3, 280229

88. Baumgarten, P.K., *Electrostatic spinning of acrylic microfibers.* Journal of colloid and interface science, 1971. **36**: p. 71–9.

89. Greiner, A. and J.H. Wendorff, *Electrospinning: A Fascinating Method for the Preparation of Ultrathin Fibers.* Angewandte Chemie. International edition in English, 2007. **46**: p. 5670 – 5703.

90. Li, D. and Y. Xia, *Electrospinning of Nanofibers: Reinventing the Wheel?* Advanced Materials, 2004. **16**: p. 1151-1170.

91. Reneker, D.H., et al., *Bending instability of electrically charged liquid jets of polymer solutions in electrospinning.* Journal of Applied Physics, 2000. **87**(9): p. 4531-4547.

92. Dersch, R., et al., *Electrospinning of Nanofibres: Towards NewTechniques, Functions, and Applications.* Australian journal of chemistry, 2007. **60**: p. 719–728.

93. Klooster, W.T., et al., *Study of the N−H···H−B Dihydrogen Bond Including the Crystal Structure of BH3NH3 by Neutron Diffraction.* Journal of the American Chemical Society, 1999. **121**(27): p. 6337-6343.

94. Elcoot, A.E.K., *Nonlinear stability of an axial electric field: Effect of interfacial charge relaxation.* Applied Mathematical Modelling, 2010. **34**(8): p. 1965-1983.

95. Taylor, G., *Electrically Driven Jets.* Proceedings of the Royal Society of London. Series A, Mathematical and Physical Sciences, 1969. **313**(1515): p. 453-475.

96. Hohman, M.M., et al., *Electrospinning and electrically forced jets. I. Stability theory.* Physics of Fluids, 2001. **13**(8): p. 2201-2220.

97. Shin, Y.M., et al., *Experimental characterization of electrospinning: the electrically forced jet and instabilities.* Polymer, 2001. **42**(25): p. 09955-09967.

98. Yarin, A.L., S. Koombhongse, and D.H. Reneker, *Bending instability in electrospinning of nanofibers.* Journal of Applied Physics, 2001. **89**(5): p. 3018-3026.

99. Spivak, A.F. and Y.A. Dzenis, *Asymptotic decay of radius of a weakly conductive viscous jet in an external electric field.* Applied Physics Letters, 1998. **73**(21): p. 3067-3069.

100. He, J., Y. Wan, and J. Yu, *Allometric scaling and instability in electrospinning.* International journal of Nonlinear Sciences and Numerical Simulation, 2004. **5**(3).

101. Shenoy, S.L., et al., *Role of chain entanglements on fiber formation during electrospinning of polymer solutions: good solvent, non-specific polymer-polymer interaction limit.* Polymer, 2005. **46**(10): p. 3372-3384.

102. Carroll, C.P. and Y.L. Joo, *Axisymmetric instabilities in electrospinning of highly conducting, viscoelastic polymer solutions.* Physics of Fluids, 2009. **21**(10): p. 103101-10.

103. Liao, I.C., S.Y. Chew, and K.W. Leong, *Aligned core-shell nanofibers delivering bioactive proteins.* Nanomedicine, 2006. **1**(4): p. 465-471.

104. Kim, C., et al., *Supercapacitors Prepared from Carbon Nanofibers Electrospun from Polybenzimidazol.* Journal of The Electrochemical Society, , 2004. **151** p. A769-A773

105. Wang, L., et al., *Electrospun carbon-cobalt composite nanofiber as an anode material for lithium ion batteries.* Scripta Materialia, 2008. **58**(5): p. 405-408.

106. Im, J.S., M.I. Kim, and Y.-S. Lee, *Preparation of PAN-based electrospun nanofiber webs containing TiO2 for photocatalytic degradation.* Materials Letters, 2008. **62**(21-22): p. 3652-3655.

107. Kameoka, J., et al., *A scanning tip electrospinning source for deposition of oriented nanofibres.* Nanotechnology, 2003. **14**(10): p. 1124.

108. Deitzel, J.M., et al., *The effect of processing variables on the morphology of electrospun nanofibers and textiles.* Polymer, 2001. **42**(1): p. 261-272.

109. Haghi, A.K. and M. Akbari, *Trends in electrospinning of natural nanofibers.* physica status solidi (a), 2007. **204**(6): p. 1830-1834.

110. Ki, C.S., et al., *Characterization of gelatin nanofiber prepared from gelatin-formic acid solution.* Polymer, 2005. **46**(14): p. 5094-5102.

111. Zong, X., et al., *Structure and process relationship of electrospun bioabsorbable nanofiber membranes.* Polymer, 2002. **43**(16): p. 4403-4412.

112. Mit-uppatham, C., M. Nithitanakul, and P. Supaphol, *Ultrafine Electrospun Polyamide-6 Fibers: Effect of Solution Conditions on Morphology and Average Fiber Diameter.* Macromolecular Chemistry and Physics, 2004. **205**(17): p. 2327-2338.

113. Hsu, C.-M. and S. Shivkumar, *N,N-Dimethylformamide Additions to the Solution for the Electrospinning of Poly(ε-caprolactone) Nanofibers.* Macromolecular Materials and Engineering, 2004. **289**(4): p. 334-340.

114. Son, W.K., et al., *The effects of solution properties and polyelectrolyte on electrospinning of ultrafine poly(ethylene oxide) fibers.* Polymer, 2004. **45**(9): p. 2959-2966.

115. Kumar, R., B. Singh, and S.S. Sekhon, *Effect of dielectric constant of solvent on the conductivity behavior of polymer gel electrolytes.* Journal of materials science, 2005. **40**: p. 1273 – 1275.

116. Arinstein, A., R. Avrahami, and E. Zussman, *Buckling behaviour of electrospun microtubes: a simple theoretical model and experimental observations.* Journal of Physics D: Applied Physics, 2009. **42**(1): p. 015507.

117. Smith, E.B., *Basic chemical thermodynamics*. 5th ed. 2004, London: Imperial College Press.

118. Demir, M.M., et al., *Electrospinning of polyurethane fibers.* Polymer, 2002. **43**(11): p. 3303-3309.

119. Casper, C.L., et al., *Controlling Surface Morphology of Electrospun Polystyrene Fibers: Effect of Humidity and Molecular Weight in the Electrospinning Process.* Macromolecules, 2003. **37**(2): p. 573-578.

120. Samarasinghe, S.R., K. Balasubramanian, and M.J. Edirisinghe, *Encapsulation of silver particles using co-axial jetting.* Journal of Materials Science-Materials in Electronics, 2008. **19**(1): p. 33-38.

121. Sun, Z., et al., *Compound Core-Shell Polymer Nanofibers by Co-Electrospinning.* Advanced Materials, 2003. **15**(22): p. 1929-1932.

122. Xin, Y., et al., *Core-sheath functional polymer nanofibers prepared by co-electrospinning.* European Polymer Journal, 2008. **44**(4): p. 1040-1045.

123. Loscertales, I.G., et al., *Micro/Nano Encapsulation via Electrified Coaxial Liquid Jets.* Science, 2002. **295**(5560): p. 1695-1698.

124. López-Herrera, J.M., et al., *Coaxial jets generated from electrified Taylor cones. Scaling laws.* Journal of Aerosol Science, 2003. **34**(5): p. 535-552.

125. Loscertales, I.G., et al., *Electrically Forced Coaxial Nanojets for One-Step Hollow Nanofiber Design.* Journal of the American Chemical Society, 2004. **126**(17): p. 5376-5377.

126. Lallave, M., et al., *Filled and Hollow Carbon Nanofibers by Coaxial Electrospinning of Alcell Lignin without Binder Polymers.* Advanced Materials, 2007. **19**(23): p. 4292-4296.

127. Li, D. and Y. Xia, *Direct Fabrication of Composite and Ceramic Hollow Nanofibers by Electrospinning.* Nano Letters, 2004. **4**(5): p. 933-938.

128. Zussman, E., et al., *Electrospun Polyaniline/Poly(methyl methacrylate)-Derived Turbostratic Carbon Micro-/Nanotubes.* Advanced Materials, 2006. **18**(3): p. 348-353.

129. Li, F., X.-Y. Yin, and X.-Z. Yin, *Linear instability of a coflowing jet under an axial electric field.* Physical Review E, 2006. **74**(3): p. 036304.

130. Li, F., X.-Y. Yin, and X.-Z. Yina, *Instability analysis of a coaxial jet under a radial electric field in the nonequipotential case.* Physics of Fluids 2006. **18**: p. 037101

131. Li, F., X.-Y. Yin, and X.-Z. Yin, *Axisymmetric and non-axisymmetric instability of an electrified viscous coaxial jet.* Journal of Fluid Mechanics, 2009. **632**(-1): p. 199-225.

132. Aylward, G. and T. Findlay, *SI Chemical Data*. 4th Edition ed. 1999: John Wiley & Sons

133. Ruo, A.-C., F. Chen, and M.-H. Chang, *Linear instability of compound jets with nonaxisymmetric disturbances.* Physics of Fluids, 2009. **21**(1): p. 012101-14.

134. Yu, J.H., S.V. Fridrikh, and G.C. Rutledge, *Production of Submicrometer Diameter Fibers by Two-Fluid Electrospinning.* Advanced Materials, 2004. **16**(17): p. 1562-1566.

135. McCann, J.T., D. Li, and Y. Xia, *Electrospinning of nanofibers with core-sheath, hollow, or porous structures.* Journal of Materials Chemistry, 2005. **15**(7): p. 735-738.

136. Díaz, J.E., et al., *Controlled Encapsulation of Hydrophobic Liquids in Hydrophilic Polymer Nanofibers by Co-electrospinning.* Advanced Functional Materials, 2006. **16**(16): p. 2110-2116.

137. Zhang, Y., et al., *Preparation of Core-Shell Structured PCL-r-Gelatin Bi-Component Nanofibers by Coaxial Electrospinning.* Chemistry of Materials, 2004. **16**(18): p. 3406-3409.

138. Palumbo, O., et al., *Decomposition of NH_3BH_3 at sub-ambient pressures: A combined thermogravimetry-differential thermal analysis-mass spectrometry study.* Journal of Power Sources, 2010. **195**(6): p. 1615-1618.

139. Reznik, S.N., et al., *Evolution of a compound droplet attached to a core-shell nozzle under the action of a strong electric field.* Physics of Fluids, 2006. **18**: p. 062101.

140. Li, D., et al., *Nanofibers of Conjugated Polymers Prepared by Electrospinning with a Two-Capillary Spinneret.* Advanced Materials, 2004. **16**(22): p. 2062-2066.

141. Reznik, S.N., et al., *Evolution of a compound droplet attached to a core-shell nozzle under the action of a strong electric field.* Physics of Fluids, 2006. **18**.

142. Hansen, C.M., *Hansen solubility parameters: a user's handbook* 2nd ed. 2007: CRC Press: Taylor and Francis Group. 519.

143. Williams, D.L. and Karl D. Kuklenz, *A Determination of the Hansen Solubility Parameters of Hexanitrostilbene (HNS).* Propellants, Explosives, Pyrotechnics, 2009. **34**(5): p. 452-457.

144. Krevelen, D.W.v. and K.t. Nijenhuis, *Properties of Polymers*. 4th ed. 2009, Amsterdam: Elsevier B.V. 844.

145. Kumar, R., B. Singh, and S.S. Sekhon, *Effect of dielectric constant of solvent on the conductivity behavior of polymer gel electrolytes.* Journal of Materials Science, 2005. **40**(5): p. 1273-1275.

146. Sekhon, S.S., N. Arora, and H.P. Singh, *Effect of donor number of solvent on the conductivity behaviour of nonaqueous proton-conducting polymer gel electrolytes.* Solid State Ionics, 2003. **160**(3-4): p. 301-307.

147. Arinstein, A. and et al., *Buckling behaviour of electrospun microtubes: a simple theoretical model and experimental observations.* Journal of Physics D: Applied Physics, 2009. **42**(1): p. 015507.

148. Flegler, S.L., K.L. Klomparens, and J.W. Heckman, *Scanning and Transmission Electron Microscopy*. 1993, UK: Oxford University Press.

149. *IGA-001 Gas Sorption Analyser*. IGA Series Overview 2011; Available from: http://www.hidenisochema.com/products/iga-series/.

150. Pungor, E., *A Practical Guide to Instrumental Analysis*. 1995, Florida: Boca Raton.

151. Sepehri, S., et al., *Spectroscopic Studies of Dehydrogenation of Ammonia Borane in Carbon Cryogel.* The Journal of Physical Chemistry B, 2007. **111**(51): p. 14285-14289.

152. Tan, W.T., et al., *Sythesis and characterisation of grafted polystrene with acrylonitrile using gamma irradiation.* Journal of Applied Sciences, 2010. **10**: p. 139-144.

153. Bernazzani, P. and R.F. Sanchez, *Structural and thermal behavior of polystyrene thin films using ATR–FTIR–NanoDSC measurements.* Journal of Thermal Analysis and Calorimetry 2009 **96**: p. 727–73.

154. Suryanarayana, C. and M. Grant Norton, *X-ray Diffraction: A practical approach*. 1998, New york: Plenum Press. 273.

155. Price, D.L. and S. Kurt, *Introduction to neutron scattering*. 1986, Orlando, Florida: Academic Press Inc. 549.

156. Squires, G.L., *Introduction to the Theory of Thermal Neutron Scattering*. 1978, Cambridge, New York: Cambridge University Press

157. ISIS. *IRIS*. 2011; Available from: http://www.isis.stfc.ac.uk/instruments/iris/.

158. ISIS. *TOSCA*. 2011; Available from: http://www.isis.stfc.ac.uk/instruments/tosca/.

159. Orme, C.J., et al., *Testing Of Polymer Membranes For The Selective Permeability Of Hydrogen.* Separation Science and Technology, 2003. **38**(12 & 13): p. 3225–3238.

160. Stephens, F.H., V. Pons, and R.T. Baker, *Ammonia-borane: the hydrogen source par excellence?* Dalton Transactions, 2007(25): p. 2613-2626.

161. Schubert, D.M., ed. Borax Pioneer. Vol. 20. 2001. 8.

162. Wolf, G., J.C. van Miltenburg, and U. Wolf, *Thermochemical investigations on borazane (BH3-NH3) in the temperature range from 10 to 289 K.* Thermochimica Acta, 1998. **317**(2): p. 111-116.

163. Li, J., F. Zhao, and F. Jing, *B--H*$^{\delta}$ *sigma bond as dihydrogen bond acceptor: Some theoretical observations and predictions.* The Journal of Chemical Physics, 2002. **116**(1): p. 25-32.

164. Bowden, M.E., G.J. Gainsford, and W.T. Robinson, *Room-Temperature Structure of Ammonia Borane.* J Australian Journal of Chemistry, 2007. **60**(3): p. 149-153

165. Matus, M.H., et al., *Reliable Predictions of the Thermochemistry of Boron−Nitrogen Hydrogen Storage Compounds: BxNxHy, x = 2, 3.* The Journal of Physical Chemistry A, 2007. **111**(20): p. 4411-4421.

166. Staubitz, A., A.P.M. Robertson, and I. Manners, *Ammonia-Borane and Related Compounds as Dihydrogen Sources.* Chemical Reviews, 2010. **110**(7): p. 4079-4124.

167. Burnett, L.J. and B.H. Muller, *Melting points of ethane and three of its deuterated modifications.* Journal of Chemical & Engineering Data, 1970. **15**(1): p. 154-157.

168. Shore, S.G. and R.W. Parry, *The crystalline compound ammonia-borane,* NH_3NH_3. Journal of the American Chemical Society, 1955. **77**(22): p. 6084-6085.

169. Lippert, E.L. and W.N. Lipscomb, *The structure of* H_3NBH_3. Journal of American Chemical Society, 1956. **78** (2): p. 503–504.

170. Hoon, C.F. and E.C. Reynhardt, *Molecular dynamics and structures of amine boranes of the type* $R_3N.BH_3$ *. I. X-ray investigation of H 3 N.BH 3 at 295K and 110K.* Journal of Physics C: Solid State Physics, 1983. **16**(32): p. 6129.

171. Hess, N.J., et al., *Neutron Powder Diffraction and Molecular Simulation Study of the Structural Evolution of Ammonia Borane from 15 to 340 K.* The Journal of Physical Chemistry A, 2009. **113**(19): p. 5723-5735.

172. Yang, J.B., et al., *Structural evolution of ammonia borane for hydrogen storage.* Applied Physics Letters, 2008. **92**(9): p. 091916-3.

173. Dillich, S., *FY 2009 Annual Progress Report* H. US Department of Energy, Fuel Cells & Infrastructure Technologies, Editor. 2009: Washington, D.C. 20585-0121. p. 389-397.

174. Baitalow, F., et al., *Thermal decomposition of B-N-H compounds investigated by using combined thermoanalytical methods.* Thermochimica Acta, 2002. **391**(1-2): p. 159-168.

175. Hausdorf, S., et al., *A procedure for the regeneration of ammonia borane from BNH-waste products.* International Journal of Hydrogen Energy, 2008. **33**(2): p. 608-614.

176. Davis, B.L., et al., *Efficient Regeneration of Partially Spent Ammonia Borane Fuel.* Angewandte Chemie International Edition, 2009. **48**(37): p. 6812-6816.

177. Sutton, A.D., et al., *Recycle of tin thiolate compounds relevant to ammonia-borane regeneration.* Chemical Communications, 2010. **46**(1): p. 148-149.

178. Shaw, W., et al., *In Situ Multinuclear NMR Spectroscopic Studies of the Thermal Decomposition of Ammonia Borane in Solution.* Angewandte Chemie International Edition, 2008. **47**(39): p. 7493-7496.

179. Metin, O.n. and S. OÌˆzkar, *Hydrogen Generation from the Hydrolysis of Ammonia-borane and Sodium Borohydride Using Water-soluble Polymer-stabilized Cobalt(0) Nanoclusters Catalyst.* Energy & Fuels, 2009. **23**(7): p. 3517-3526.

180. Jun-Min, Y., et al., *Iron-Nanoparticle-Catalyzed Hydrolytic Dehydrogenation of Ammonia Borane for Chemical Hydrogen Storage13.* Angewandte Chemie International Edition, 2008. **47**(12): p. 2287-2289.

181. Chandra, M. and Q. Xu, *A high-performance hydrogen generation system: Transition metal-catalyzed dissociation and hydrolysis of ammonia-borane.* Journal of Power Sources, 2006. **156**(2): p. 190-194.

182. Bluhm, M.E., et al., *Amineborane-Based Chemical Hydrogen Storage: Enhanced Ammonia Borane Dehydrogenation in Ionic Liquids.* Journal of the American Chemical Society, 2006. **128**(24): p. 7748-7749.

183. Miller, A.J.M. and J.E. Bercaw, *Dehydrogenation of amine-boranes with a frustrated Lewis pair.* Chemical Communications, 2010. **46**(10): p. 1709-1711.

184. Denney, M.C., et al., *Efficient Catalysis of Ammonia Borane Dehydrogenation.* Journal of American Chemical Society, 2006: p. 12048–12049.

185. Feaver, A., et al., *Coherent Carbon Cryogel Ammonia Borane Nanocomposites for H2 Storage.* The Journal of Physical Chemistry B, 2007. **111**(26): p. 7469-7472.

186. Gutowska, A., et al., *Nanoscaffold Mediates Hydrogen Release and the Reactivity of Ammonia Borane.* Angewandte Chemie International Edition, 2005. **44**(23): p. 3578-3582.

187. Hu, M.G., R.A. Geanangel, and W.W. Wendlandt, *The thermal decomposition of ammonia borane.* Thermochimica Acta, 1978. **23**(2): p. 249-255.

188. Sit, V., R.A. Geanangel, and W.W. Wendlandt, *The thermal dissociation of* NH_3BH_3. Thermochimica Acta, 1987. **113**: p. 379-382.

189. Karkamkar, A.J., C.L. Aardahl, and T. Autrey, *Recent Developments on Hydrogen Release from Ammonia Borane.* Material Matters, 2007. **2**: p. 6-9.

190. Wolf, G., et al., *Calorimetric process monitoring of thermal decomposition of B-N-H compounds.* Thermochimica Acta, 2000. **343**(1-2): p. 19-25.

191. Stowe, A.C., et al., *In situ solid state 11B MAS-NMR studies of the thermal decomposition of ammonia borane: mechanistic studies of the hydrogen release pathways from a solid state hydrogen storage material.* Physical Chemistry Chemical Physics, 2007. **9**(15): p. 1831-1836.

192. Bowden, M., et al., *The thermal decomposition of ammonia borane: A potential hydrogen storage material.* Current Applied Physics, 2008. **8**(3-4): p. 498-500.

193. Heldebrant, D.J., et al., *The Effects of Chemical Additives on the Induction Phase in Solid-State Thermal Decomposition of Ammonia Borane.* Chemistry of Materials. **20**: p. 5332–5336.

194. Kim, H., et al., *Determination of Structure and Phase Transition of Light Element Nanocomposites in Mesoporous Silica: Case study of NH3BH3 in MCM-41.* Journal of the American Chemical Society, 2009. **131**(38): p. 13749-13755.

195. Wang, L.-Q., et al., *Hyperpolarized* ^{129}*Xe NMR Investigation of Ammonia Borane in Mesoporous Silica.* Jounal of Physical Chemistry C, 2009. **113**: p. 6485–6490.

196. Schellenberg, J., *Syndiotactic Polystyrene: Synthesis, Characterization, Processing, and Applications*, ed. J. Schellenberg. 2009, New jersey: John Wiley and Sons Inc.

197. Chen, H., H. Xu, and P. Cebe, *Thermal and structural properties of blends of isotactic with atactic polystyrene.* Polymer, 2007. **48**(21): p. 6404-6414.

198. Wang, D.L., K. Li, and W.K. Teo, *Phase separation in polyetherimide/solvent/nonsolvent systems and membrane formation.* Journal of Applied Polymer Science, 1999. **71**(11): p. 1789-1796.

199. Dror, Y., et al., *One-Step Production of Polymeric Microtubes by Co-electrospinning.* Small, 2007. **3**(6): p. 1064-1073.

200. Arinstein, A. and E. Zussman, *Postprocesses in tubular electrospun nanofibers.* Physical Review Letter E 2007. **76**: p. 056303.

201. Dayal, P. and T. Kyu, *Dynamics and morphology development in electrospun fibers driven by concentration sweeps.* Phys. Fluids, 2007. **19**: p. 107106-1 - 107106-9.

202. Dayal, P., et al., *Experimental and theoretical investigations of porous structure formation in electrospun fibers.* Macromol., 2007. **40**: p. 7689-7694.

203. Guenthner, A.J., et al., *Dynamics of hollow nanofiber formation during solidification subjected to solvent evaporation.* Macromol. Theory Simul., 2006. **15**: p. 87-93.

204. Megelski, S., et al., *Micro- and nanostructured surface morphology on electrospun polymer fibers.* Macromol., 2002. **35**: p. 8456-8466.

205. Casper, C.L., et al., *Controlling Surface Morphology of Electrospun Polystyrene Fibers: Effect of Humidity and Molecular Weight in the Electrospinning Process.* Macromol. , 2003. **37**(2): p. 573-578.

206. Medeiros, E.S., et al., *Effect of relative humidity on the morphology of electrospun polymer fibers.* Can. J. Chem., 2008 **86**: p. 590–599.

207. Pai, C.-L., M.C. Boyce, and G.C. Rutledge, *Morphology of porous and wrinkled fibers of polystyrene electrospun from dimethylformamide.* Macromol., 2009. **42**: p. 2102-2114.

208. Medeiros, E.S., et al., *Effect of relative humidity on the morphology of electrospun polymer fibers.* Canadian Journal of Chemistry, 2008 **86**: p. 590–599.

209. Saeki, S., et al., *Upper and lower critical solution temperatures in polystyrene solutions.* Macromol., 1972. **6**: p. 246-250.

210. Li, F., X.-Y. Yin, and X.-Z. Yin, *Instability analysis of a coaxial jet under a radial electric field in the nonequipotential case.* Phys. Fluids, 2006. **18**(3): p. 037101-13.

211. Hohman, M.M., et al., *Electrospinning and electrically forced jets. I. Stability theory.* Phys. Fluids, 2001. **13**(8): p. 2201-2220.

212. Li, F., X.-Y. Yin, and X.-Z. Yin, *Axisymmetric and non-axisymmetric instability of an electrified viscous coaxial jet.* J. Fluid Mech., 2009. **632**(-1): p. 199-225.

213. Beerbower, A., *Surface free energy: A new relationship to bulk energies.* J. Colloid Interface Sci., 1971. **35**(1): p. 126-132.

214. Hansen, C.M. and E. Wallström, *On the Use of Cohesion Parameters to Characterize Surfaces.* J. Adhes., 1983. **15**(3): p. 275-286.

215. Palumbo, O., et al., *Decomposition of NH_3BH_3 at sub-ambient pressures: A combined thermogravimetry-differential thermal analysis-mass spectrometry study.* J. Power Sources, 2010. **195**(6): p. 1615-1618.

216. Sun, Y.S. and E.M. Woo, *Morphology and crystal structure of cold-crystallized syndiotactic polystyrene.* Polymer, 2001. **42**(5): p. 2241-2245.

217. Dollase, W.A., *Correction of intensities for preferred orientation in powder diffractometry: application of the March model.* Journal of Applied Crystallography, 1986 **19**: p. 267-272.

218. Lovell, A., et al., *Quantum Delocalization of Molecular Hydrogen in Alkali-Graphite Intercalates.* Physics Review Letters, 2008. **101**: p. 126101.

219. Watanabe, K., et al., *Sorption of Molecular Hydrogen by Potassium Graphite.* Nature, Phys. Sci., 1971: p. 160.

220. Watanabe, K., et al., *Molecular-sieve type sorption on alkali graphite intercalation compounds.* Proceedings of the Royal Society A: Mathematical, Physical and Engineering Sciences, 1973. **333**: p. 51-67.

221. Dresselhaus, M.S. and G. Dresselhaus, *Intercalation compounds of graphite.* Advances in Physics, 2002. **51**(1): p. 1-186.

222. Rouquerol, F., J. Rouquerol, and K. Sing, *Adsorption by powders and porous solids*. 1999, San Diego Academic Press.

223. Pace, E.L. and A.R. Siebert, *Heat of Adsorption of Parahydrogen and Orthodeuterium on Graphon.* The Journal of Physical Chemistry, 1959. **63**(9): p. 1398-1400.

224. Kuc, A., et al., *Hydrogen Sieving and Storage in Fullerene Intercalated Graphite.* Nano Letters, 2006. **7**(1): p. 1-5.

225. Dimitrakakis, G.K., E. Tylianakis, and G.E. Froudakis, *Pillared Graphene: A New 3-D Network Nanostructure for Enhanced Hydrogen Storage.* Nano Letters, 2008. **8**(10): p. 3166-3170.

226. Murray, J.J. and A.R. Ubbelohde, *Electronic Properties of Some Synthetic Metals Derived from Graphite.* Proceedings of the Royal Society of London. Series A, Mathematical and Physical Sciences, 1969. **312**(1510): p. 371-380.

227. Daumas, N. and A. Herold, C. r. hebd. Seanc. Acad. Sci. Paris C 1969. **268** p. 373

228. Enoki, T., S. Suzuki, and M. Endo, *Graphite Intercalation Compounds and Applications*. 2003: Oxford University Press.

229. Solin, S.A. and H. Zabel, *The physics of ternary graphite intercalation compounds.* Advances in Physics, 1988. **37**(2): p. 87 - 254.

230. Deng, W.-Q., X. Xu, and W.A. Goddard, *New Alkali Doped Pillared Carbon Materials Designed to Achieve Practical Reversible Hydrogen Storage for Transportation.* Physical Review Letters, 2004. **92**(16): p. 166103.

231. Patchkovskii, S., et al., *Graphene nanostructures as tunable storage media for molecular hydrogen.* Proceedings of the National Academy of Sciences of the United States of America, 2005. **102**(30): p. 10439-10444.

232. Nixon, D.E. and G.S. Parry, *Formation and structure of the potassium graphites.* British journal of applied physics, 1968. **1**: p. 291-299.

233. Arai, Y., Y. Shirikawa, and S. Tamaki, *Structural properties of low dimensional potassium metal in intercalated graphite.* Journal of Non-Crystalline Solids, 1996. **205-207**: p. 803-806.

234. Hastings, J.B., W.D. Ellenson, and J.E. Fischer, *Phase transitions in potassium intercalated graphite:* KC_{24} Physical Review Letters, 1979. **42**(23): p. 1552.

235. Nixon, D.E. and G.S. Parry, *Order-disorder transformation in potassium graphite.* Nature, 1967. **216**: p. 909-10.

236. DiCenzo, S.B., *Relaxed incommensurate structure of the intercalant layer in higher stage graphite intercalation compounds.* Physical review. B, 1982. **26**(10): p. 5878-5881

237. Rousseaux, F., et al., *X-ray study of the liquid and solid phases of the alkali metals in KC_{24} and CsC_{24}-intercalated graphite single crystal.* Physical Review. B 1990. **42**(1): p. 725.

238. Terai, T. and Y. Takahashi, *Formulation of isotherms for low-temperature absorption of H_2 and D_2 on KC_{24} prepared from natural graphite.* Synthetic Metals, 1989. **34**: p. 329-334.

239. Deng, W.-Q., X. Xu, and W.A. Goddard, *New alkali doped pillared carbon materials designed to achieve practical reversible hydrogen storage for transportation.* Physics Review Letters, 2004. **92(16):**(16): p. 166103.

240. Cabria, I., M.J. Lopez, and J.A. Alonso, *Enhancement of hydrogen physisorption on graphene and carbon nanotubes by Li doping.* The Journal of Chemical Physics, 2005. **123**(20): p. 204721-9.

241. Stead, W.J., P. Meehan, and J.W. White, *Librations of hydrogen in stage II caesium graphite, C24Cs.* Journal of the Chemical Society, Faraday Transactions 2: Molecular and Chemical Physics, 1988. **84**(10): p. 1655-1668.

242. Silvera, I.F., *The solid molecular hydrogens in the condensed phase: Fundamentals and static properties.* Reviews of Modern Physics, 1980. **52**(2): p. 393.

243. Ebert, L.B., *Intercalation Compounds of Graphite.* Annual Review of Materials Science, 1976. **6**: p. 181-211.

244. Fennessey, S.F. and R.J. Farris, *Fabrication of aligned and molecularly oriented electrospun polyacrylonitrile nanofibers and the mechanical behavior of their twisted yarns.* Polymer 2004. **45**(2004): p. 4217-4225.

245. Chand, S., *Review: Carbon fibers for composites.* Journal of Materials Science, 2000. **35**(6): p. 1303-1313.

246. Zussman, E., et al., *Mechanical and structural characterization of electrospun PAN-derived carbon nanofibers.* Carbon, 2005. **43**(10): p. 2175-2185.

247. Im, J.S., et al., *The effect of embedded vanadium catalyst on activated electrospun CFs for hydrogen storage.* Microporous and Mesoporous Materials, 2008. **115**(3): p. 514-521.

248. Li, M., G. Han, and B. Yang, *Fabrication of the catalytic electrodes for methanol oxidation on electrospinning-derived carbon fibrous mats.* Electrochemistry Communications, 2008. **10**(6): p. 880-883.

249. Shin, M.K., et al., *Enhanced conductivity of aligned PANi/PEO/MWNT nanofibers by electrospinning.* Sensors and Actuators B: Chemical, 2008. **134**: p. 122-126.

250. Xie, X.-L., Y.-W. Mai, and X.-P. Zhou, *Dispersion and alignment of carbon nanotubes in polymer matrix: A review.* Materials science and Engineering 2005. **49**(4): p. 89-112.

251. Yun, K.M., et al., *Nanoparticle filtration by electrospun polymer fibers.* Chemical Engineering Science, 2007. **62**(17): p. 4751-4759.

252. Brandl, W., et al., *Production and characterisation of vapour grown carbon fiber/polypropylene composites.* Carbon, 2004. **42**(1): p. 5-9.

253. Malkov, G.S. and E.R. Fisher, *Pulsed Plasma Enhanced Chemical Vapor Deposition of Poly(allyl alcohol) onto Natural Fibers.* Plasma Processes and Polymers, 2010. **7**(8): p. 695-707.

254. Chand, S., *Review: Carbon fibers for composites.* Journal of Materials Science, 2000. **35**: p. 1303 – 1313.

255. Diefendorf, R.J. and E. Tokarsky, *High Performance Carbon Fibers.* Polymer Engineering & Science, 1975. **15**(3).

256. Bennet, S.C., D.J. Johnson, and W. Johnson, *Strength-structure relationships in PAN based carbon fibres.* Journal of Materials Science, 1983. **19**: p. 3337-3347.

257. Simitzis, J. and S. Soulis, *Correlation of chemical shrinkage of polyacrylonitrile fibres with kinetics of cyclization.* Polymer International, 2008. **57**: p. 99–105.

258. Clarke, A.J. and J.E. Bailey, *Oxidation of Acrylic Fibres for Carbon Fibre Formation.* Nature, 1973. **243**: p. 146.

259. Grassie, N. and R. McGuchan, *Pyrolysis of polyacrylonitrile and related polymers.* European Polymer Journal, 1970. **6**: p. 1277-1291.

260. Keller, B.A., C. Lowe, and R. Hany, *Investigation of the Thermal Degradation of Polyacrylonitrile on Various Glasses.* European Polymer Journal, , 1970. **6**: p. 1277-1291.

261. Fitzer, E., W. Frohs, and M. Heine, *Optimization of stabilization and carbonization treatment of PAN fibres and structural characterization of the resulting carbon fibres.* Carbon, 1986. **24**(4): p. 387-395.

262. Keller, B.A., C. Löwe, and R. Hany, *Investigation of the thermal degradation of polyacrylonitrile on various glasses.* Surface and Interface Analysis, 1994. **22**(1-12): p. 284-289.

263. Ko, T.-H., S.-c. Liau, and M.-F. Lin, *Preparation of graphite fibres from a modified PAN precursor.* Journal of Materials Science, 1992. **27**: p. 6071-6078.

264. Rasband, W.S., *Image Processing and Analysis in Java*. 1997-2008, U. S. National Institutes of Health B, http://rsb.info.nih.gov/ij/: Maryland.

265. Grassie, N. and R. McGuchan, *Pyrolysis of polyacrylonitrile and related polymers--I. Thermal analysis of polyacrylonitrile.* European Polymer Journal, 1970. **6**(9): p. 1277-1291.

266. Fujimoto, H., *Theoretical X-ray scattering intensity of carbons with turbostratic stacking and AB stacking structures.* Carbon, 2003. **41**(8): p. 1585-1592.

267. Li, Z.Q., et al., *X-ray diffraction patterns of graphite and turbostratic carbon.* Carbon, 2007. **45**(8): p. 1686-1695.

268. Howells, W.S., et al., *The MODES User Guide* 2010: Oxforshire, UK.

269. Gilbert, E.P., P.A. Reynolds, and J.W. White, *Characterisation of a basal-plane-oriented graphite.* Journal of Chemical Society, Faraday Transactions 1998. **94**(13): p. 1861-1868.

270. Geissler, P.L., *Temperature Dependence of Inhomogeneous Broadening: On the Meaning of Isosbestic Points.* Journal of American Chemical Society, 2005. **127** p. 14930-14935.

List of Publications

1) Zeynep Kurban, Arthur Lovell, Derek Jenkins, Steve Bennington, Ian Loader, Alexander Schober , Neal Skipper, *European Polymer Journal* **46** (2010) 1194–1202

2) Zeynep Kurban, Arthur Lovell, Stephen M. Bennington, Derek W. K. Jenkins, Kate R. Ryan, Martin O. Jones, Neal T. Skipper, and William I. F. David, *Journal of Physical Chemistry C* **114** (2010), 21201–21213